Ultrafast out of equilibrium dynamics of materials driven by terahertz and/or optical excitations

Guénolé Huitric

UNIVERSITÉ DE RENNES 1

THESE DE DOCTORAT DE

L'UNIVERSITE DE RENNES 1

ECOLE DOCTORALE N° 596
Matière, Molécules, Matériaux
Spécialité : Physique

Par

Guénolé HUITRIC

Ultrafast out of equilibrium dynamics of materials driven by terahertz and/or optical excitations

Thèse présentée et soutenue à Rennes, le 06 décembre 2022
Unité de recherche : Institut de Physique de Rennes UMR 6251
Thèse N° :

Rapporteurs avant soutenance :

Pascal Ruello Professeur des Universités, IMMM, Le Mans - France
Nathalie Viart Professeure des Universités, IPCMS, Strasbourg - France

Composition du Jury :

Président : Etienne Janod Directeur de Recherche CNRS, IMN, Nantes - France
Examinateurs : Shinichiro Iwai Professeur des Universités, Tohoku University, Sendai - Japan

Dir. de thèse : Christophe Odin Maître de Conférences HDR, IPR, Rennes - France
Co-dir. de thèse : Eric Collet Professeur des Universités, IPR, Rennes - France

Acknowledgments

I would like to acknowledge all the people who contributed on a scientific level to my PhD work, or supported me during this journey.

First, I would like to thank all members of my PhD jury (Pr. Etienne Janod, Pr. Nathalie Viart, Pr. Shinichiro Iwai, Pr. Pascal Ruello) for the fruitful scientific discussions and for the time they spent on this task.

Then, I would like to express my gratitude to Christophe Odin and Eric Collet. Both of them are great individuals, excellent supervisors and they make a particularly complementary duo. They helped me growing as a scientist. The ending of my PhD was quite epic but the result that came out from our intensive discussions was worth it.

Also, I would like to thank Yann Le Gal (ISCR) and people from the IMN team (Michael Rodriguez-Fano, Julien Tranchant, Zohra Khaldi) for the synthesis, preparation and characterization of the samples I have been investigating: TTF-CA and V_2O_3 respectively.

I would like also to thank Valérie, Bénédicte, Amandine and both Nathalie for their help.

If I have enjoyed so much my 3 years in Rennes, it is because the science I have been dealing with was extremely interesting but maybe even more due to the persons around which were great people. Therefore, I would like to thank Maciej Lorenc, Lucas Gournay, Marius Hervé, Thomas Gauthier, Bertrand Toudic, Ela Trzop, Niels Keller, Hervé Cailleau, Laurent Guérin, Marina Servol, the rest of the Materials and Light team, Céline Mariette, Marco Cammarata, Olena Popova and Jeanne Kergomard. Special thanks to Roman Bertoni and Nicolas Godin, who are good at experimental task, but not so good at darts, as well as Gaël Privault, who is the best PhD colleague that someone can hope for.

Also, I want to thank Eric Millour for providing the motivation to study physics and Régis Gauthier to carry on a PhD.

Then, I would like to express my gratitude to my parents, my brother, the rest of my entire family, my friends and my rugby team for their support. Finally, there are no words to express to Marion how important she was during this journey. I am so grateful and lucky.

Contents

Résumé

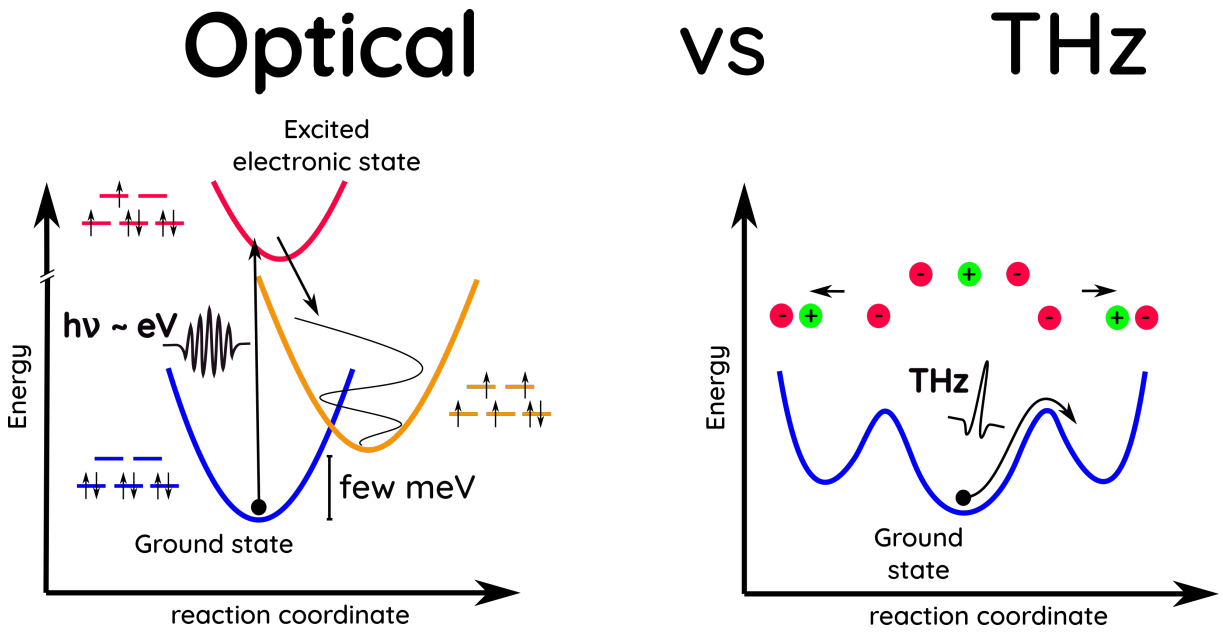

Figure 1: Réprésentation schématique des differentes courbes d'energie potentielle correspondants aux différents états rencontrés lors de l'excitation et la relaxation. Gauche: excitation visible; Droite: excitation THz.

La miniaturisation des composants électroniques et l'augmentation de leur vitesse atteindra bientôt une limite. Par conséquent, de nouveaux moyens de stockage de l'information doivent être trouvés. Une solution possible est l'utilisation d'impulsions lumineuses ultra-brèves pour modifier les propriétés d'un matériau sur demande et à des échelles de temps extrêmement courtes.

Dans les années 1990, Zewail et al. [Zewail, 2000] a montré qu'il était possible de déclencher et observer des transformations chimiques ultra-rapide au niveau moléculaire à l'aide de techniques "pompe-sonde". Ce type de technique utilise deux lasers à impulsions ultra-brèves. Le premier, appelé "pompe" excite le système et le promeut dans un état hors-équilibre. Le second: la "sonde" suit l'évolution d'une propriété physique perturbée par l'excitation. En modifiant le délai entre ces deux lasers, il est possible de reconstruire des dynamiques d'excitation et de relaxation à l'échelle de la picoseconde ou femtoseconde. L'utilisation de longueurs d'onde de pompe et/ou de sonde appartenant à différentes parties du spectre électromagnétique permet d'explorer différents phénomènes physiques. L'étude temporelle permet également de désenchevêtrer les contributions provenant des différents degrés de liberté internes du matériau.

Dans les cristaux moléculaires, une excitation locale peut déclencher une réponse coopérative [Koshihara et al., 1999], qui entraîne parfois une modification macroscopique de l'état du matériau: une transition de phase photo-induite [Nasu, 2004; Koshihara et al., 2022]. Ces transitions de phase photo-induite sont généralement déclenchées par des impulsions visibles. Malheureusement, ce type d'excitation engendre généralement des transitions électronique qui transfèrent une

énergie excédentaire importante au matériaux, ce qui induit une augmentation significative de sa température. L'état final préféré sera donc généralement celui de plus haute entropie. Au contraire, avec l'avènement des impulsions THz intenses (plusieurs centaines de kV/cm), il est possible de déposer une énergie plus faible. En effet, l'énergie par photon correspondant à ce type de radiation équivaut à quelques meV contre quelques eV pour une impulsion visible. Aussi la fréquence faible et l'important champ électrique associé aux THz permettent de modifier l'ordre polaire dans les matériaux. Un meilleur contrôle de l'état final peut donc être atteint (Voir Fig.1).

Le contrôle des matériaux par impulsions THz est un champ scientifique émergent. Ce type de radiation a déjà été utilisé pour induire des transitions de phase de type métal-isolant [Liu et al., 2012] ou encore de type paraelectrique-ferroélectrique [Li et al., 2019]. Dans cette thèse, nous avons étudié le contrôle des propriétés des matériaux par impulsion THz à travers l'excitation sélective de leurs différents degrés de libertés. Dans un premier temps seront discutés les différents montages et développements expérimentaux réalisés pendant ce travail. Ensuite on développera la génération et la propagation d'ondes de déformations dans la phase métallique du V_2O_3. On s'intéressera donc ici à l'interaction entre l'impulsion et le sous-système électronique. Puis, on étudiera la réponse d'un matériau (TTF-CA) à l'excitation résonante d'un de ses modes polaires (interaction avec le réseau). Ce mode étant impliqué dans une transition de phase paraelectrique-ferroelectrique, la possibilité d'induire cette transition sera donc évoquée.

A l'institut de Physique, une source de THz intense a été mise en place [Gournay, 2022]. Les THz sont générées dans un cristal de Niobate de Lithium ($LiNbO_3$) par la technique dite "d'inclinaison du front d'onde". A la sortie du cristal, après focalisation du faisceau à l'aide d'une série de miroirs paraboliques, on obtient un faisceau d'environ 800µm x 1100 µm de largeur à mi-hauteur au point focal. Le champ électrique maximal obtenu à cette position est de 250 kV/cm, avec une enveloppe spectral qui s'étend de 0 à 2.5 THz. On peut donc utiliser ce type de source comme pompe et/ou sonde.

La détection des THz se fait par échantillonnage électro-optique (EOS). Cette technique cohérente est basée sur l'effet Pockels. Le passage d'un champ électrique dans un cristal de détection (exemple: ZnTe, GaP) modifie ses indices de réfraction. La polarisation d'un faisceau de sonde est donc modifiée par cette biréfringence induite. Ce changement de polarisations permet ensuite de remonter au champ électrique THz. La géométrie entre les polarisation des faisceaux THz et sonde ainsi que les angles du cristal de détection sont donc primordiaux afin de quantifier la valeur du champ électrique THz. J'ai donc réalisé une calibration et optimisation de ce dispositif. Ce travail m'a également permis de mettre en place un montage expérimental de spectroscopie THz (THz TDS). Dans cette thèse, l'utilisation de ce montage a notamment permis de confirmer la bonne installation du système cryogénique, mise en lumière par l'évolution des modes d'absorption de l'Arginine avec la température. Enfin, ce montage s'est avéré intéressant comme outil de caractérisation (évaluation de la métallicité du V_2O_3 par exemple). D'autres montages expérimentaux peuvent êtres conçus en utilisant cette source de THz intenses. La majeure partie de cette thèse a donc été passé à mettre en place, développer et utiliser un montage pompe THz-sonde optique. Cette fois, au lieu de sonder dans la gamme THz, la sonde est localisée dans le domaine visible. On cherche donc à suivre les modifications de propriétés optiques du matériau (Réflexion/Transmission) induites par les impulsions THz dans cette gamme spectrale.

J'ai commencé par développer et utiliser ce dispositif pompe THz-sonde Optique pour étudier la génération et la propagation d'ondes de déformations dans le V_2O_3. Ce composé appartient à la famille des isolants de Mott. À pression atmosphérique et température ambiante, il se trouve dans une phase paramagnétique métallique (PM). L'application d'un pression négative suffisante entraîne une transition vers une phase isolante sans changement de propriétés magnétiques (PI: Isolant paramagnétique). Un important saut de volume a lieu à la transition ce qui semble

indiquer que les effets élastiques sont significatifs. Le but de ce travail est donc d'étudier ces effets élastiques (ondes de déformations) dans la phase PM pour, à terme, envisager une transition de phase induite par ce type de contraintes. Ce type de transition de phase a déja été réalisé dans un autre composé présentant une important saut de volume à la transition: le Ti_3O_5 [Mariette et al., 2021].

Lorsqu'une impulsion lumineuse est absorbée par un matériau, la température de son réseau augmente. La dilatation engendrée par cette hausse de température induit donc des contraintes. Ces dernières sont relâchées par la génération d'une onde de déformation qui se propagera à la vitesse du son dans le matériau. Le profil de cette onde de déformation est influencé par le profil d'absorption de l'impulsion lumineuse dans le matériau. Dans ce travail, nous avons donc étudié comment la longueur d'onde de pompe influe sur ce profil d'onde. La détection étant un autre élément clé des expériences pompe-sonde, nous nous sommes également intéressé à l'effet de la modification de la longueur d'onde de sonde.

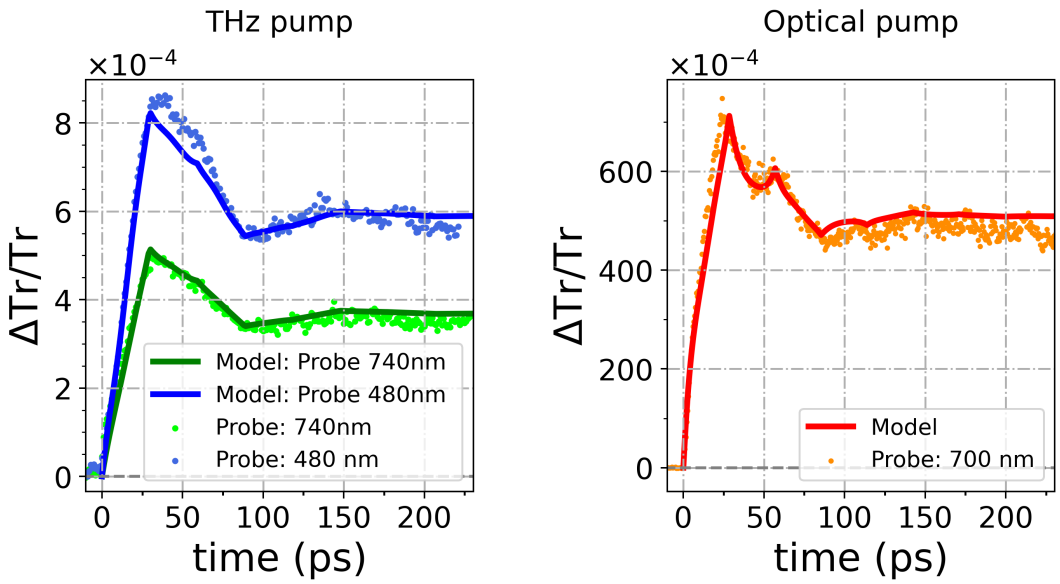

Figure 2: Signaux photo-induits (points) et leurs modélisations respectives (lignes) obtenus dans le V_2O_3 via différents dispositifs experimentaux. Gauche: Pompe THz Sonde 740 nm (vert) et 480 nm (bleu). Droite: Pompe visible (540 nm) Sonde 700 nm.

Dans la Fig.2 sont présentés les résultats expérimentaux Pompe THz / optique -Sonde optique obtenus en configuration de transmission. A gauche, on peut voir le signal photo-induit obtenus en utilisant une pompe THz (Sonde 740 nm: vert et Sonde 480 nm: bleu), et à droite celui obtenu avec une pompe visible (Sonde 700 nm). Ces signaux sont liés à la propagation d'ondes de déformations générées par effet thermoélastique.

On peut observer des similitudes entre tous ces signaux photo-induits: une augmentation du signal pendant environ 30 ps, suivi par une diminution jusqu'à 90 ps. On obtient alors un plateau qui dure plus de 800 ps. Dans une couche mince de 210 nm de V_2O_3, le temps acoustique correspond environ à 30 ps. On observe donc que les temps caractéristiques correspondants aux changements de comportement du signal photo-induit coïncident à des multiples du temps acoustique.

Un modèle thermoélastique nous a permis de reconstruire la structure des signaux photo-induits pour les deux types d'excitation (lignes dans la Fig.2), à condition de considérer qu'il y a inégalité entre l'impédance de la couche et celle du substrat. On notera que ce modèle permet de reproduire la différence majeure de signal induit par pompe THz et celui par pompe visible,

observable autour de 60 ps. En effet dans le cas visible, la baisse de signal semble s'opérer en deux temps et être arrondi, alors que dans le cas THz cette chute semble bien plus linéaire. D'après ce modèle, cette différence peut-être directement reliée à la différence de profils d'absorptions. Ce modèle a également permis d'extraire le profil de ses ondes de déformations à n'importe quel délai et profondeur dans l'échantillon, ce qui a confirmé que les ondes de déformations étaient bien plus homogènes dans le cas THz.

Le modèle thermoélastique permet également de prévoir un changement d'amplitude induit par une modification de la longueur d'onde de sonde (Voir à gauche dans Fig.2).

Enfin, une étude quantitative confirme que l'importante différence d'amplitude entre le cas pompe THz et celui pompe visible est principalement liée à la densité d'énergie déposée dans la couche mince. Il est important de noter que, de part l'homogénéité spatiale et la cohérence de l'excitation THz, d'importantes interférences constructives sont générées, ce qui tend à augmenter le dépôt d'énergie.

En conclusion, nous avons mis en lumière les nombreux avantages offerts par l'excitation THz (homogénéité spatiale, cohérence, faible densité d'énergie et augmentation de température limitée) pour générer des ondes de déformations. Cela peut s'avérer utile dans le but de réaliser des transitions de phase par ondes de déformations dans les matériaux possédant d'importantes différences de volume entre leurs phases.

L'autre grand axe de cette thèse porte sur l'excitation directe d'un phonon optique dans le TTF-CA. Ce mode étant impliqué dans la transition paraélectrique-ferroélectrique, cette excitation pourrait être particulièrement pertinente dans le but de contrôler les propriétés macroscopiques du matériau.

Le TTF-CA est un composé à transfert de charge construit à partir d'un empilement de molécules donneuses (TTF) et accepteuses (CA) d'électrons. Au dessus de T_{NI}=81 K, les molécules sont neutres et à égales distances les unes des autres. Sa structure est centrosymétrique. En dessous de T_{NI}, une dimérisation et un transfert de charge apparaissent de manière concomitante. Le composé est un ferroélectrique ionique. La transition de phase displacive entre cette structure paraélectrique et ferroélectrique est associée à un mode Bu qui s'amollit en s'approchant de T_{NI}. L'excitation direct de ce mode peut donc potentiellement entraîner cette transition de phase (Voir Fig.3). Dans ce travail, nous utiliserons un montage pompe THz Sonde Optique pour exciter ce mode ferroélectrique dès lors qu'il rentre dans la bande spectrale THz.

Le résultat obtenu à 100 K est présenté dans la Fig.3. Ce signal photo-induit est purement positif. Il est composé d'une première contribution à t= 0 ps suivi d'une ou plusieurs oscillations. Ce type de signaux a déjà été observé par Morimoto et al. [Morimoto, Miyamoto, Yamakawa, Terashige, Ono, Kida and Okamoto, 2017]. Il a été interprété comme le mouvement des parois de domaines ioniques induit par champ THz.

Selon nous, ce signal est composé de deux contributions. L'une est une réponse instantanée qui peut provenir de la réponse électronique ou bien de phonons de fréquences élevées et l'autre est la réponse à une excitation résonante du mode ferroélectrique Bu par l'impulsion THz. Cette dernière prend la forme de la convolution du champ électrique THz avec l'oscillation correspondant au mode ferroélectrique. A l'aide de considérations de symétrie, on peut montrer que, dans la phase paraélectrique (centrosymétrique), ces contributions doivent être élevées au carré. Notre modèle est donc constitué d'une contribution type effet Kerr ($\propto E_{THz}(t)^2$) et d'une oscillation purement positive. La période réelle de cette oscillation est donc égale au double de la période observée. Une modélisation (Voir violet à droite Fig.3) nous a permis d'extraire la fréquence de ce mode. Celle-ci est proche de celle mesurée par Masino et al. [Masino et al., 2003]. De plus, l'extraction de cette fréquence à plusieurs températures semble suivre l'amollissement mesuré par Masino et al.. Ces arguments sont donc en faveur d'une excitation résonante du mode ferroélectrique Bu.

Enfin une mesure proche de la transition (T$\approx T_{NI}$+4 K) résulte en un signal particulièrement

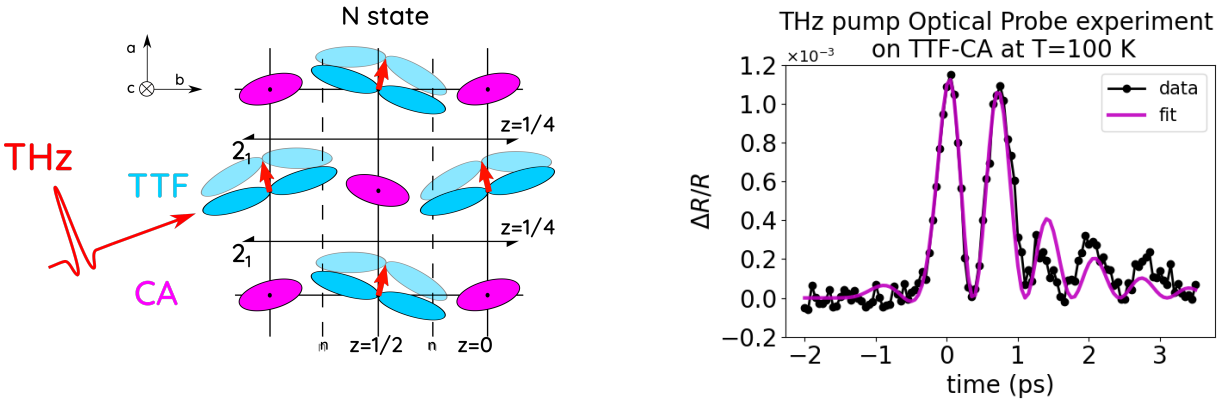

Figure 3: Gauche: Représentation schématique du mouvement qui fait suite à une excitation du mode férroelectrique par une impulsion THz; Droite: Comparaison entre le signal photo-induit obtenu à 100 K et la modélisation correspondante

différent des précédents (obtenus à plus hautes températures). Il est plutôt semblable à celui obtenu par Miyamoto et al. [Miyamoto et al., 2013] dans la phase de ferroélectrique (T$<T_{NI}$). Il est donc possible que nous ayons induit une transition de phase par excitation directe du mode ferroélectrique. Bien que la moyenne non nul du signal photo-induit semble être un autre argument en faveur de cette théorie, plusieurs mesures complémentaires devraient être réalisées pour confirmer cette tendance (mesure en fonction de la puissance, SHG etc ...).

En conclusion, nous avons démontré que l'utilisation d'impulsions THz dans le TTF-CA permet l'excitation directe du mode ferroélectrique Bu. Cette excitation étant impliquée dans la transition de phase paraélectrique-ferroélectrique, cela pourrait permettre d'induire cette transition de manière contrôlée.

Ce travail de thèse était axé sur le contrôle des matériaux par impulsions THz. Nous avons vu que ce type d'impulsion peut interagir avec différents degrés de libertés internes du matériau: électrons dans le cas du V_2O_3 et réseau pour le TTF-CA et par conséquent déclencher divers phénomènes (ondes de déformations, modification de la structure). L'étude approfondie de ces phénomènes nous a permis de prouver que, dans les deux cas, l'excitation THz était un outil adéquate pour modifier les propriétés des matériaux de manière plus contrôlée.

Introduction

The downscaling of electronic components and the increase of their speed will reach a limit. In this matter, new ways of storing information must be found. One of the solution might be the use of ultrashort light pulses to switch material properties on demand at ultrashort timescale. Triggering new stable macroscopic orders in materials by ultrafast optical or terahertz pump pulses is a difficult challenge, complicated by the interplay between multiscale, microscopic mechanisms, and macroscopic excitation profiles in samples.

In the 1990's, Zewail et al. [Zewail, 2000] showed the possibility to trigger and observe ultrafast chemical transformations at the molecular level using optical pump-probe techniques operating in the femtosecond range. A pump-probe experiment is a stroboscopic technique that makes use of two ultrashort laser pulses. The pump excites the system and triggers a non-equilibrium state. The probe monitors the evolution and relaxation pathway of the perturbed system as a function of the time delay between pump and probe. It allows to follow very fast physical phenomena occurring in the picosecond or femtosecond range (10^{-15} to 10^{-12} s). Typical monitored physical properties are optical transmission or reflectivity, crystalline structure (X-ray diffraction), etc. Using different parts of the electromagnetic spectrum offers a great variety of possibilities to excite and probe material degrees of freedom such as electrons, phonons, acoustic waves, magnons, polarons in both diluted phases and condensed matter.

In molecular crystals, a local excitation can trigger a global cooperative response [Koshihara et al., 1999], sometimes leading to a macroscopic modification of the state of the material: a photo-induced phase transition (PIPT) [Nasu, 2004; Koshihara et al., 2022]. Generally, optical excitation with visible light is used to induce such PIPT in materials. However, the excess energy provided to the system is very large, leading to significant thermal effects. While these effects can be useful to bring the system into a state of higher entropy, some states, and especially those of lower entropy, are inaccessible with classical optical excitation. Nowadays, more selective and direct control are needed in the field of material science.

Since the recent developements in Table-top TeraHertz (1 THz = 33 cm^{-1} = 300 µm = 4 meV) sources [Reimann, 2007] almost single cycle pulses with electric field amplitude larger than 100 kV/cm [Hirori et al., 2011] can be generated in the laboratory. This opens new excitation pathways, for instance resonant or non-resonant excitation of optical lattice vibrations that drives some structural phase transitions while reducing thermal effects [Kampfrath et al., 2013]. For those reasons, THz excitation appears to be an interesting tool to perform an ultrafast tuning of material property in a more controlled way [Salén et al., 2019; Nicoletti and Cavalleri, 2016].

During my thesis, I investigated the response of V_2O_3 (Mott insulator) and charge transfer compound TTF-CA to a THz or optical excitation. I developed and optimized a pump/probe set-up that allows the use of either THz or Optical excitation. Experimental results are supported by suitable models.

This manuscript is organized as follow:

In chapter 1, first, I make an introduction to pump-probe experiments. Second, I present the THz generation and detection techniques used in the "Materials and Light" team of the IPR. Third, I detail the characterization of the current setup and finally the experimental developments

required for the THz pump Optical probe and THz Time Domain Spectroscopy set-ups.

In chapter 2, I first discuss the generation and propagation of strain waves. For this purpose, I introduce the basics of the strain detection by ultrafast lasers. Then, I present photoinduced out-of-equilibrium physics reported in the V_2O_3. This system undergoes a Mott transition with an important change of volume. It shows that elastic effects are important in such transition. As a consequence, I studied the generation and propagation of strain waves in a Paramagnetic Metallic (PM) thin film of V_2O_3. I compared the signals obtained for two different excitation wavelengths (visible and THz) and various excitation powers. By comparing these two types of excitations, we deduced that the strain waves were generated via a thermoelastic process. Also, the differences in the transient signals were assigned to the difference in pump penetration depth. This penetration depth is of primary importance because it directly impact the strain depth profile. Finally, we studied the response of another thin film as a function of the temperature. This particular film undergoes two phase transitions (Insulator – Metal – Insulator) in temperature. The response will therefore vary as a function of the phase fraction. The comprehension of such phenomena may help in tailoring strain profiles for future strain-induced phase transitions in V_2O_3.

In chapter 3, I will first introduce the material studied : the mixed-stacked charge-transfer molecular compound TTF-CA (tetrathiafulvalene-p-chloranil). This system exhibits a neutral-ionic phase transition coupled to a ferroelectric structural symmetry breaking. Then, I will present experimental results I obtained by using intense THz excitations. These data can be interpreted as resulting from a resonant excitation by the THz pulse of the ferroelectric mode involved in the paraelectric to ferroelectric phase transition. This interpretation, supported by a model, differs from the current one reported in literature. More specifically, in my manuscript the transient change of reflectivity induced by an intense THz pulse is now interpreted as a combination of an instantaneous response originating from an intermolecular CT and the response of the resonant excitation of the Bu ferroelectric mode of TTF-CA. This mode is involved in the neutral-ionic phase transition, and its frequency is contained within the THz envelope ($\approx$ 1 THz). When approaching the temperature of the neutral-ionic transition, an additional signal is observed and interpreted as a transient change of CT. THz-driven activation of symmetry-breaking modes is a promising way to induce transient dynamical response that may move the system towards a ferroelectric phase.

Chapter 1

THz single cycle pulses to pump or probe materials: experimental set-up

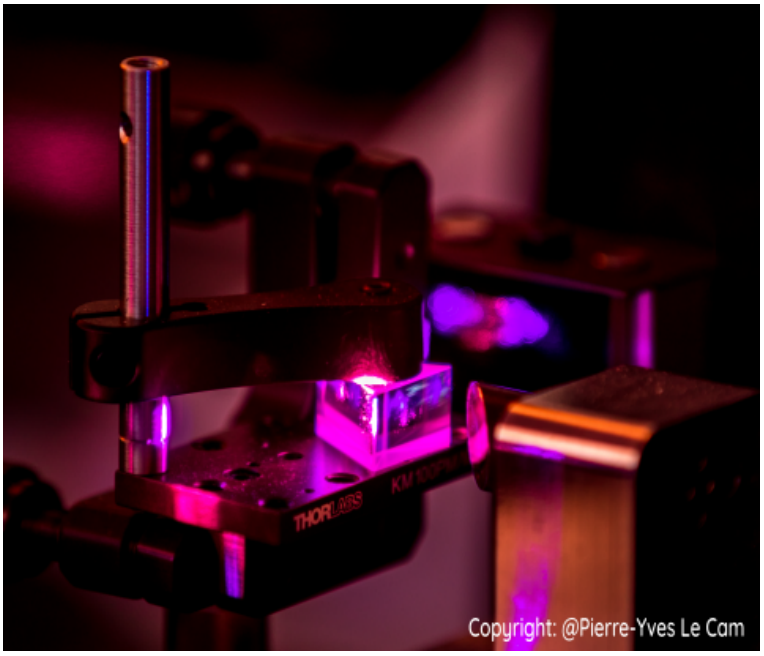

1.1 THz Generation and detection

1.1.1 Generalities about pump/probe experiments and THz radiation

The pump-probe technique is a time resolved technique used to overcome the time resolution limitation of fast electronics (10^{-10} s). A pump probe experiment is using two pulsed lasers (See Fig. 1.1). The pump is used to excite the system and to bring it out of its equilibrium state. A second laser is used to monitor a physical property that has been modified by the pump excitation : the probe. It is a stroboscopic technique. Series of excitations/relaxation and measurements are repeated. Between two series, the difference between the arrival time of the pump and the probe is incremented. A simultaneous arrival time for the pump and probe corresponds to a delay time equal to 0. At negative delay the probe monitors the physical property at its equilibrium state. No excitation has occurred yet. At positive delays, the physical property might be modified following the excitation. Time resolution is determined by the pulse duration of both pump and probe. It is therefore possible to reconstruct dynamics down to 10^{-12} s (picosecond: ps)/10^{-15} s (femtosecond : fs). Ultrafast phase transitions can even be revealed by this technique [Koshihara et al., 1999].

Electromagnetic waves spanning from THz to X-Rays can be used as pump or probe. These different electromagnetic radiations being related to different transitions, the most appropriate combination of wavelengths for pump and probe must be selected for the physics we are interested in. For example, X-rays can be used to probe atomic motions, optical beams (visible range) to trigger or follow electronic transitions and TeraHertz beams as probe to track the collapsing of bands gaps [Miyamoto et al., 2018] or excite soft phonon modes in ferroelectric systems [Li et al., 2019].

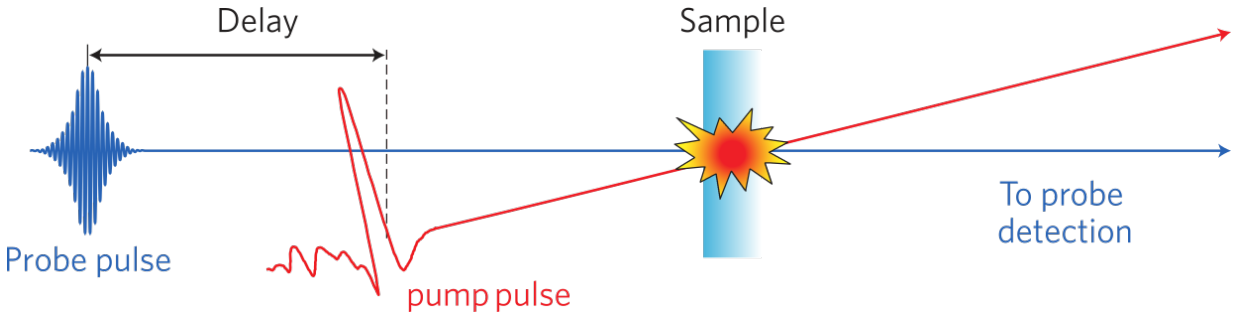

Figure 1.1: Schematic representation of a pump-probe experiment. Adapted from [Kampfrath et al., 2013]

A TeraHertz wave (labelled THz later) is an electromagnetic radiation located between infrareds and microwave radiations. In the XX's century, it was often inserted in the « far infrared » region. This frequency range spanning from 0.3 to 30 THz is of particular interest in the solid-state physics because its low frequency range matches with very slow motions (phonon, magnons, large amplitude vibrations of heavy molecules etc.) occurring in solids [Lee, 2009]. In semiconductors, band-gaps may also fall in this region. While the THz are quite common in the every day life (blackbody radiation), in the second half of the XX's century due to technical issues, this region was labeled as « THz gap » because of the lack of efficient source and detection systems. At the end of the XX's century effort were made to obtain broadband and intense THz sources. One of the first breakthrough came in 1985 when D.H Auston [Auston and Cheung, 1985] successfully generated and detected THz radiation via photo-conductive antenna. In 2002, Hebling et al. [Hebling et al., 2002] showed that it was possible to obtain very THz intense sources using a velocity matching method for pulses generated by optical rectification in non-centrosymmetric crystals. Nowadays several techniques has been developed to obtain broader or more intense THz

generations [Kitaeva, 2008; Salén et al., 2019] (See Fig.1.2).

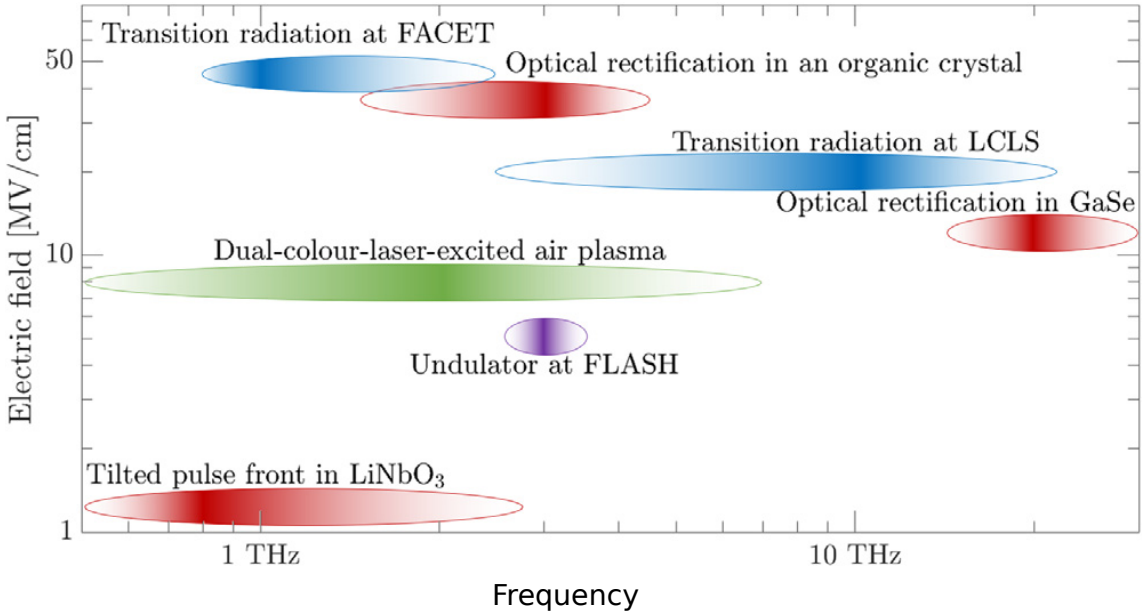

Figure 1.2: Various techniques to generate Intense THz pulses are represented by ellipses. The x axis is the frequency. The horizontal width of ellipses represents the bandwidth of the source. The central frequency is given by the brightest color inside these ellipses. The y axis position of the ellipses is the maximum field strength reachable by this technique. Adapted from [Salén et al., 2019]

The intensity and the spectral range of the THz radiation make this beam very versatile and suitable to be used as both pump and probe in time resolved experiments.

In this section, we present our experimental set-up.

1.1.2 THz Generation

1.1.2.1 Generalities

THz generation can be obtained from strong femto or picosecond laser pulses "Optical Rectification". This process can be understood using nonlinear optics principles. As a matter of fact, with the very high electric fields delivered by laser pulses, nonlinear polarization generates new frequency combinations, and is responsible of optical rectification, second harmonic generation, difference frequency generation, two-photon absorption, etc.

The polarization induced by the electric field can be written using a power expansion as a function of the electric field E(t):

$$P(t) = \epsilon_0 \chi^{(1)} E(t) + \epsilon_0 \chi^{(2)} E(t)^2 + \epsilon_0 \chi^{(3)} E(t)^3 + ... \tag{1.1}$$

$$P(t) = P^{(1)}(t) + \underbrace{P^{(2)}(t) + P^{(3)}(t) + ...}_{P^{NL}(t)} \tag{1.2}$$

where the first term corresponds to the linear polarization and the following terms correspond to the non linear polarization. With an increase of the electric field, higher order terms will become more and more relevant. The second order polarization will be non zero only in non centrosymmetric media while odd terms will always be present. The Optical rectification is a second order non linear effect, and is therefore contained in $P^{(2)}(t)$.

Considering a monochromatic beam, the complex electric field can be written as follows:

$$E(t) = \frac{E_0(\omega)e^{-j\omega t} + c.c}{2} \tag{1.3}$$

where c.c stands for complex conjugate.

The second order polarization is [Boyd, 2020]:

$$P^{(2)}(t) = \epsilon_0\chi^{(2)}E(t)^2 = \underbrace{2\epsilon_0\chi^{(2)}E_0E_0^*}_{P_{OR}} + \underbrace{\epsilon_0\chi^{(2)}E_0^2e^{-2j\omega t} + c.c}_{P_{SHG}(t)} \tag{1.4}$$

In the monochromatic case, the optical rectification is responsible for the dc component ($\omega = 0$) of the non linear polarization obtained by combining an electric field of frequency ω and its complex conjugate corresponding to frequency ω, with a zero sum $\omega + (-\omega) = 0$.

The second term is the Second Harmonic Generation (SHG) (at frequency 2ω) obtained by the combination of two photons of same frequency $\omega + \omega = 2\omega$.

Now we consider a polychromatic beam with frequencies spanning from ω_0 to $\omega_0 + \Omega$. By difference frequency between any two frequencies ω_1 and ω_2 in $[\omega_0,\omega_0+\Omega]$; it is possible to obtain a *quasi-DC* polarization at $\Omega' = \omega_1$ - ω_2.

In the case of continuous frequency distribution, the polarization in the frequency domain can be written:

$$P_{OR}(\Omega') = \frac{\epsilon_0}{2\pi}\int_0^{+\infty}\chi^{(2)}(\Omega',\omega+\Omega',-\omega)E(\omega+\Omega')E^*(\omega)d\omega \tag{1.5}$$

where $\Omega' \leq \Omega$. With femtosecond laser pulses, this process generates THz pulses, depending of the incoming pulse frequency bandwidth.

1.1.2.2 Phase matching

In any non linear effect, the generation efficiency strongly depends on the phase matching between the different radiations involved in the process. In our case, the phase matching condition is written as [Nahata et al., 1996]:

$$\Delta k = \underbrace{[k(\omega+\Omega) - k(\omega)]}_{Optical} - \underbrace{k(\Omega)}_{THz} = 0 \tag{1.6}$$

where k is the wavevector.

Considering that the spectral width of the Optical pulse is very small compared to its central frequency i.e $\Omega << \omega$, we can write at first order:

$$k(\omega+\Omega) - k(\omega) = \Omega\Big(\frac{dk}{d\omega}\Big) \tag{1.7}$$

leading to the phase matching condition:

$$\begin{aligned}\Delta k &= \Omega\Big(\frac{dk}{d\omega}\Big)_{\omega=\omega_0} - k(\Omega)\\ &= \frac{\Omega}{v_g^{opt}(\omega_0)} - \frac{\Omega}{v_\phi^{THz}(\Omega)}\\ &= 0\end{aligned} \tag{1.8}$$

where v_g^{opt} is the group velocity of the visible pulse and v_ϕ^{THz} is the phase velocity of the THz pulse.

The phase matching condition is therefore fulfilled when, in the generation medium, the group velocity of the optical pulse matches the phase velocity of the TeraHertz pulse generated upon the travel. This condition is easily obtained in some materials such as Zinc Telluride, Gallium Phosphide or organic cristals such as DAST, allowing a colinear geometry for the TeraHertz Generation.

1.1.2.3 THz Generation in $LiNbO_3$

In our setup we use a Lithium Niobate crystal $LiNbO_3$ to generate THz. With a space group R3c, the highest coefficient is the d_{33}=168pm/V (for stoichiometric $LiNbO_3$) [Hoffmann and Fülöp, 2011]. Thus, the highest polarization is obtained when the excitation pulse is along the c axis of the $LiNbO_3$, and the resulting emitted THz pulse will be polarized along this c axis.

$$P_{THz}(\Omega') = \frac{2\epsilon_0}{2\pi} d_{33} \int_0^{+\infty} E(\omega + \Omega') E^*(\omega) d\omega \tag{1.9}$$

For the case of Lithium Niobate [Hoffmann and Fülöp, 2011], the important difference between the refractive indices (n_g^{opt}=2.25 at 800nm and n_{THz}=4.96) implies different group velocities for the THz and Optical radiations and results in a non fulfillment of the phase matching requirement.

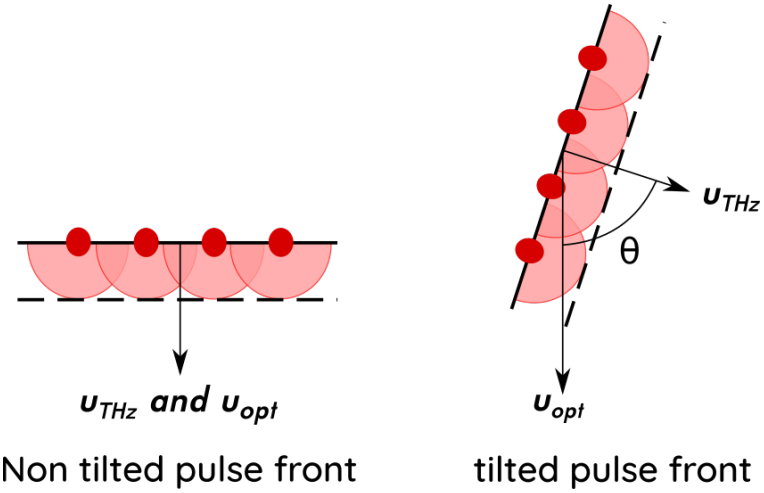

Figure 1.3: Schematic representation of THz generation. Left: in a non tilted pulse front configuration. Right: tilted pulse front configuration

In order to overcome this phase mismatching problem and allow a sufficiently long interaction length between the THz radiated and the optical pulse used for the generation, we use the tilted front technique [Hebling et al., 2002]. This technique is based on the lowering of the effective group velocity of the optical pulse by geometrical means.

According to Fresnel-Huygens principle, every point of a wavefront acts as a source of wavelets propagating spherically. Considering all the point sources (red dots in Fig.1.3) along the wavefront, the resulting wave will propagate colinearly with the optical beam. In this case, THz are interfering constructively in the forward direction and destructively in any other (See left panel of Fig.1.3). But, a tilt of the optical pulse wavefront will lead to a propagation of wavelets in a direction that is perpendicular to the wavefront, and moving at a speed v_{phi}^{THz}. Now the relevant optical speed is the projection of the group velocity pointing in the u_{opt} on the THz propagation direction u_{THz}. As a consequence, the phase matching condition is now (See [Hebling et al., 2002]):

$$v_{gr}^{opt} cos(\theta) = v_{\phi}^{THz} \tag{1.10}$$

where θ is the angle between the optical beam propagation direction and the perpendicular direction of the tilted wavefront.

Experimentally, the tilt of the wavefront is usually obtained using a reflection grating.

1.1.3 TeraHertz detection by Electro-Optical Sampling

External perturbations of different nature (mechanical, electrical etc) might affect temporarily the distribution of charges and modifies the optical properties of the solid. In particular, the linear

electro-Optic effect (or Pockels effect) can be used to detect terahertz electric fields.

When the THz propagates in a non-centrosymmetric material, at first order its refractive index is modified as follows:

$$n(E_{THz}) = n(0) + \Delta n(E_{THz}) = n(0) + rE_{THz} \tag{1.11}$$

The quasi-static THz electric field change the index of refraction of this material by $\Delta n(E_{THz}) = rE_{THz}$, with r the electro optic coefficient. Consequently, it will modify the phase of a copropagating optical probe by $\Gamma \sim \frac{2\pi\Delta n(E_{THz})d}{\lambda_{probe}}$ where d is the crystal thickness. Thus, it will also modify its polarization state. Measuring the change of polarization state of the optical probe beam gives the THz electric field amplitude as a function of time. This detection system is called EOS (stands for Electro-optical sampling). The detection crystals are often Zincblende cristals (e.g ZnTe or GaP). They are of -43m point group symmetry (cubic) and uniaxial (optical axis is the c axis).

1.2 Intense THz beam used as pump or probe in time resolved experiments as a function of temperature

In the IPR department "Materials and light", a pulsed THz setup is developed to obtain high electric fields (a few hundred kV/cm) able to switch material properties in the picosecond range when used as a source, or to measure the complex refractive index when used as a probe.

In this section, the development and optimization of the THz setup is described.

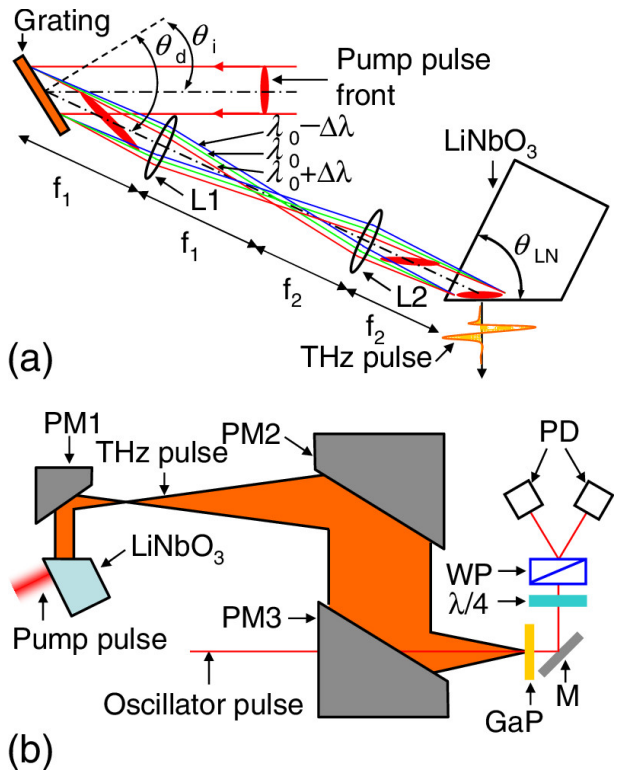

Figure 1.4: Schematic representation of the setup used to generate and detect THz radiation. (a): path of the 800 nm used to generate THz on $LiNbO_3$. The tilt of the 800 nm is obtained by a reflective grating. L1 and L2 are cylindrical lenses. (b): THz radiation focused down to 1mm of FWHM using a set of three parabolic mirrors (PM). The THz radiation are detected using an Electro-Optical system (GaP: detection crystal, $\lambda/4$ is a Quarter Wave plat, WP: Wollaston prism and PD: photodiodes). Figure from [Hirori et al., 2011])

1.2.1 Characterization of the source

1.2.1.1 THz source

The 3.5 W output of an Elite Amplifier (Coherent) is focused on a MgO doped 6mol% congruent $LiNbO_3$ crystal (isocele triangular prism with 15mm Xcut base. Base angle at 63°. Height=10mm) to generate vertically polarized THz radiation. To obtain the phase matching, the pulse front is tilted following the procedure presented by Hirori et al. [Hirori et al., 2011] (See Fig. 1.4), using a reflectivity grating [Gournay, 2022].

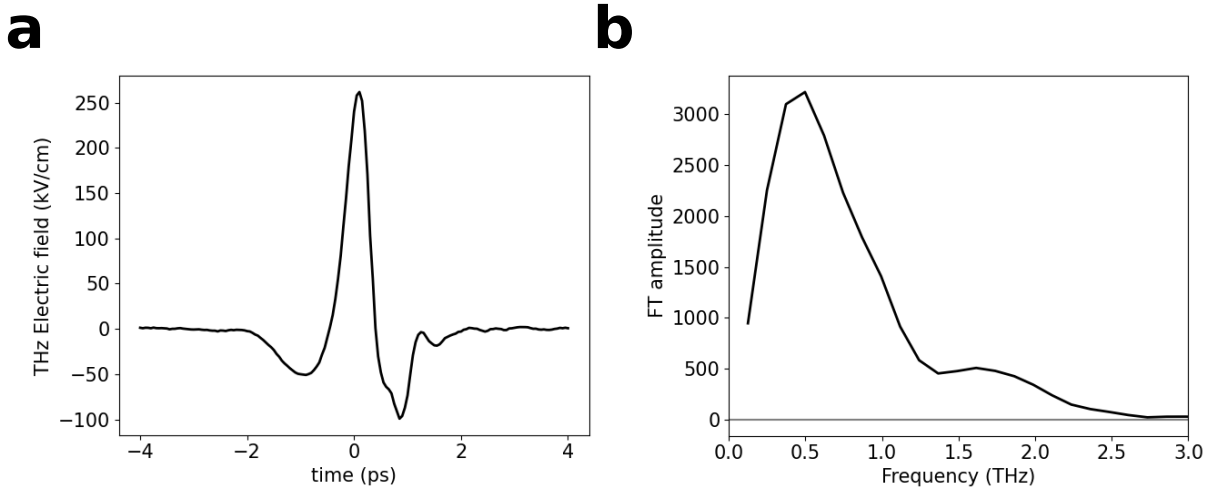

Figure 1.5: **a**: THz electric field times traces E(t) measured by EOS. **b**: Modulus of the Fourier Transform of E(t). Humidity: 4%.

The $LiNbO_3$ crystal is followed by a set of parabolic mirrors PM1, PM2, PM3 with respective focal length of 15.0 mm, 152.4 mm and 50.8 mm. With this procedure, at the focal spot, the beam waist of the THz radiation is equal to 800 by 1100μm of FWHM, measured by Pyroelectric Camera (Pyrocam III) (Fig. 1.6). After an Electro Optical Sampling (EOS) (See setup in Fig.1.4), the peak electric field amplitude is calculated and is equal to few hundreds of kV/cm ($\approx 250 kV/cm$) (**a** Fig.1.5). The bandwidth of the THz is spanning from 0 to 2.5 THz (**b** Fig.1.5).

1.2.1.2 Beam attenuation

In the lab, the attenuation of the beam is obtained by two means: THz polarizers or Si wafer.

The THz beam amplitude can be attenuated using a pair of THz polarizers (Tydex). These polarizers are polypropylene based polarizers covered by grooves coated with Al. The transmission axis is perpendicular to the grooves direction.

The transmission direction of a first polarizer, placed in between PM2 and PM3 is set vertical. A second THz polarizer is installed upstream, in a rotating mount. The rotation of this polarizer by an angle θ with respect to the vertical transmission axis of the first polarizer allows the progressive attenuation of the THz electric field amplitude, with a constant polarization along the vertical axis. This attenuation follows:

$$E_{THz}(\theta) = E_0 \, cos^2(\theta) \tag{1.12}$$

where $E_0 = E_{THz}(\theta = 0)$

In Fig.1.7 (Left: red dots) is shown the measurement of the maximum amplitude of the transient signal as a function of the rotation angle (θ) of the polarizer using an Electro Optical Sampling detection. The relation (1.12) is confirmed experimentally (See blue line in Left Fig.1.7).

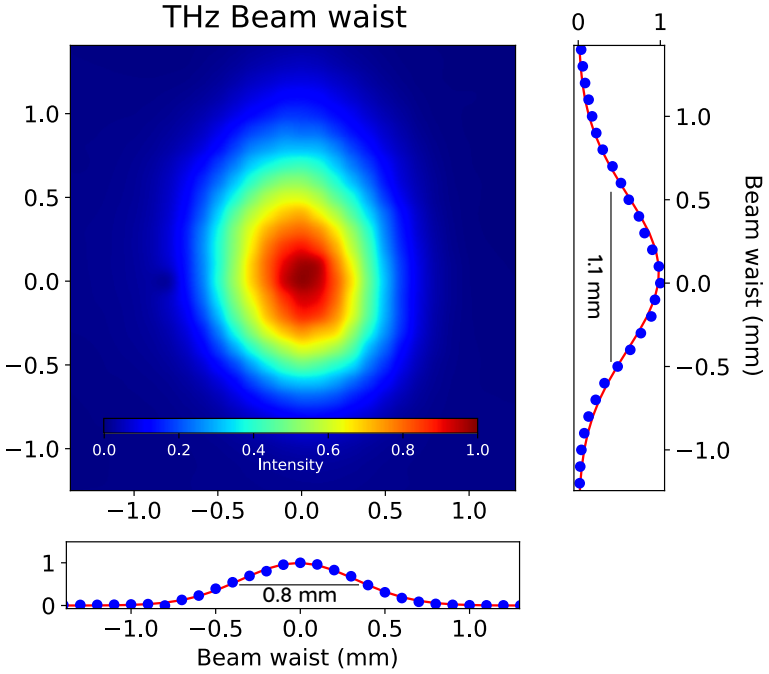

Figure 1.6: THz beam waist measured by a Pyroelectric camera.

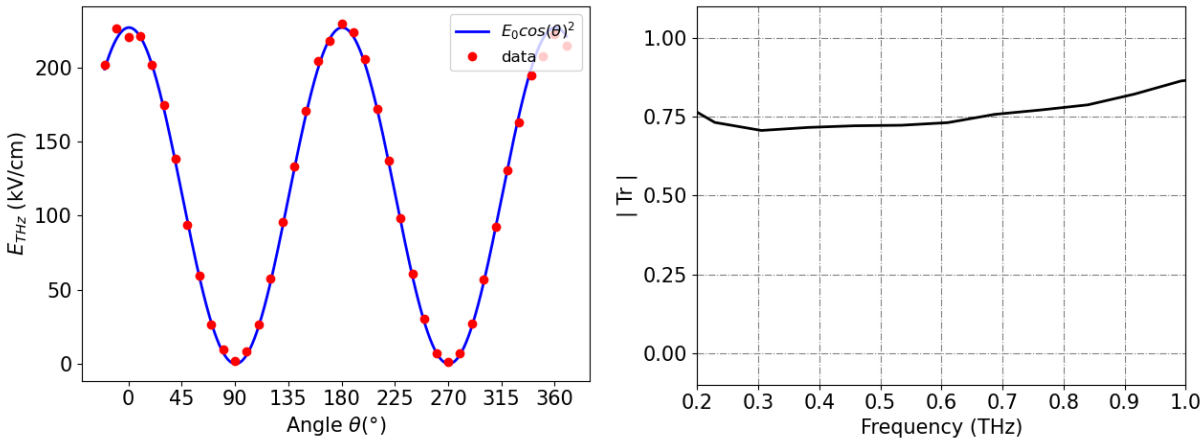

Figure 1.7: Left: Measure of the THz electric field amplitude $E_{THz}(\theta)$ as a function of the θ angle (i.e angle between the transmission axis of the rotating polarizer with respect to vertical transmission axis of the fixed one) (orange dots). The blue line represents the $E_{THz}(\theta) = E_0\ cos^2(\theta)$ function with E_0=226 kV/cm. Right: Modulus of the complex transmission of the 275 µm thick Si wafer presented in the range 0.2-1.0THz.

The beam can be attenuated using silicon sample. In our case, we used 275µm thick Si wafers. In the frequency range 0.2-1.0 THz, we found that its transmission was frequency independent and equal to 0.75, as seen in Fig.1.7. The reduction of the THz beam is discontinuous and follows $E_{THz} = E_0 \times 0.75^n$ where n is the number of Si wafer.

The addition of Si wafers is straightforward compared to the heavy setup that has to be mounted for the THz polarizers. Nevertheless, the THz polarizers were preferred because they offer a continuous control of the THz electric field amplitude.

1.2.1.3 Removal of parasitic visible beams

Part of the intense 800 nm is used to generate the THz beam, with a conversion efficiency from the 800 nm to the THz that is not equal to 1. As presented in section 1.1.2.1, some SH is also generated during this process. Also, part of the 800 nm photons can be reflected at the crystal surface or transmitted through the $LiNbO_3$ (See Fig.1.8). Finally some of these photons are propagating almost colinearly with the THz beam.

Since these parasitic beams have the same repetition rate as the THz beam, they perturb the detection (EOS or lock-in).

They usually have a wavelength equivalent to the probe wavelength used during the experiments, preventing the use of optical filters. To remove these parasitic beams, a beam dump was installed next to the $LiNbO_3$ (See Fig.1.8). Physical barriers (black and non reflecting) were installed to partition the experimental set-up. The photons propagating colinearly with the THz beam were stopped by a Teflon plate installed in between the PM2 and PM3. We checked that the THz response of the Teflon plate was flat within the pulse bandwidth.

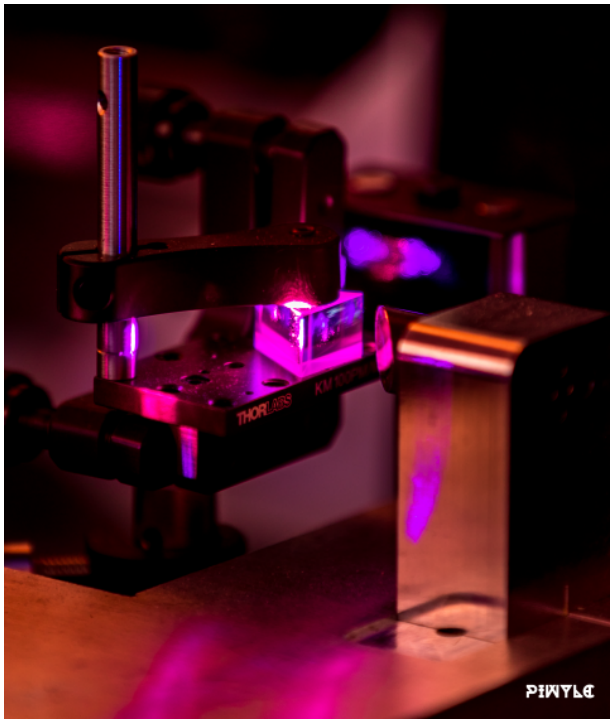

Figure 1.8: Photography of the $LiNbO_3$ prism in his holder. The beam dump is seen behind. Copyright: @Pierre-Yves Le Cam.

1.2.1.4 Influence of humidity

The concentration of water vapor in the air is very important when dealing with THz sources because it is absorbed by water. In frequency domain two major absorption lines can be observed: one at 1.13 THz and the other at 1.7 THz (Right Fig.1.9)[Lee, 2009]. This absorption is also seen in the time domain : the THz amplitude is decreased and delayed oscillations are seen (Left Fig.1.9).

A box installed around the THz setup, purged with dry air allows to get rid of part of the humidity. Two hours of purge reduces the humidity from 40% to 7%. It results in the removal of the absorption lines. The THz envelope is much less chaotic (brown in Right Fig.1.9). In the time domain, the majority of the oscillations disappears. Maintaining this low humidity content is particularly important for the THz TDS because the envelope will contain less absorption lines

but also because it increases the high frequency FT amplitude implying a broadening of the TDS spectrum.

This box can be opened from the top to perform the beam alignment (Fig.1.10). During the scan, the box is closed. A small aperture permits the introduction of the cryogenic cooling head. The N_2 flow enhance the purge and allows to reach a humidity level of 3%.

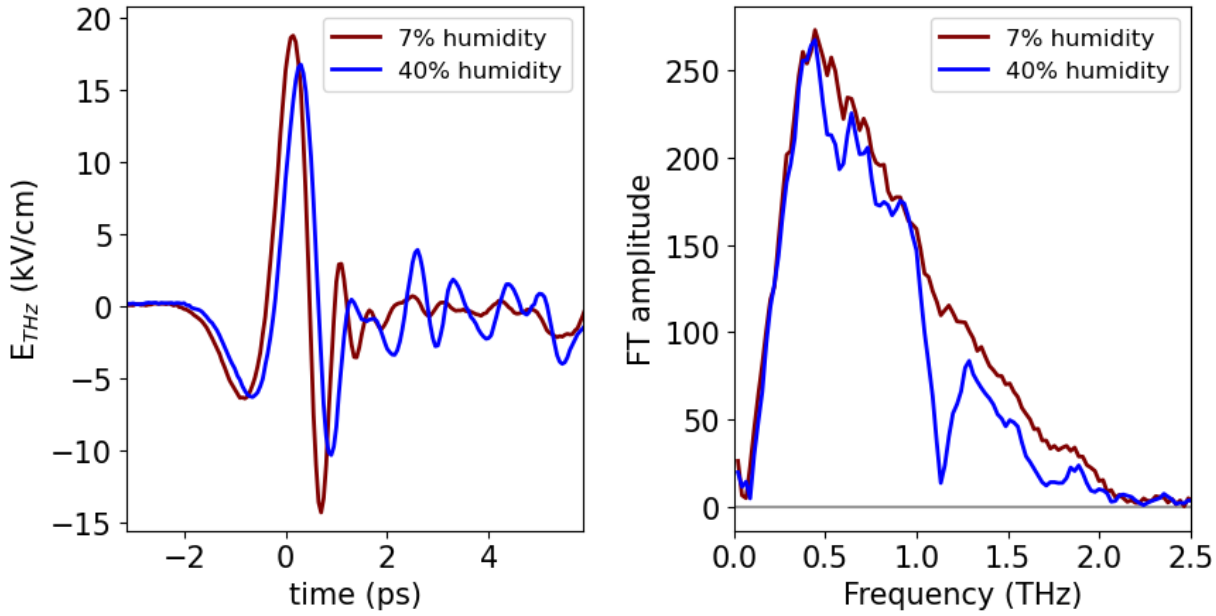

Figure 1.9: Left: Times traces of the THz electric field obtained at a humidity level of 7% (brown) and 40% (blue). Right: Their respective Fourier Transform

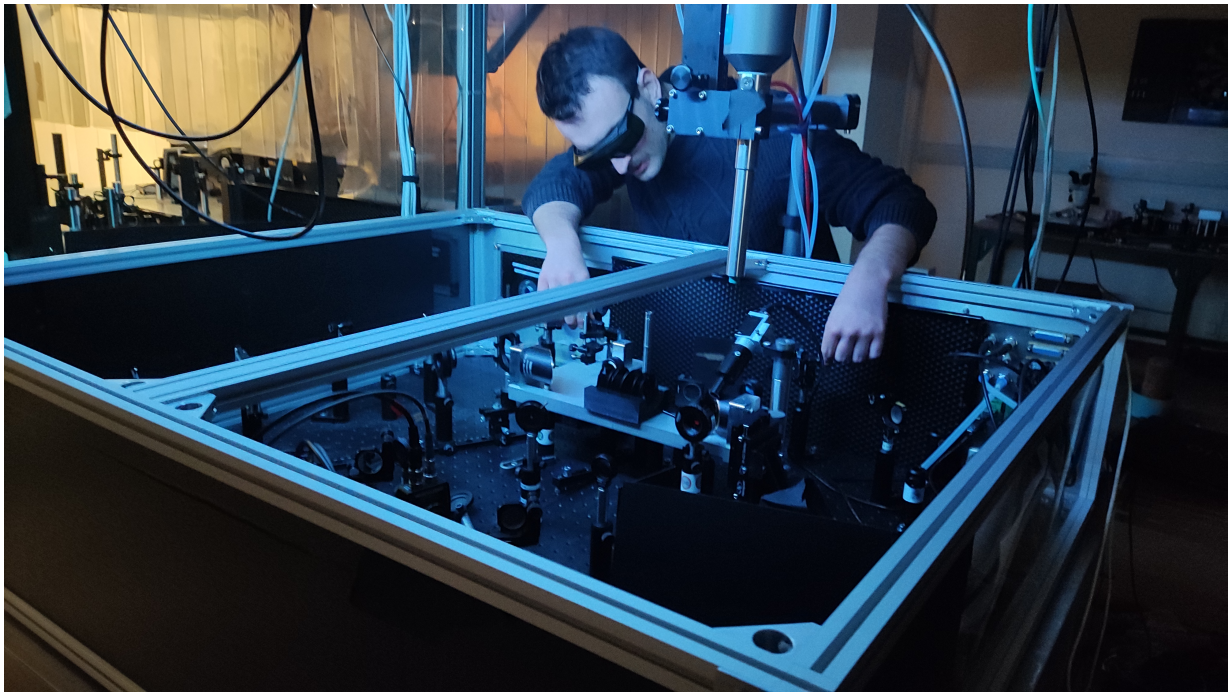

Figure 1.10: Purged box surrounding the THz source.

1.2.2 EOS setup and THz electric field amplitude

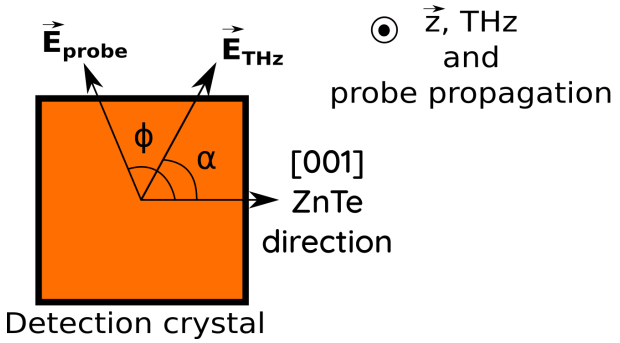

Figure 1.11: Presentation of the EOS configuration. α is the angle between the [001] ZnTe direction and E_{THz}. ϕ is the angle between the [001] ZnTe direction and E_{probe}

The optimization of the EOS detection system is critical in terms of alignment and polarization control. As explained in section 1.1.3, the linear electro optic effect (Pockels effect) is used to measure the THz pulse amplitude as a function of time.

The modification of the refractive index induced by the THz beam depends on the relative orientation of the probe crystal axes, and on the polarization state of the copropagating THz and optical probe beams (See Fig.1.11). When $r_{41}E_{THz}$ is small compared to 1, the expression of Δn is:

$$\Delta n = n^3 r_{41} E_{THz}[-cos(2\theta)cos(\alpha) + 2cos(\alpha + 2\theta)]/2 \tag{1.13}$$

where α is the angle between the [001] ZnTe direction and E_{THz} and $tan(-2\theta) = 2tan(\alpha)$.

The induced birefringence Δn in the detection crystal change the probe beam linear polarization to an elliptic polarization. A quarter wave plate (QWP) is placed after the detection crystal to transform the linearly polarized probe light to circular polarization. Without phase shift (meaning with no TeraHertz Field), a circular polarization is obtained. On the other hand, if a phase shift exists, the linearly polarized probe light becomes elliptical in the detection crystal. A Wollaston prism placed after the quarter wave plate splits the circular or elliptical polarizations into two complementary components, monitored separately by two photodiodes.

The difference ΔI and the sum I_{tot} of the intensities of the two channels are then used to quantify the phase shift. The relative intensity variation is [Planken et al., 2001]:

$$\frac{\Delta I}{I_{tot}} = sin(2(\phi - \theta))sin(E_n X) \tag{1.14}$$

where $E_n = \omega L n^3 r_{41} E_{THz}/(2c)$ and X=$[-cos(2\theta)cos(\alpha) + 2cos(\alpha + 2\theta)]$.

In the case where $E_n \times X$ is small i.e small phase shift induced by the THz field over the crystal thickness L, we can approximate equation (1.14) as:

$$\frac{\Delta I}{I_{tot}} = sin(2(\phi - \theta))E_n X = \frac{\omega L r_{41} n^3 E_{THz}}{2c}[cos(\alpha)sin(2\phi) + 2sin(\alpha)cos(2\phi)] \tag{1.15}$$

In this case, the modulation of the signal has two global extrema of opposite sign, 180° apart from each other and separated by local extrema. For a small phase shift, the global and local extrema are easily distinguishable (See blue dashed line in Fig.1.13).

In Fig.1.13 (green dots) are presented our experimental results about the importance of the angle between the THz polarization and the [001] axis of ZnTe (angle α) on the signal modulation. When the probe (horizontal) and the THz (vertical) polarizations are perpendicular to each other, a maximum modulation is obtained when the THz are perpendicular (90° or 270°) to the [001] ZnTe axis. Typically, the largest intensity modulation is found only when $\vec{E}_{THz}$ and $\vec{E}_{probe}$ are perpendicular or parallel.

The agreement between the theoretical expression given by Planken et al. [Planken et al., 2001] and the experimental results allows us to conclude that our EOS is properly installed.

The final optimum geometry is shown in Fig.1.12.

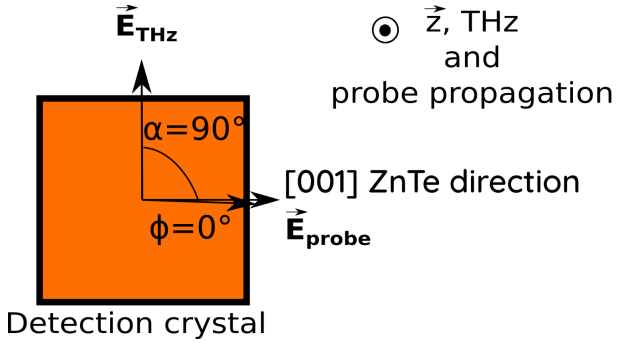

Figure 1.12: Presentation of the optimum EOS configuration. α is the angle between the [001] ZnTe direction and E_{THz}. ϕ is the angle between the [001] ZnTe direction and E_{probe}

Using n and r_{41} from the literature, the THz electric field can be estimated:

$$E_{THz} = arcsin(\frac{\Delta I}{I_{tot}})\frac{c}{\omega L r_{41} n^3 t_c} \tag{1.16}$$

where $t_c = 2n/(1+n)$ i.e the transmission coefficient of the detection crystal.

Parameter	Value	Reference
ZnTe		
r_{41}	4.04 pm/V	[Wu and Zhang, 1996]
n (visible)	2.85	[Wu and Zhang, 1996]
t (THz) / n (THz)	0.48 / 3.2	[Gallot et al., 1999]
thickness	500 or 1000 µm	
GaP		
r_{41}	0.88 pm/V	[Berozashvili et al., 1989]
n (visible)	3.2	[Edward and Palik, 1985]
t (THz) / n (THz)	0.46 / 3.34	[Hirori et al., 2011]
thickness	300 µm	

Table 1.1: Parameters used for the computation of the THz electric field amplitude. r_{41} is the electro optic coefficient. n the refractive index and t the Fresnel transmission coefficient, here: $t = 2/(n_{THz}+1)$. Away from resonant phonon frequencies, the static value of the electro-optic coefficient can be taken as a good approximation for its THz value [Coutaz, 2012].

By delaying the arrival time of the probe with respect to the pump, the time traces of THz electric field are obtained. The Fourier transform of this signal provides the THz envelope.

We note that the choice of the detection cristal is determinant. Crystals with important electro-optical coefficient and large thickness will undergo a greater phase shift and will therefore be much more sensitive to weak electric fields. It is convenient to keep a phase shift far from the maximum modulation. Therefore, as the Electric field increase, it will be necessary to reduce the phase shift either by introducing Si wafer to attenuate the THz field or by changing the detection crystal (ZnTe to GaP). We use a GaP crystal to measure the source field, and ZnTe for TDS like experiments. Their characteristics are found in Table.1.1

1.2.3 Cryogenic cooling system

I implemented a cryostream cooler (Oxford Cryostream). This device enables the cooling of sample of millimeter size from room temperature down to 85 K (N_2 stream) with a precision of

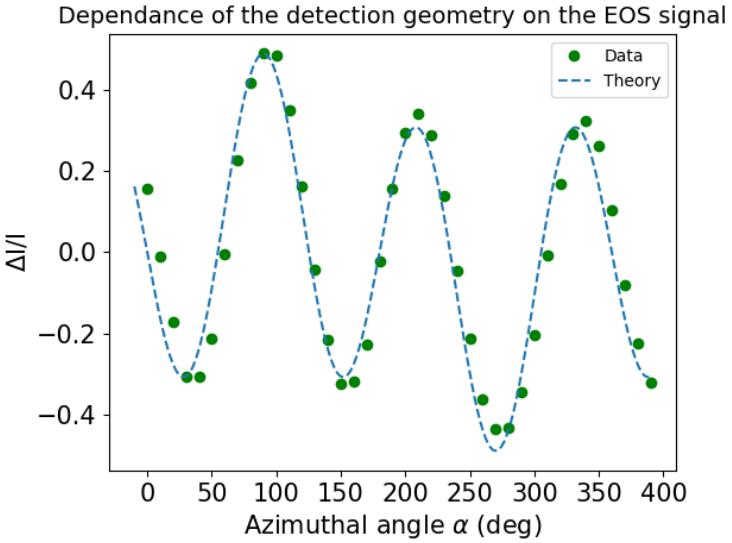

Figure 1.13: Study of the signal modulation as a function of the angle (α) between the THz polarization direction and the [001] ZnTe axis for a THz and probe polarization perpendicular to each other. Experimental results compare to the theory from [Planken et al., 2001]

$\pm$0.1 K.

Jewariya et al. [Jewariya et al., 2010] performed a THz TDS experiment on microcrystalline powder pellets of L-arginine ($C_6H_14N_4O_2$) and showed the important anharmonicity of the 1.09 THz vibrational mode. The frequency of this mode increases from between 0.95 THz at 300 K and 1.09 THz at 13 K. These results suggests to use L-arginine to verify the quality of our cryogenic cooling system. L-Arginine is also quite inexpensive. I prepared a 0.6 mm thick pellet of pure

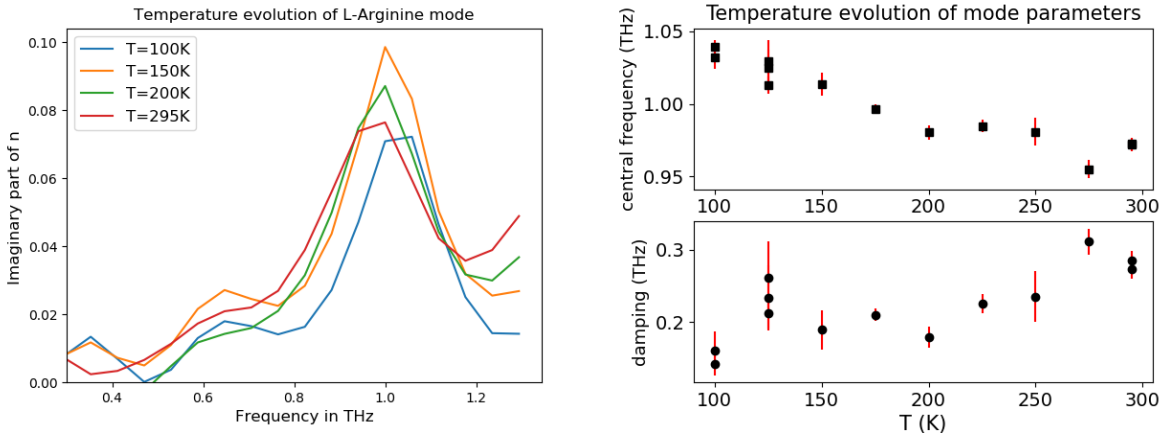

Figure 1.14: Left: Temperature evolution of the imaginary part of the refractive index for a 0.6 mm thick L-Arginine pellet measured in the THz range. Right: frequency (upper panel) and damping (lower panel) extracted from fit.

L-Arginine pressed under 500 bar. Using the TDS setup detailed in a next section, I extracted the imaginary part of the refractive indices as a function of frequency for different temperatures (right panel of Fig.1.14). A clear increase of the mode frequency is observed on cooling. However, to disentangle the contribution arising from the mode located around 1 THz and the other located around 1.6 THz [Jewariya et al., 2010], I performed a fit of the absorption profile using the sum

of two Lorentz oscillators [Fischer et al., 2002]:

$$\epsilon(\nu) = \epsilon_\infty + \frac{S_1\,\nu_1^2}{\nu_1^2 - \nu^2 - i\,\nu\Gamma_1} + \frac{S_2\,\nu_2^2}{\nu_2^2 - \nu^2 - i\,\nu\Gamma_2} \tag{1.17}$$

where ϵ_∞ is the high frequency dielectric function, S_j being the strength of the oscillator, ν_j its central frequency, Γ_j the linewidth, ν the frequency and the subscript j correspond to the mode located at 1.09 THz (1) and 1.59 THz (2).

The fit parameters of the main mode (resonance frequency and damping) as a function of temperature are presented in the right panels of Fig.1.14. The mode hardens from roughly 0.9 THz at RT to 1.04 THz at 100 K. The damping (See Right Fig.1.14 lower panel) is a decreasing function of temperature.

To compare our data with the one obtained by Jewariya et al., we approximated the mean frequency as a function of temperature using equation [Zelsmann et al., 1984]:

$$\nu_T = \nu_0 - \frac{2\,\chi\,k_B}{h}\,T \tag{1.18}$$

where T is in K, k_B is the Boltzmann constant, h is the Planck constant and χ the Morse anharmonic parameter.

In this approximation, the frequency decreases linearly on heating, with a slope that depends on the Morse anharmonic parameter χ. This parameter also drives the thermal expansion.

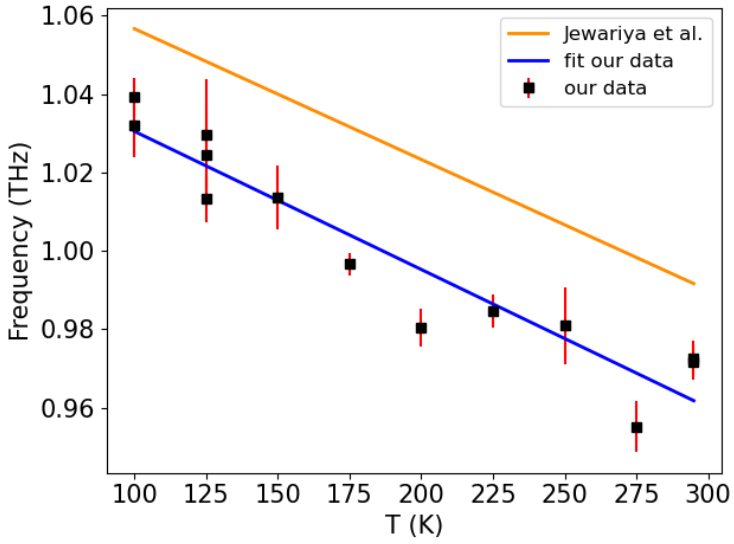

Figure 1.15: Temperature dependence of the frequency of the mode located around 1 THz. In Black are presented our experimental data. The temperature dependence of the expriment performed by Jewariya e al. was simulated using equation 1.18 with $\nu_0 = 1.09$ THz, $\chi = 0.008$. A linear fit (blue) of our dataset gave a similar slope but a different frequency $\nu_0 = 1.066$ THz

Inserting the parameters given by Jewariya et al. ($\chi = 0.008$)), we obtained a line which is slightly above our data points (orange Fig.1.15, but with the right slope. A good fit of our data is obtained using $\nu_0 = 1.066THz$, slightly smaller than the value of 1.09 THz given in ref [Jewariya et al., 2010]. The quite good linear behavior of the frequency shift is in favor of a good linearity of the temperature at the sample as a function of the setpoint. The difference in frequencies at zero temperature may come from both different sample qualities and a temperature shift between our set-up and the one used in the article. In this latter case, we can estimate the temperature shift to be $(1.09 - 1.066) \times 3000 = 72K$, much too large to be significant. So, at least part of the difference come from the sample quality.

As a summary, the cryostream succesfully cools down the millimetric samples. Nevertheless, a proper calibration of the cryostream could be done with samples undergoing very sharp phase transitions.

1.2.4 THz pump/Optical probe setup

The whole THz pump/Optical probe setup was constructed around the already existing THz source. On the pump path, the only difference is the introduction of a chopper to reduce the repetition rate (1 kHz) down to 500 Hz.

The probe path starts at the output of an Optical Parametric Amplifier seeded by a 800 nm output ($560\mu J$) of an Elite amplifier (Coherent) (repetition rate 1 kHz). This OPA was aligned and calibrated by myself to cover the visible and the near IR range. The output of this OPA is sent to a delay stage. This stage modifies on demand the probe arrival time. Using a beam splitter, part of the beam is sent to a photodiode (channel B on Fig . 1.16) connected to a lock-in detector to monitor the probe fluctuations. The other part of the probe beam is carefully focused at the sample position (after PM3). The spatial and temporal overlaps between the pump and the probe were obtained using a Pyroelectric camera. For wavelengths larger than 500-600 nm the temporal overlap could be obtained using an EOS detections. The sample is then installed at the position of the spatial overlap of pump and probe. The transmitted or reflected probe beam was collected and focused on a photodiode (A on Fig. 1.16) connected to a lock-in detection. A balance configuration (A-B) is used to reduce the noise floor. By comparing the probe signal obtained at 500 Hz and 1 kHz, the photo-induced signal originating from the THz pump is extracted by the Lock-in detector.

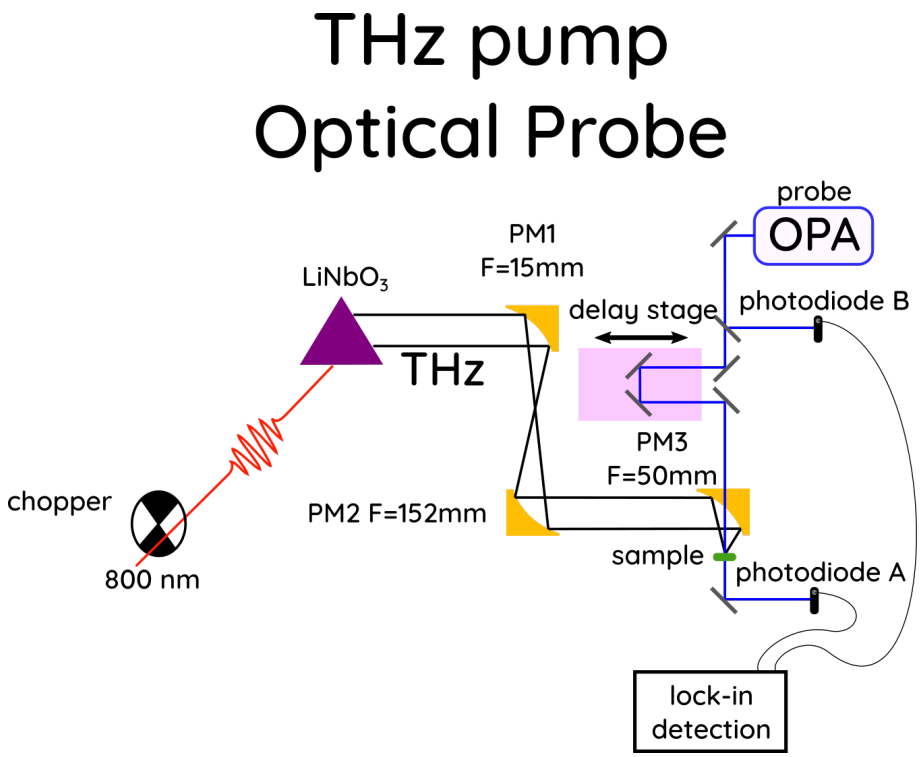

Figure 1.16: a) Schematic representation of the THz Pump Optical Probe setup in transmission configuration. The intense THz pump beam is focused at the sample position. The output of an OPA is used as a probe beam. The transmitted probe is sent to a lock-in detector

1.3 THz Time Domain Spectroscopy

Time Domain Spectroscopy (THz TDS) is a coherent technique that allows the extraction of the complex dielectric function of materials in the THz range. Contrary to other common spectroscopy techniques, both the phase and modulus of the Transmission can be calculated. It allows to directly recover the real and imaginary parts of the refractive index without using Kramers-Kronig relations. This technique also permits the measurement of low frequency absorption lines such as phonons modes and can, for example, be used to study soft modes in ferroelectrics. As it will be shown in Chapter 3, such modes can be directly excited by THz beam. This technique is therefore complementary to the THz Pump Optical Probe one. Non linear spectroscopy can also be performed using very intense THz Electric fields.

I built this setup during my thesis to characterize THz low frequency modes or for instance THz conductivity in V_2O_3 thin films. The very low frequency of the THz is particularly suited to study the change of metallicity of compounds. But, lots of phenomena and experimental conditions can lead to a misinterpretation of the result. Thus, after presenting the setup and the working principle, I will show how Fabry-Perot effects, birefringence and surface rugosity can perturb the resulting spectra.

1.3.1 THz TDS: the setup

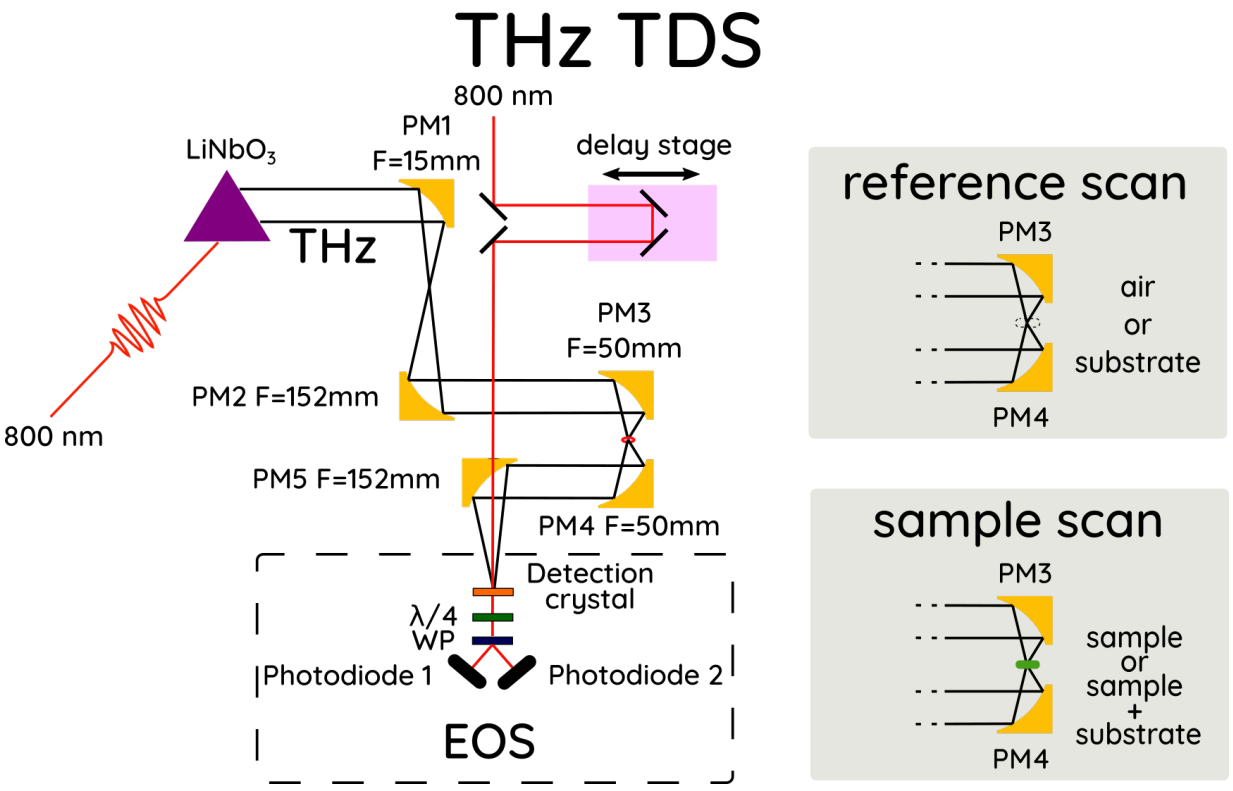

Figure 1.17: a) Schematic representation of the THz-TDS setup. The reference and the sample scan configurations differ at the focal spot in between PM3 and PM4 (cf grey areas). Upper grey area: In the reference scan, at the focal spot, the air or a susbtrate are set in the THz path. Lower grey area: In the sample scan, at the focal spot, the sample and its substrate (if existing) are set in the THz path. PM stands for Parabolic Mirror. $\lambda/4$ is a quarter wave plate. WP: Wollaston Prism. F is the focal length

The THz TDS setup (See Fig.1.17) is an extension of the setup presented earlier for the generation of intense THz fields where the THz exiting from the $LiNbO_3$ are focused using a set

of 3 parabola. The focal point located after the PM3 will be the sample position. Since the aim of this technique is to measure the THz beam transmitted through the sample and compare it to the reference THz beam, I added a supplementary parabola (PM4) to collect the THz beam after the sample. Finally, a fifth parabolic mirror is used to focus the beam in order to perform an EOS detection at this second focal spot (after PM5). The time traces of the THz transmitted through the sample will be called a "sample scan" (See lower grey area). Finally, the sample is removed and a reference scan is monitored (See upper grey area). The comparison between the sample scan and a reference scan will provide informations on the low frequency absorption of the sample.

1.3.2 Principle

Like in every spectroscopy technique, the aim is to obtain the absorption lines or the transmission in the frequency domain. The particularity is that this frequency domain information is obtained via a coherent measurement in the time domain (See first line in Fig.1.18). Using EOS detection, it is possible to obtain the time traces of the THz electric field in different configurations: with the sample in the THz beam path (sample scan) and without (reference scan). The signal of the sample scan will be shifted towards higher delay due to the travel time in the sample. Also, if the sample owns some marked absorption lines, time domain oscillations will be present (See Right of the first line in Fig.1.18).

The Fourier Transform of each scan gives the frequency domain envelope of the THz radiation (second line). The THz envelope of the sample scan will be attenuated and possibly includes the absorption lines (cf second line). To highlight the absorption lines and quantify both the attenuation and the phase shift induced by the sample, the complex transmission is calculated:

$$\tilde{Tr}(\omega) = E_s(\omega)/E_r(\omega) = |\tilde{Tr}|e^{i\phi} \tag{1.19}$$

where $\tilde{Tr}$ is the complex transmission, E(ω) is the Fourier Transform of THz electric field collected during either the sample scan (subscript s) or the reference one (subscript r), $|\tilde{Tr}|$ is the modulus and ϕ is the angle.

This complex transmission is usually presented in two parts. The modulus and the phase are used to compute the dielectric function (ϵ_1 and ϵ_2) or refractive indices.

$$\epsilon = \epsilon_1 + i\epsilon_2 \;\; and \;\; \tilde{n} = \sqrt{\epsilon} = n + i\kappa \tag{1.20}$$

where i is the pure imaginary number ($i^2 = -1$)

1.3.3 Extraction of the sample complex refractive index

1.3.3.1 Thick sample with low absorption

A thick sample designs a sample where the travel time between the first transmitted signal and the first echo after one reflection and one transmission are well separated.

Thus, neglecting echoes, the transmission is:

$$\tilde{Tr}(\omega) = \frac{4\tilde{n}}{(\tilde{n}+1)^2} \underbrace{e^{-(\kappa)\omega L/c}}_{absorption} \times \underbrace{e^{i(n-1)\omega L/c}}_{phase} \tag{1.21}$$

In the case of low absorption ($\kappa << n$), the real part of the refractive index is extracted by [Jepsen et al., 2011; Fastampa et al., 2017]:

$$n(\omega) = 1 - \frac{c\,\phi(\omega)}{\omega\, d} \tag{1.22}$$

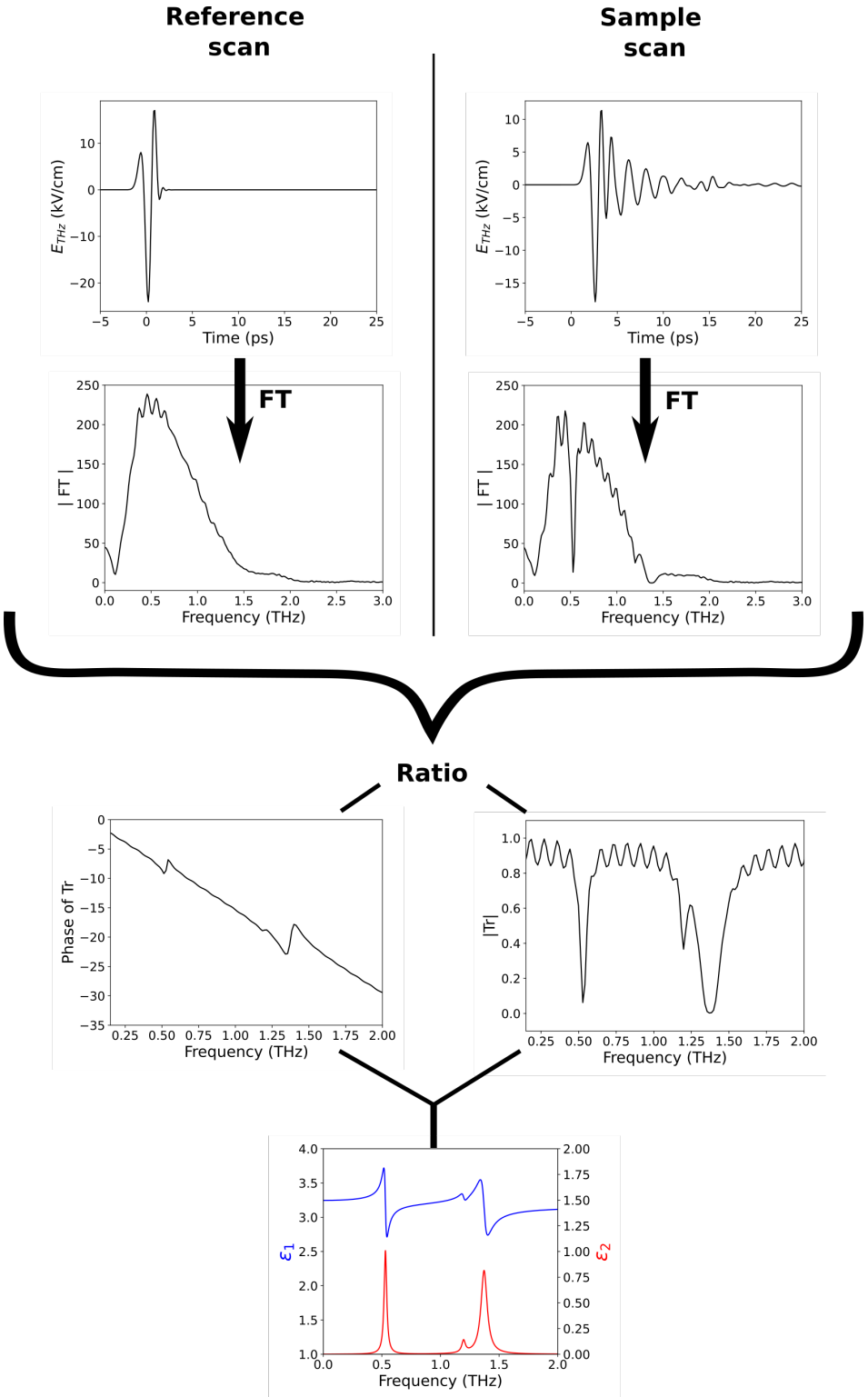

Figure 1.18: THz TDS procedure. The figures are simulating a THz TDS experiment performed on α-Lactose (material properties from [Roggenbuck et al., 2010]). The first line represents the time domain data acquisition obtained from the EOS for both the reference and sample scans. The second line: respective Fourier Transform. Third line: Calculated phase (left) and modulus of the transmission (right) obtained from the ratio of the FT. Fourth line: resulting complex dielectric function (adapted from [Roggenbuck et al., 2010])

and the imaginary part of the refractive index:

$$\kappa(\omega) = -\frac{c}{\omega\, d}\, ln\left(|Tr|\frac{(n+1)^2}{4n}\right) \tag{1.23}$$

However, the extraction of these indices is usually not straightforward. Often, in the sample, internal reflections leads to interferences (Fabry-Perot effects). For sake of simplicity, these oscillations are removed. Indeed, FP effects appear as time domain replica of the THz main pulse leads. A time domain truncation of the scan suppress those features but can drastically diminish the frequency resolution of the experiment. Unfortunately, for thin sample or complex system made of several layers, if the echoes can not be truncated , the equation presented above do not hold anymore. Nevertheless, iterative procedures allow to take into account these frequency oscillations to extract the complex refractive index [Duvillaret et al., 1996].

I prepared a 0.7±0.1 mm thick pellet of α-lactose, pressed under hydraulic press. This compound is a cheap and extensively studied sample with well known modes in the THz range [Kaushik et al., 2012; Wang et al., 2020; Hineno and Yoshinaga, 1974]. It is used as a benchmark sample to verify the quality of the THz TDS setup. The extracted refractive indices is shown in Fig.1.19..

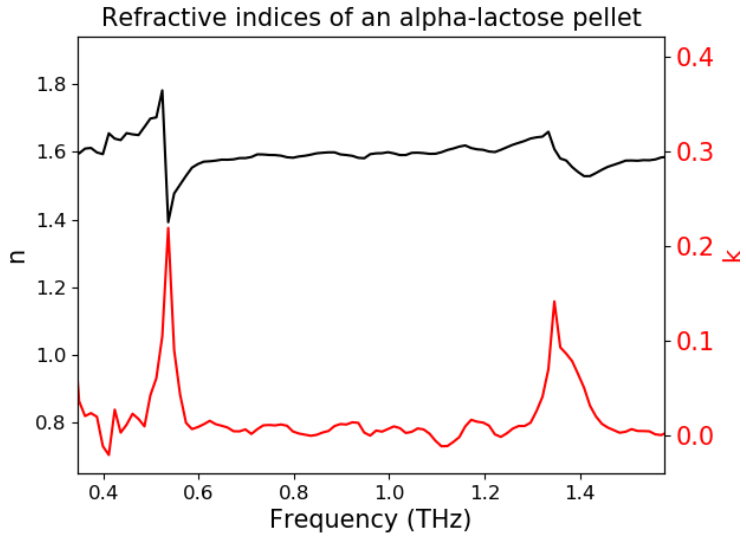

Figure 1.19: Extraction of the real (black) and imaginary (red) part of the refractive index of an α-Lactose pellet from a THz TDS experiment

The two main absorption features, found by Roggenbuck et al. [Roggenbuck et al., 2010], located at 0.5 and 1.37 THz are clearly reproduced. The weaker feature located 1.2 THz is less visible. Disregarding the absorption features, the baseline of the real part of the refractive index is approximately equal to 1.8 in their experiment. In our case, it is closer from 1.6±0.2. The discrepancy between the value can therefore be attributed to the uncertainty of the thickness measurement but also to a difference in the pellet synthesis. A different pressure used for the construction of this pellet would lead to a different density, and consequently, a different refractive index.

1.3.3.2 Fabry Perot effect and their consequences

In THz TDS, a very sensitive THz detection is obtained by Electro-Optical Sampling. The polarization of the pump and the probe must be in a particular configuration with respect to the principal axis of the detection crystal. It allows a coherent detection of the THz. The sensitivity

of this technique implies that even weak time domain echoes and polarization modification are detected. For this reason, I discuss hereafter, how internal reflections (FP effects) affect the TDS measurement and can lead to a misinterpretation of the results.

As explained earlier, the EOS detection technique required to quantitatively measure the THz electric field uses a detection crystal (ZnTe, GaP etc ...) (represented in orange in the Fig.1.17 and Fig.1.20). The introduction of the detection crystal in the THz path lead to the addition of two interfaces: one between the air and the detection crystal and the other between the detection crystal and the air. These interfaces partly transmit and reflect the THz pulse. As a consequence, the probe beam will interact with the main THz pulse ((1) in Fig.1.20) but also with pulses undergoing one or several reflections at the interfaces (labelled (2) and (3)). These pulses are weaker time domain replica of the main THz pulse and are usually gathered in the term "Fabry Perot effects" (FP).

These replica ((2),(3) and (2')) are temporally shifted with respect to the main pulse ((1) and (1')) by an integer value of round trip duration (p×10.6 ps for ZnTe, where p is a positive integer, see Fig.1.20).

The time traces of reference scan are often less complicated to interpret because fewer components are present in THz path. It is constituted of a main pulse (1), located at t=0 ps and corresponding to the THz beam going through the detection crystal without any reflection but also of two replica (2) and (3) of this main pulse corresponding to reflections inside the detection crystal (one or two round trips). Concerning the sample scan, the introduction of the sample adds at least two interfaces, if it is not more when the sample is deposited on a substrate. As a consequence additional FP effects within the sample (4'), and eventually within both the sample and the detection crystal appear (not shown in Fig.1.20). Depending on the sample thickness and refractive indices, these FP effects originating from the sample can appear prior or after the one from the detection crystal. In the case presented here, this FP from the sample appears before the one originating from the ZnTe.

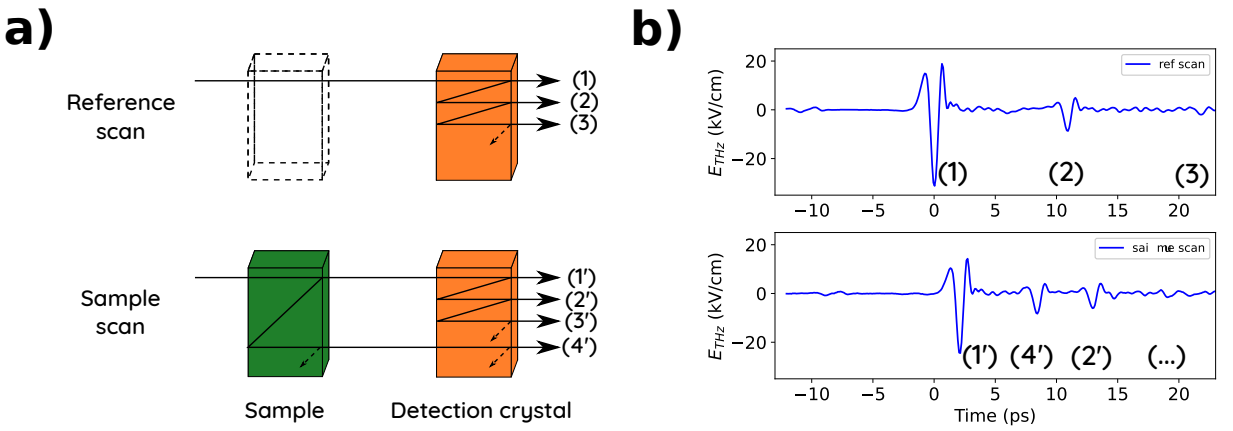

Figure 1.20: a) Schematic representation of the possible paths taken by the electromagnetic wave for both types of scan: the reference and the sample scan. b) Corresponding times traces of the THz electric field obtained from experiments. Upper panel: reference scan. Lower panel: Sample scan. Labels in parenthesis relate the time domain feature to its corresponding path.

For sake of simplicity, in Fig.1.20 is presented one of the easiest situation: the THz-TDS of a highly reflective non absorptive thick sample e.g Si wafer (275μm thick). Since no clear absorption lines are visible in Si, no time domain oscillations will be observed. The introduction of the sample will only lead to a phase shift and additional FP effects.

As explained, the reference signal ((b) top panel in Fig.1.20) is made a main pulse (1) and

two replica (2) and (3) appearing at 11.6 and 23.2 ps respectively and attributed to the reflected THz pulse measured after one and two round trips in the detection crystal.

Concerning the sample scan, several observations can be made. First, due to the introduction of the Si wafer as a sample, the arrival time of the main pulse (1') is shifted towards larger delays. This shift is roughly equal to (n_{Si}-1)d/c=2.4 ps (using $n_{Si} = 3.42$). Its attenuation is related to the transmission of the Si wafer ($|Tr| \approx 0.7$). At t=8.5 ps, an echo originating from a round trip inside the sample is seen (4'). Due to reflection coefficients, its amplitude is divided by three with respect to (1'). For longer delays, the other echo ((2')) comes from round trip inside the detection crystal, similarly to the one presented in the reference scan (2).

The first step of the modelization is to determine the incident electric field. This information can be deduced from the main feature (1) of the reference scan. This feature represents the radiation that didn't undergo any reflection. By removing from (1) the attenuation caused by the interfaces of the detection crystal and the phase shift corresponding the travel through this crystal, the incident electric field can be reconstructed. Using sample and detection crystal thicknesses and refractive indices, the application of transfer Matrices [Mitsas and Siapkas, 1995; Katsidis and Siapkas, 2002] allows to model the reference and the sample scan (See Fig.1.20).

Concerning the THz-TDS of the Si wafer, these simulations are found to be in good agreement with the experimental results. In the time domain, the FP effects originating from the detection crystal (2)(3) but also the one from the Si wafer (4') are reproduced (not shown here). The Fourier transform of the time traces are presented in Fig.1.21. The FT of the reference scan and the sample are very different. While only one oscillation seems to be involved in the FT of the reference scan, a beat is present for the sample scan. This difference comes from the different origin of their respective FP effects. For both scans the full scan length was used. As a consequence the FP (2) and (3) are considered in the FT of the reference scan while the (2') and (4') are considered for the FT of the sample scan. In the reference scan, the origin of the contribution (2) and (3) is equivalent. Since they are equally spaced in time domain, only one oscillation will appear in the frequency domain. The maxima are separated by 0.1 THz, consistent with the 10.6 ps round trip duration. The Fourier Transform envelope of the reference scan is modulated by this 0.1 THz period oscillation. The sample scan is more complicated. Indeed, in this case, the two FP are originating from either the sample or the detection crystal. Their periodicity is different. The one originating from the detection crystal will still lead to oscillation of period equal to 0.1 THz but the one originating from the sample will generate oscillation of 0.16 THz period due to the 6.2 ps round trip duration in the Si wafer. This sum of oscillations will create a beat, modulating the Fourier Transform of the sample scan.

For both sample and reference scan, the simulation reproduces the time domain echoes and therefore the spectral oscillations (See Left Fig.1.21).

These oscillations are sometimes hiding weaker signals. For a simpler analysis, it is common to truncate all the FP effects by a temporal windowing. Thicker detection crystals and sample will be preferred to delay the echoes. As a counterpart, the detection crystal will be able to measure weaker THz fields, which is sometimes a problem for non-linear THz-TDS.

If these oscillations can not be removed, iterative algorithms will be used to extract the desired parameters.

1.3.4 Introduction of partial incoherence: effect of surface roughness

Here is presented the impact of surface roughness on the collected THz spectra. When the sample surface or interfaces are not perfectly flat but are made of irregularities of different height, the THz beam will be scattered on these surfaces [Mitsas and Siapkas, 1995]. As a consequence, the transmission and reflection spectra will be impacted by this loss of intensity.

This phenomenon can be simulated used a generalized Transfer matrix [Mitsas and Siapkas, 1995; Katsidis and Siapkas, 2002]. In this case, the Fresnel coefficients found in the dynamical

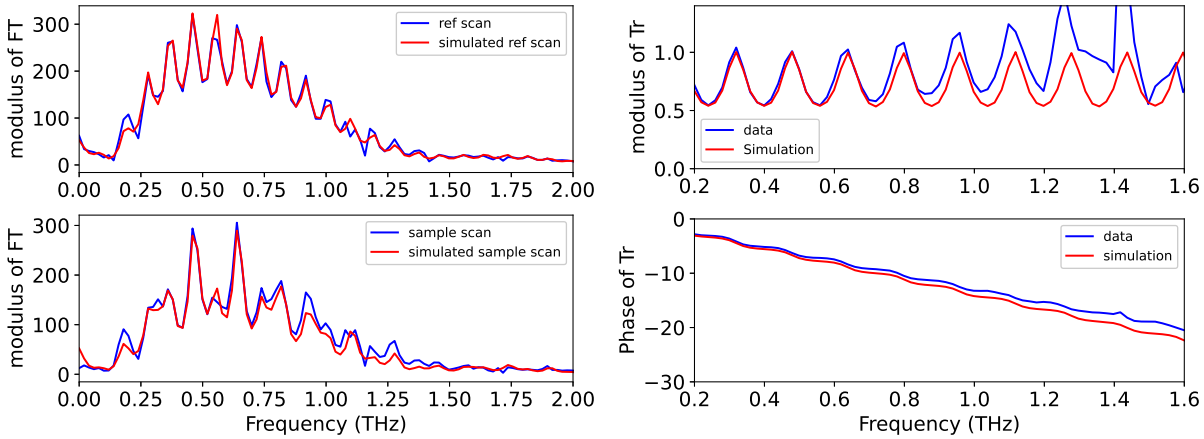

Figure 1.21: Left: In blue is presented the Fourier Transform of the time traces resulting from the reference scan (upper panel) and sample scan (lower panel). In red is shown the simulations. Right: Transmission (upper panel) and phase (lower panel) extracted from the ratio of these Fourier Transform. Simulations are shown in red.

matrices D_m are modified. They are corrected by a term accounting for the phase difference induced by the irregularities. In Fig.1.22 is presented the Fourier analysis of a THz TDS experiment on a millimeter thick pellet of α-Lactose. Several scan were performed on different positions on the pellet surface. The beam is experiencing different surface roughness. For the position 1, the roughness is sufficiently small to observe FP effects. At the position 2 these interferences are not visible anymore. The THz envelope starts to collapse at frequencies greater than 0.5 THz. This collapse seems to be larger at greater frequencies. Finally at the position 3, nearly a third of the FT amplitude is lost for frequencies larger than 0.5 THz.

In the right panel of the Fig.1.22 is presented the simulation for various roughness between 0 and 50µm. This simulation seems to fit well with the experiment and explains the loss of oscillation and the decrease of the THz envelope for large frequencies.

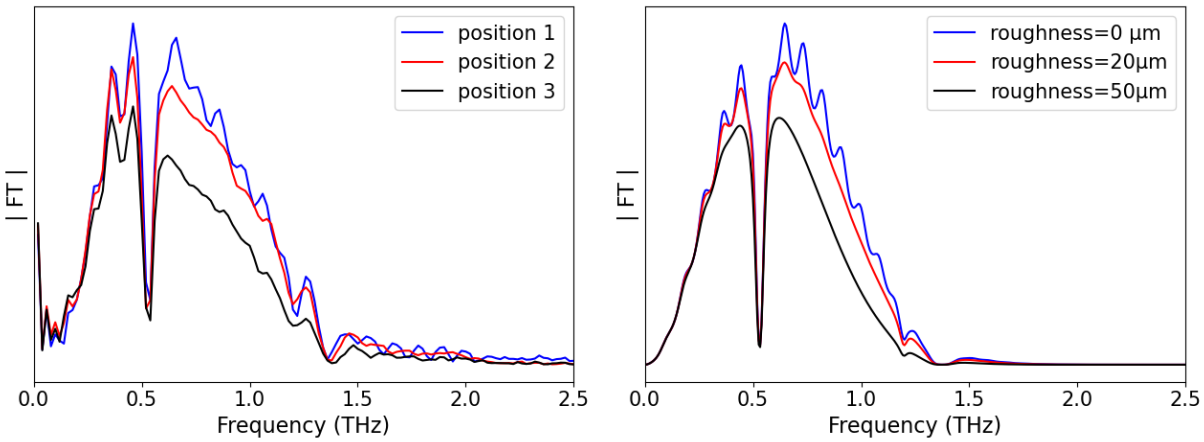

Figure 1.22: Left: THz-TDS Fourier analysis of an α-Lactose pellet. The different scans were taken at different sample position and probe different surface roughness. Right: Simulation of the addition of partial incoherence in the transfer matrix accounting for the surface roughness.

This loss of coherence is of primary importance because it causes a decrease of the amplitude of the collected THz beam that can be falsely interpreted as absorption lines. A careful sample synthesis/deposition is therefore required to avoid surface irregularities.

1.3.5 Time and Frequency spaces: quartz plate as a model birefringent material

In solid state physics, scientists are often dealing with crystalline material exhibiting birefringence. These materials can be used as waveplates. A proper selection of the quartz crystal thickness allows to use it as a monochromatic Half waveplate (HWP) or Quarter waveplate (QWP). For spectroscopy purpose, due to the bandwidth of the spectrum, much more complex systems (achromatic waveplates) are preferred [Masson and Gallot, 2006].

The coherency of the EOS detection technique allows to observe, in time domain, the pulse separation induced by birefringence in a THz-TDS experiment.

In this section, a THz TDS study of a quartz plate is presented. Quartz is a birefringent uniaxial material. In the THz range, its birefringence is equal to Δn=n_e-n_o=0.048 [Charlemagne and Handi, 1969; Grischkowsky et al., 1990] (with n_o=2.108). This value is more than 4 times larger than the one found in the visible range.

In this experiment I used a 5.277mm thick quartz crystal (HWP at 0.6 THz). Since our THz envelope is spanning from 0 to 2.5 THz, the phase retardance Γ goes from 0 to 4.2π using $\Gamma = \omega \Delta n L/c$.

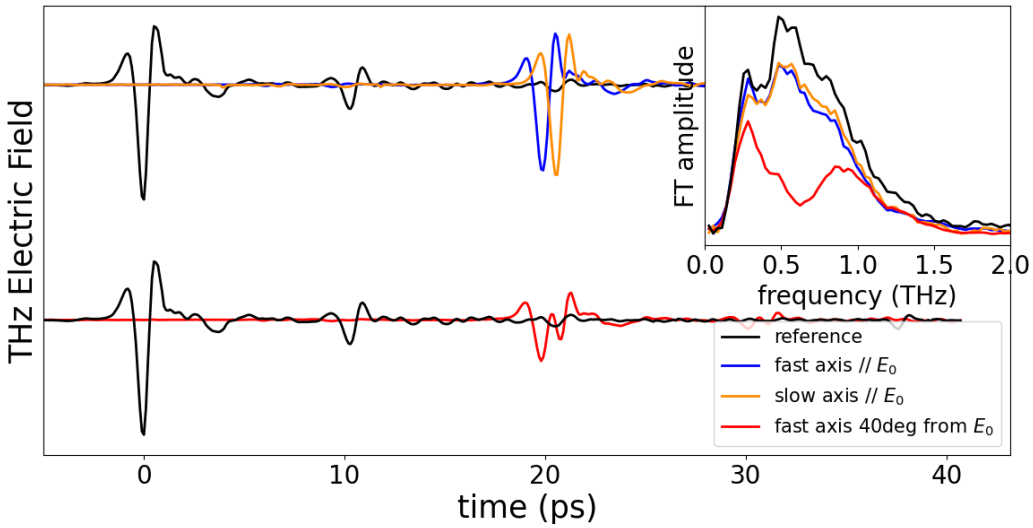

Figure 1.23: THz-TDS of Quartz plate for various crystal orientations. blue: time domain traces of the sample scan with the THz polarization along the fast axis. orange: along the slow axis. Red: At 40° from the fast axis. Black: reference scan. Inset: respective Fourier Transform.

The initial THz polarization $\vec{E_0}$ is set vertical. The polarization of the 800 nm probe for the EOS detection is horizontal. The ZnTe [001] axis is oriented to obtain a maximum THz induced intensity modulation (e.g $\alpha = 90°$ or 270°, cf subsection 1.2.2). The result of this THz TDS experiment on quartz is shown in Fig.1.23. A reference scan (black Fig.1.23) is taken prior the introduction of the quartz plate. The quartz plate is then introduced with its fast axis along the THz polarization $\vec{E_0}$ (vertical).

The introduction of the quartz sample with the fast axis along the THz polarization shifts the appearance of the main pulse by 19.9±0.1 ps (see blue Fig.1.23). This value is in agreement with the expected phase shift (n_{fast}-1)d/c ≈ 19.5 ps induced by the installation of the sample in the THz path.

The rotation of the quartz by 90° makes the slow axis coincide with the THz polarization $\vec{E_0}$ (vertical) (See orange Fig.1.23). In terms of pulse shape and amplitude, the results are similar to

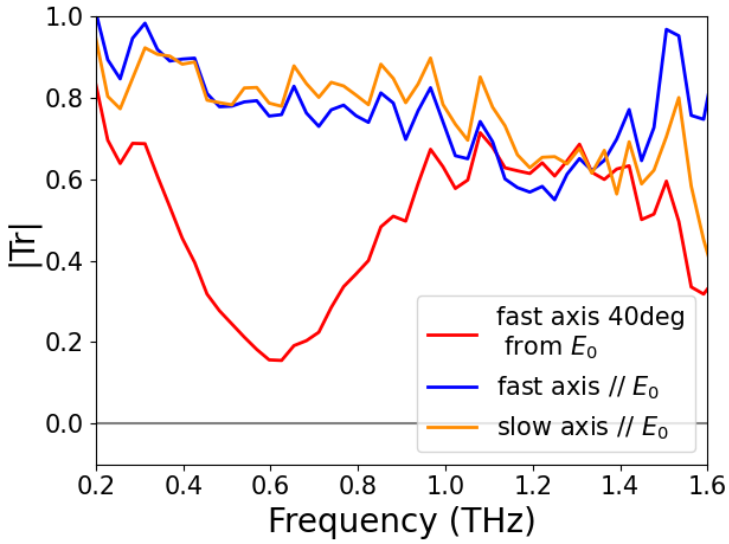

Figure 1.24: Modulus of the Transmission. Orange: E_{THz}// slow axis. Blue E_{THz}// fast axis (orange). Red: E_{THz} is 40° from the fast axis

the one along the fast axis. The major difference is the phase shift. Indeed, the THz detection time is shifted by 0.9± 0.2 ps towards larger delays. This value is in agreement with the value obtained from the theory ($\Delta t = \Delta n d/c \approx 0.84$ ps with $\Delta n = 0.048$).

The analysis of the Frequency domain data allows to draw several conclusions. First the THz envelope (inset Fig.1.23) is very similar when the THz polarization is set along the fast axis or the slow axis. The modulus of the transmission($|\tilde{Tr}(\omega)| = FT_{sample}(\omega)/FT_{ref}(\omega)$)(Fig.1.24) is almost frequency independent, meaning that, within the observed frequency range, no important dispersion exist. Also, looking at the Fourier analysis (or transmission) at 40° from the fast axis, it is evident that the time domain pulse splitting affects the envelope. This time domain splitting ($\delta t = 0.9$ ps) causes oscillations of 1.1 THz period in the Frequency domain. A first oscillation period is observed in red in Fig.1.24. At larger rotation angles (close to 45°), a zero transmission can be achieved around the 0.65 THz.

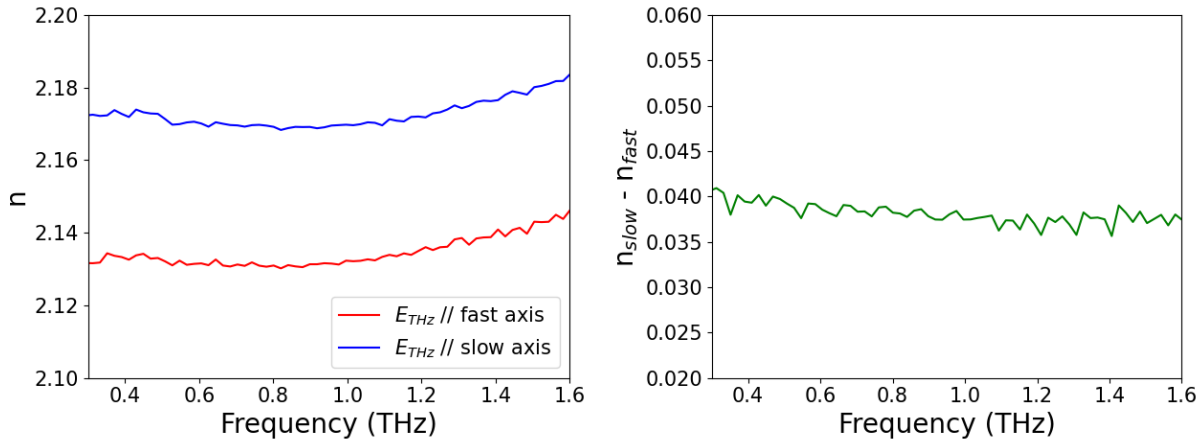

Figure 1.25: Left:Extracted real part of the refractive index of quartz measured when the THz polarization is set along the fast (red) or slow (blue) axis. Right: corresponding birefringence: $\Delta n = n_{slow} - n_{fast}$

For both axes, the real part of the refractive index can be considered as frequency inde-

pendent within our spectral window (Fig.1.25). We found $n_{fast} = 2.132 \pm 0.006$ (red) and n_{slow}=2.170±0.006 (blue) ($\Delta n = 0.04 \pm 0.01$, See Right Fig.1.25). While the value of the birefringence is in agreement with the literature, the values of the refractive indices are a bit larger than the one found in [Charlemagne and Handi, 1969; Grischkowsky et al., 1990] ($n_{fast} = 2.108$ and $n_{slow} = 2.156$).

Concerning the time domain signal obtained when the fast axis is at 40° from the initial THz polarization $\vec{E_0}$ (red in Fig.1.23). The output THz pulse is divided into two pulses of approximately equivalent amplitude traveling at a different speed in the quartz and with a different polarization (See red in Fig.1.23).

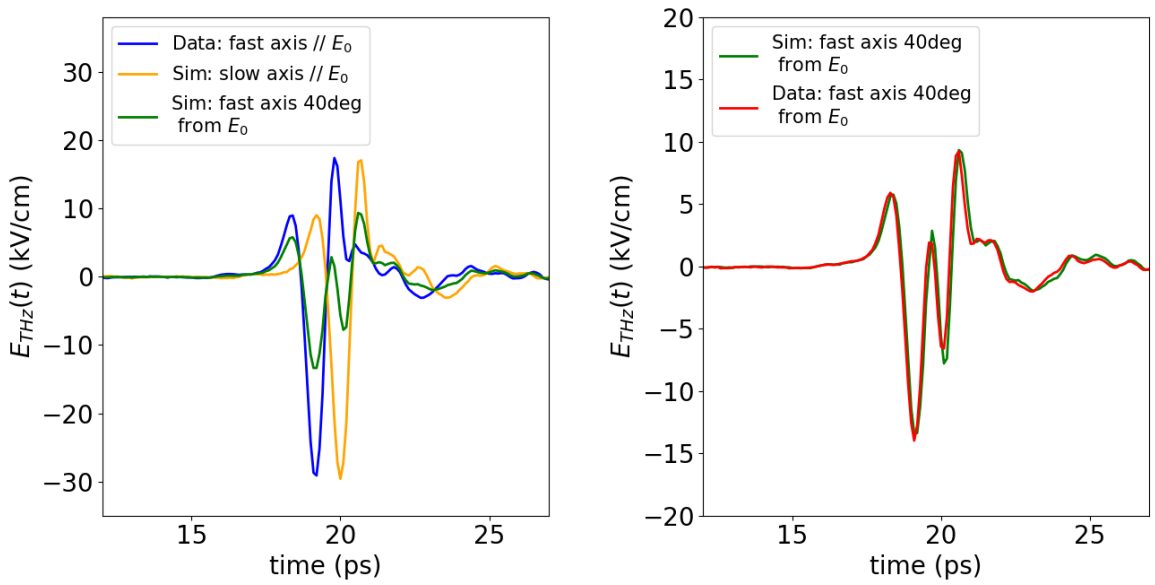

Figure 1.26: Left: simulated THz time traces for E_0// slow axis (orange) and E_0 at 40° from the fast axis (green). In blue, experimental results along the fast axis (when E_0// fast axis) . Right: Comparison between the simulation (green) and experimental results (red) when the E_0 is 40° from the fast axis

To simulate this phenomena, we have to consider two effects. First, the two projections of the THz field along the fast and slow axis of the quartz waveplate travel with a different velocity. Second, the EOS detection process changes the signal amplitude as a function of the incoming THz polarization.

By combining both effects, we can write the resulting signal as:

$$S_\theta(t,\theta) = S_{fast}(t)cos^2(\theta) + S_{slow}(t)sin^2(\theta) \tag{1.24}$$

Where $S_{fast}(t)$ and $S_{slow}(t)$ are respectively the signal when the input polarization is along the fast or slow axes. Using this formula, we found a good agreement between the experimental results (red in Right Fig.1.26) and the simulation (green in Right Fig.1.26). Interestingly, we also found that approximating $S_{slow}(t)$ by $S_{fast}(t - d\Delta n/c)$ also reproduce well the data, as expected when the dispersion is negligible.

As a summary, this study shows the difficulty of the study of birefringent materials. When the measurement is not performed along the principal axis of the sample, a polarization splitting occurs. The FT amplitude and calculated parameters arising from this analysis become quantitatively inaccurate because the detection is not optimized anymore. Also an important decrease of the transmission originating from the time domain splitting can be observed and falsely interpreted

as an absorption lines. But, it also highlight how a time domain analysis allows disentangling different contributions and contributes to a better understanding of the spectral domain results.

1.4 Conclusion

Intense TeraHertz pulses are a relevant tool to control material properties. In this chapter, after the presentation of generalities on the generation and detection of THz pulses, I focused on the presentation of the intense THz source developed in the "Materials and light" team of the IPR. The THz setup is enclosed inside a box purged by dry air, lowering the humidity from 40% to 4%. Thus, the parasitic absorption lines originating from the water vapor are removed from the THz spectral envelope. The introduction of a cryogenic cooling system allows to perform experiments from room temperature to 85 K.

After a careful characterization of the polarization dependent EOS detection, the time traces of the TeraHertz pulses were extracted. The electric field amplitude that we reach via the pulse front tilting technique in $LiNbO_3$ [Hebling et al., 2002] is 250 kV/cm for a bandwidth spanning from 0.3 to 2 THz. Such an intense THz single cycle can be used as both pump or probe. For this purpose, I built two complementary set-ups: a THz-TDS set-up and a THz pump/optical probe one.

The quality of the THz-TDS set-up has been verified using benchmark samples (α-Lactose and L-Arginine). For instance, the hardening of the 1.09 THz peak of L-Arginine upon cooling confirmed the good installation of the cryogenic system. I also performed a THz TDS of quartz to highlight the complexity of the time and Fourier domains implied by the birefringence of samples. The resulting signals depend on both the sample and EOS geometry. We also pointed out that some artifacts in the modulus of the transmission come from the temporal pulse splitting induced by birefringence.

In the future, several experimental developments may improve the THz set-up. The THz generation efficiency can be increased by a change of grating, change of focalization conditions on the $LiNbO_3$, lowering the crystal temperature [Vicario et al., 2013], reducing the divergence at the exit of the $LiNbO_3$ etc. A greater electric field amplitude can also be obtained using a second amplifier for the probe path. It would permit to separately optimize the compression of both pulses. This increase of field amplitude would open new perspectives to develop a broadband detection set-up (THz pump white light probe), which is usually less sensitive. Finally, a loss of centrosymmetry and generation of transient polarization can be tracked by detecting THz induced Second Harmonic Generation.

As shown in the following chapters, the THz-TDS and the THz pump/Optical probe setups are used to study various scientific subjects (e.g generation and detection of strain waves in metals and resonant excitation of soft modes in ferroelectrics).

Chapter 2

THz or Optical pump/Optical probe responses of V_2O_3 thin films

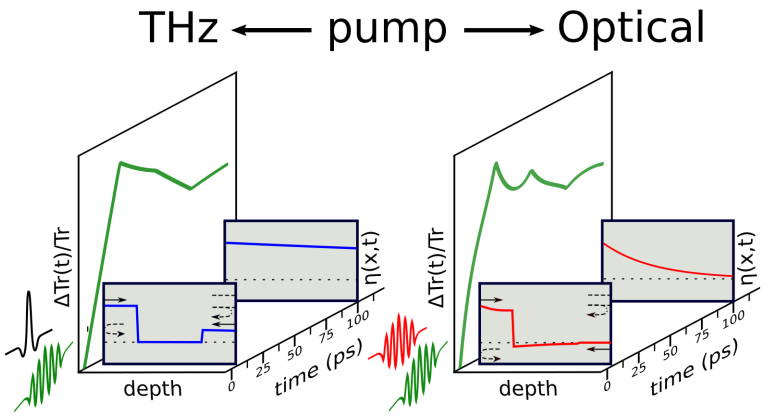

2.1 Introduction

The study of Photo-Induced Phase Transitions (PIPT) is in constant development, owing to new experimental techniques and progress in the physical and theoretical interpretation [Koshihara et al., 2022]. Moreover, the recent possibility to generate almost single cycle terahertz pulses of high intensity offers appealing perspectives for the excitation and investigation of coherent lattice vibrations [Hirori et al., 2011; Vicario et al., 2015; Kampfrath et al., 2013; Nicoletti and Cavalleri, 2016; Salén et al., 2019]. It was soon recognized that, in addition to the microscopic excitation mechanisms, the macroscopic excitation profile is also strikingly important both for the generation of new phases, their propagation in space and time, and interpretation of collected data.

The finite penetration depth and hence excitation profile of the pump will induce an inhomogeneous distribution of phase nuclei from the surface, that may propagate in the depth of the sample (for instance, photo-induced metallic domains in an insulating phase [Okamoto et al., 2004; Okimoto et al., 2009]).

The initial spatial pattern is determined by the excitation profile and mechanism, and subsequent evolutions (nucleation, phase front propagation) are driven by corresponding spatial gradients. This spatial and dynamical mixture of sample properties modulates the sample dielectric function, whose effects are probed through time-resolved optical reflectivity or transmission measurements. A model of the full optical detection process was developed in the seminal work by Thomsen et al.[Thomsen et al., 1986], pointing out the role and interplay of the pump and probe in the interpretation of the transient signal.

It is admitted that optical pump microscopic excitation processes are mainly mediated by electrons, while terahertz pulses can also interact directly with the lattice through infrared active phonon modes.

Among possible transformations that are triggered by such ultrafast strong pulses are coherent phonons or strain-waves [Matsuda et al., 2015; Ruello and Gusev, 2015].

In addition to possible applications to probe material properties, such strain wave were shown to be able to drive a semi-conductor to metal phase transition [Mariette et al., 2021] in volume-changing material (e.g Ti_3O_5). Another possible candidate for such strain-induced phase transition is V_2O_3.

Vanadium sesquioxide V_2O_3 is the working horse in the study of Mott-Hubbard phase transitions [Mott and Peierls, 1937; Hansmann et al., 2013]. The ultrafast response of such materials in pump-probe experiments are very important both for the understanding of the underlying physics, and for potential applications.

This chapter deals with strain waves in V_2O_3. We focus on the generation and detection of strain waves in the PM phase of some V_2O_3 thin films. First, I will present how strain wave propagation can be detected during pump-probe experiments and which parameters influence the photo-induced signal. Then, using several pump/probe setups (THz or optical pump/optical probe), I will study the importance of the excitation profile and the probe wavelength. Finally, since the V_2O_3 can undergo several phase transitions, this understanding will be used to interpret a more complex photo-induced signal obtained in the presence of other phases.

2.1.1 Optical response for a depth dependent refractive index and strain

In a pump-probe experiment, the pump beam induces a perturbation (e.g strain) in the system. The time evolution of some physical parameters impacted by this perturbation are monitored by the probe. These parameters can be the cell parameters, the generation of second harmonic, a change of optical properties such as reflectivity or transmission. The change of optical property reveals a modification of the dielectric function or refractive index of a material. Therefore by following this change of dielectric function, one can obtain information about the time evolution of the perturbation.

In this section, we summarize the basic idea behind the generation and detection of strain waves by picosecond laser.

First, we present a very general model dealing with the detection of a perturbation by the modification of its optical properties. This model has been presented by Thomsen et. al [Thomsen et al., 1986] and extended by Matsuda et. al [Matsuda et al., 2015]. It explains the time evolution of the probe reflectivity during the propagation of a perturbation. Then, we focus on the case where the perturbation is a strain wave generated via thermoelastic mechanism. We discuss the propagation of a strain wave in impedance-matched film on a substrate [Schick et al., 2014] and the importance of the microscopic origin of the thermoelastic stress on the photo-induced signal [Levchuk et al., 2020].

2.1.1.1 Optical response for a depth dependent refractive index in a semi-infinite material

The model introduced by Thomsen et al. can be applied to any mechanism causing a depth dependent dielectric function such as change in charge carriers concentrations, or diffusion process. They considered the modulation of the dielectric function as follows:

$$\Delta\epsilon(z) \sim F\delta(z - z') \tag{2.1}$$

and

$$F = \Delta\epsilon(z') \tag{2.2}$$

where z' represent the perturbation coordinate. At z=z', there is a discontinuity in refractive index. As a consequence, the incident beam will be reflected by both the free surface (Bo) and the interface (B') located a z=z' (See Fig.2.1). The path difference between the two beams introduces interferences.

By solving the wave equation around the discontinuity position [Matsuda et al., 2015], one can compute the reflection coefficient r' originating from the discontinuity.

As a consequence, summing the contributions from two reflected beams Bo and B', the total reflection coefficient becomes, at normal incidence:

$$r = r_0 + \delta r = r_0 + t_0\tilde{t}_0\frac{ik_0^2}{2k_1}\int_0^{+\infty}\Delta\epsilon(z)e^{2ik_1 z}dz \tag{2.3}$$

where $k_0 = 2\pi/\lambda$ is the vacuum wavector, $t_0 = \frac{2}{1+\tilde{n}}$ the vacuum to film transmission coefficient, $r_0 = \frac{\tilde{n}-1}{\tilde{n}+1}$ the vacuum to film reflection coefficient $\tilde{t}_0 = \frac{2\tilde{n}}{1+\tilde{n}}$ the film to vacuum transmission coefficient, n_0 the vacuum complex index, $n_1=\sqrt{\epsilon_1}$ the complex index of the film, $k_1 = k_0\tilde{n}$ the wavector in the film and $\epsilon(z) = \epsilon_1 + \Delta\epsilon(z)$ the perturbed complex dielectric constant of the film.

Now we consider a very general case where the perturbation ψ is simply modifying the complex refractive indices of the material through partial derivatives: $\Delta\tilde{n}(z) = \frac{\partial\tilde{n}}{\partial\psi}\psi$ (where $\tilde{n}$ represents the complex refractive index of the material for a defined wavelength). For example, in the case of a strain pulse $\frac{\partial\tilde{n}}{\partial\eta}$ is the photo-elastic constant.

In the case of a small real valued perturbation, the perturbed dielectric function becomes: $\Delta\epsilon(z,t) \approx 2\tilde{n}\frac{\partial\tilde{n}}{\partial\psi}\psi(z,t)$ at first order because $\tilde{\epsilon} = \tilde{n}^2$. We introduced here a time dependence of the perturbation, assuming that it is quasistatic on the timescale of the probe process. This is for instance justified in elastic processes where the speed of sound is much smaller than the speed of light.

We can now compute the transient reflectance caused by a depth dependent refractive index. For sake of clarity, it is common to separate probe and pump related functions. The perturbation ψ will be the only pump related functions. For the probe, we gather all the variables in a "sensitivity" function f(z) as suggested by Thomsen et al.. This function is measuring how sensitive the probe is to the perturbation [Thomsen et al., 1986].

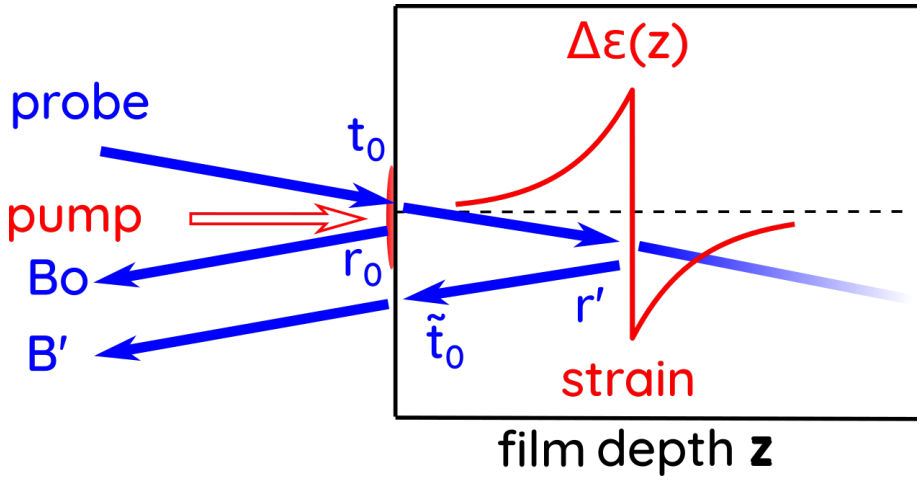

Figure 2.1: Schematic representation of the different reflections of the incident probe beam (in blue) caused by both the free surface and the dielectric function perturbation $\Delta\epsilon(z)$ near z' (represented in red). In this scheme, as an example, we considered that this discontinuity was caused by a propagating strain wave generated via a thermoelastic process. Bo: reflected beam by the free surface. B': reflected beam by the internal spatial modulation of the dielectric constant.

Using the relation $\delta R \approx 2Re(r_0^*\delta r)$, the time dependent change of reflectance becomes:

$$\Delta R(t) = \int_0^{+\infty} f(z)\psi(z,t)dz \tag{2.4}$$

with

$$f(z) = A[\frac{\partial n}{\partial \psi}sin(2k_1z - \phi) + \frac{\partial \kappa}{\partial \psi}cos(2k_1z - \phi)]e^{-z/\zeta_{pr}} \tag{2.5}$$

This function f(z) gathers all the probe related variables such as the complex refractive index of the material (contained in A in Eq. (2.5)), the probe wavelength and penetration depth ζ_{pr}, the partial derivatives of the refractive index with respect to the perturbation (e.g photo-elastic constant in the case of strain pulses) and interference conditions.

From equation 2.5, we can see that the sensitivity function is made of damped oscillations. But the amplitude of these oscillations vary quite importantly with the experimental conditions. Indeed, for example, while for reflectivity the amplitude is large (See section 2.2.1), in Transmission configuration the sensitive function is much flatter as a function of the sample depth. It can be understood as follows: for the reflectivity configuration, for small depth, the two outgoing beams have not been attenuated much, this leads to important interferences and large amplitude oscillations. One the contrary, the interference measured at the end of the sample will be much weaker because of a larger traveled distance.

2.1.1.2 Strain wave generated via thermoelastic process

In this section we focus on the spatial profile of the perturbation. We consider a particular case, where the perturbation is a propagating strain wave $\eta(z,t)$.The strain is define as follows: $\eta = \frac{\partial u}{\partial z}$ where u is the displacement along the z axis, i.e the depth. This strain wave can originate from various mechanisms: thermoelastic effects, electostriction, deformation potential or inverse piezoelectricity [Ruello and Gusev, 2015]. In the following parts, we focus on strain wave generated via thermoelastic mechanism following an energy absorption induced by a laser pulse.

A laser beam directed towards an opaque sample is absorbed. It leads to a rapid rise of lattice temperature ΔT. Due to the thermal expansion, a thermoelastic stress is set in the sample. This stress is the source of strain waves propagating inside the sample at the speed of sound. For isotropic solids, the stress-strain equation relating those phenomena is the following:

$$\sigma_{zz} = 3\,\frac{1-\nu}{1+\nu}\,B\eta_{zz} + \sigma'_{zz} \tag{2.6}$$

where $\sigma'_{zz} = -3B\beta\Delta T$ is the thermoelastic stress, B the bulk modulus, ν the Poisson ratio, β the linear expansion. The speed of sound is obtained from $\rho v^2 = 3\,\frac{1-\nu}{1+\nu}\,B$, where ρ is the density.

From this expression, we understand that the strain profile is governed by the thermoelastic stress shape. It means that the spatial profile of the temperature rise or the pump penetration depth are determinant. Varying this penetration depth will impact the resulting strain.

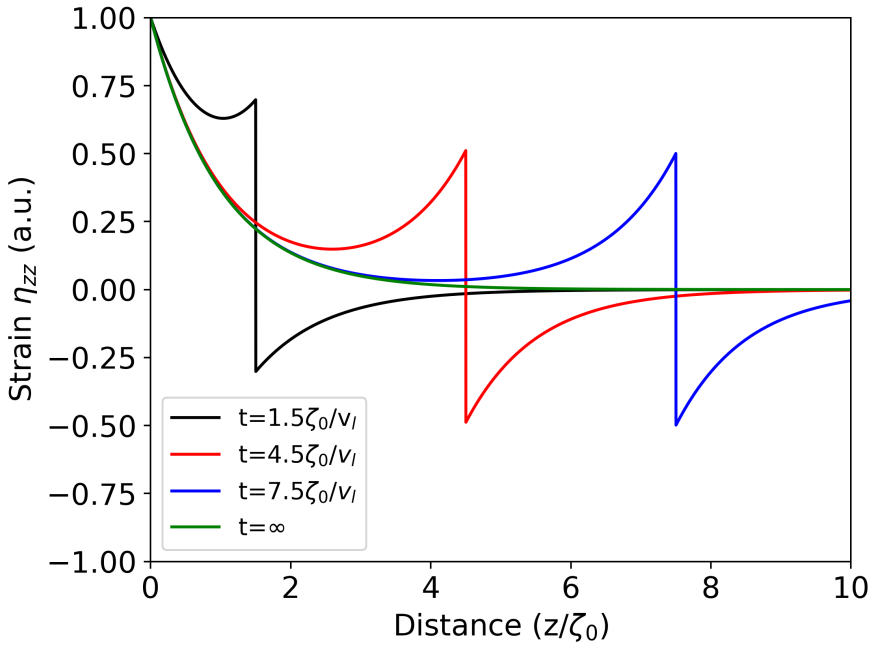

Figure 2.2: Propagation of a strain wave, generated via a thermoelastic process, in a semi-infinite medium. Strain η_{zz} as a function of the the normalized depth z/ξ_{pu}, represented for various time delays from the pump excitation. Adapted from [Thomsen et al., 1986]

Under specific boundary (free surface ...) ($\sigma_{zz} = 0$ at z=0) and initial ($\eta_{zz}, \partial\eta_{zz}/\partial t$ and u_z=0) conditions, they demonstrated that the resulting strain is:

$$\eta_{zz} = \eta_0 e^{-z/\xi_{pu}} - \frac{\eta_0}{2}[e^{-\frac{z+v_l t}{\xi_{pu}}} + e^{-\frac{|z-v_l t|}{\xi_{pu}}}\,sgn(z-v_l t)] \tag{2.7}$$

where ξ_{pu} is the pump penetration depth,v_l the speed of sound, and sgn the sign function.

In Eq.2.7, we can notice that two terms contribute to the strain. Both of them are related to the pump penetration depth. If we consider that there is no heat diffusion, the first term is a contribution that remains at large times when the strain pulse has traveled away far in the sample. The second term is made of two time dependent functions. Those propagating functions account for the propagation of two strain waves triggered at the free surface and directed towards +z and -z direction at t=0 ps. The strain propagating towards the -z direction will be reflected by the free surface. At this air-material interface, the reflection coefficient being negative, the sign of the strain will be changed. Thus as a consequence a bipolar strain wave will be launched and propagates towards the +z direction, inside the material.

At short delays with respect to the pump arrival, the transient and propagating contributions are superimposing. Close to the free surface, after the strain propagation, only the static contribution and its characteristic exponential decay remain, (seen in green in Fig. 2.2). In this semi-infinite model, far away from the free surface, the bipolar contribution is the only one contributing to the strain (See blue curve in Fig2.2). It is centered on z=vt, and as an extension of

about z=vt-5ξ_{pu} to z=vt+5ξ_{pu}. The bipolar contribution is well separated from the static one when vt>> 5ξ_{pu}.

Using equation (2.6), the stress can be reconstructed. Its spatial profile is equivalent to the propagating contribution of the strain. Thus, at any depth, the stress profile is similar to the strain obtained far away from the free surface.

Once the strain profile has been determined, it is possible to compute the time dependent modulation of the reflectivity thanks to an integration over the whole sample thickness. In this semi-infinite model, both static and propagating parts contribute at any time.

2.1.1.3 Impedance-matched film on a substrate

For a film on a substrate, we have to consider the effect of the film-substrate boundary that reflects and transmits the strain wave. We have thus to generalize the semi-infinite model. This case is considered by Schick et al. for an impedance-matched film on a substrate. An essential parameter of the model and experiment is the ratio between the film thickness and the pump penetration depth $\delta = d/\xi_{pu}$, where d is the thickness of the sample and ξ_{pu} is the pump penetration depth.

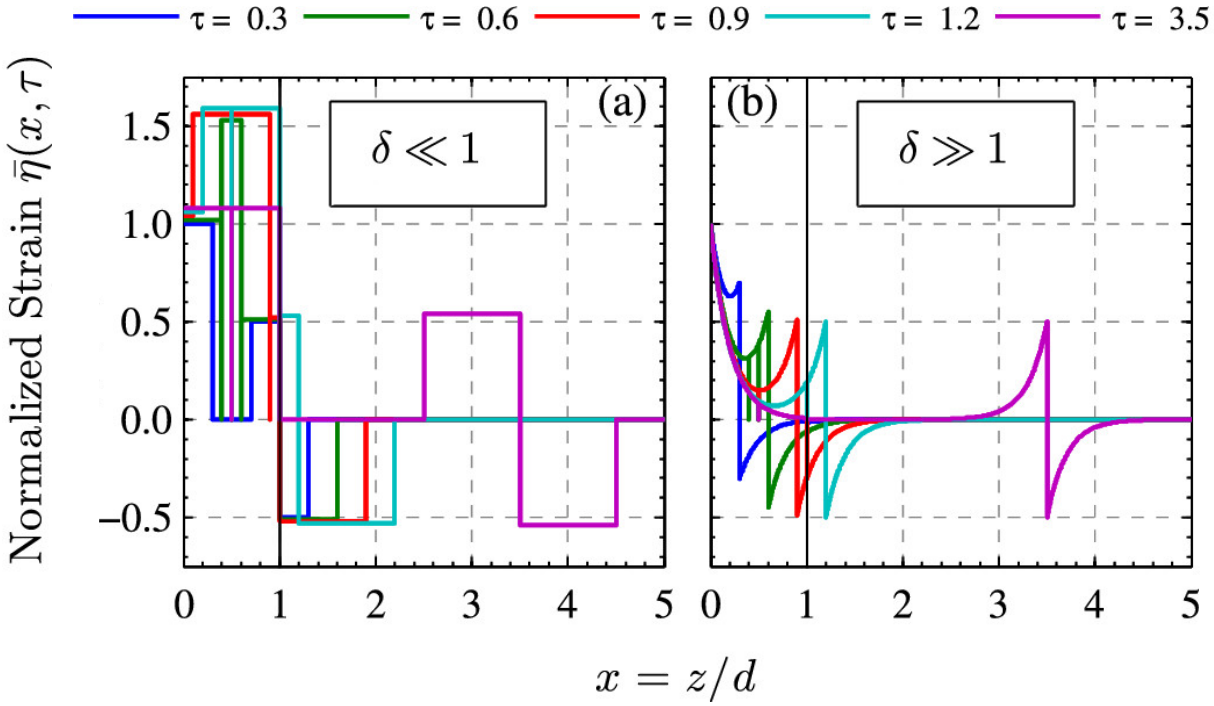

Figure 2.3: Strain propagation in the sample and the substrate, as a function of the normalized sample depth x=z/d, and taken for various time delays following the strain generation. The influence of the shape factor δ is studied. Figure adapted from [Schick et al., 2014]

In this section, we will present this difference of behavior for various δ values. We will start with the case δ»1 (ξ_{pu} << d), when the pump is completely absorbed within the sample thickness. This limit corresponds to the work done by Thomsen et al. using a semi-infinite model. The excitation is exponentially decaying. Without heat diffusion, the rise of temperature is limited in space and thus, the only region were an unbalanced stress is set is at the free surface. As a consequence, a strain wave is triggered from the free surface (where the laser impacted the sample) towards the sample-substrate interface. At short delays (or small depth), both static and propagating components contribute to the strain (See blue curve in upper right panel of Fig.2.3). At larger depth, on approaching the sample-substrate interface, only the bipolar propagating component remains (See purple curve in upper right panel of Fig.2.3 for $x = z/d$<1). Due to the small penetration depth of the pump, this bipolar strain is particularly rounded and follows an

exponential trends. While the propagating strain is in the sample, the signal is both tensile and compressive. Using the normalized temporal coordinate $\tau = vt/d$, at $\tau = 1$, due to the impedance matching, the propagating components enters in the substrate with no reflection. The total strain remaining in the sample is tensile.

The second case presented is the other limiting case: $\delta \ll 1$. In this case the excitation is homogeneous over the whole sample thickness leading to the triggering of equivalent strain waves at both free surface and sample-substrate interface. Because the absorption profile is flat, the strain waves has a squared like shape. After a characteristic time greater than $\tau = 0.5$, the two strains are adding up progressively, the maximum signal is obtained at a time corresponding to half a round trip ($\tau = 1$). At this time, the propagating strain that started at the free interface is entering in the substrate. On the contrary, the strain initially launched at the interface is reflected at the free surface and keeps propagating in the sample. An almost purely tensile strain is obtained within the film due to the homogeneous excitation.

2.1.1.4 Influence of the microscopic origin of the thermoelastic stress

Recently, a comparison of coherent acoustic phonon generation by terahertz and near infrared ultrashort pump pulses (1.55 eV), and therefore originating from different mechanisms were carried out on Chromium and Aluminium metallic thin films (≈14 nnm and ≈20nm respectively) with the same probe wavelength (400 nm) [Levchuk et al., 2020]. It is demonstrated that terahertz pulse pumping in metals generates coherent phonons by a thermoelastic process, through an ultrafast Joule effect. For the optical pump, this process arises by an intraband hot electron relaxation by heat transfer to the lattice degrees of freedom.

For the Cr film, the signal obtained (See Fig.2.4) for both types of excitations was a fast rise of the signal followed by a coherent oscillation of 4.2 ps period (238 GHz). This rise of the signal was interpreted as an increase of the lattice temperature (incoherent phonon population) followed by the breathing of the thin film, meaning a modulation of the displacement (labeled u in section 2.1.1.2) of both interfaces. The signal seems to decay slowly, which is a signature of a non finished heat diffusion. The amplitude of the coherent acoustic phonon is found to be similar for the two types of excitations, at equivalent deposited energy. Also, the frequency of the breathing being function only of the speed of sound and on the thickness of the material, the resulting oscillation period is equivalent. A similar comparison can be made for the Al thin film.

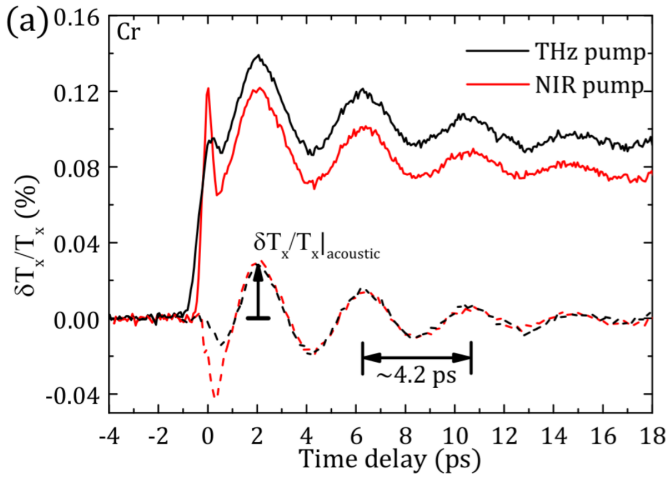

Figure 2.4: Transient modulation of the optical transmission (lines) following a THz (black) or NIr excitation (red), in a 14 nm Cr thin film. The dashed lines represent the oscillatory components of the photo-induced signals. Figure from [Levchuk et al., 2020]

The similar response of the very thin metallic film to both excitation processes, the linear behavior of the signal upon increasing the deposited energy and the 238 GHz frequency (for Cr film) coherent acoustic phonon mode, seems to confirm that the strain wave was released due to a thermoelastic process. Therefore, the conclusion is that, except for features located at t=0 ps, the preferred relaxation channel leading to the thermoelastic stress is not determinant in the coherent acoustic phonon generation.

2.1.2 V_2O_3: a prototypical Mott insulator

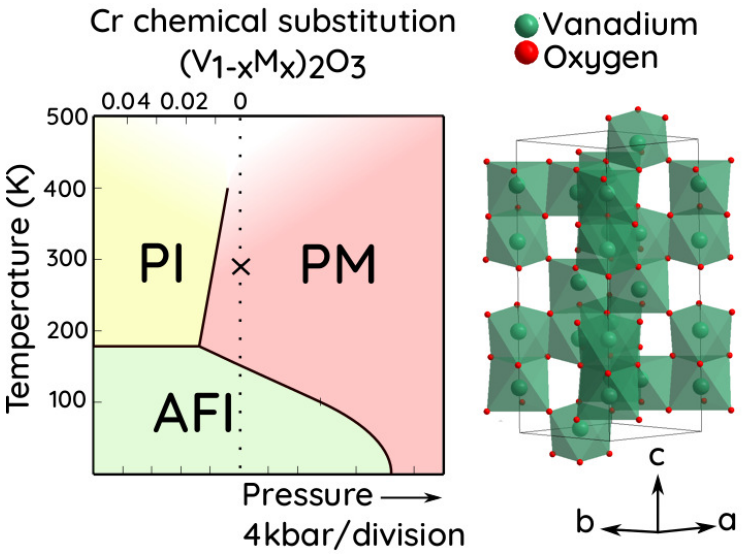

Figure 2.5: Phase diagram of V_2O_3 (PM : Paramagnetic Metal ; PI : Paramagnetic Insulator ; AFI : Anti ferromagnetic Insulator) and structure in the PM phase. Left figure adapted from McWhan et al. [McWhan et al., 1973].

Vanadium sesquioxide V_2O_3 is often seen as the prototypical system to study Mott transition [Hansmann et al., 2013]. At room temperature and pressure, V_2O_3 is in a paramagnetic correlated metallic phase, with a corundum structure with two V_2O_3 formula units in the rhombohedral $R\bar{3}c$ unit cell (Fig.2.5).

Upon cooling, it undergoes a first order symmetry-breaking (from the corundum to a monoclinic structure) phase transition from a Paramagnetic Metal (PM) to Antiferromagnetic Insulator (AFI) phase near 160K. A third phase (Paramagnetic Insulator PI) can also be obtained from the PM phase via an isostructural phase transition, by changing pressure or chemical doping (Fig.2.5). In this case, the magnetic properties (paramagnetic) are maintained through the phase transition. This transition from the PM to PI phase is called a "Mott transition".

2.1.2.1 State of the art: pump/probe experiments on V_2O_3

In order to improve the performances of electronic components, the reduction of the delay time needed for the electrical resistive switching is also a major point. Therefore, pump probe experiments is regarded as the most suited technique to both control the Mott transition and for the understanding of such transition via the temporal decorrelation of possible electronic and lattice contributions.

In pump probe experiments, depending on the type of excitation, the process leading to a phase transition can vary: photo-thermal, electron tunneling, strain induced. In this section we will a give a brief overview of the studies related to photo-induced phase transition in V_2O_3.

The temperature being the easiest control parameter several studies related to photo-induced phase transition in V_2O_3, are focusing on an AFI to PM phase transition at constant pressure, even though the ultimate goal is to study the PM-PI Mott transition in V_2O_3.

Abreu et al. performed an Optical-pump terahertz-probe experiment and realized a metallization of the AFI phase triggered by the absorption of the pump laser beam. The metallization and its dynamic is explained by a nucleation and 2D growth process (See Fig.2.6) well described by an Avrami model [Abreu et al., 2015].

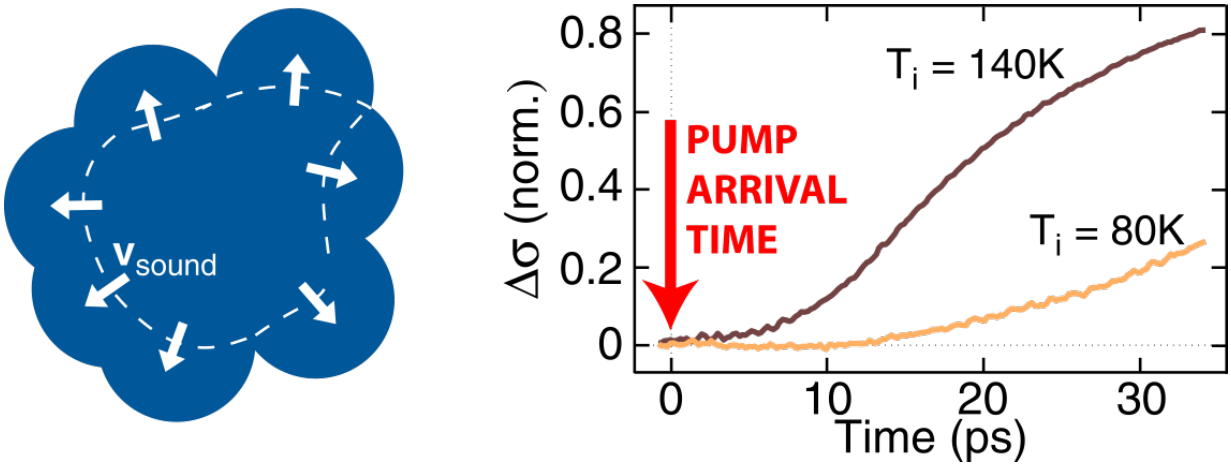

Figure 2.6: Left: Schematic representation of the ballistic nucleation and growth of metallic grains in the insulating phase. Right: transient modulation of the THz conductivity following an Optical pump excitation, as a function of the initial temperature T_i. Faster dynamics are measured for higher T_i. Adapted from [Abreu et al., 2015]

A much slower but non-thermal resistive switching in Mott insulator nanowires was achieved via the application of nanosecond voltage pulses [Kalcheim et al., 2020]. Applying nanosecond voltage pulses leads to the promotion of charge carriers in some in-gap trap states and modifies the doping level, responsible for the switching. This study clearly highlights the importance of defect concentration for non-thermal resistive switching.

Among the few studies of the transmission of V_2O_3 in the PM phase near room temperature, we only found one dealing with a terahertz pump and an optical probe, Giorgianni et al.[Giorgianni et al., 2019]. Under very intense THz electric field (8 MV/cm), a Zener-like tunneling inducing the metallization of low temperature V_2O_3 was also reported [Giorgianni et al., 2019]. This purely electronic Insulator to Metal Transition was seen at 4 K. Increasing temperature leads to the emergence of a competition between this process and the thermal one. The later progressively becomes predominant. The transmission data were acquired on a very short time $<$6 ps, at 175 K. As a consequence, acoustic timescales were not discussed.

2.1.2.2 Towards strain induced Mott transition in V_2O_3

A recent work done by Mariette et al. [Mariette et al., 2021] showed that in materials exhibiting an important jump of volume at the transition, such as Ti_3O_5, the generation and propagation of strain waves could induce a phase transition. Therefore, this technique may be applied to the Mott transition of V_2O_3.

Liu et al. [Liu et al., 2011] studied a 400 nm thick V_2O_3 film at various temperatures, with an optical pump and TeraHertz/Optical probe within 250 ps. They started from the antiferomagnetic insulating phase and induced photo-thermal phase transition towards the PM phase. In the PM phase, the laser absorption leads to the generation and propagation of a tensile strain wave implying a shift towards the PI phase.

Additional results focusing on acoustic effects are shown in the supplementary material of their article, where two acoustic echoes were evidenced.

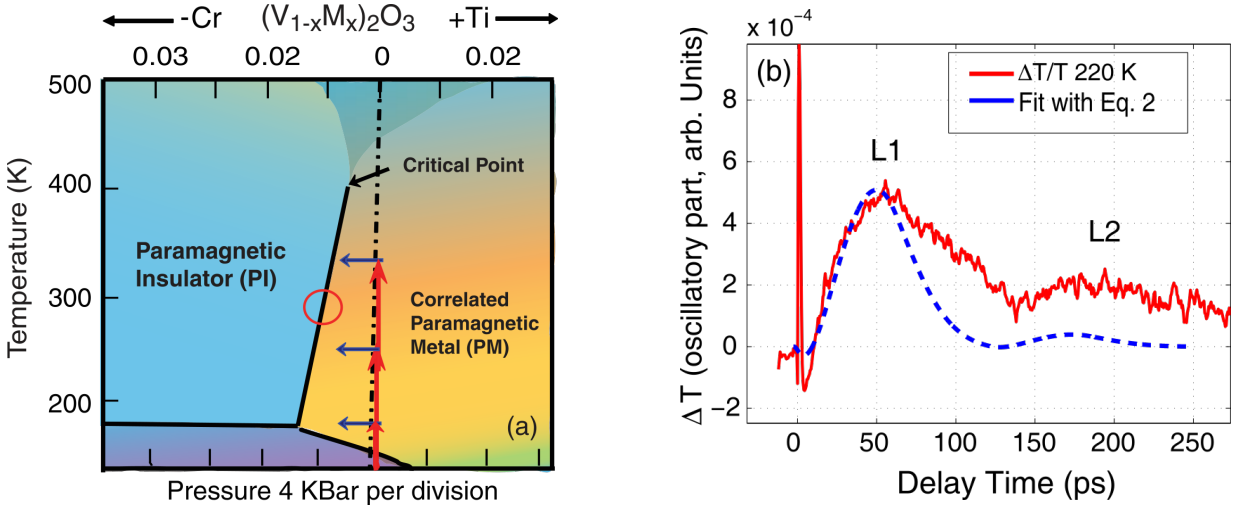

Figure 2.7: Left: Phase diagram of V_2O_3 [Liu et al., 2011]. The arrows represent the pathway of the system following the Optical excitation. red: photo-thermal process, blue: strain induced. Right: Oscillatory component of an Optical pump/THz probe experiment obtained in Transmission configuration [Liu et al., 2011]. red: experimental datas. blue: fit.

2.1.3 Our work

I presented the basic idea behind the generation and detection of a strain wave in a material using pump-probe experiments. The aim of this work is to provide additional informations about the generation and propagation of strain waves in V_2O_3 with respect to the literature [Liu et al., 2011; Mansart et al., 2010; Abreu et al., 2017] (See Right Fig. 2.7). We hope that these new evidence will help, in the future, to perform strain shaping and ultrafast phase transformations in volume changing materials.

In the case of a sample of finite thickness deposited on a semi infinite substrate, we can consider the resulting photo-induced signal as made of four contributions [Matsuda and Wright, 2002], which are presented in equation 2.8. This formula is valid for both Reflectivity and Transmission configuration. The $\Delta I/I(\mathrm{t})$ variable accounting for the change of collected intensity will be replaced by $\Delta R/R(\mathrm{t})$ (R for reflectivity) or $\Delta Tr/Tr(\mathrm{t})$ (Tr for transmission) depending on the configuration used. The sensitivity functions f_1 and f_2 and also the prefactors A and B will be changed accordingly.

$$\begin{aligned}\frac{\Delta I}{I}(t) =& Re\left[\int_0^d \frac{\partial \tilde{n_1}}{\partial \eta}\tilde{f}_1(z,\lambda_{pr},n_1,n_2,d)\eta(z,t)\,dz + \int_0^z \frac{\partial \tilde{n_2}}{\partial \eta}\tilde{f}_2(z,\lambda_{pr},n_1,n_2,d)\eta(z,t)\,dz\right.\\ &\left. + Au(0) + Bu(d)\right]\end{aligned} \tag{2.8}$$

where $\tilde{f}$ is the sensitivity function, η the strain, z is the depth coordinate, $\frac{\partial \tilde{n_1}}{\partial \eta}$ the photo-elastic constant and u the displacement. In all those variables the subscript 1 and 2 accounts for the thin film and the substrate respectively.

The first contribution accounts for the depth dependent dielectric function in the thin film caused by the perturbation. The second one is a similar contribution in the substrate. The third

and fourth are directly proportional to the interface displacement (u(0) and u(d)) and are not depth dependent.

In the following, we consider that the first contribution is sufficient to explain all the experimental results. As a consequence the transient change of intensity in Transmission or Reflectivity configuration is approximated as follows:

$$\frac{\Delta I}{I} \approx Re\left[\int_0^d \frac{\partial \tilde{n_1}}{\partial \eta} \tilde{f}(z, \lambda_{pr}, n_1, n_2, d)\eta(z)\, dz\right] \tag{2.9}$$

where $\tilde{f}$ corresponds to $\tilde{f_1}$ in equation 2.8.

Equation (2.8) highlights that an important number of parameters influence the photo-induced signal. Hereafter, are presented some TeraHertz or Optical pump Optical/probe experiments performed at room temperature, on a V_2O_3 thin film, in various experimental conditions. It allows to observe their impact on the transient signal. We first study a modification of the sensitivy function by changing the probe wavelength and measurements in two types of configurations: Reflectivity or Transmission. Second, we discuss pump related parameters and subsequent modification of the strain η. Third, a study of the power dependence and a comparison between two pump wavelengths will be shown. Finally, the data are interpreted using a model of thermoelastic generated stain-waves. The strain waves are reconstructed at any depth and time following the pump excitation. Consequences of pump and probe parameters are discussed.

2.2 Experimental methods and models

As it was discussed in the introduction, pump related parameters are not the only parameters relevant to define the photo-induced signal. In this section, we discuss the optimization of the experimental set-up in terms of configuration (Reflectivity and Transmission) and probe wavelength.
.

2.2.1 Modification of the sensitivity function through a change of configuration: Transmission or Reflectivity

In figure 2.8 is presented a modelization of the sensitivity function inside the thin film for both Reflectivity or Transmission configurations. The thickness of the V_2O_3 film is set to a 210 nm to match experimental conditions. The probe wavelength is 480 nm.

Several observations can be made from Fig. 2.8. First, both real and imaginary part of the sensitivity function are relatively flat as a function of the depth for the Transmission configuration ($\tilde{f}(z) = \tilde{f}$). While the imaginary part of the sensitivity function is non zero in Transmission, its real part oscillates weakly around 0. Thus, we have $\tilde{f} \approx iIm(\tilde{f})$ for the Transmission configuration. Those observations remains valid over the whole visible spectrum.

The Reflectivity configuration is different in every aspects. Both real and imaginary part of the complex sensitivity function are following a high amplitude damped oscillator trend as a function of depth. Those two sinusoidal functions oscillate around 0. They have a different phase but are of equivalent amplitudes. The amplitudes of those oscillations are much greater than in the Transmission configuration.

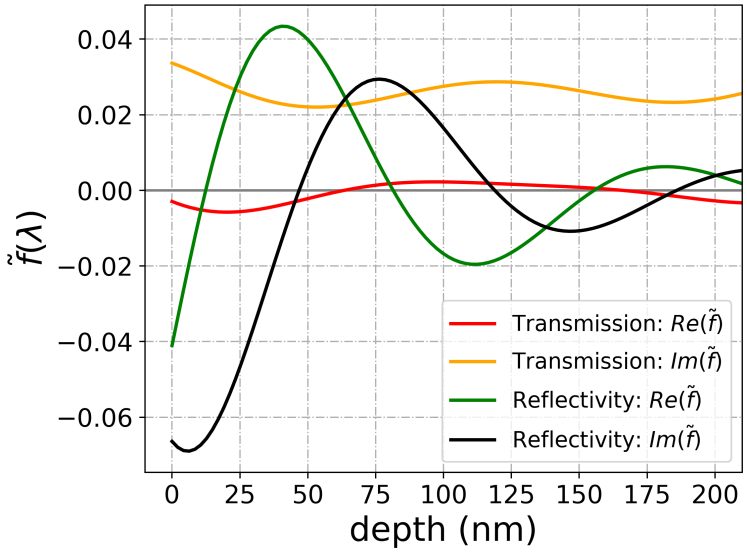

Figure 2.8: Comparison of Sensitivity functions for ΔR/R and ΔTr/Tr configurations for λ_{probe}=480 nm

2.2.2 Influence of the phase of the photoelastic constant on the photoinduced signal

From equation (2.9), we see that the real part of the product between the complex photo-elastic constant and the complex sensitivity function $Re(\frac{\partial\tilde{n}}{\partial\eta}\tilde{f})$ is relevant to understand the photo-induced signal.

The photo-elastic constants are complex parameters which are complicated to measure and are often considered as unknown parameters. In this section we will study the evolution of the product $Re(\frac{\partial\tilde{n}}{\partial\eta}\tilde{f})$ as a function of the value of the photo-elastic constant. For sake of simplicity, $\frac{\partial\tilde{n}}{\partial\eta}$ being a complex number, we will split the modulus and the phase as follows:

$$\frac{\partial\tilde{n}}{\partial\eta} = \left|\frac{\partial\tilde{n}}{\partial\eta}\right| e^{i\phi} \tag{2.10}$$

and

$$\tilde{f} = |\tilde{f}| exp(i\phi_f) \tag{2.11}$$

$$Re(\frac{\partial\tilde{n}}{\partial\eta}\tilde{f}) = \frac{\partial n}{\partial\eta}Re(\tilde{f}) - \frac{\partial\kappa}{\partial\eta}Im(\tilde{f}) = |\tilde{f}|\left|\frac{\partial n}{\partial\eta}\right| exp(i(\phi+\phi_f)) \tag{2.12}$$

The modulus $\left|\frac{\partial\tilde{n}}{\partial\eta}\right|$ acting only as a scaling factor, we will focus only the influence of the phase factor $e^{i\phi}$.

In Fig. 2.9 is presented the modelization of the real part of the product $e^{i\phi}\tilde{f}$ probed at a 480 nm wavelength, for various ϕ angles. It means studying a different ratio between the Real and Imaginary part of the photo-elastic constant.

In Transmission configuration, at 480 nm, a change of phase is leading to a modulation of Re(exp($i\phi$)$\tilde{f}$) between approximately +Im(f) and -Im(f) as it is proportional to $-|Im(\tilde{f})|sin(\phi)$. In other word, in transmission, the change of phase leads to a modification of the amplitude of the photo-induced signal but not of its shape.

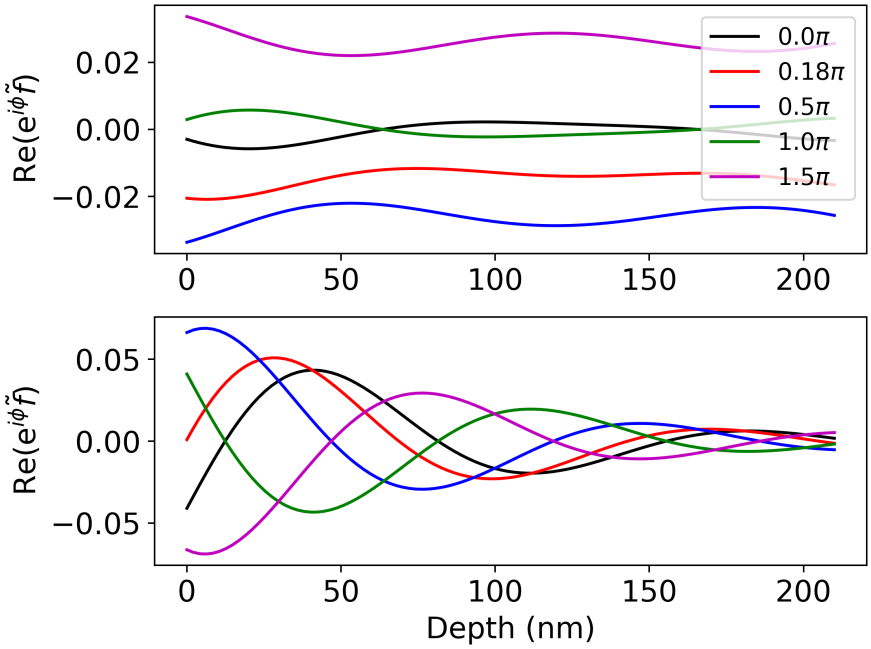

Figure 2.9: Influence of the phase ϕ of the photoelastic constant on the function Re($e^{i\phi}\tilde{f}$), at 480 nm probe wavelength, for both Transmission and Reflection configuration. Upper: Transmission. Lower: Reflectivity

In Reflection configuration, the product Re($e^{i\phi}\tilde{f}$) is a damped oscillation. The modification of the phase of the photo-elastic constant leads to a dephasing of this damped sinusoid. For $\phi = \pi/2$ and $\phi = 3\pi/2$, meaning a predominance of the imaginary part of the photo-elastic constant, the probe is very sensitive to the strain propagation, close to the free surface (small depth). To a lesser extent, a predominance of the real part ($\phi = 0 + p\pi$ where p is an integer) leads to a good sensitivity over the first nanometers. On the contrary, close to the intermediate case (e.g $\phi = 0.18\pi$), the probe is quasi not sensitive to the propagation of the strain on the first nanometers.

As a conclusion, due to the flatness of the product Re($e^{i\phi}\tilde{f}$) in transmission, equation (2.9) is much simpler. Indeed, the photo-induced signal is proportional to the integral of the strain wave over the whole sample thickness. On the contrary, the reflectivity function is the integral over the whole thickness, of the strain, modulated by a damped sinusoidal function. As a result, the transient reflectivity may contain an additional oscillation caused by the modulation of the sensitivity function. The weight of this oscillations is determined by the complex photo-elastic constant amplitude and its phase by the phase of the photo-elastic constant.

As a consequence, the reflectivity configuration can be suited to track strain propagation close to the free surface due to its sensitivity. Combined with the transmission measurement it may allow to extract the photo-elastic constants amplitude and phase.

2.2.3 Experimental results for transmission and reflectivity

Using the THz pump Optical probe setup presented in fig. 2.10 it is possible to compare both configurations using a 540nm probe. In Fig.2.11, we present the results with THz and probe beams coming from the sapphire or the sample side.

While the signals obtained in Transmission seem to be made of only a 30 ps rise followed by a decrease up to 90 ps and finishing with a plateau, an additional oscillation seems to constitute the

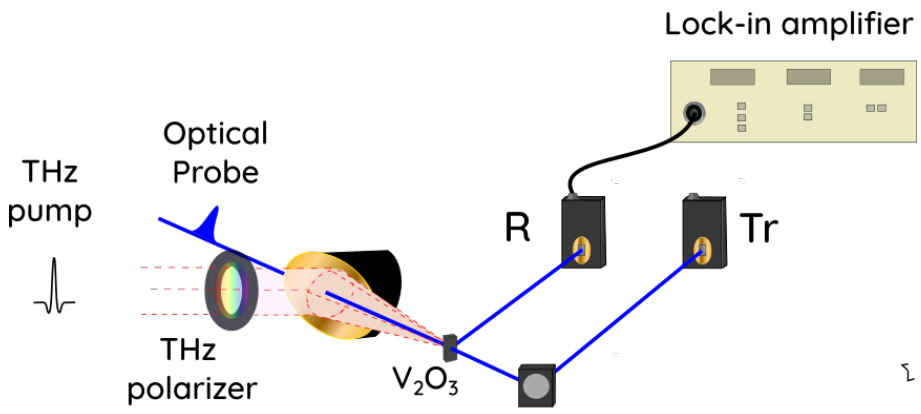

Figure 2.10: Schematic representation of the experimental setup for the TeraHertz pump Optical probe experiments on a V_2O_3 thin film. Both Reflectivity (R) and Transmission (Tr) configuration can be chosen

signal obtained in Reflectivity. This oscillation is attributed to the depth dependent sensitivity function in this configuration, which was detailed previously.

Also, the amplitude of the signal obtained in Reflectivity configuration is not changing a lot when entering by the other side of the sample, while the signal obtained in transmission is approximately 2 times greater when the beams entered from the sapphire side. Since the interpretation of these results are still under discussion, we will focus on the case where the pump beam is on the V_2O_3 side.

Since the transmission configuration allows a greater signal to noise ratio and is also composed of fewer depth dependent parameters, it will be much easier to follow the propagation of the strain as a function of time. In the light of this observations, the following sections will be mainly focusing on the results obtained in Transmission configuration.

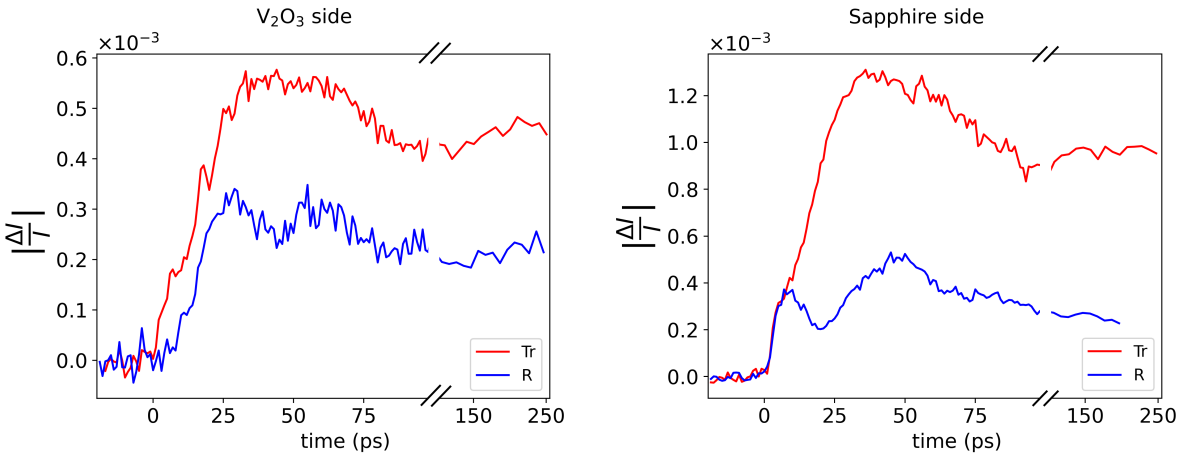

Figure 2.11: TeraHertz Pump Optical (540 nm) probe photo-induced signal obtained in either Reflectivity or Transmission configuration, on a 210 nm V_2O_3 thin film deposited on sapphire. Left: pump and probe on V_2O_3 side. Right: pump and probe on sapphire side

2.2.4 Modification of the sensitivity function as a function of probe wavelength

The photo-induced signal is also influenced by probe related parameters (refractive index, probe penetration depth) through the sensitivity function $\tilde{f}$ (See equation (2.14)). By changing the probe

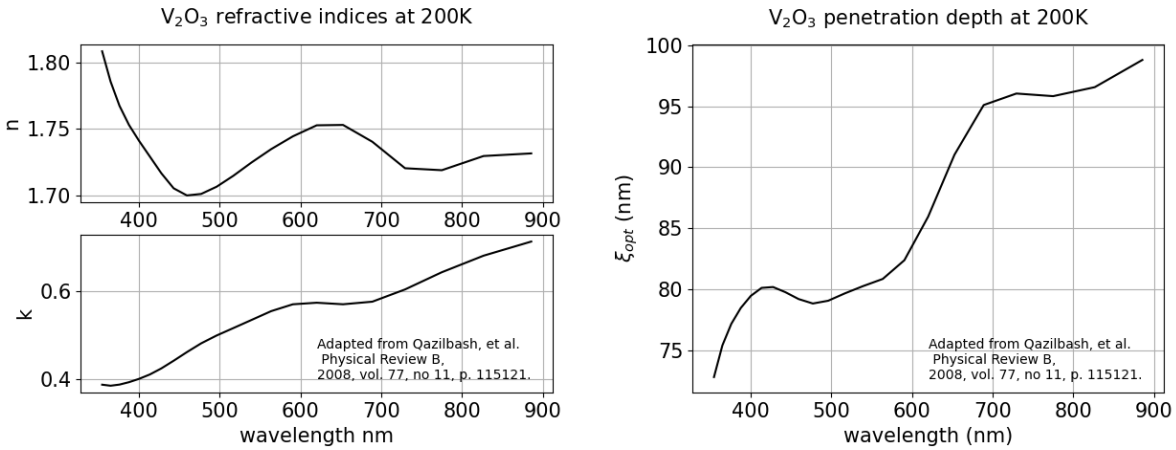

Figure 2.12: Left: Refractive indices of V_2O_3. Upper: real part. Lower: imaginary part. Right: Resulting optical penetration depth of V_2O_3 as a function of the wavelength. Both figures are adapted from Fig.7 [Qazilbash et al., 2008]

wavelength, the interference conditions and the absorption of the probe beams are influenced. A proper selection of two probe wavelengths with non equivalent sensitivity functions should allow the observation of different photo-induced signals. Experimentally, it is done by selecting wavelength with very different complex refractive index.

.

By changing the probe wavelength from 480 nm to 740 nm, the important difference in refractive indices and, as a consequence, in penetration depth (Fig. 2.12) results in distinguishable sensitivity functions (Fig. 2.13). This depth dependent sensitivity function varies both in terms of amplitude and shape. While, for 740 nm, this function is quite monotonic, for 480 nm, oscillations appear. Concerning its amplitude, the ratio of the sensitivity function integrated over the whole sample thickness is approximately equal to 1.6 leading to a similar scaling of the photo-induced signal amplitude.

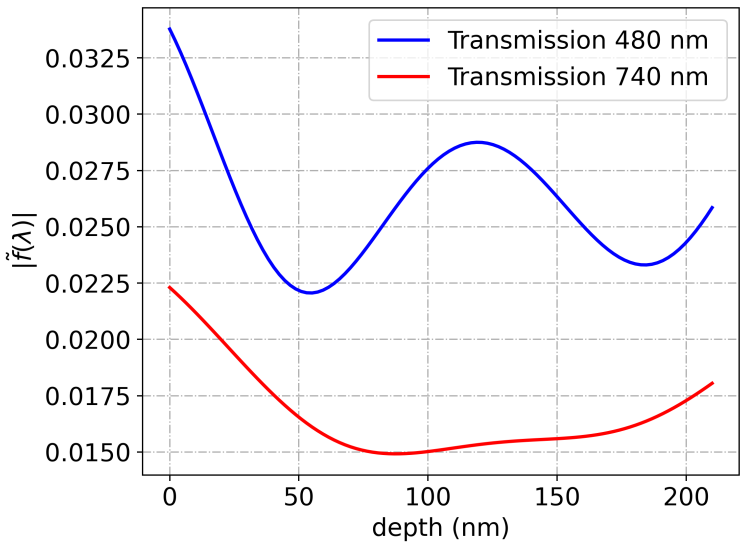

Figure 2.13: Modulus of the sensitivity function for probe beams transmitted through a 210 nm V_2O_3 sample

2.2.5 Summary

Using refractive indices given in the literature, it is possible to simulate the sensitivity function corresponding to different wavelengths and configurations. We have shown that the sensitivity function obtained in Transmission could be considered as flat within our experimental conditions. On the contrary, in Reflection, this function is a damped oscillator. The experimental results confirmed that, in Reflectivity, this depth dependent profile of the sensitivity function induces additional oscillations in the transient signals. The interpretation of such signals becomes more complex. For this reason, to study the propagation of strain waves, we will use the Transmission configuration.

Hereafter, for the THz set-up, we will use two different probe wavelengths. If it is possible, a 740 nm probe is selected to match with the probe wavelength used in the Optical pump experiment. If a higher sensitivity is required (e.g Power dependence), a 480 nm will be preferred.

2.3 Strain generation and propagation in V_2O_3

2.3.1 Impact of a change of pump penetration depth

This section is based on the paper "Impact of the terahertz and optical pump penetration depths on generated strain waves temporal profiles in a V_2O_3 thin film" [Huitric et al., 2022].

In this section, we compare the optical response on acoustic timescale of a V_2O_3 Paramagnetic Metallic (PM) thin film excited by a TeraHertz pump or an Optical pump, at room temperature. We show that the penetration depth of the deposited energy has a strong influence on the shape of the optical transmission signal, consistent with the modulation of permittivity by the superposition of depth-dependent static strain, and dynamical strain waves traveling back and forth in the sample layer. In particular, the temporal modulation of the optical transmission reflects directly the excitation profile as a function of depth, as well as the sign of the acoustic reflection coefficient between the film and the substrate. The acoustic mismatch between the V_2O_3 layer and the substrate was also measured. The raw data were interpreted with a one-dimensional analytical model, using three fitting parameters only. We also pointed out problems coming from the subtraction of more or less unjustified background time functions that may hamper the data interpretation.

2.3.1.1 Materials and Methods

2.3.1.1.1 Sample preparation In the following chapter, unless it is mentioned, the thin film of V_2O_3 used for the experiments was deposited on a c-cut (0001) sapphire substrate by sputtering of a vanadium target in Ar discharge. Post-deposition annealing at 530°C in a reducing atmosphere yields a 210±10 nm thick crystallized and single-phased V_2O_3 layer.

The sample thickness of 210 nm was chosen on the one hand because it is higher than the penetration depth of the optical pump (80 nm), and lower than that of THz pump (1300 nm) used in pump-probe experiments presented in this work. On the other hand, a thickness of 210 nm results in an optical density $OD \approx 1$ (probe penetration depth is 95 nm), which usually provides a good contrast in ultrafast transmission measurements.

2.3.1.1.2 Experimental set-up and simulations Schematics of the experimental setups are given in Fig.2.14c where THz pump/optical probe and optical pump/optical probe techniques are used. The output of a femtosecond regenerative amplifier (Coherent) that delivers 100 fs pulses at 1 kHz repetition rate is split and used for both pump and probe beams. For the THz

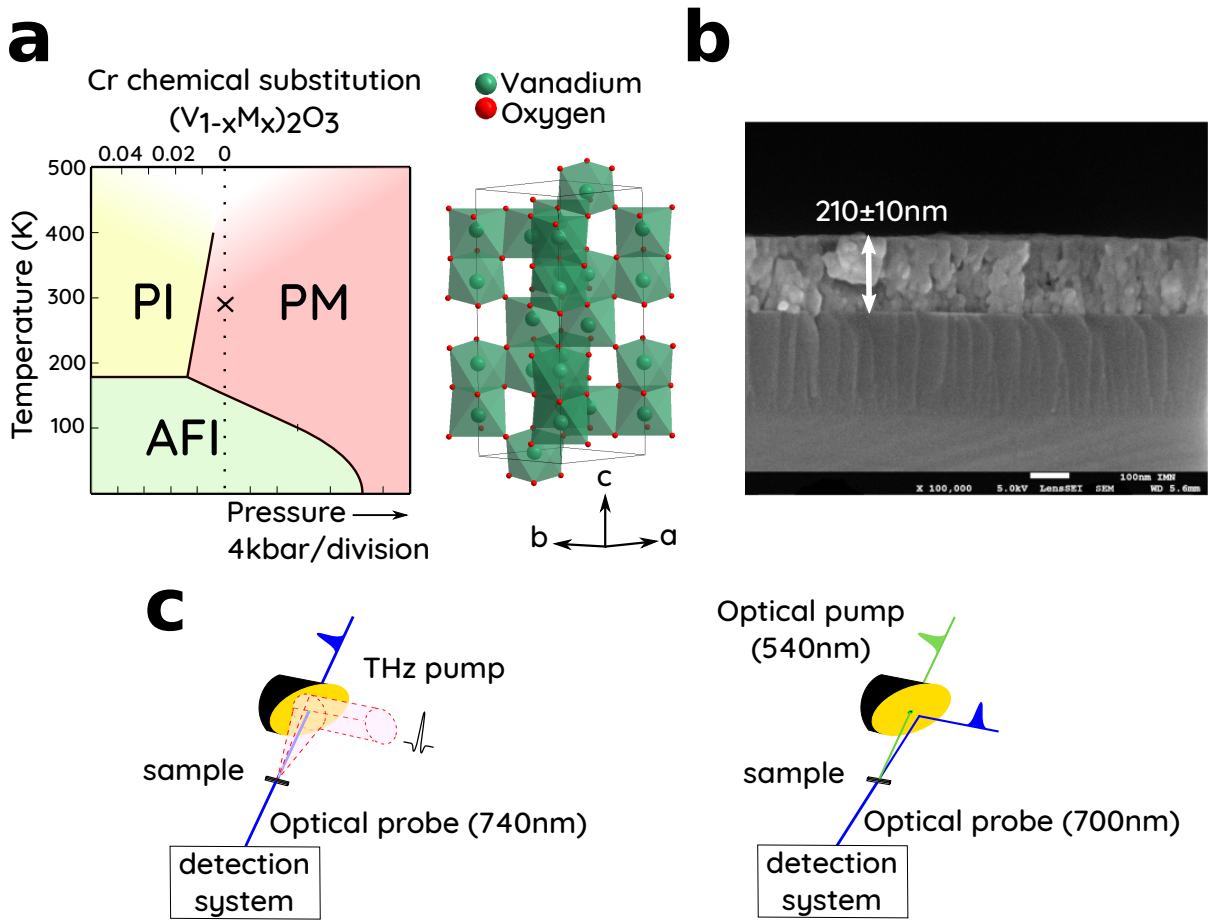

Figure 2.14: (a) Phase diagram of V_2O_3 (PM : Paramagnetic Metal ; PI : Paramagnetic Insulator ; AFI : Anti ferromagnetic Insulator) and structure in the PM phase. (b) Scanning Electron Microscope image. The film thickness was measured as 210±10 nm. (c) Experimental setups for the terahertz pump or optical pump/optical probe.

experiments, the main part (3 mJ) of the amplifier output is used to generate intense THz fields by optical rectification using the tilted-pulse-front technique [Yeh et al., 2007; Hirori et al., 2011] in $LiNbO_3$. We obtain a fluence of 1 $\mu J/mm^2$ and an electric fields reaching 250 kV/cm (measured by Electro-Optical Sampling EOS). The remaining output of the amplifier seeds an OPA (TOPAS Light Conversion) in order to obtain the 740 nm pulse used as probe. The photo-induced signal is recorded with a lock-in detection. For the optical pump experiment, we use the output of an OPA as pump. The wavelength is set to 540 nm and its fluence fixed to 35 $\mu J/mm^2$. Due to experimental constraints, in this setup, a 700 nm probe wavelength is preferred. Both experiments are performed in transmission configuration at nearly normal incidence.

In this way, we measured the temporal relative variation of the optical transmission $\frac{\Delta T_r}{T_r} = [T_r(\text{on}) - T_r(\text{off})]/T_r(\text{off})$, where "on" and "off" mean respectively with and without pump. Eventually, a time-independent constant corresponding to the mean signal at negative times was subtracted. No other data treatments have been performed, nor any part of the signal removed.

Data reduction and all simulations were performed with home-made Python codes, that uses Numpy [Harris et al., 2020] and Scipy[Virtanen et al., 2020] libraries. Figures were drawn with Matplotlib[Hunter, 2007].

The parameters used for the simulations presented later are coming from literature or our own measurements and are gathered in the table 2.1.

Parameter	Value	Reference
Al_2O_3 (sapphire)		
ρ	3.98 g/cm^3	
v_{001} (sound velocity)	11.23x10^5 cm/s	[Winey et al., 2001]
Z_s (acoustic impedance)	44.7x10^5 g/cm^2/s	
n (visible)	1.76	[Tropf et al., 1995]
n (THz)	3.07	[Grischkowsky et al., 1990]
V_2O_3 (PM)		
ρ	4.87 g/cm^3	
v_{100} (sound velocity)	7.37x10^5 cm/s	[Yelon and Keem, 1979]
Z (acoustic impedance)	35.9x10^5 g/cm^2/s	
$\tilde{n}$ @540nm	1.73 + 0.54 i	[Qazilbash et al., 2008]
$\tilde{n}$ @700nm	1.74 + 0.58 i	[Qazilbash et al., 2008]
$\tilde{n}$ @740nm	1.72 + 0.61 i	[Qazilbash et al., 2008]
ξ_{THz}	1300 nm	From THz-TDS
ν_p (Poisson coefficient)	0.33	
C_p (heat capacity)	3.25 J/K/cm^3	[Keer et al., 1976]

Table 2.1: Parameters used in the simulations. i^2=-1

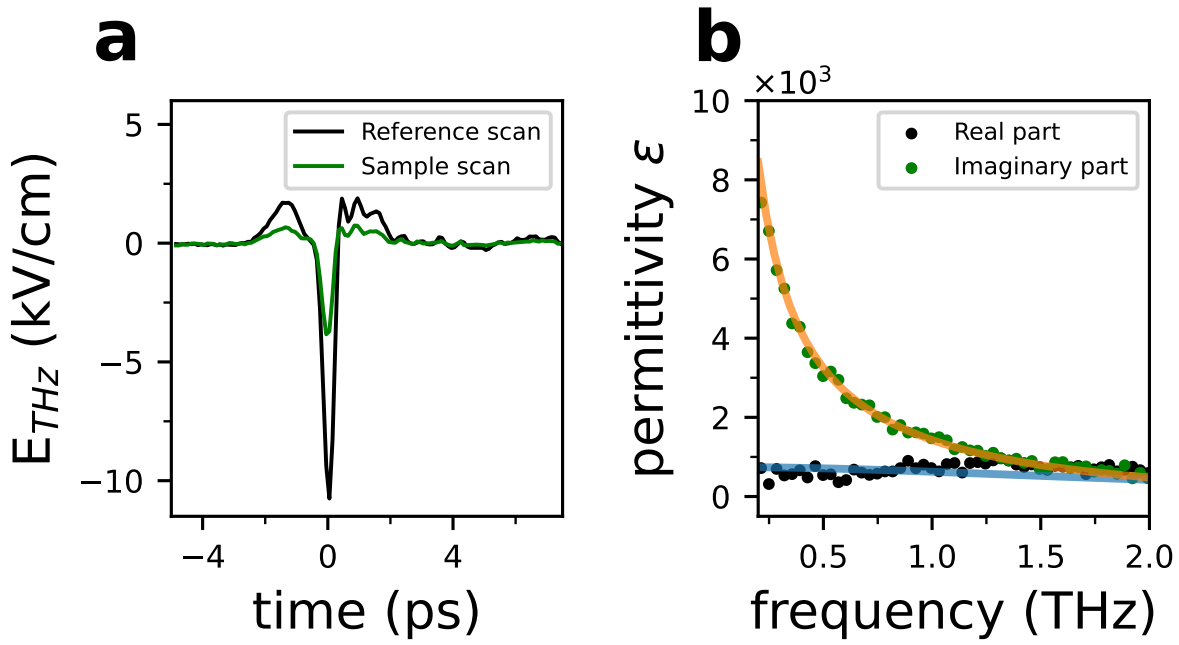

Figure 2.15: Terahertz Time Domain Spectroscopy of V_2O_3 at room temperature. (a) Electric field waveform as a function of time : bare substrate and substrate with thin film sample. (b) Experimental real ϵ_1 and imaginary ϵ_2 parts of the dielectric function as a function of frequency. The continuous lines are the best fit using a Drude model.

2.3.1.1.3 Characterization through THz-TDS The V_2O_3 sample was characterized by Terahertz Time Domain Spectroscopy (TDS). The time traces of the THz electric Field, measured by Electro Optical Sampling (EOS) with a 1mm thick ZnTe crystal, are shown in Fig.2.15a. From their Fourier transforms, we extracted the complex dielectric function of the film using Tinkham Formula [Glover III and Tinkham, 1957; Jepsen et al., 2011; Neu and Schmuttenmaer, 2018]. The mean absolute value of the transmission is $T \approx 0.375$, from which a static conductivity of $\sigma_o \approx$1000 S/cm was calculated from Tinkham formula [Glover III and Tinkham, 1957]. This estimation is close to those obtained with the same type of samples by THz-TDS [Liu et al., 2011;

Abreu et al., 2017; Luo et al., 2017]. The frequency dependence of the real and imaginary parts of the dielectric function are shown in Fig.2.15b, with the best fit using Drude's model for the conductivity Eq.2.13:

$$\epsilon_\omega = \epsilon_1 + i\,\epsilon_2 = \epsilon_\infty + i\frac{\sigma_\omega}{\omega\epsilon_o} \text{ where } \sigma_\omega = \frac{\sigma_o}{1+i\omega\tau} \tag{2.13}$$

where ω is the angular frequency (rad/s), ϵ_o is the vacuum dielectric permittivity and ϵ_∞ the dielectric function at infinite frequency. We obtained an electronic scattering rate $\Gamma = 1/\tau \approx 14.3 \pm 0.2$ THz, and a static conductivity of $\sigma_o \approx 1000$ S/cm. These values are consistent with those obtained in [Vecchio et al., 2015; Luo et al., 2017]. These parameters will be used in the following to calculate the sample refractive index at terahertz frequencies.

2.3.1.2 Results and Analysis.

2.3.1.2.1 Modulation of optical transmission by Terahertz or Optical pump. In the following we report the comparison of temporal relative transmission variation using either a THz pump or an optical pump. The THz pump EOS temporal trace, shown in Fig.2.16c, has a maximum electric field ≈ 250 kV/cm and typical full duration ≈ 4 ps. The energy power spectrum has its maximum near 0.5 THz (Fig.2.16d) with a FWHM≈ 0.5 THz. The optical pump at 540nm has a duration of 100 fs. For experimental reasons, we could not use exactly the same probe wavelengths, 740 and 700 nm respectively for THz and optical pumps. However, it can be shown that the sensitivity function (see below Fig.2.20b) that determines how the probe interacts with the permittivity modulation induced by the pump are almost equal over the full film thickness, since the ratio of the complex index to wavelength $\tilde{n}/\lambda$ are very close (difference of less than 6% for the real part, and 1% for the imaginary part).

The temporal evolution of the raw relative transmission variation $\frac{\Delta T_r(t)}{T_r}$ is presented on Fig.2.16 for both pumps, with probes at almost the same wavelength.

Two features are immediately apparent. First, both signals increase within about ≈30 ps, reaching a maximum before decaying to an almost constant plateau value for delay times larger than ≈90 ps. In fact, for larger times, small oscillations modulate the plateau. For instance a bump appears near ≈ 150 ps in the terahertz pump profile. It is less clear for the optical pump profile. Second, the magnitude of the relative transmission variation with the optical pump is larger than the value with the terahertz pump, as expected from the largest available energy and fluence of the optical pulse.

Most significant is the difference in the profiles within the 35-90 ps time range. While the decay is rather uniform for the terahertz profile, a *dip* near ≈44 ps, and second maximum at ≈56 ps are clearly seen for the profile with the optical pump, making this profile strikingly different from the terahertz profile. Moreover, an additional strong sharp peak signal appears at very short time delays.

By noting that an acoustic timescale is the travel time of a wave from the top surface to the interface of the film with the substrate, that is in our case $\tau_a = d/\mathsf{v}_{\mathsf{sound}}$ ≈29 ps, and an electronic time-scale is typically a few 0.1 picoseconds, we can split our analysis into two parts.

First, we analyse in more details the optical short-time trace, that was studied with a shorter time-step of 0.01 ps, as presented in Fig.2.16e. This photo-induced signal can be divided in three contributions. A first ultrafast response is located just after the pump arrival and lasts for less than 0.5 ps (See Fig.2.16e). This feature is related to the photon-electron interaction. At larger time delays, oscillations on a slowly growing background are perceptible. The extraction of the oscillating component is done by removing the two other contributions. The peak is fitted by the convolution of a Gaussian of full width at half height 120 fs, with an exponential decay of 80 fs time constant, while the increasing background is reproduced thanks to a first order polynomial. The Fourier Transform of the remaining oscillating component unveils a 7.2 THz mode (see Fig.2.16g), in accordance with the frequency of the $\mathbf{A}_1 g$ optical phonon mode previously measured through

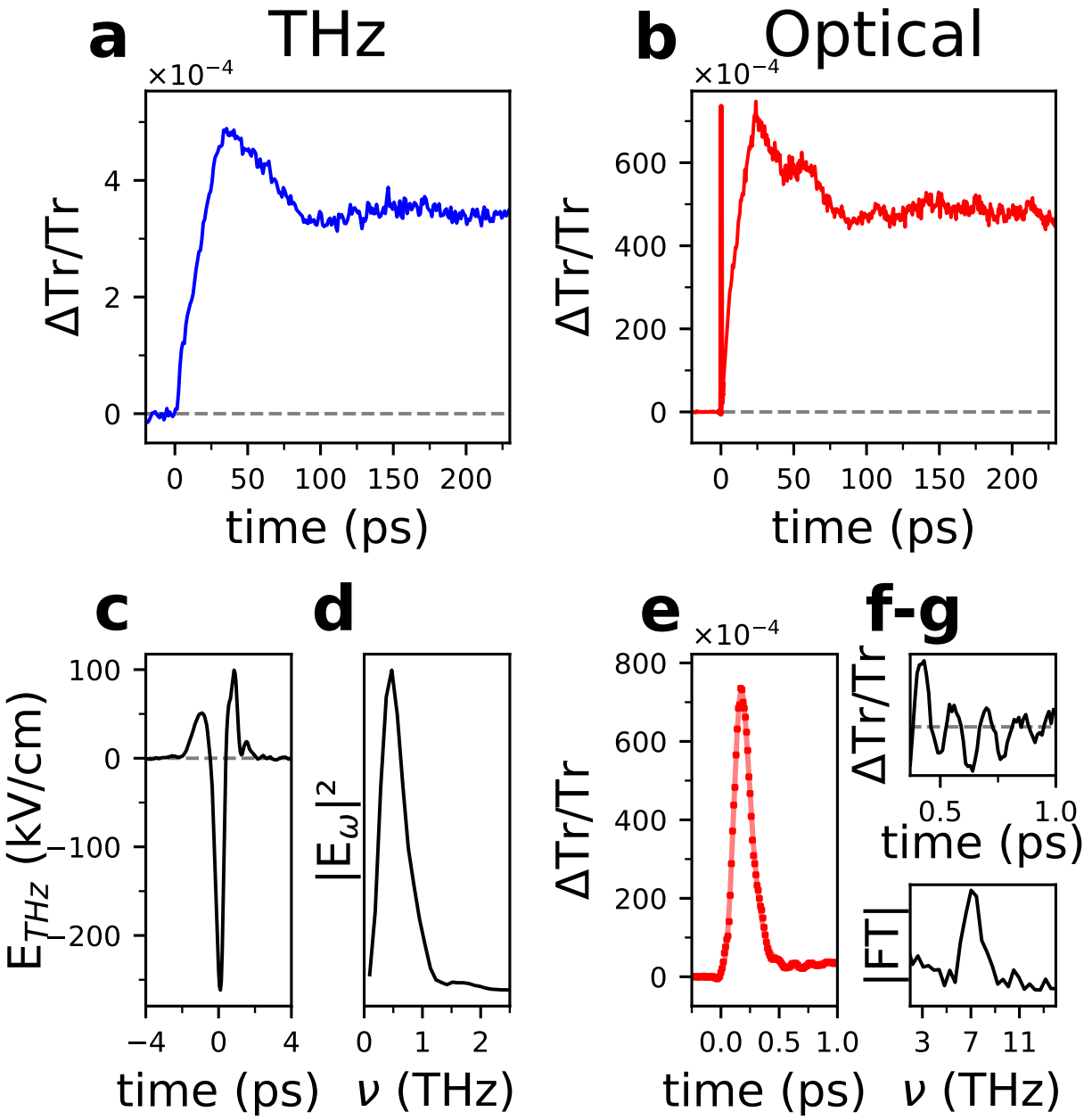

Figure 2.16: (a) and (b) : Relative optical transmission as a function of time $\frac{\Delta T_r(t)}{T_r}$. Raw data are presented. (a) THz pump .(b) Optical pump (540 nm). For t≤1.5 ps the time-step is 0.01 ps, while for t≥2 ps, the time-step is 0.5 ps. (c-d) Terahertz pump electric field waveform as a function of time, and corresponding squared modulus of the Fourier transform $|E_\omega|^2$. (e-g) Short-time analysis of the optical pump transmission acquisition shown in (b) : (e) Raw data (points) and best fit (continuous line) ; (f-g) Evidence of coherent phonon excitation : (f) Resulting transmission after subtraction of the peak and background as a function of time, and (g) the corresponding modulus of the Fourier transform.

Raman [Kuroda and Fan, 1977; Lantz et al., 2017] and pump-probe experiments [Mansart et al., 2010; Lantz et al., 2017; Misochko et al., 1998]. Concerning the THz pump experiment, neither the peak nor any oscillation were detected. The lack of oscillating component is due to the long THz excitation (∼1 ps) compared to the period of the phonon mode (∼0.14 ps), which washes out the oscillations due to the dephasing.

Second, as discussed before, for times larger than 1 ps, the features of the data fall in the acoustic timescale, the positions of peaks and dips corresponding more or less to multiples of the acoustic travel time $= n \times \tau_a$ with n an integer. More precisely, we will show that the measured relative transmission variations as a function of time comes from the modulation of the complex dielectric function by photo-induced elastic strain-waves. For metals, the strain waves are usually generated by a thermoelastic mechanism [Thomsen et al., 1986; Matsuda et al., 2015; Ruello and Gusev, 2015; Levchuk et al., 2020]. In this process, part of the pump pulse energy is absorbed by the electrons, which thermalize in a few hundreds of femtoseconds. During and after the pump pulse, the electronic and lattice degrees of freedom exchange energy through electron-phonon coupling and equilibrate to a common temperature, typically within less than a few picoseconds, a process that is usually described with a two-temperature model [Anisimov et al., 1974]. This almost instantaneous heating of the lattice, at the elastic timescale, induces a thermal stress by inhomogeneous thermal expansion related to the pump energy deposition profile. The related strain modulates the dielectric function as a function of position and time, giving rise to a time-dependent optical transmission variation.

In the following, we use the simplest one-dimensional model to interpret our data with the minimum number of fitting parameters.

2.3.1.2.2 Thermoelastic Model The relative transmission variation $\frac{\Delta T_r(t)}{T_r}$ depends both on the pump excitation profile that determines the strain pulse shape $\eta(x,t)$, and on the probe pulse transmission through the perturbed sample. The pioneering work of Thomsen et al.[Thomsen et al., 1986] with a semi-infinite sample was generalized to a multilayer system by Matsuda et al.[Matsuda and Wright, 2002].

In the following, we consider a layer of thickness d on top of a semi-infinite substrate Fig.2.17a. Note however that a more complete model, with a finite-width substrate, gives identical results.

Assuming that the permittivity, or refractive index, is modulated by the strain, and using the approximation $\Delta\tilde{n}(x,t) = \frac{\partial\tilde{n}}{\partial\eta}\eta(x,t)$, the relative change of transmission can be written as :

$$\frac{\Delta Tr(t)}{Tr} = \mathfrak{Re}\left(\frac{\partial\tilde{n}}{\partial\eta}\int_0^d \eta(x,t)\tilde{f}(x,\lambda_{pr},\tilde{n},\tilde{n_s},d)dx\right) \tag{2.14}$$

where $\mathfrak{Re}$ stands for the real part of a complex number, and $\tilde{f}(x,\lambda_{pr},\tilde{n},\tilde{n_s},d)$ is a complex-valued "sensitivity function" [Thomsen et al., 1986]. This sensitivity function describes the interaction of the probe with the permittivity modulation, and accounts to both absorption and interferences effects. The parameters are the probe wavelength λ_{pr}, the film and substrate complex refractive indexes $\tilde{n}$ and $\tilde{n_s}$, and the film thickness d. All these values are known either from bibliography or direct measurement (see Table .2.1).

In this equation, we made the assumption that the derivative of the film photoelastic complex constant $\frac{\partial\tilde{n}}{\partial\eta}$ is not a function of position. It is an unknown that can only be estimated by fitting the data.

The strain profile $\eta(x,t) = \frac{\partial u(x,t)}{\partial x}$, were $u(x,t)$ is the displacement, can be obtained by solving the two coupled elastic-wave equations :

$$\frac{\partial^2 u}{\partial t^2} = \mathsf{v}^2\frac{\partial^2 u}{\partial x^2} - \mathsf{v}^2\frac{\partial\eta_{th}}{\partial x} \text{ for } 0 \leq \mathrm{x} \leq \mathrm{d} \tag{2.15}$$

$$\frac{\partial^2 u_s}{\partial t^2} = \mathsf{v}_s^2\frac{\partial^2 u_s}{\partial x^2} \text{ for } \mathrm{x}>\mathrm{d} \tag{2.16}$$

The subscript s indicates the substrate. The last term in the left hand side of the first equation is the thermal strain, defined as.

$$\eta_{th}(x,t) = \eta_o \exp(-x/\xi_{pump})\Theta(t),\ \eta_o = \beta_T\Delta T_o\frac{1+\nu_p}{1-\nu_p} \tag{2.17}$$

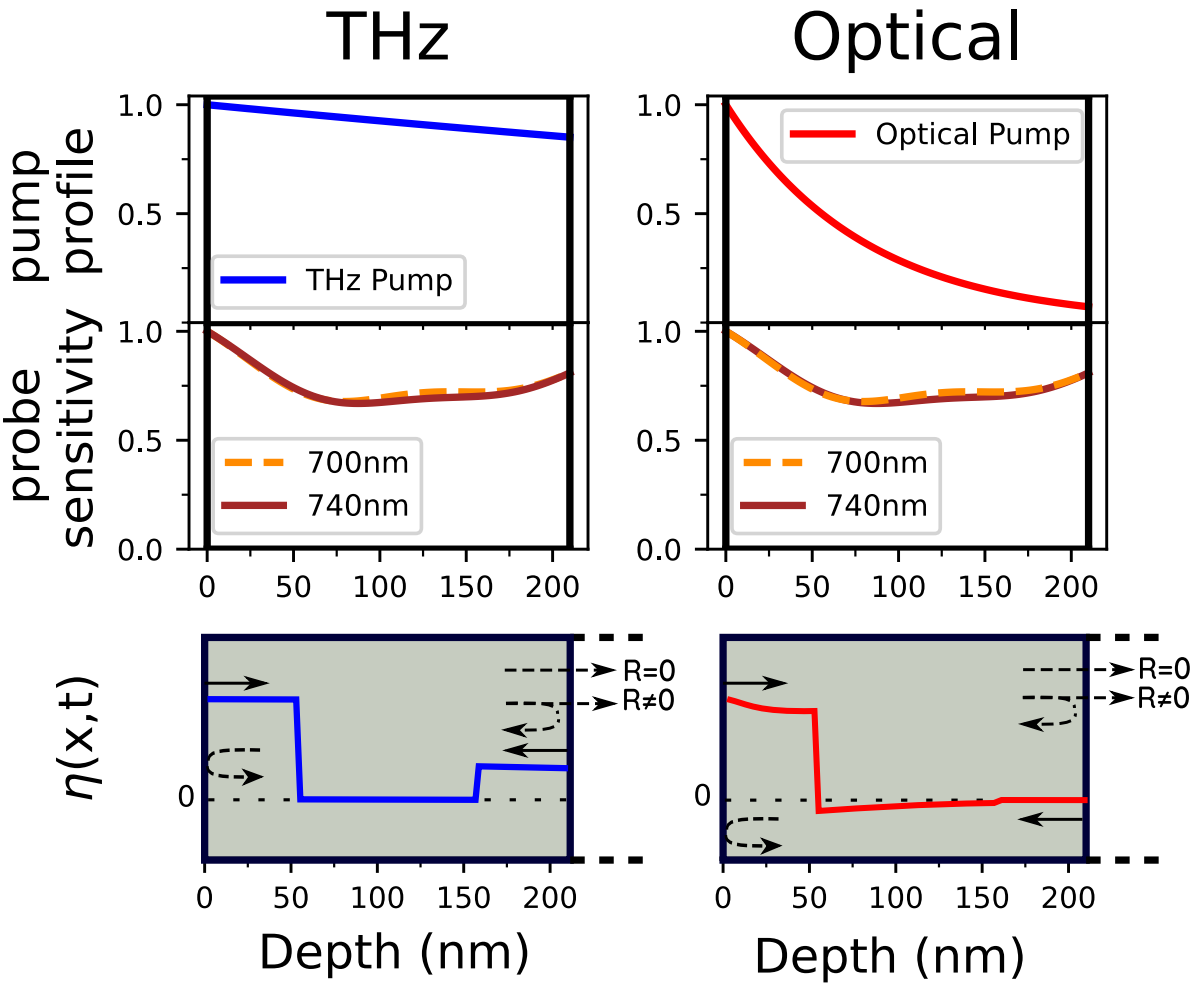

Figure 2.17: Left : THz pump and right : Optical pump. First line : Excitation profiles and modulus of the sensitivity function in the thin film. Parameters correspond to the real parameters of the experiment. All functions were normalized to one at x=0 for clarity. Second line : Sketch of the thin-film and substrate interfaces and strain waves.

$\Theta(t)$ is the Heaviside function, ξ_{pump} the pump penetration depth, β_T the linear expansion coefficient, ΔT_o the initial lattice maximum temperature rise at the surface, and ν_p the film Poisson ratio. The validity domain of such a system of equations is discussed for instance in [Thomsen et al., 1986; Matsuda et al., 2015]. The initial temperature jump is related to pump fluence F_p, intensity reflection coefficient R_p and sample heat capacity per unit volume C, by the formula $\Delta T_o = \frac{(1-R_p)F_p}{C\xi}$. It is worth to mention however that the details of the energy exchange mechanisms that produce the initial lattice displacement, and thus strain, are not important in this model, as long as the initial photo-induced lattice perturbation is very fast compared to the acoustic timescale, leading to an approximate stepwise temporal rise.

Thus, four dimensionless parameters determine the solutions. First, the strain wave reflection coefficient R defined as

$$R = \frac{Z_s - Z}{Z_s + Z} \tag{2.18}$$

where Z_s and Z are respectively the substrate and thin film acoustic impedances ($Z = \rho v_{sound}$ with ρ the density). Second the ratio $K = \frac{d}{\xi_{pump}}$ of the film thickness d and the pump penetration depth ξ_{pump}. If K$\ll$ 1, the excitation profile is almost constant within the film, whereas the

exponential decay is strongly marked when K$\gg$ 1. Third, $V = \frac{\mathsf{v}}{\mathsf{v}_s}$ the ratio of sound velocities in the layer and the substrate. And finally the initial strain at the top-layer surface η_o.

Using Laplace transforms methods, the solutions of Eq.2.16, $u(x,t)$ and $\eta(x,t)$ in the film and the substrate, were calculated analytically, with the initial conditions of no displacement and strain, as well as zero velocity, at t=0, and boundary conditions of continuous displacement and stress at the film-substrate interface, and free surface at the air-layer interface (zero-stress condition).

Thus, by combining the solutions of Eq.2.16, and the formula Eq.2.14, it is possible to simulate and fit the data, as explained below.

We show in Fig.2.17b the normalized excitation profiles for the two pumps and sensitivity functions at the two probe wavelengths, using values from Table .2.1. As expected, the terahertz excitation is almost constant over the whole film thickness (ξ_{THz}=1300 nm), in contrast to the optical excitation that has a penetration depth of ξ_{540nm}=80 nm. As already said above, the probe sensitivity function $\tilde{f}(x, \lambda_{pr}, \tilde{n}, \tilde{n_s}, d)$ are very close to each other, and the difference has a negligible effect on the transmission. Thus, we can conclude that if a change of transmission is observed, it is a consequence of the different pump excitations. Interestingly, we also note that the probe sensitivity function is almost constant, despite the ξ_{probe}=95 nm penetration depth of the 700 or 740 nm probes. This is a consequence of finite size thickness that lead to constructive interferences within the film.

To get further insight into the interpretation of the data $\frac{\Delta T_r(t)}{T_r}$, we first discuss a rough approximation of Eq.2.14. Assuming a constant complex-valued sensitivity function $\tilde{f}(x,...) = \tilde{f}(...)$, Eq.2.14 can be easily simplified to

$$\frac{\Delta T_r(t)}{T_r} \approx \mathfrak{Re}\left(\frac{\partial \tilde{n}}{\partial \eta}\tilde{f}(...)\int_0^d \eta(x,t)dx\right) = \mathfrak{Re}\left(\frac{\partial \tilde{n}}{\partial \eta}\tilde{f}(...)\right)\int_0^d \frac{\partial u(x,t)}{\partial x}dx$$

Thus

$$\frac{\Delta T_r(t)}{T_r} \approx \mathfrak{Re}\left(\frac{\partial \tilde{n}}{\partial \eta}\tilde{f}(...)\right)[u(d,t) - u(0,t)] = \mathfrak{F}\,\Delta u(t) \tag{2.19}$$

where $\Delta u(t) = u(d,t) - u(0,t)$ and $\mathfrak{F} = \mathfrak{Re}\left(\frac{\partial \tilde{n}}{\partial \eta}\tilde{f}(...)\right)$. Within this approximation, the relative transmission variation is simply proportional to the variation of the film thickness $\Delta u(t)$.

The behavior of $\Delta u(t)$ for both terahertz and optical pumps, as well as snapshots of the strain profile $\eta(x,t)$ at typical times, is illustrated in Fig.2.18, using values from Table.2.1 , and three values of the strain reflection coefficient $R = 0$ (matched layer), $R = \pm 0.2$. The behavior of the strain spatial profile is interesting (Fig.2.18c and d), and can be understood using three contributions. A time-independent contribution corresponding to the initial temperature profile, and a propagating and counter-propagating strain waves launched at the free surface and film-substrate surface by the initial stress impulse. The resulting strain is the sum of these three contributions, and evolves depending on the reflections at the free surface or film-substrate interface. At each reflections on the film-substrate interface, the amplitude of the strain-wave is multiplied by R, resulting in a magnitude after n round trips of duration $2\tau_a = 2d/\mathsf{v}$ reduced by a factor R^n. Thus, for times $\gg 2n\tau_a$ long enough such that $R^n \ll 1$, only the time-independent strain (static strain) survives. Thus, we expect the time-independent strain to determine the magnitude of the plateau. Of course, we expect other phenomena to modulate the shape of the transmission signal. For instance, the static strain being related to a temperature profile, and thus to a temperature gradient, heat diffusion, loss and transfer, will smooth and wash away the temperature gradient, and strain, till thermodynamical equilibrium is reached. But, since in Fig.2.19 the plateau amplitude remains constant for delays greater than 700 ps, such phenomena are negligible on the studied timescale, and are not taken into account in this model. As remarked by Schick et al. [Schick et al., 2014] who treated the case of a matched layer $R = 0$, the full strain presents a positive and negative contributions in the limit $d \gg \xi_{pump}$. In the opposite limit $d \ll \xi_{pump}$, the strain has almost the same sign over all the film thickness. It was explained by

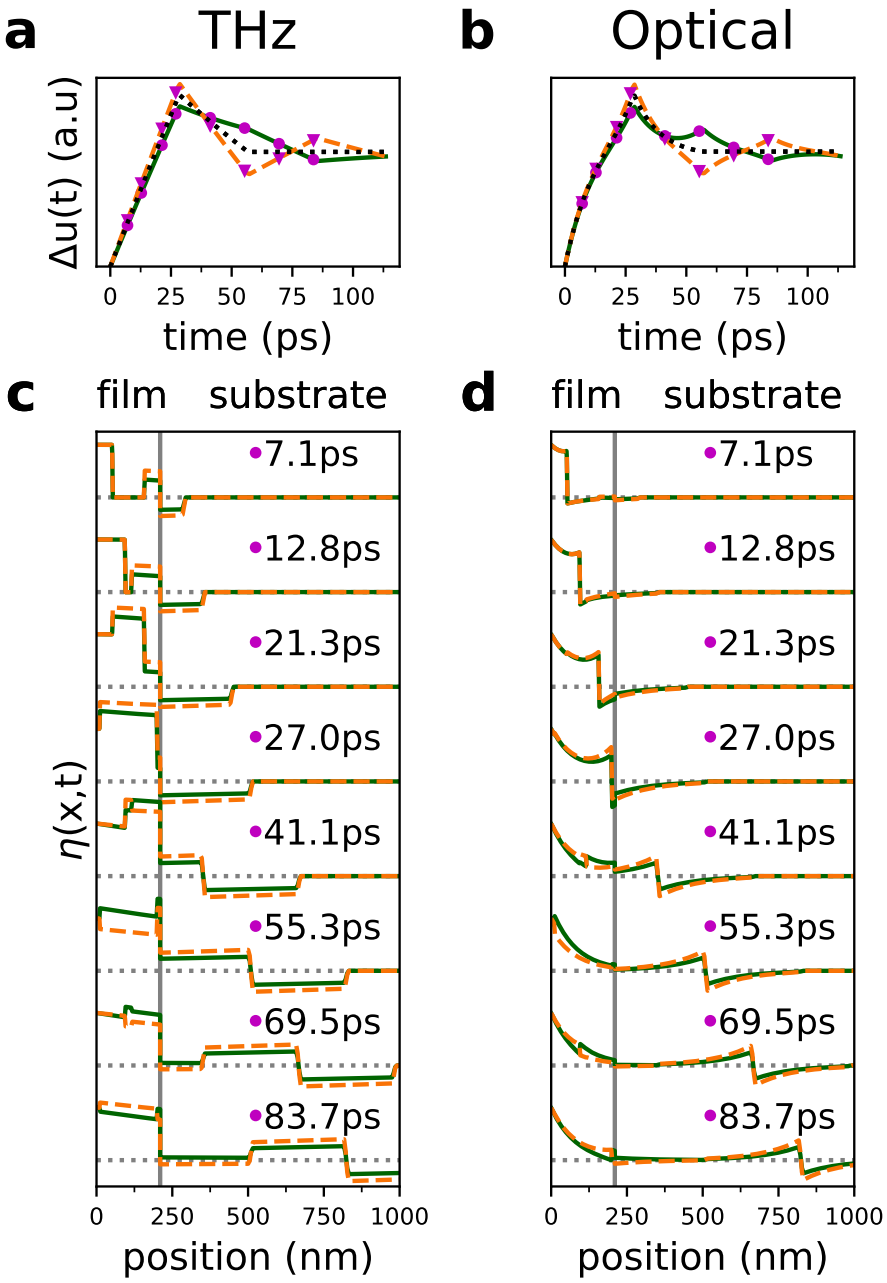

Figure 2.18: Temporal evolution of $\Delta u(t)$ (a,b) and snapshots of the strain profile $\eta(x,t)$ (c,d) within the top layer and the substrate as a function of position at some selected times. Left column (a,c) and right columns (b,d) correspond respectively to THz and optical pump. Panels a and b represent $\Delta u(t)$ with matched layer R=0 (black dotted line) or unmatched $R = \pm 0.2$ ($R = -0.2$ orange dashed line and $R = +0.2$ green continuous line). Markers are placed at times at which corresponding strain wave snapshots are plotted as a function of position. Panel c and d : strain wave profiles $\eta(x,t)$ in the thin film (left of the vertical black line) or in the substrate (right of the vertical black line) at a given time, as a function of position. Horizontal dotted gray lines represent zero strain $\eta = 0$ line for each time. For the simulation, the sound velocity in the substrate was set to 1.5v.

the fact that the static strain always compensate the strain wave. This conclusion remains valid in our model, at least for the small considered reflection coefficient magnitude $|R| < 0.2$.

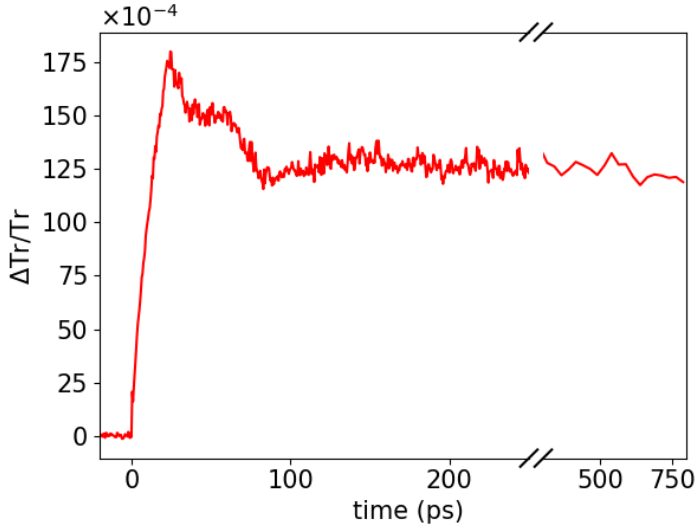

Figure 2.19: Relative optical transmission $\frac{\Delta T_r(t)}{T_r}$ following an optical (540 nm) excitation, as a function of time. For t≤250 ps the time-step is 0.5 ps, while for t≥250 ps, the time-step is 25 ps.

Clearly, a comparison of the simulations shown in Fig.2.18a,b with the raw data of Fig.2.16 shows that the studied V_2O_3 film is not matched to the sapphire substrate. If the layer were matched, $\Delta u(t)$ would reach a plateau after the strain wave launch at the film-substrate interface has traveled back and forth in the film, that is $2\tau_a = 2d/\mathrm{v} \approx 58$ ps (black dotted lines of Fig.2.18a,b). But experimental data show a variation over more than 90 ps. Considering now the unmatched case, we can determine the sign of the reflection coefficient. For $R < 0$, a dip below the plateau value appears near time $2\tau_a$, which is inconsistent with Fig.2.16. Thus we conclude that R is positive, $R > 0$, meaning that the sapphire acoustic impedance is larger than the one of the V_2O_3 film $Z_s > Z$.

2.3.1.2.3 Analysis To go further in the analysis of the data, we fitted data obtained from the terahertz and optical pumps with this simplest possible model using the full Eq.2.14, and the analytical solution of Eq.2.16.

First, the terahertz penetration depth deserves particular attention, because of the frequency distribution of energy $|E_\omega|^2$ of the terahertz excitation pump pulse, shown in Fig.2.20.

From the optical conductivity measured by TDS, and Drude's formula Eq.2.13, we calculated the complex refractive index (real and imaginary parts in Fig.2.20a), and penetration depth $1/\alpha_\omega$ (Fig.2.20b). As shown by the figures, these parameters strongly depend on frequency, rising the question of choosing an effective penetration depth in the formula. We model the intensity absorption profile by a weighted average of the absorption profile at each frequency

$$I(x) \sim \int d\omega P_\omega \alpha_\omega e^{-\alpha_\omega x} \sim \frac{1}{\xi_{THz}} e^{-x/\xi_{THz}}$$

with probability P_ω of absorbing energy within ω and $\omega + d\omega$ defined as

$$P_\omega = \frac{|E_\omega|^2}{\int d\omega |E_\omega|^2}$$

From the numerical integration of Eq.2.3.1.2.3, we obtained the effective penetration depth for the terahertz pump $\xi_{THz} \approx 1300$ nm. In fact, the mean absorption profile is almost indistinguishable to the one at single frequency 0.5 THz over all film thickness.

Second, among the fitting parameters, the photoelastic constants $\frac{\partial n}{\partial \eta}$ and $\frac{\partial \kappa}{\partial \eta}$, where n and κ are respectively the real and imaginary parts of the complex refractive index $\tilde{n}$, are usually

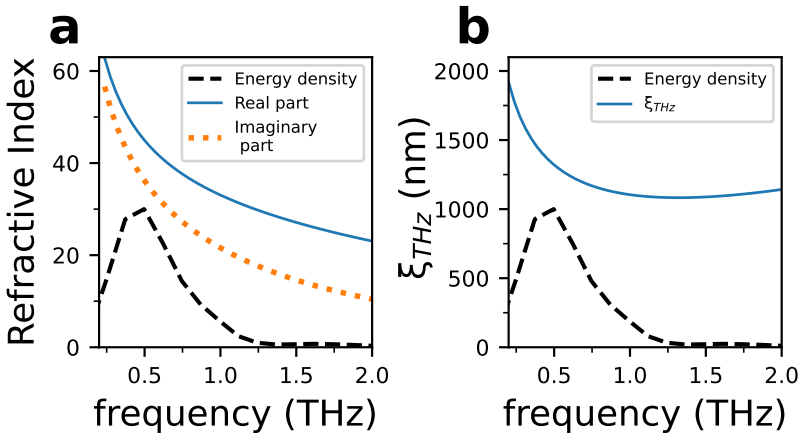

Figure 2.20: (a) Real and imaginary parts of the thin film complex index at THz frequencies, as given by the TDS experiment. (b) Corresponding THz penetration depth as a function of frequency. The dashed line represents the terahertz pump pulse spectral density $|E_\omega|^2$ with arbitrary unit.

difficult to estimate. We tried to fit these parameters to our data, without success. But as already mentioned before, the fact that the sensitivity-function is almost position independent combines the photo-elastic constants with the scaling factor, making difficult or impossible to distinguish both parameters that are strongly correlated. We also verified that a change of the photo-elastic constants values could be almost compensated by a change of the scaling factor. Thus, we choose to separate the magnitude from the phase as $\frac{\partial\tilde{n}}{\partial\eta} = \left|\frac{\partial\tilde{n}}{\partial\eta}\right| e^{-i\phi_n}$. The photo-elastic magnitude $\left|\frac{\partial\tilde{n}}{\partial\eta}\right|$ is incorporated to the overall scaling factor, while the phase ϕ_n was calculated from the relationship $\frac{\partial n}{\partial\eta} = -1.63\frac{\partial\kappa}{\partial\eta}$ that was used in [Liu et al., 2011; Abreu et al., 2017].

Therefore, we ended with *only three* fitting parameters : the acoustic reflection coefficient R, and two scaling factors to adjust the amplitudes to the terahertz or optical-pump results. All the other parameters were obtained from the bibliography or measured in the laboratory, and fixed to the corresponding values (Table.2.1).

The best fit is presented in Fig.2.21, and shows an overall very good agreement with the data for a three-parameter fit. We would like to stress again that the model fits the overall relative optical transmission variation data without any other corrections, including the rising, decreasing and pseudo-plateau parts. In particular, the result of the exponential excitation profile of the optical pump is well reproduced, as well as the small oscillation coming from the reflection of the strain pulse at the film-substrate interface. Interestingly, for the optical pump, it shows that the round shape of the rising part when t<25 ps is also given by the exponential excitation profile, in addition to other possible mechanisms such as non-instantaneous heating, heat diffusion or loss, that are not taken into account in the model.

The value of fitted acoustic reflection coefficient $R \approx 0.18 \pm 0.02$, is larger than the expected value $R \approx 0.11$ calculated from densities and sound velocities extracted from the bibliography (Table.2.1). From R, we obtain the ratio of substrate to film acoustic impedance $Z_s/Z \approx 1.44$. It gives an effective acoustic impedance of V_2O_3 of $Z \approx 31.0\ 10^5 g/cm^2/s$ instead of $Z = 35.9\ 10^5 g/cm^2/s$ using density and sound velocity along (110) from bibliography, since our sample has a preferential orientation along (110). This small discrepancy of -14% may have different origins.

First, a density change due to internal stress/strain created during the synthesis process might be invoked. However, such effects are usually smaller than 1% in V_2O_3 films (see eg Ref.[Kalcheim

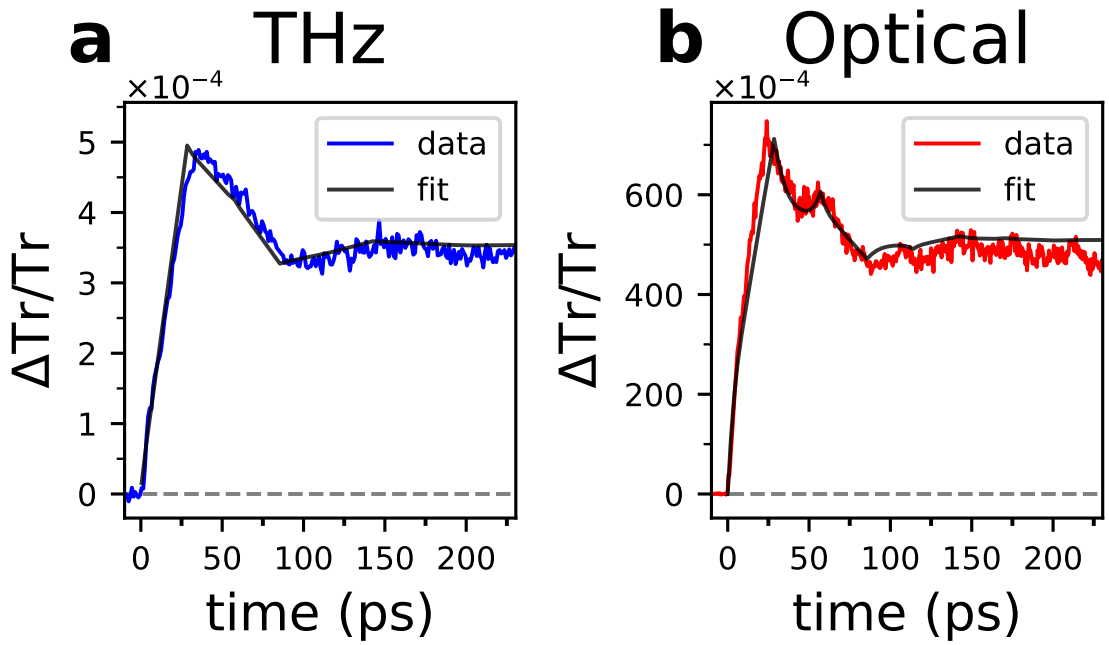

Figure 2.21: Relative optical transmission as a function of time $\frac{\Delta T_r(t)}{T_r}$, and best fit results with only three parameters. Experimental raw data are presented. (a) THz pump.(b) Optical pump. Only points every 0.5 ps are shown.

et al., 2020]) and cannot account for the observed 14% differences in R values.

Second, values from the bibliography come usually from single crystal samples, that cannot be directly compared to thin films. As a matter of fact, the thin film sample has a heterogeneous structure, with typical grain sizes estimated to be around 25-30 nm, as revealed by the SEM image of Fig.2.14b. This dense mixture of nanocrystals introduces orientational disorder, and changes the effective density because of the presence of holes or porosity. To different orientations correspond different elastic constants and sound velocities. As a result, the measurement over the beamsize would give an effective acoustic impedance by spatial averaging. For instance, in disordered inhomogeneous systems [Fouque et al., 2007], an effective density and elastic stiffness are obtained by averaging the density, and the *inverse* of the elastic stiffness. It results in an effective sound velocity that can be smaller than the components velocities. In our case, the presence of holes or less dense components decreases the effective density, and thus the acoustic impedance.

2.3.2 Effect of the probe wavelength

From the section 2.2.4, we expect that a change of probe wavelength from 480 nm to 740 nm will impact the amplitude of the photo-induced signal. The figure 2.22 presents the photo-induced signal obtained for a THz excitation probed at either 480 nm or 740 nm. Experimentally, as expected, the amplitude of the signal increased by a factor equal to 1.65±0.02, in agreement with the one obtained theoretically, when the 740 nm probe wavelength was changed to 480 nm.

It is important to mention that, for such a change of probe wavelength, while a difference in the shape of the sensitivity function should cause a significant difference in the normalized photo-induced signal, the signal to noise ratio of the present experiment do not allow us to confirm this tendency. Thus, we will consider that the amplitude was the only observed difference. Since only the amplitude is modified, the photo-elastic constant can be considered , in our case, as independent of the probe wavelength.

Using the model presented earlier, it is possible to predict the modification of amplitude

induced by the change of wavelength. Starting from the experiment performed at 480 nm, we implemented all the pump related parameters (penetration depth and photo-elastic constant) and probe related parameters (wavelength, penetration depth, real part of the refractive index) given in the literature. The adjustment of only 3 parameters (the sound velocity, the reflection coefficient and the scaling) allowed us to reconstruct the transient signal (See blue lines in Fig.2.22). Then, we were able to predict the signal obtained for the other probe wavelength (740 nm) by keeping the pump related parameters and the adjustable parameters fixed and modifying only the probe related parameters that is just changing the value of the complex refraction index of the sample. As a consequence, only the sensitivity function has been changed. The result of the prediction of the photo-induced signal for $\lambda_{pr} = 740$ nm from the one obtained at 480 nm is shown in Fig. 2.22 (See green lines). The magnification factor equal to 1.6 is reproduced by the theory. The agreement between the experiment and the model is very satisfying.

Being able to predict the amplitude of the signal is of particular interest for the study of strain propagation. It allows to select the wavelength giving the best signal to noise ratio and be sensitive to pump related effect. On the contrary, it can be useful to diminish the sensitivity to the strain contribution if the signal is made of several contributions, in order to focus on others.

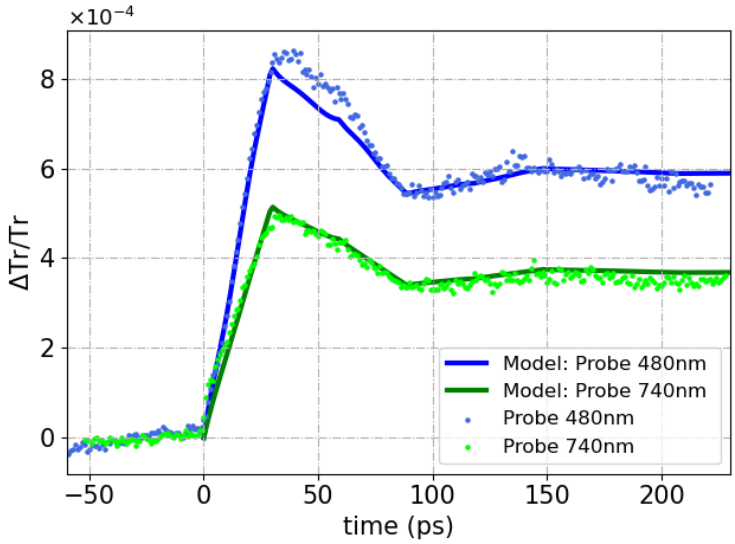

Figure 2.22: transient optical transmission of V_2O_3 following a THz excitation. Experimental transient signals (dot in the figure) obtained for two different probe wavelengths: 480 nm (blue) and 740 nm (green); and their corresponding theoretical representation (lines)

2.3.3 Effect of the pump power

In this section,we analyze the photo-induced signal amplitude as a function of the incident power and compare the results obtained with a THz or Optical pump.

As suggested by Thomsen et al., thermoelastic effects are related to the energy density absorbed by the sample, per unit volume: W(z). One of the method to prove the thermoelastic origin of a photo-induced signal is to compare the amplitude of the signal obtained for various pump excitation wavelengths [Levchuk et al., 2020], at equivalent absorbed energy density. Unfortunately, as it will be seen later, it is difficult to use this technique if the two excitation profiles imply very different shape factors δ and refractive indices n_1.

To tackle this problem, we compare the ratio of the signal amplitudes obtained experimentally in the case of a THz and Optical excitation to the ratio expected by the theory. For the optical experiment, the excitation profile is exponentially decaying and the majority of the beam is absorbed before reaching the interface with the substrate since ξ_{opt} <d (d=210 nm and ξ_{opt}=80

nm). On the contrary, for the THz experiment, the very important penetration depth compare to the film thickness implies a flat excitation profile (ξ_{THz}=1300 nm). In this study we compare those two limiting cases.

Due to the weakness of the signal in the THz experiment, the most sensitive probe wavelength was selected (480 nm). The experimental constraints inherent to the Optical pump setup forced us to use a different probe wavelength (700 nm). Thus, the correction of the sensitivity function, linked to this change of probe wavelength and presented earlier, will also be taken into account in the theoretical ratio.

2.3.3.1 Experimental results

First is presented the study of the transient signals obtained at room temperature as a function of the excitation power, for both Optical and THz excitation (See Fig. 2.23).

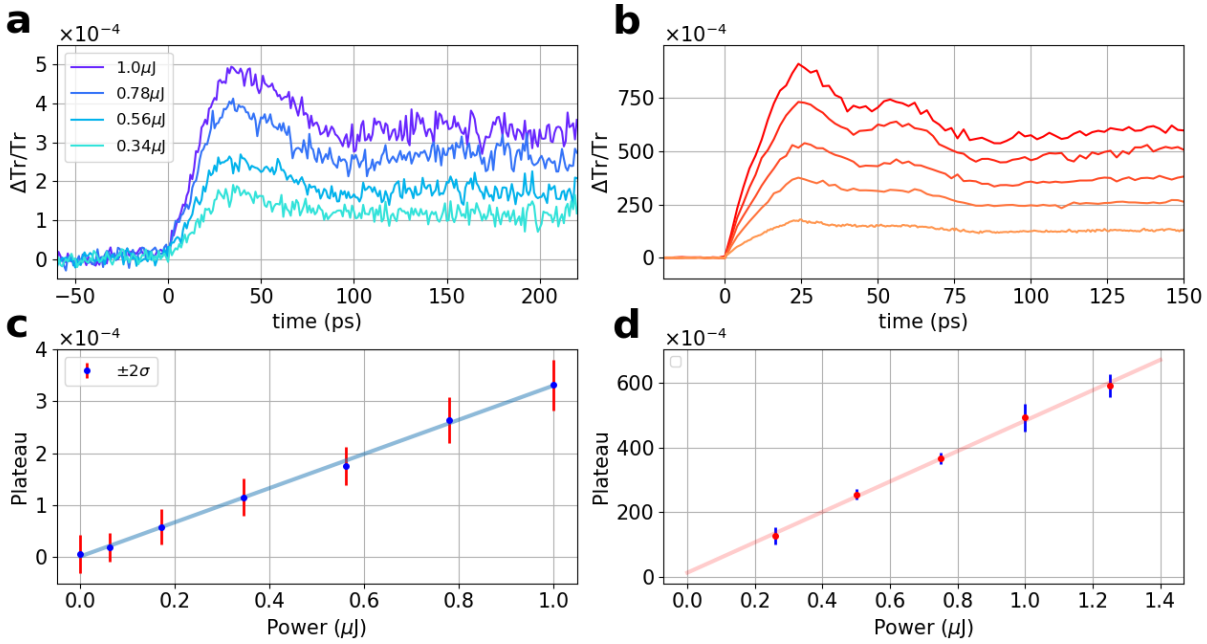

Figure 2.23: Transient optical transmission for various excitation powers (a) THz pump Optical (480 nm) probe. Optical (540 nm) Pump/Optical (700 nm) probe . (c) and (d) : amplitude of the plateau (signal for t>100 ps) as a function of the excitation power. (c): THz pump (d) Optical pump

For a THz excitation, the power was modified using a pair of THz polarizers. The power varies quadratically with respect to the electric field amplitude. A first polarizer was set in the collimated THz beam, before the parabolic mirror. Its transmission axis was kept vertical. A second polarization was installed upstream, on a rotating mount. By changing the polarization direction of the rotating mount with respect to the vertical direction, the projection of the TeraHertz electric field amplitude on the transmission axis of the other polarizer will be reduced leading to an attenuation of the field amplitude. The power was measured in maximum transmission configuration using a calibrated pyroelectric detector and was found to be equal to 0.95 uJ. The dimensions were 0.8 by 1.1 mm of Full Width Half Maximum (FWHM) (See Fig.2.25), measured at the focal point, by a pyroelectric camera (Pyrocam III Ophir Optronics). It gives a beam area of 1.0 mm^2 (A=$\pi\omega^2/2$, where $\omega = \frac{FWHM}{\sqrt{2ln(2)}}$). Therefore the maximum fluence was 0.95 uJ/mm^2.

Concerning the optical excitation, we studied the amplitude of the signal for different powers spanning from P=1.25 uJ to P=0.25 uJ. The power was reduced using a variable neutral density

filter wheel. The FWHM of the beam was measured by the knife edge method and was found to be equal to 160 μm. The beam area was equal to 0.029 mm^2. Therefore, the maximum fluence was 34 $\mu J/mm^2$.

In Fig.2.23 is represented the transient transmission for various pump power for both THz pump Optical probe (**a**) and Optical pump Optical probe (**b**) experiments. On the left hand side, is shown the results for the THz excitation, probed at 480 nm. As it can be seen in this figure, the amplitude of the signal is affected by the reduction of the electric field or excitation power. In **c** is presented the amplitude of the long delays mean value (time>100 ps). This amplitude scales quadratically with the THz electric field amplitude. It means that the signal is proportional to the deposited energy. After normalization (not shown here), we can confirm that rising the power only leads to a scaling of the signal and that no significant difference such as non linear effects are seen from this change of excitation power.

Concerning the Optical pump/Optical probe experiment (right hand side **b** and **d**), the probe wavelength is 700 nm. The conclusion listed above for the THz case are also valid for this type of excitation: the signal is also proportional to the power or deposited energy and no non linear effects are observed.

Experimentally, we found that the ratio between the slopes is:

$$A_{exp} = \langle \frac{\Delta Tr_{opt}}{\Delta Tr}(time > 100ps) \rangle / \langle \frac{\Delta Tr_{THz}}{\Delta Tr}(time > 100ps) \rangle = 143 \pm 20.$$

2.3.3.2 Energy deposition in a semi-infinite or multi-layer system

It is not sufficient to observe a proportionality between the deposited energy and the amplitude of the photo-induced signal to conclude that the origin of the signal is thermoelastic. Indeed other effects that scale linearly with the excitation power could contribute to this photo-induced signal. In this section, we determine the energy absorbed/deposited, per unit volume, inside the sample for both excitations and integrate it over the film thickness. Then, if the computation of this theoretical ratio of absorbed fluence A_{th} is similar to the ratio of the slopes obtained experimentally A_{exp}, it will confirm that the origin of the photo-induced signal is mainly thermoelastic.

First, a few assumptions must be taken into account:

- Even though the pump and probe conditions are different in both experiments, the complex photo-elastic parameter $\partial\tilde{n}/\partial\eta = \partial n/\partial\eta + j\partial\kappa/\partial\eta$ are equal at both probe wavelengths. In fact, the results of Fig.2.22 where the probe wavelength effect could be explained by just changing the film index implies this assumption. The same value will be used for both cases.
- From Fig.2.8 in section 2.2.1 , we can consider that the sensitivity function is constant over the whole sample thickness for both 480 nm and 700 nm.
- For the sake of simplicity, we will use the static thermal strain $\eta_{th}(z) = \eta_0 e^{-z/\xi_{pump}}$ to compare the amplitudes of these two experiment. It is equivalent to compare the plateau obtained experimentally at large times.

As a consequence, the change of transmission can be rewritten using the deposited energy (W(z)), per unit volume, inside the film and at a depth z, as follows:

$$\frac{\Delta Tr}{Tr} \propto f(\lambda_{pr}, n_1, n_2, d) \int_0^d W(z)\, dz \tag{2.20}$$

where d is the thin film thickness, $f(\lambda_{pr}, n_1, n_2, d)$ is the sensitivity function.

As a first approximation, one can consider a semi-infinite model. In this case, the energy deposited per unit volume W(z) is [Thomsen et al., 1986]:

$$W(z) \approx \frac{F(1-R)}{\xi_{pu}} e^{-z/\xi_{pu}} \tag{2.21}$$

with $(1-R) = \frac{4n_1}{|1+\tilde{n_1}|^2}$, F is the fluence, ξ_{pu} is the pump penetration depth.

However, due to flatness of the THz excitation profile, this approximation is not accurate. We should generalized to a multi-layer model to account of all the energy absorption. This was done by Matsuda et al. [Matsuda and Wright, 2002].

The mean absorbed energy per unit volume, measured over the electromagnetic wave period can be written as follows:

$$W = -\frac{d < \Pi(t) >}{dz} \frac{2\pi}{\omega} \tag{2.22}$$

where ω is the angular frequency, and z is the propagation direction, $\Pi(t)$ is the Poynting vector which quantify the directional power flux of an electromagnetic wave.

We consider a two layer model where an absorbing layer of index $\tilde{n_1}$ and finite thickness d=210 nm is deposited on a semi-infinite substrate of refractive index $\tilde{n_2}$ with $\tilde{n_1} \neq \tilde{n_2}$. The incident beam enters the absorbing layer side (film) and several possible reflections occurs at both interfaces (air-film and film-substrate). The system is now composed of waves directed towards the right direction and others towards the left direction. Interferences can originate from the interaction of these multiple propagating waves. Consequently, the energy deposited per unit volume in this absorbing film of finite thickness is [Matsuda and Wright, 2002]:

$$W(z) = \frac{F}{\xi_{pu}} n_1 \left[|A|^2 e^{-z/\xi_{pu}} + |B|^2 e^{z/\xi_{pu}} + 2Re\left(AB^* e^{i2k_0 n_1 z} \right) \right] \tag{2.23}$$

where F is the fluence (incident energy per unit area), ξ_{pu} is the penetration depth of the pump beam, n_1 is the real part of the refractive index $\tilde{n_1}$.

In this equation, the first term corresponds to the propagation of all the electromagnetic waves, incident and reflected, directed towards the right direction. The second term corresponds to the one propagating towards the left direction and the third term corresponds to the interferences between propagating waves.

When d>> ξ, meaning the case where the film is absorbing the totality of the beam in less than the film thickness d, there are no left propagating waves inside the sample nor any interference (B=0). Under these considerations, the result of eq.(2.21) can be found from eq.(2.23).In our case, for the optical pump experiment, the film is sufficiently absorbing ($\xi \approx 80$ nm in the visible range and d=210 nm) to fall in the semi-infinite limit whereas the full model should be considered for a THz excitation.

We computed the energy deposited per unit volume inside the thin film (W(z)) for an incident fluence F=1J/nm^{-2} in both THz and Optical excitation cases, using the two types of models, equations (2.23) and (2.21). The result of this computation is shown Fig.2.24. First, for equivalent incident fluence, W(z=0) is much more important for an Optical excitation. This is partly caused by the important free surface reflection coefficient R in the THz range. Secondly, the strong absorption of the Optical beam in the film leads to a small contribution of the left propagating waves and interferences. As a consequence, for the Optical excitation, the results obtained using the semi-infinite and multi-layer model are very similar.

For the THz, as it is highlighted in the right panel of Fig. 2.24, the result obtained in the two-layer model is 30 times larger than the one obtained in the semi-infinite model. Indeed,

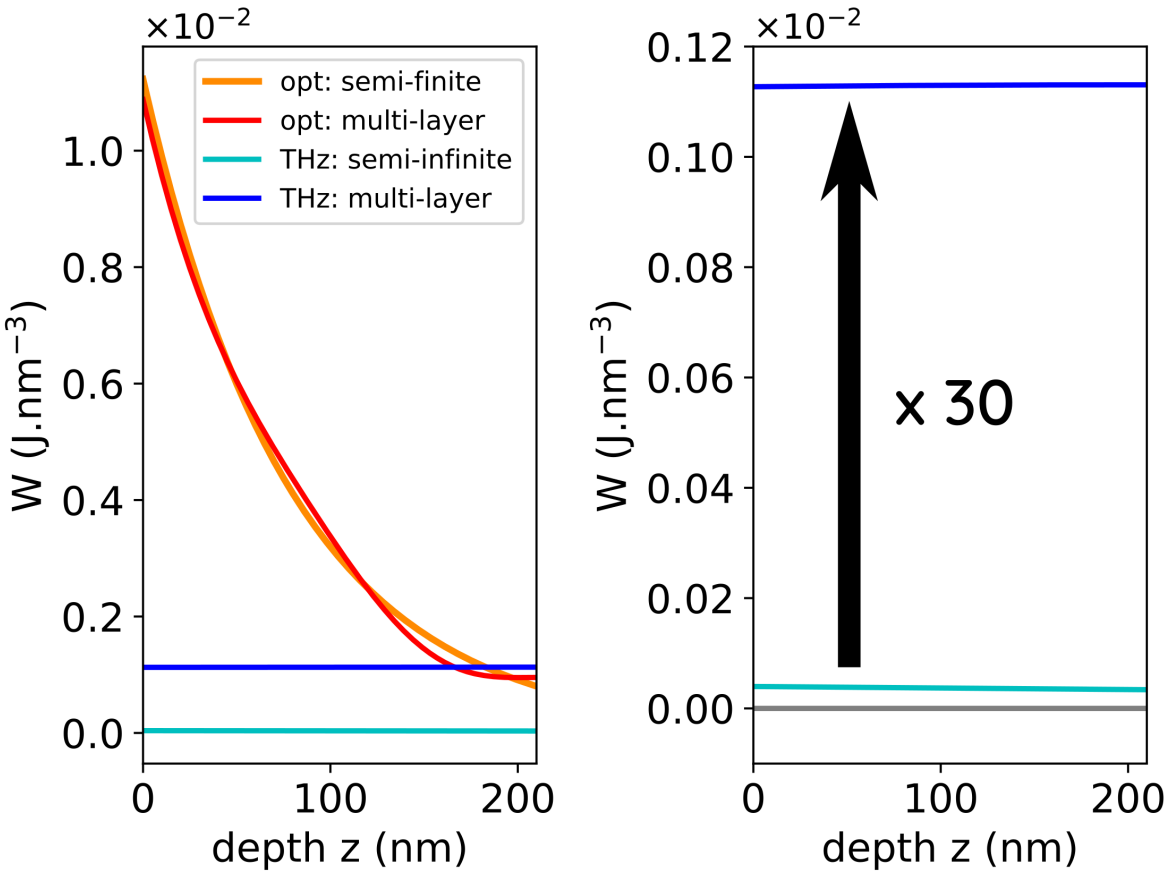

Figure 2.24: Left: Computation of the Energy deposited per unit volume inside the 210 nm V_2O_3 thin film for an arbitrary incident fluence F=1J.nm^{-2}. We compared the results obtained using the semi-infinite model (orange for Optical and cyan for THz excitation) and the one obtained using the finite model (considering also the left propagating waves and interferences) (red for Opt. and blue for THz). Right: Zoom on the THz case

the flatness of the THz excitation profile makes the left propagating waves non-negligible. Thus, coherent constructive interferences enhance the actual absorbed fluence.

As a summary, while the semi-infinite model gives a very satisfying result in the Optical excitation case, for the THz it leads to an underestimation of the mean deposited energy per unit volume W of a factor roughly equal to 30 in our case.

From equation (2.20) and (2.23), the ratio A_{th} can be calculated as:

$$A_{th} = \frac{f_{700nm} \int_0^d W_{opt}(z)\, dz}{f_{480nm} \int_0^d W_{THz}(z)\, dz} \tag{2.24}$$

The sensitivity functions are related by $f_{480nm} = 1.6 f_{700nm}$. The ratio of the incident fluences is equal to 34. We found a theoretical ratio of the amplitude of transient signals $A_{th} \approx 80$, which is 2 times smaller than the one found experimentally ($A_{exp} = 143 \pm 20$).

Nevertheless, with regards to all the assumptions done, we can say that the theoretical model explains the main part of the difference between the transmission amplitude measured for THz or optical excitation. It shows that the signal is proportional to the injected power. Combined with previous simulations using strain waves, it indicates that the origin of the photo-induced signal is mainly thermoelastic.

2.3.4 Summary

In this section, using experimental results and modelizations, I showed that various pump related parameters but also probe related parameters were influencing the resulting transient signal.

First, the role of the pump profile on the temporal evolution of ultrafast optical time-resolved transmission response of a thin film of vanadium sesquioxide in the metallic phase was studied for two types of pumps : a terahertz pump and an optical pump. Using raw relative transmission data and only three fitting parameters, the temporal profile of the relative optical transmission for both pumps was analysed within the thermoelastic framework over a 250 ps time range, corresponding to the acoustic timescale of this V_2O_3 film. For a given pump beam of penetration depth ξ_{pump} absorbed by a sample of thickness d (shape factor $\delta = d/\xi$), while similar results were obtained for excitations leading to equivalent δ factors [Levchuk et al., 2020], by using thicker films ($\delta_{THz} \neq \delta_{opt}$) we were able to observe differences between the photo-induced response originating from terahertz and the one from optical pump excitations.

We could find very few studies dealing with a THz pump Optical probe setup in V_2O_3. While some were focusing on ultrafast phenomena in the PM phase under very high electric field [Giorgianni et al., 2019], and others were focusing on photothermal metallization of the AFI phase [PhD thesis Abreu, 2014], none of them were treating thermoelastic strain waves generation and propagation induced by THz pulses in the PM phase.

Nevertheless, similar results, but with a reflectivity setup $\Delta R/R$ and optical pumps, were presented by [Abreu et al., 2017] or [Mansart et al., 2010]. Note these authors only presented the oscillatory part of the signal after removal of some time varying background.

We would like to point out that the extraction of the "oscillating" contributions may obscure the presence or absence of the contribution of a static strain. Our analysis demonstrated the importance of this static strain in the interpretation of the plateau observed for both excitation processes.

This methodology allowed us to evidence that the terahertz absorption profile is almost homogeneous over the film thickness (large penetration depth compared to film thickness). Conversely, the optical pump presents a marked exponential decay within the sample whose shape governs the transmission temporal profile at all times. These differences in excitation profiles are directly observed on the shape of the transmission transients.

While the strain wave was found to be bipolar for the Optical excitation, it appeared to be unipolar for the THz, as suggested by [Schick et al., 2014]. This peculiarity could be of primary importance in the view of performing a strain-induced Mott transition in V_2O_3.

We showed that the superposition of strain waves to the static strain plays a central role in the interpretation of the data, the former having a contribution that decreases as time increases, the latter determining the plateau value within the acoustic timescale, and for time much smaller than heat transfer timescales. The crucial steps in the data interpretation was to use full raw relative optical transmission data with no time-varying "background" removal. Note also that the transmission sensitivity function being almost flat, it can catch the effect of static strain and dynamical contribution with a small distortion, in contrast to reflectivity sensitivity functions.

From the material point of view, we also measured the acoustic impedance mismatch between V_2O_3 film and sapphire substrate ($R \approx 0.2$). Such a mismatch was unexpected, and gives another important control parameter in addition to usual ones (X-rays, four-points resistivity measurements, SEM...), to improve the synthesis methodology and better control the quality of the films in the design of new electronic or opto-electronic devices.

Then, by comparing the pump power dependence obtained experimentally for both THz and Optical exitation to theoretical computation we concluded that the main origin of the signal is thermoelastic. Also, in the THz case, the flatness of the absorption profile generate a non negligible amount of left propagating waves that will interfere coherently with the right propagating waves. These interference increases the absorbed THz fluence by a factor 30.

Finally, we studied the impact of a change of probe wavelength on the transient signal. In a

THz pump Optical probe experiment we showed that a change of probe wavelength from 480 to 740 nm leads to a reduction of the signal amplitude by a factor 1.6. Using a model we were able to predict this important modification of the signal amplitude.

2.4 Study of a V_2O_3 thin film with residual stress

2.4.1 Sample preparation and characterization

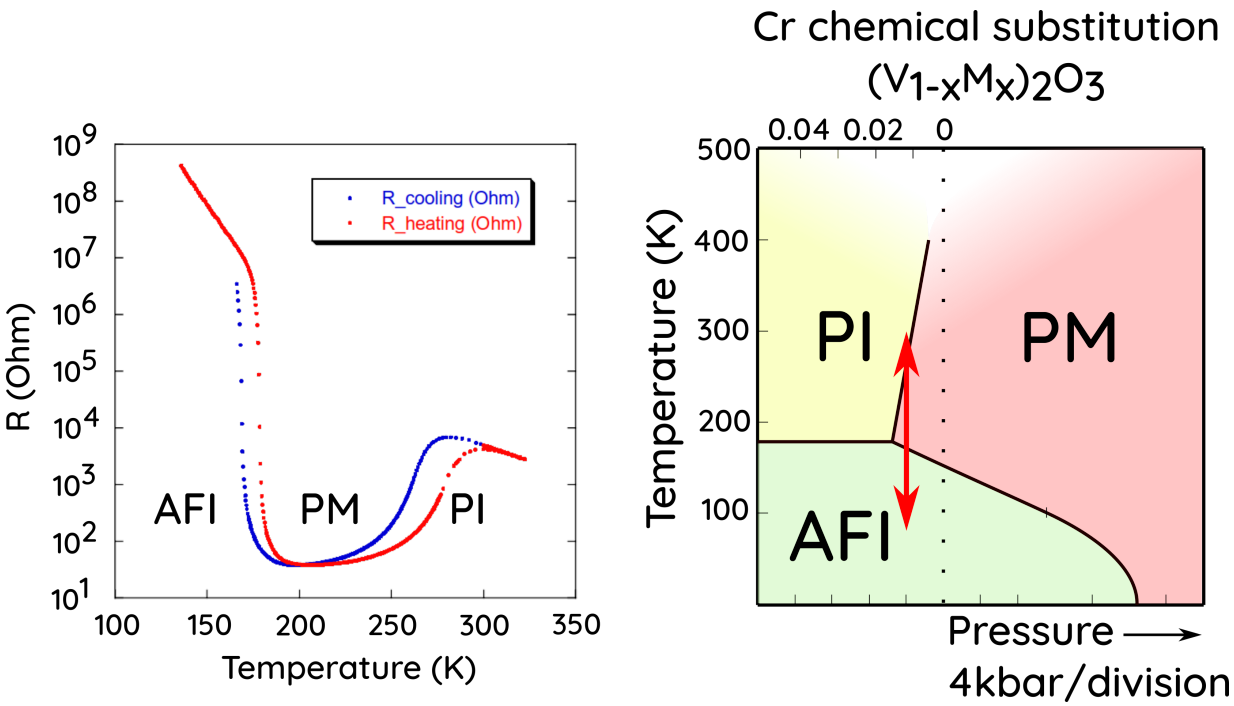

Figure 2.25: Left: Resistivity of the V_2O_3 sample via four-probe technique (provided by IMN Nantes). Right: Phase diagram of V_2O_3, adapted from [McWhan et al., 1973], the red arrow represents the range of temperature studied.

A vanadium metallic film made at the IMN (Nantes, France) was deposited on a SiO_2/Si substrate through magnetron sputtering of a vanadium target in Ar plasma. A subsequent heating at 800°C in Ar/5% H_2 atmosphere, but with the residual presence of oxygen, allows obtaining a crystallized V_2O_3 film of thickness 210 ± 10 nm. Under a precise temperature cycling, a residual stress is obtained and leads to a shift of the position in the phase diagram which is equivalent to applying a negative external pressure or substituting Vanadium atoms by Chromium. The four-probe technique revealed a very rare thermal behavior were two thermal hysteresis were observed (at roughly 170 and 260 K) on this sample. Indeed, upon lowering the temperature, the sample goes from a high resistance phase, to a reduced one at 170 K<T<260 K. The resistivity grows again to reach a different high resistance phase at T < 170 K.

The sample is in the paramagnetic insulating (PI) phase at room temperature, instead of having a metallic behavior (PM) for unstrained samples. Upon decreasing temperature, the sample undergoes two phase transitions. A Mott transition from paramagnetic insulator (PI) to paramagnetic metallic phase (PM) at 260 K. At lower temperature (T≈ 170 K), a symmetry breaking phase transition from the PM phase to the antiferromagnetic insulating phase (AFI).

Using the phase diagram, this thermal behavior allowed to conclude that the residual stress is equivalent to the substitution of approximately 1% of Vanadium atoms (See red arrow in the right part of Fig.2.25) by Chromium, or applying a negative pressure of -4 kbar.

2.4.2 THz Time Domain Spectroscopy

In this section, we present preliminary pump/probe experiments on this sample using our experimental set-up. The complex transmission of the sample is calculated in the THz range using the TDS setup :

$$\tilde{Tr}(\omega) = \frac{FT_{sample}(\omega)}{FT_{reference}(\omega)} \tag{2.25}$$

where FT stands for Fourier Transform. The sample scan corresponds to time traces measured through the thin film and its substrate while the reference scan is taken through the substrate only.

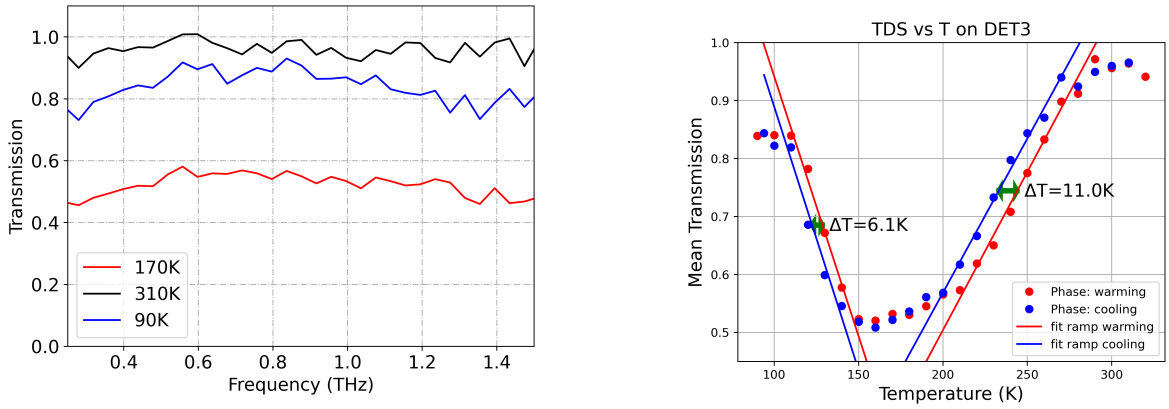

Figure 2.26: Left: Modulus of the transmission obtained at various temperatures from THz-TDS measurements on V_2O_3 sample with residual strain. Right: Mean value of the transmission modulus for frequency spanning from 0.4-1.4 THz as a function of temperature.

The modulus of the transmission as a function of frequency is shown in Fig.2.26. In the experimental frequency range, the transmission is almost flat as a function of frequency. As expected, at T=90 K and T=310 K, a high transmission (between 0.85 and 0.95) is observed due to the high Resistivity of the sample. Indeed, the insulating behavior imply that the THz radiation will not be absorbed because its energy is smaller than the gap. On the contrary, the small resistance observed in fig.2.25 illustrates a metallic behavior. Thus the free carriers will absorb the THz radiation and contribute to the reduction of the Transmission (Tr $\approx$ 0.55).

Using the formula given by Glover et al. [Glover III and Tinkham, 1957], known as Tinkham formula, it is possible to extract the THz effective conductivity of the film from the modulus of the transmission as:

$$\sigma = \left(\frac{1}{|\tilde{Tr}|} - 1\right)\frac{n_s + 1}{d\, Z_0} \tag{2.26}$$

where Z_0=376.7 Ω is free space impedance, n_s the refractive index of the substrate (n_s=3.41, measured by THz TDS), d the film thickness (200 nm). Because the transmission is almost frequency independent, we will use the mean transmission modulus over the frequency range 0.4-1.4 THz to increase the signal to noise ratio.

Figure 2.27 represents the calculated THz effective conductivity as a function of temperature for both warming and cooling temperature ramps. This variable is inversely proportional to the resistance measured by the four-probe technique but cannot be compared quantitatively. Nevertheless, their temperature evolution can be discussed.

Two thermal hysteresis are also observed through THz-TDS. This measurement seems to confirm that the hysteresis obtained at lower temperature, between the AFI and PM phase is narrower ($\approx$ 6 K) than the one obtained between PI and PM phase ($\approx$ 11 K).

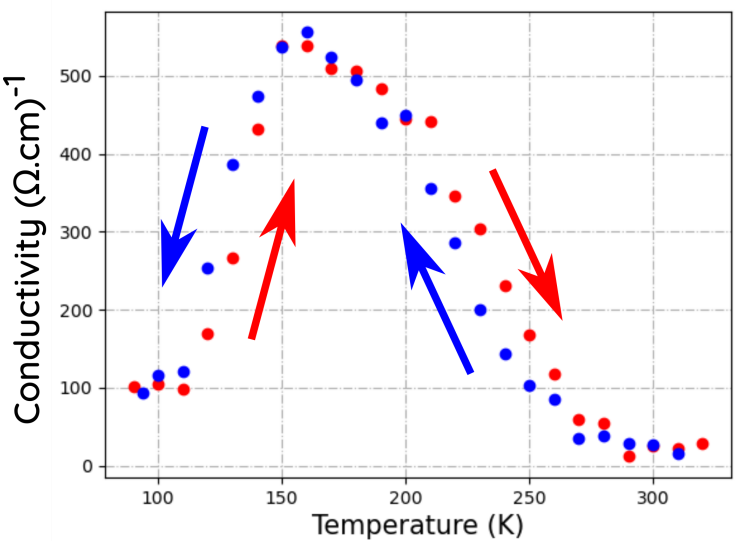

Figure 2.27: THz conductivity extracted from THz Time Domain Spectroscopy of the strained V_2O_3 thin film as a function of temperature, calculated from Eq.(2.26).

Concerning their position, it can be noticed that the THz-TDS measurement is not in accordance with the four-probe technique. Indeed, the temperature evolution of the THz-TDS is shifted to lower temperatures by 40 K compared to the four-probe technique.

Several reasons can explain this discrepancy. First, the difference in cooling system between the two experiments. A closed cryogenic setup was used for the four probe measurement. For the THz-TDS the temperature is controlled by a cryogenic N_2 stream (open) (Oxford cryostream) optimized for micrometric single crystal. Second, in the case of a bulky sample, the power provided by the cryogenic stream to cool the sample might be insufficient to reach this temperature. As a consequence, the temperature of the sample can be inhomogeneous and higher than the one provided by the temperature monitoring. Third, the four-probe technique is sensitive to the surface conductivity. This conductivity might differ from the one measured through the whole sample by THz-TDS depending on the phase proportions as a function of the depth.

In the intermediate range of temperature, considered as being the zone of stability of the PM phase, the calculated conductivity was equal to $\sigma \approx 500\Omega^{-1}.cm^{-1}$. This value is two times smaller than the conductivity reported in literature. This smaller dc conductivity can be the result of a higher crystallinity or morphology defect concentration for example [Abreu et al., 2017].

2.4.3 THz pump/Optical probe experiments

In fig.2.28 is presented the transient photo-induced signal obtained on this "three-phases" sample, in reflection configuration (the Si substrate is opaque to the probe), as a function of temperature. In **a** is presented the result for a temperature range spanning from 130 K to 230 K. At those two temperatures, signals with large amplitude but different signs are found. Therefore in **b** and **c** is found a study around these particular temperature.

Starting from room temperature, no photo-induced signal is detected (See Fig.2.28**b**). On decreasing temperature, a steplike feature starts to appear (At T=265 K). Its amplitude grows down to T=225 K. At this temperature the step function reaches its maximum amplitude (See Fig.2.28**b**). For even lower temperatures the signal amplitude starts to decreases. At 170 K (See Fig.2.28**a**), the signal is not a steplike function anymore. This signal is similar to the one obtained in other PM phase V_2O_3 sample. Below 160 K, the signal becomes negative and follows

an exponential trend. The amplitude of this negative signal increase with the decrease of the temperature and reaches a maximum around 130 K. For T<130 K, the signal slowly vanishes (See 115 K in Fig.2.28**c**).

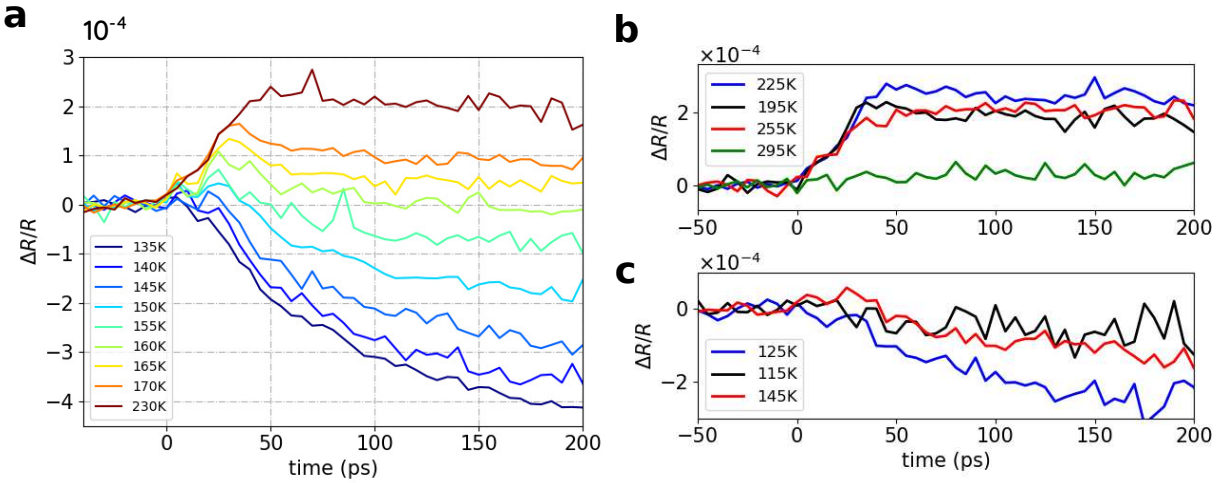

Figure 2.28: THz pump/Optical probe reflectivity transient of the "three phases" V_2O_3 thin film as a function of temperature.(a) Study for temperature between 135 K and 230 K. (b): Study focusing around 225 K. (c): Study focus around 125 K

Using the temperature dependence conductivity obtained in THz TDS, it is possible to interpret the data obtained during the THz pump/Optical probe experiment.

At room temperature, the system is in the PI phase, no THz are absorbed due to this insulating behavior. As a consequence, no photo-induced signal is observed in the THz pump/Optical probe experiment.

At 265 K, the conductivity starts to grow, sign of the coexistence of PM and PI phases. THz are partly absorbed by the PM phase. The unusual steplike function could originate from the concomitant photo-induced responses of both phases.

At 170 K, the system reaches its maximum conductivity. The PM phase is predominant. It results in a signal similar to the one presented during this chapter, observed in other PM phases and assigned to the propagation of strain waves within the film. For lower temperatures, the decrease of conductivity indicates the presence of the AFI phase.

At T=130 K, we can consider that there is an equivalent proportion of AFI and PM phases. As reported in literature [Abreu et al., 2015; Gray et al., 2018; Abreu, 2014], the photo-induced signal obtained in region where both an insulating and the metallic phases coexists in highly correlated compounds follows an exponential trend of negative sign. They are usually assigned to nucleation and growth of a metallic fraction under the transition temperature. Gray et al. suggested a multi-step process where a THz driven current caused by the acceleration of photo-induced carrier or free electrons of small metallic fractions present in the non conductive phase leads to electron-phonon scattering and as a consequence, a rise of the lattice temperature. This temperature rise is then sufficient, close to T_{IMT} to induce the metallization of the sample, propagating at the sound speed [Abreu et al., 2015]. In our case, the exponential trend seems abnormally slow compared to similar experiments [PhD thesis Abreu, 2014] performed on a film of 95 nm thickness, where the rising time was estimated to 17 and 14 ps for THz and Optical excitation respectively. The difference in film thicknesses (200 nm vs 95 nm) between this experiment and the one presented here is not sufficient to explain the one obtained in terms of time constants.

For $T \leq 115$ K, the conductivity increases slowly and reaches a plateau. The AFI phase is predominant. The photo-induced signal is nil because the THz are not absorbed anymore.

For intermediate temperatures between 130 and 170 K (See **a**), performing a weighted sum of the PM (positive signal at T=170 K) and AFI (negative exponential trend at T=135 K)

contributions should permit the modelization of the temperature dependence of the photo-induced signal.

2.4.4 Summary

In this section was presented a pump/probe study performed on a V_2O_3 thin film with internal stress. By changing temperature, this sample undergoes two different phase transitions: one from PI to PM and the other from PM to AFI. The use of both THz TDS and THz pump Optical probe provides complementary informations. Indeed, since the THz conductivity gives hints on the phase predominance, it gives a better understanding of the photo-induced signal obtained in the THz pump/Optical probe experiments. In the temperature range studied, the signal seems to be related to the phase fraction of PI, PM and AFI phase. For T>260 K there is no photo-induced signal because of the low THz conductivity. For T<260 K, a positive signal related to the propagation of strain waves in the PM phase is present. Following a decrease of temperature, this signal is balanced by a negative exponential trend probably related to the metallization of the AFI phase. For T<115 K, the vanishing of the signal is linked to the disappearance of the PM phase.

2.5 Conclusion

For controlling materials at the macroscopic scale with strong ultrafast pulses, the strain-stress profile is a key feature, and we have shown in this chapter that Terahertz or optical pumps generate different profiles. With this respect, Terahertz excitation allows to induce a more spatially homogeneous excitation over the film depth than optical pump. Thus, we expect thermalization effects that depend on temperature gradients $\frac{\partial T}{\partial x}$ to be minimized. For the THz excitation, the homogeneous absorption profile also allows coherent interferences that increases the absorbed energy over the sample thickness.

Concerning the strain profile, we were able to reconstruct it using a transmission configuration to minimize probe sensitivity function effects. Interestingly, our unmatched layer model predicts that the strain does not change sign when the excitation is almost uniform over the full film thickness, in agreement with the matched layer model [Schick et al., 2014], at least in the range $|R| < 0.2$ of our simulations. On the other hand, when the intensity decreases exponentially, tensile and compressive strain develop inhomogeneously in the film thickness. This change of sign of the strain, or not, within the sample may be of importance in the study of PIPT where the strain or stress-waves are at the origin of the driving mechanisms that trigger the phase transformation. The comprehension of such phenomena may help in tailoring strain profiles to study ultrafast phase transformations of volume changing materials such as V_2O_3.

This study also showed how important is the probe process to be able to analyze quantitatively the change of dielectric constant induced by the pump. We highlighted the great advantages offered by almost single-cycle THz pulse excitation to control strain-stress generation over optical pump : spatial homogeneity, coherence, low-deposited energy and temperature rise.

Chapter 3

Response of the ferroelectric molecular material TTF-CA to THz excitation

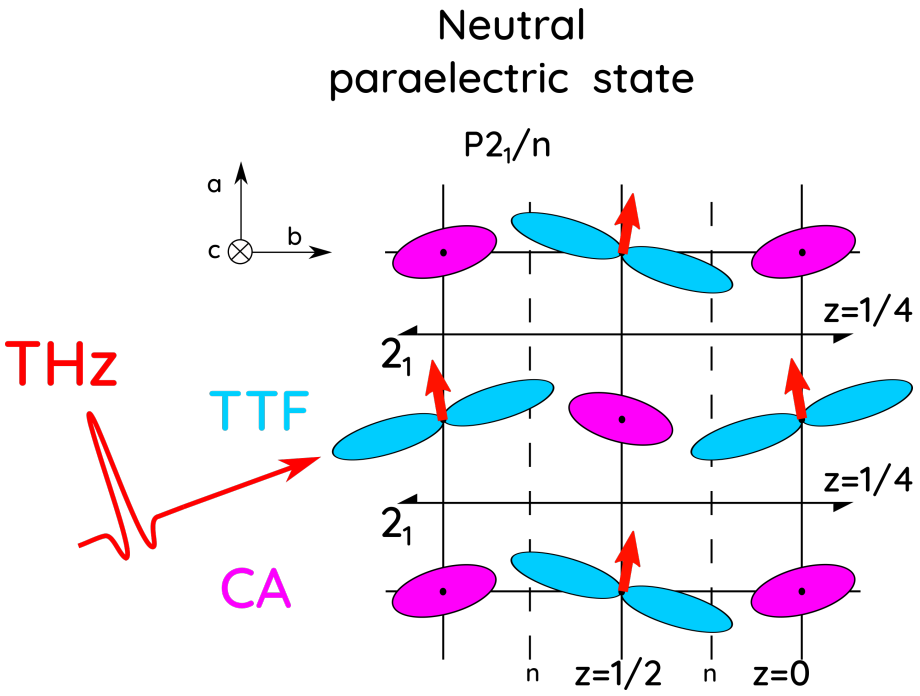

Part I: Ferroelectricity in TTF-CA

3.1 Introduction to ferroelectricity

3.1.1 Definition

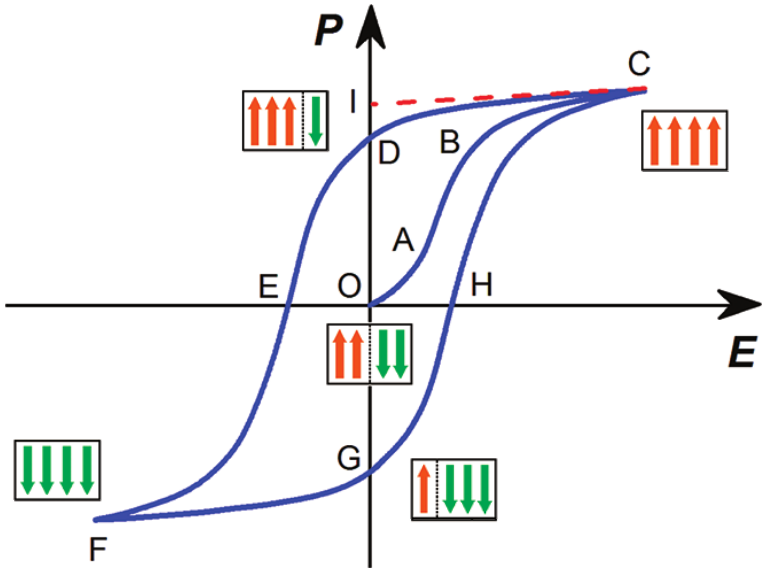

Figure 3.1: P-E hysteresis loop of a ferroelectric material. Adapted from [Zhang and Xiong, 2012]

The ferroelectric materials are a type of dielectrics that are also a subgroup of pyroelectrics (and therefore piezoelectrics). Thus, to properly define ferroelectrics, one must explain the piezoelectricity and pyroelectricity.

Piezoelectricity is the property of a material to exhibit an electric polarization under a mechanical stress. This property is derived from symmetry considerations. Only non-centrosymmetric classes can be piezoelectrics, but in the 21 non centro-symmetric classes, 20 classes are piezoelectric. Some of these classes of piezoelectrics can exhibit a spontaneous polarization that can be modified by the temperature. Those materials are called polar crystals or pyroelectrics. In such crystals, in each unit cell, the electric dipole moment is naturally non-zero.

In a sense, a ferroelectric compound is a pyroelectric or polar crystal below the so-called Curie temperature (Tc) and non-pyroelectric above this temperature [Ashcroft and Mermin, 2022]. Just below this transition temperature, it is possible to reverse the direction of the spontaneous polarization using an electric field of reasonable strength. Therefore ferroelectrics are usually defined as materials exhibiting a spontaneous polarization (pyroelectric) that can be reversed through the action of an external electric field.

By symmetry considerations, the spontaneous polarization present on different sites of the material can point in various directions. Regions where the electric dipole moments point in the same direction are called domains. From one domain to the other, the direction of the electric polarization changes. The separation between domains is called Domain Wall (DW).

Now, we consider in Figure 3.1 the evolution of polarization with an external electric field in the case where only two opposite directions for the polarization are allowed and therefore only 2 types of domains exist. In the ideal case, with no external electric field applied, there should be compensation between "positive" and "negative" polarizations because the number and the size of the domains of opposite polarization may be equally populated. At first, at low electric field strength, the net polarization will follow the classical P-E curve along the OA path shown in Fig.3.1. Upon increasing the external electric field, part of the domains will see their polarization flipped to align with the external electric field. The net polarization will keep increasing along the B-C path until reaching a maximum value called "saturation" net polarization. At this saturation value, all the constituting dipoles will point the same direction and form only one

domain. Decreasing the field amplitude down to zero will not bring the system back to the initial zero polarization state. A remanent polarization will be measured at this point D. The zero net polarization will be obtained at negative field values: -E_c (called coercive field, where E_c>0). This field amplitude is the value required to invert the polarization direction at point E. At larger negative field amplitude, another saturation will be found. The only domain will be oriented in the opposite direction with respect to the previous case. From this point, increasing the field will lead to a symmetrical behavior and the formation of a P-E hysteresis loop, characteristic of ferroelectrics materials.

3.1.2 Discovery of ferroelectrics

The discovery of the ferroelectricity is very closely related to the evolution of the scientific knowledge of one compound: the Potassium sodium tartrate tetrahydrate called “Rochelle Salt” or Seignette’s salt, name given following its first synthesis in 1655 by E. Seignette in La Rochelle [Cross and Newnham, 1987]. This compound was first used in medicine, but the interest of the community grew after the discovery of pyroelectricity and piezoelectricy in Rochelle Salt by Brewster and Curie brothers during the XIX’s century. In the beginning of the XX’s century and the arrival of the first World War, piezoelectric materials were extensively studied e.g by W. Cady) for military purposes (sonar). In 1917, following Anderson’s galvanometer results on Rochelle Salt, J. Valasek established the analogy between such dielectric properties and ferromagnetism [Valasek, 1920], giving rise to the term "ferroelectricity". Later, J. Valasek reported the first ferroelectric hysteresis loop (measured in the Rochelle Salt) [Valasek, 1921].

The use of ferroelectrics is, nowadays, widespread as sensors or random access memories for example, especially since the discovery of ferroelectricity in perovskites, such as BaTiO3.

3.1.3 Ferroelectric Phase Transition

A ferroelectic phase transition is characterized by the symmetry change, which allows the appearence of a net polarization. It is described in the frame of the Landau theory, through an "order parameter". The order parameter is a thermodynamical variable quantifying how the symmetry of the low temperature phase (LT) deviates from the symmetry of the high temperature phase (HT). Macroscopically, this parameter is thus taken as 0 in the HT phase and non zero in the LT one.

In a ferroelectric phase, the macroscopic representation of the order parameter is the electric polarization. In the case of a continuous phase transition, the macroscopic polarization is zero above T_c and non-zero below. This temperature will separate the paraelectric (HT) from the ferroelectric (LT) phase, while for discontinuous phase transitions both phases may coexist within the thermal hysteresis.

In the literature, two main mechanisms were introduced to explain the appearance of a macroscopic polarization below T_c and ferroelectric phase transition. They are classified into displacive phase transitions and order-disorder ones.

For materials exhibiting ferroelectric phase transitions of displacive type, such as $BaTiO_3$ shown in Fig.3.2, the appearance of the macroscopic polarization is caused by a symmetry breaking due to the relative and collective displacement of anions and cations, corresponding to the soft phonon mode. The low temperature structure is just a distorted case of the high temperature one. Because of the group-subgroup relationship between the symmetries of the HT and LT space groups, it is possible to identify the symmetry of the mode(s) involved and responsible for the symmetry breaking. In some cases, we can consider that the displacements from the high T

structure to the low T structure are driven by a single lattice vibration mode with no restoring force. Such a mode is called a "soft mode" and is characterized by a decrease of its frequency approaching T_c. For proper ferroelectrics, such decrease of the frequency must appear at the Γ point of the Brillouin zone since there is no multiplicity of the unit cell at T_c.

For materials exhibiting ferroelectric phase transitions of disorder type, such as $NaNO_2$ shown in Fig.3.2, in every unit cell, at each time, the local polarization is non zero, but its orientation randomly fluctuates in time and space. It results in a zero mean value of the total polarization for the high temperature structure. Below T_c, this parameter is ordering itself to select only one configuration. It results in a non zero mean value for the macroscopic polarization. In the case of $NaNO_2$, the Na atom is usually considered as fixed and NO_2^- electric dipoles can point, randomly, in either along the + or - b directions. Crossing the critical temperature this NO_2^- unit might undergo a rotation to order and align with the others. In this way, a net polarization is created (Fig 3.2).

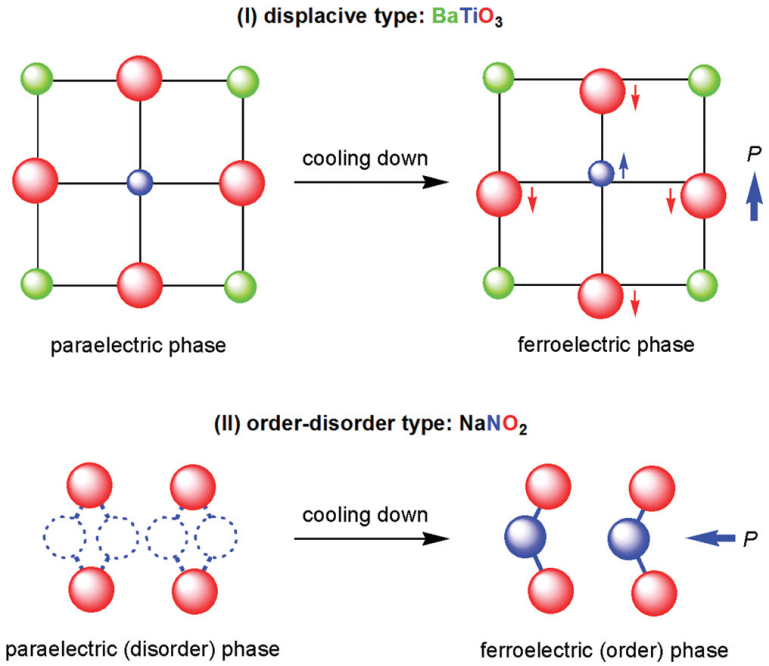

Figure 3.2: Schematic representation of a typical displacive type phase transition: $BaTiO_3$ (upper panel) and order-disorder type phase transition: $NaNO_2$ (lower panel). Adapted from [Zhang and Xiong, 2012]

3.2 Manipulating ferroelectrics with light

For years now, ferroelectric materials have been used as constituents of electronic devices. Mainly used, at first, as sensors or actuators, thanks to their piezoelectric and pyroelectric properties, their unique capability of polarization reversal made this type of compound suitable for RAM applications [Scott, 2007]. For this reason, the sub-picosecond and complete manipulation of polarization in ferroelectrics could enable the creation of higher speed electronic devices.

Far from the ultrafast control, at first, the electrode poling technique was used to periodically flip the polarization inside ferroelectrics. This technique is restricted to 2D materials [Guo et al., 2021]. Other recent developments dealing with polarization switching in BFO [Yang and Alexe, 2018](tip-enhanced optical switching,) enables to manipulate materials down to the sub-microsecond timescales. Also, Chen et. al [Chen et al., 2016] used a femtosecond optical beam to perform a laser poling and switch the domain polarization of a $LiNbO_3$ waveguide. A multi-photon absorption process in this compound induced an important temperature gradient leading

to a thermoelectric field that exceeds the coercive field strength.

Finally, we can cite the emergent possibilities offered by the use of ultrashort and intense THz pulses. One of the first advantages of this technique is the very high electric field that can be obtained via some specific generation techniques (e.g. Optical Rectification). Indeed, using electric fields whose amplitude are orders of magnitudes higher than the coercive fields may result in an alignment of the dipole in the ferroelectric phase and a possible transient net polarization induced from the paraelectric phase. Also, their very low photon energy (1 THz is 4 meV) induces a reasonable temperature rise of the sample and minimizes the thermal perturbation of the ferroelectric ordering. Moreover the THz envelope contains frequencies spanning from 0 to 2 THz, which correspond to the typical frequency of soft mode, close to the Curie Temperature. Since the ferroelectric modes are polar, it is possible to resonantly excite such modes in the paraelectric phase. If the amplitude of this oscillation induced by THz radiation is important, a trapping in the ferroelectric phase can be obtained [Li et al., 2019]. For all of these reasons, intense THz pulses represent a great asset in the view of ultrafast manipulation of ferroelectric polarization.

In the following section, an example of THz manipulation of ferroelectric polarization will be treated in order to give an insight on the possibilities given by this technique and introduce the motivation behind our work on TTF-CA.

3.2.1 TeraHertz control of ferroelectric Polarization

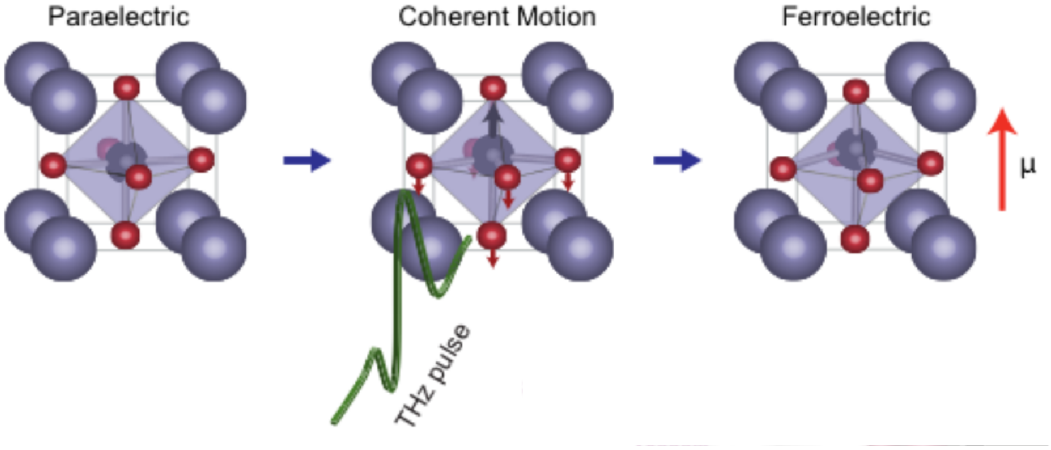

Figure 3.3: Schematic representation of a resonant excitation, by a THz intense pulse, of a soft mode in $SrTiO_3$ leading to a transient ferroelectric behavior. Adapted from [Li et al., 2019]

Light induced phenomena are dealing with out of equilibrium dynamics and do not necessarily involve phases present in the equilibrium phase diagram. Indeed phase transitions can be driven towards so called "hidden phases" which are never observed at thermal equilibrium. This is the case presented below, where a paraelectric $SrTiO_3$ is driven into a hidden ferroelectric phase through the coherent excitation of a soft mode.

As it is mentioned above, many perovskites appear to be ferroelectrics under a Curie Temperature. $BaTiO_3$ and $PbTiO_3$ are textbook paraelectrics undergoing one or several phase transitions to a ferroelectric phase. For $SrTiO_3$, even though the crystalline structure is similar, the situation is quite different. This compound undergoes a phase transition from a cubic to a tetragonal paraelectric phase at T=105 K [Müller et al., 1968]. Differently from other perovskites, at lower temperature, instead of becoming ferroelectric, zero-point quantum fluctuations disorders the system and prevents it to manifest any macroscopic ferroelectric behavior. This result in a so called Quantum Paraelectric Phase (QPE) at T<4 K. Nevertheless, this compound still shows a soft

mode behavior until T_c=36 K. In their paper, [Li et al., 2019] showed that the resonant excitation of the very soft polar mode responsible for the ionic displacement from the high temperature phase to the hidden ferroelectric one (See Fig.3.3) can trigger a transient ferroelectric order.

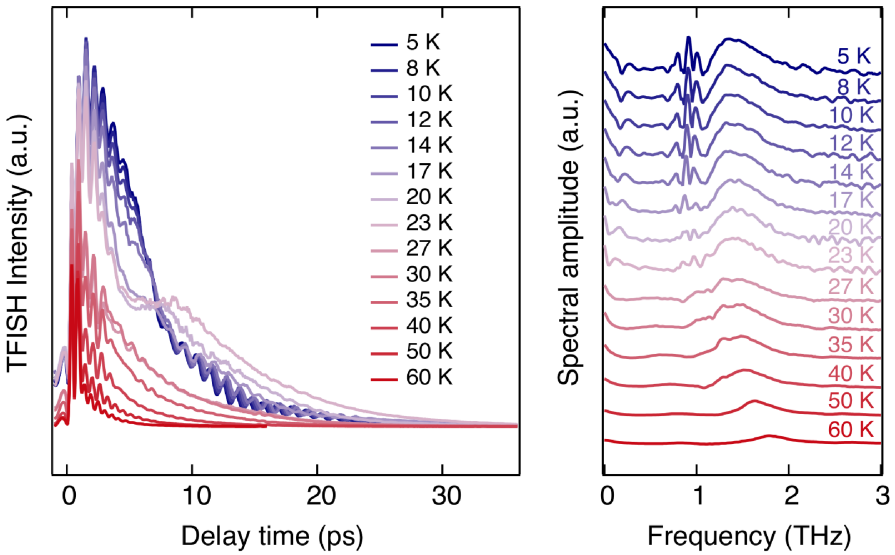

Figure 3.4: THz Pump SHG probe experiment in $SrTiO_3$. Time evolution of the TeraHertz Field induced Second Harmonic, for various temperatures (left) and their corresponding Fourier Transforms (right). Adapted from Fig. S3 Supplementary materials [Li et al., 2019]

They performed a TeraHertz-Pump Second Harmonic Generation (400 nm) probe on 10x10x0.5 mm^3 $SrTiO_3$ single crystal with a maximum Electric Field reaching 550 kV/cm. The temperature ranged studied was spanning from 5 to 60 K (See Fig.3.4). The result obtained at maximum field amplitude as a function of the temperature was compared to results obtained at 5 K varying the Electric Field amplitude.

They showed that, approaching T_c, a TeraHertz Field Induced Second Harmonic Generation appeared. Due to the centrosymmetric structure of the paraelectric phase, no Second Harmonic Generation should be measured. The non-zero remanent SHG signal after the THz excitation is an unambiguous signature for the symmetry breaking involved in the paraelectric to ferroelectric phase transition.

It can be noticed that below the Quantum temperature T_q, the signal is clearly enhanced. Indeed, it is very likely that the energy barrier between the QPE and the ferroelectric phase is much lower than between the conventional paraelectric phase present above the "Quantum" temperature and the ferroelectric phase, because, in the first case, only the quantum fluctuations have to be overcome. This should result in a much more efficient perturbation, below T_q, toward the ferroelectric phase.

Analyzing the THz Pump SHG probe signal (Fig.3.4), we see that two contributions are present. First, an oscillation is appearing at around 1.8 THz for T=60 K and clearly softening until 1.4 THz at 30 K. Also, upon cooling, an increasing baseline signal is appearing and remaining well after the THz excitation. It decays slowly and survives for longer delays when the temperature is decreased. On a physical point of view, this exponential decay has been attributed to the electric dipole moment orientation and the signature of a transient creation of ferroelectric order. This signal lasts for longer delays at low temperature due to an increased dipolar correlation. Concerning, the oscillating component, it is explained that when the initial structure is centrosymmetric, the symmetry breaking ionic displacement around this inversion symmetry will result in a signal appearing at twice the frequency of the actual mode as symmetry is broken when atoms move along both + or - directions. Considering this argument, by dividing by two

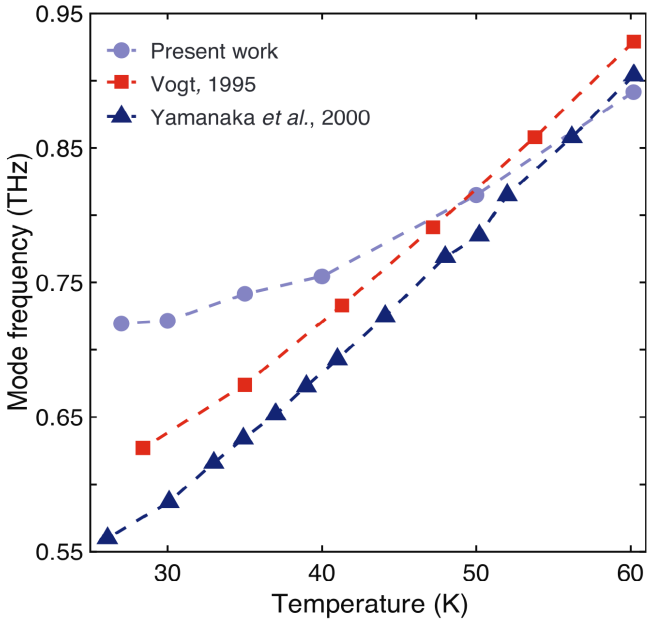

Figure 3.5: Temperature evolution of the soft mode frequency in $SrTiO_3$. Adapted from Fig.S6 Supplementary Material [Li et al., 2019]

the frequency obtained through the Fourier Transform of the signal of Fig.3.4, the grayish points in the Fig.3.5 were obtained. The authors showed that this curve fits well with the soft mode measured in the literature. At temperature lower than T_q, a second oscillatory component appear when the ionic displacement is important. It is the result of a coupling between the soft mode and another mode. But since the growing background is the proof of a global alignment of dipoles and steady state creation, the centrosymmetry is clearly lost. Therefore atoms will oscillate around a new equilibrium position, out of the inversion symmetry, and this mode coupled to the soft mode will appear in the SHG signal at its frequency and not twice of it.

Also, a measurement as a function of the amplitude of the TeraHertz electric field has been carried out (Fig.3.6). At T=5K, a reduction of the TeraHertz field amplitude results in a drastic decrease of the signal following the same trend than a change in temperature. At low temperature and low field the signal is similar to the one obtained at 60 K with 550 kV/cm. Indeed, only an oscillatory component and no more steady state can be seen. It proves that a THz field threshold must be exceeded to obtain sufficiently large ionic displacement inducing a transient ferroelectric phase.

3.3 Neutral-ionic phase transition in TTF-CA

3.3.1 Introduction TTF-CA

The tetrathiafulvalene-*p*-chloranil (TTF-CA) is a mixed-stacked molecular compound (See Fig. 3.7) made of stacks where electron donors (D) and acceptors (A) molecules alternate [Buron-Le Cointe et al., 2017]. In this family of compounds, the small distances between the D and A entities lead to an overlap of π orbitals and a partial charge transfer. In the case of small ionicity ρ <0.5 the compound will be considered in his neutral phase, while an ionicity greater than 0.5 will tend towards a more ionic phase. The balance between the cost of DA ionization and the Madelung energy gain is determining the state of the compound. An increase of pressure, or a thermal contraction stabilizes the ionic phase through an enhancement of the Madelung energy, causing a neutral to ionic phase transition.

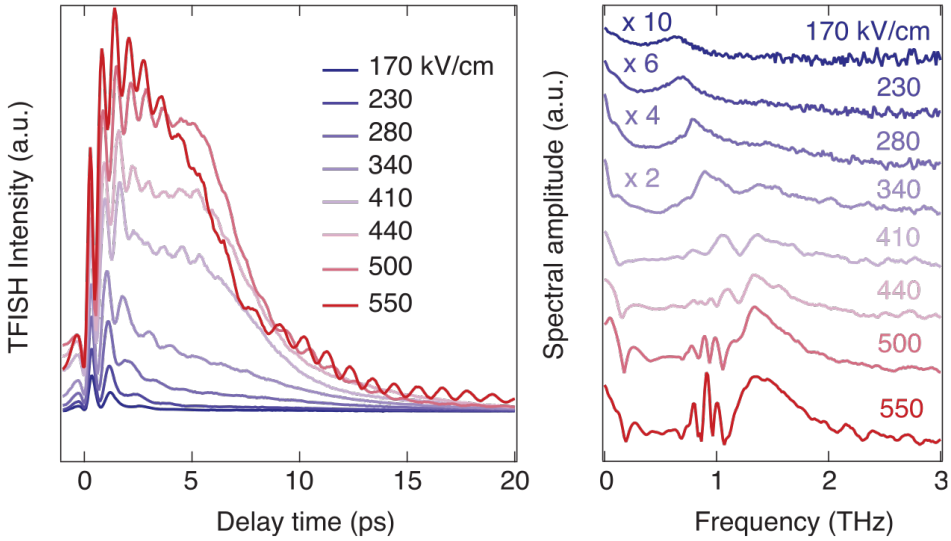

Figure 3.6: Time evolution of TeraHertz Field induced Second Harmonic, for various electric field amplitudes, in $SrTiO_3$ (left) and their corresponding Fourier Transforms (right). Adapted from [Li et al., 2019]

TTF-CA is one of the compounds exhibiting such neutral ionic phase transitions [Torrance et al., 1981], which occurs at T_{NI}=81 K, between a Van der Waals neutral phase ($\rho = 0.3$) and an ionic one ($\rho = 0.6 - 0.7$ [Jacobsen and Torrance, 1983]). At this temperature, the partial charge transfer occurs from a donor (TTF) and the following acceptor (CA). Considering that such change is occurring only along the stacking axis (a) added to a very weak interchain interaction, the TTF-CA is usually reduced to a 1D system and pictured as a succession of D and A molecules.

While in an ideal case of zero ionicity and non dimerized system, the situation goes from D^0 A^0 D^0 A^0 D^0 A^0 to D^+ A^- D^+ A^- D^+ A^-, in the TTF-CA, the situation is different with a transition from a paraelectic non dimerized system $D^{+\rho_N}$ $A^{-\rho_N}$ $D^{+\rho_N}$ $A^{-\rho_N}$ $D^{+\rho_N}$ $A^{-\rho_N}$ (with ρ_N=0.3) to a dimerized ferroelectric system: ($D^{+\rho_I}$ $A^{-\rho_I}$) ($D^{+\rho_I}$ $A^{-\rho_I}$) ($D^{+\rho_I}$ $A^{-\rho_I}$) or ($A^{-\rho_I}$ $D^{+\rho_I}$) ($A^{-\rho_I}$ $D^{+\rho_I}$) ($A^{-\rho_I}$ $D^{+\rho_I}$) (with ρ_I=0.7). As seen from this picture, a symmetry breaking dimerization of the D and A species occurs concomitantly with the totally symmetric charge transfer as the pairing may be (D^+A^-) or (A^-D^+) as the donor moves closer to one of its neighboring acceptor. The concomitant change of ionicity and relative motion of D and A ions is responsible for the appearance of a net polarization and a ferroelectric behavior at low temperature. Consequently, a ferroelectric phase transition occurs from neutral paraelectric phase towards an ionic ferroelectric phase.

Another interesting feature is that the net Polarization in TTF-CA is not directed towards the direction expected from the relative motions of the ions in the case of the displacive type ferroelectricity, but on the opposite side. The reason for this unexpected behavior is the importance of another type of ferroelectricity called "electronic ferroelectricity". In this case, the appearance of a net polarization is linked to an electronic charge transfer (CT) and not the movement of ions [Kobayashi et al., 2012]. In the TTF-CA, this contribution is more than one order of magnitude larger than the conventional "ionic one" but also pointing in the opposite direction (See Fig.3.8).

In the TTF-CA the neutral and ionic phases are quasi degenerated meaning that only a small perturbation is sufficient to drive one state into an other. Also, the electrons being much more susceptible than ions, a potential manipulation of the net polarization could be achieved on much shorter timescales using THz intense sources than those obtained for a system with a more conventional type of ferroelectricity.

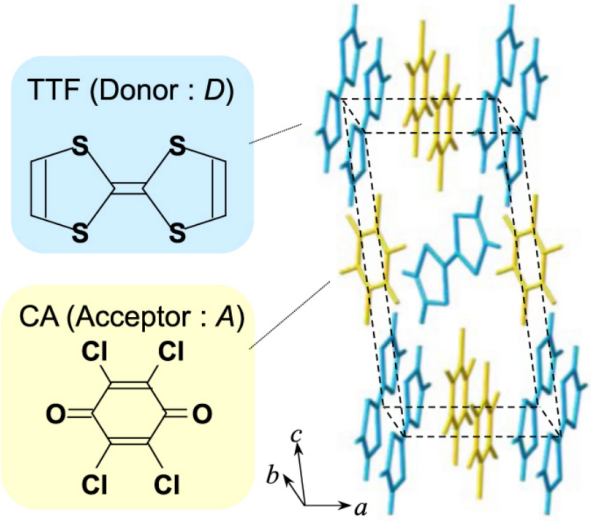

Figure 3.7: 3D view of the TTF-CA unit cell and its constituting building blocks molecular structure (TTF and CA). Adapted from Fig. 5(a) [Miyamoto et al., 2018]

For this reason, some groups investigated the response of the TTF-CA to intense THz [Miyamoto et al., 2013, 2018; Morimoto, Miyamoto, Yamakawa, Terashige, Ono, Kida and Okamoto, 2017; Morimoto, Miyamoto and Okamoto, 2017].

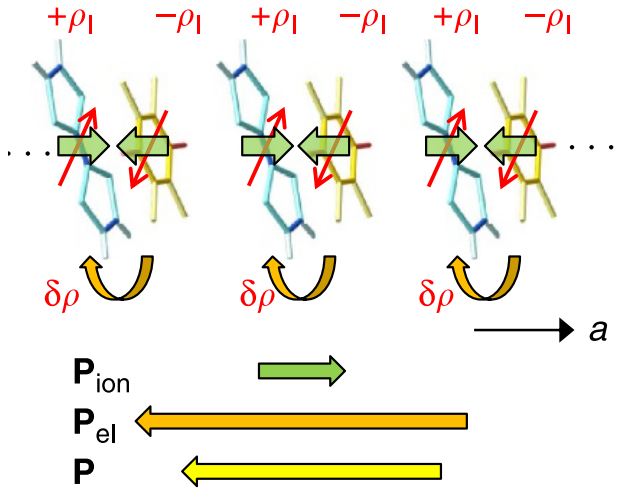

Figure 3.8: Representation of the two contributions to the net polarization (yellow) in the ionic ferroelectric phase of TTF-CA. Green arrows represent the ionic displacement causing the "ionic" polarization. In orange arrows are represented the charge transfer causing the electronic polarization. Adapted from [Miyamoto et al., 2018]

3.3.2 Focus on the first order neutral-ionic phase transition

Above T_{NI}, TTF-CA is a non-dimerized quasi-neutral system, with a crystalline space group $P2_1/n$. (Fig.3.9). In the crystalline packing, the TTF and CA molecules are sitting on inversion centers. The symmetry elements relating the two DA pairs of the unit cell are: a 2_1 screw axis parallel to the $\vec{b}$ axis and a n glide plane perpendicular to it.

On lowering the temperature, this compound undergoes a first order phase transition, towards the low temperature space group Pn. This is due to a dimerization of the DA pairs, giving rise to polar stacks, which get ordered in a ferroelectric way with the lost of the 2_1 screw axis. This

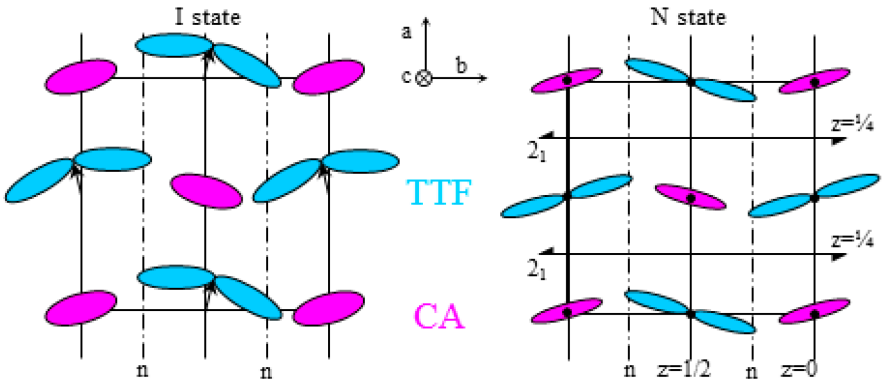

Figure 3.9: Schematic representation of the unit cell of TTF-CA for both neutral high temperature (right) and ionic low temperature (left) phases. Adapted from [Buron-Le Cointe et al., 2017]

symmetry breaking translates in the diffraction pattern, through the appearance of the (0 k 0) : k = 2n + 1 Bragg peaks, previously forbidden in the $P2_1/n$ space group where the 2_1 screw axis exists. [Le Cointe et al., 1995]. The glide plane is maintained and still relates the two DA pairs, meaning that, along b direction, the displacement of a molecule in one direction (e.g -b) is compensated by the movement of another molecule in the next chain (+b)(See arrow on Fig. 3.14). Consequently, the electric polarization lies in the (a,c) plane. The symmetry breaking order parameter, describing the $P2_1/n \rightarrow Pn$ change of space group transforms therefore as the Bu representation of the 2/m point group of the $P2_1/n$ HT phase.

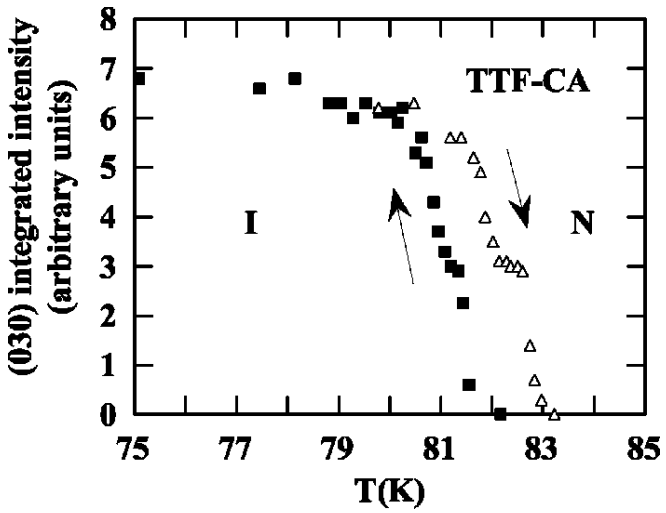

Figure 3.10: Temperature evolution of the integrated intensity of the (030) Bragg peak in TTF-CA. The black squares represents the measurements performed upon cooling. The white triangles upon warming. Adapted from [Buron-Le Cointe et al., 2003]

In both phases, the ionicity is non-vanishing meaning that even in the high temperature phase, the system is in a "quasi" neutral state with formation of dipoles due to charge splitting. Above T_{NI}, the centrosymmetry prevent the appearance of a net polarization. Below T_{NI}, due to the loss of screw axis and inversion center, the net polarization is non-vanishing and results in a ferroelectric behavior.

Buron et al [Le Cointe et al., 1995] used the appearence of (0k0) Bragg peaks with k odd in the ferroelectric phase to study the thermal hysteresis based on the thermal dependence of the intensity of the characteristic (030) Bragg peaks [Buron-Le Cointe et al., 2003]. As shown in

Fig.3.10 the NI transition occurs around 81 K on cooling and 83 K on warming.

3.3.2.1 Choice of the appropriate order parameters

For TTF-CA, the chosen thermodynamical potential will be different than for common ferroelectrics. At atmospheric pressure, its N-I phase transition occurs at T_{NI}=81 K. At this temperature, several phenomena occur simultaneously: a symmetry breaking dimerization of the (DA) or (AD) pairs and a totally symmetric charge transfer. As a consequence, the development of the thermodynamical potential through the Landau theory is particular because two order parameters need to be used. One will be symmetry breaking order parameter and will be govern by the group-subgroup relationship. The second order parameter is a totally symmetric order parameter, similar to the Landau theory developed for isostructural phase transition such as Mott transition or liquid-vapor phase transition.

At atmospheric pressure, the phase transition occurs on cooling from a Neutral paraelectric phase and an Ionic ferroelectric one. In some P,T conditions, the scenario can be very different. Above a triple point located around T=210 K and P=510 MPa (See Fig.3.11), two transition lines can be crossed by changing the temperature, resulting in a sequential ionization and dimerization of the DA pairs. Starting from high temperature, the system undergoes a Neutral paraelectric to Ionic paraelectric phase transition. At lower temperature it undergoes a ferroelectric phase transition from the Ionic paraelectric towards the I ferroelectric phases. It results in a phase diagram very similar to solid-liquid-phase transition [Buron-Le Cointe et al., 2017].

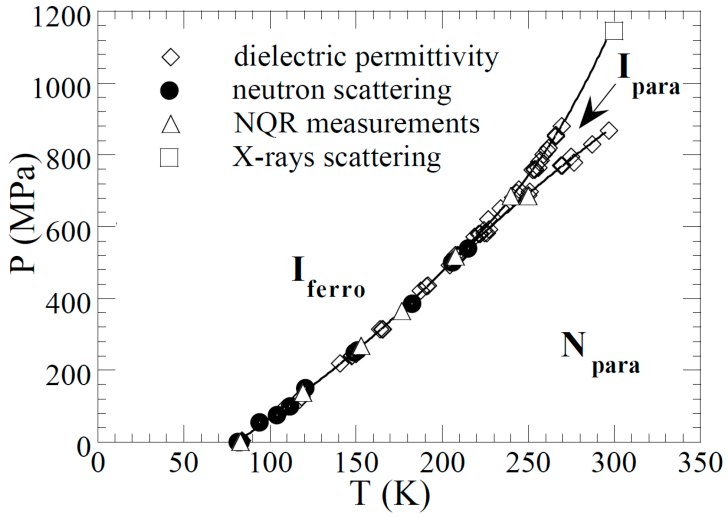

Figure 3.11: pressure-temperature phase diagram of TTF-CA. Adapted from [Buron-Le Cointe et al., 2017]

Both transformations, related to CT and ferroelectric order, are described with order parameters belonging to different representations. The non-symmetry-breaking CT belongs to the Ag representation of the 2/m point group of the HT phase, while the ferroelectric order belongs to the Bu representation. At temperature and pressure lower than the triple point these two order parameters couple and transform concomitantly during the one step phase transition. At higher pressure they occur sequentially.

Starting from high temperature and low pressure conditions, by increasing the pressure, the first line crossed is separating the Neutral paraelectric phase from the Ionic paraelectric phase. The charge transfer has been changed. We will therefore select the ionicity q as the order parameter for this phase transition. This change of ionicity can be seen as a totally symmetric change of some typical bond lengths at the transition.

The second transition line crossed by increasing the pressure is a phase transition from an Ionic

paraelectric phase to an Ionic ferroelectric phase. In this case, a macroscopic polarization appears following a symmetry breaking displacement of DA pairs occurring at the phase transition. The resulting electronic polarization p will be taken as the symmetry breaking order parameter.

3.3.2.2 Landau developpement for TTF-CA

As explained by Cailleau et al [Buron-Le Cointe et al., 2017], the complete Landau development describing the first order phase transition occurring at 81 K and atmospheric Pressure in the TTF-CA must be seen as a mix between two independent potentials: one for the symmetric breaking part and the other for the totally symmetric. Coupling terms of lowest order must also be added to take into account the coupling between the two order parameters.

Symmetry breaking

The Landau development of the Gibbs energy with the symmetry breaking order parameter p reaches:

$$G^S(p) = G_0^S + \frac{1}{2}Ap^2 + \frac{1}{4}Bp^4 + ... \tag{3.1}$$

where all the prefactors a_i are phenomenological parameters and G_0^S includes contributions different from symmetry breaking. Only even terms are allowed, as the Gibbs energy is even with respect to p. Domains with opposite p are equivalent by symmetry. A and B coefficient depend on T and P and B>0 is required for stability. In the high symmetry phase A>0 and the equilibrium value of p=0. In the low symmetry phase A<0 and the equilibrium value of $p \neq 0$.

Totally symmetric

While usually, all the terms of the power serie of q are kept in the totally symmetric development, Kuznetsov et. al suggested in their paper, that a renormalization of the order parameter allow a simplification of the potential function. Using this renormalization, it is possible to get rid of the third order term. The key point is that the potential function includes a linear term. For TTF-CA, we will use the totally symmetric order parameter $2(q - q_c)$, where $q_c = 1/2$. Therefore q>1/2 corresponds to the I state while q<1/2 corresponds to the N state. In this case, the totally symmetric potential describing the electronic instability can be written as follows:

$$G^T(q) = G_0^T + \frac{1}{2}A'(q-q_c)^2 + \frac{1}{4}B'(q-q_c)^4 - H'(q-q_c) + ... \tag{3.2}$$

Here again the different coefficients are temperature dependent. In the high temperature phase, the positive H' favors a neutral state, while in the low temperature phase the negative H' favors an ionic state.

Total

In the case of the neutral-ionic transition, where both non-symmetry breaking electronic instability and symmetry-breaking instability coexist, it is necessary to take into account both aspects, and to include, at least, the lowest order coupling term (q-qc)p^2 allowed by symmetry.

$$G(p,q) = G_0 + \frac{1}{2}Ap^2 + \frac{1}{4}Bp^4 + \frac{1}{2}A'(q-q_c)^2 + \frac{1}{4}B'(q-q_c)^4 - H'(q-q_c) + \frac{1}{2}\lambda(q-q_c)p^2 + \frac{1}{2}\mu q(1-q)p^2 \tag{3.3}$$

In their papers Azzolina et. al [Azzolina et al., 2020; Collet and Azzolina, 2021] , used similar potentials to describe the coupling between other types of electronic instabilities (charge transfer or spin transition) and symmetry breaking. They explained that the coupling term comes from

the coupling of the symmetry breaking order parameter and the non-symmetry breaking order parameter to the volume strain, which can give rise to simultaneous or sequential changes of electronic state and symmetry. Indeed, a non coupled relation would result in a different and independent transition temperature for each order parameter. The system would, as a consequence, transit between the two phases at a single set of control parameters e.g P,T. The linear quadratic term accounts for the opening of the transition lines between the low temperature phase and the high temperature phase (and also a widening of the thermal hysteresis). A higher order coupling term was not required to properly represent the behavior of the system as a function of the control parameters. Due to the presence of two order parameters, the potential in eq.3.3 discussed by Buron-Le Cointe et al.[Buron-Le Cointe et al., 2017] is represented as a 2D (p,q) map (See Fig.3.12). Different phase diagrams can be obtained via the modification of parameters and coupling conditions and the study of the stable states. With the proper conditions, simultaneous and sequential phase transition can be reproduced. It applies particularly to the solid-liquid-gas-like phase diagram of TTF-CA (See Fig. 3.11) with its concomitant or non concomitant change of ionicity and symmetry.

The stable and metastable states of the potential shown in equation (3.3) are found by the minimization of the potential with respect to each order parameter. Fig.3.12 shows the stable neutral paraelectric phase ($q<0.5$, $p=0$) and the two ionic ($q>0.5$) ferroelectric states with opposite polarization ($p>0$ or $p<0$) corresponding to the two ferroelectric domains.

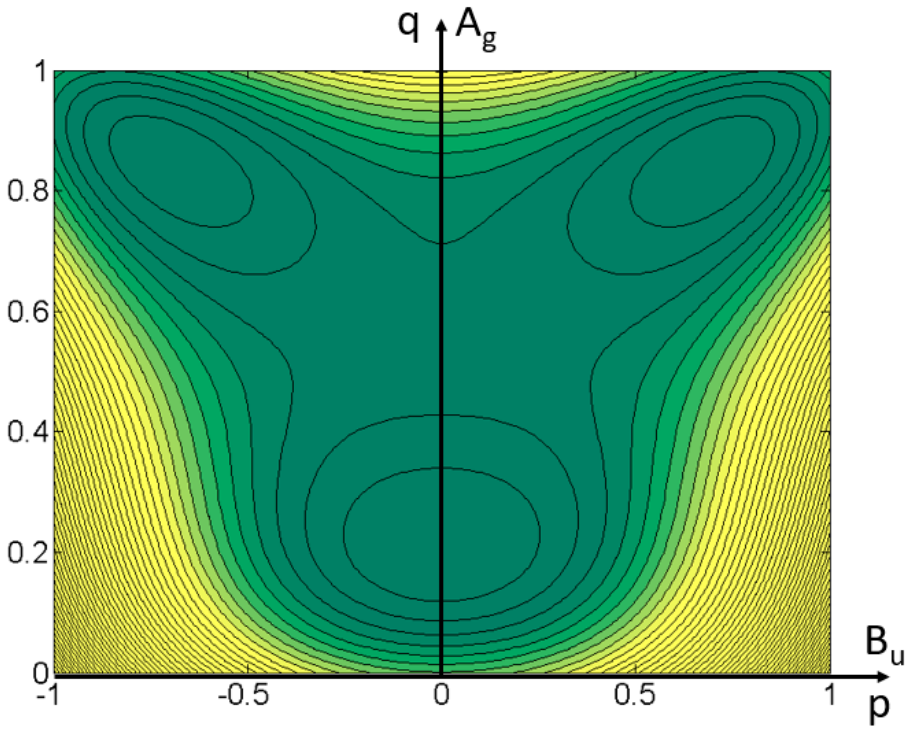

Figure 3.12: Two dimensional representation of Gibbs free energy for TTF-CA as a function of both symmetry breaking (p) and completely symmetric (q) order parameters. Adapted from [Buron-Le Cointe et al., 2017]

3.3.3 Ferroelectric soft mode in TTF-CA

For a displacive phase transition, the mode responsible for atomic displacements from the high symmetry phase to the low symmetry phase corresponds to the vibrational movement of an optical phonon mode. By studying the temperature behavior of this mode, from high temperature to the transition temperature, a lowering of its frequency value can be observed. This is due to a

C_{2h}	E	C_2	I	m		
Ag	1	1	1	1	Ry	X^2,Y^2,Z^2,XZ
Bg	1	-1	1	-1	Rx,Rz	XY,YZ
Au	1	1	-1	-1	Y	
Bu	1	-1	-1	1	X,Z	

Table 3.1: character table of C_{2h} point group

softening of the restoring force. Thus, this mode is called a "soft mode". In theory, a further decrease of the temperature (below T_c) would lead to negative frequency values and will be the sign of an instability of the mode and of the structure. This is why, the system moves towards a more stable phase with another equilibrium structure. This low temperature structure can be seen has a "frozen" oscillation, of the high temperature phase along the directions described by the soft mode. The symmetry of the mode is given by the group-sub-group relationship between the high and low symmetry structures.

The identification of the soft mode is of primary importance to study the critical behavior and ferroelectric instabilities. As the number of atoms per unit cell is increasing, the number of modes grows. This identification is therefore more difficult in molecular materials.

In TTF-CA, (as seen in Fig.3.7), there are 4 molecules per unit cell (2 TTF and 2 CA molecules), all sitting on inversion centers. Therefore, due to symmetry considerations, only 4 half molecules of TTF and 4 half molecules of CA are required to describe the low frequency phonon modes in the unit cell in a "rigid body" approximation. Each of these half molecules has 3 translational and 3 rotational degrees of freedom. Considering them as rigid, we count up to 48 different modes (6x(4+4)), classified according to their symmetry.

In the high temperature phase, the structure belongs to the C_{2h} point group. The symmetry operations related to this group are, the identity (E), a 2 fold axis (C_2), a mirror (m) and an inversion center (I). The character table of this point group is shown in (Table 3.1) and corresponds to four different irreducible representations: Ag, Bg, Au, Bu. The Ag being a totally symmetric behavior with respect to all the symmetry operations.

The 48 modes can be equally separated into those 4 irreducible representations:

$$\Gamma^{HT} = 12Ag + 12Au + 12Bg + 12Bu \tag{3.4}$$

Among those modes, 3 are acoustic modes (translational X,Y,Z):

$$\Gamma_a^{HT} = 1Au + 2Bu \tag{3.5}$$

Therefore, in this simple description of low frequency phonon modes made of rigid asymmetric units in the crystalline cell, there are 45 optical modes of rotation (Rx,Ry,Rz) and vibration (X^2,Y^2,Z^2,XY,XZ,YZ) remain:

$$\Gamma_o^{HT} = 12Ag + 11Au + 12Bg + 10Bu \tag{3.6}$$

According to the rule of mutual exclusion, in a centrosymmetric structure, no normal mode of vibration can be both Infrared and Raman active. All the Ag and Bg vibrational modes can be detected through Raman spectroscopy. On the contrary, all of the Au and Bu modes induce a net change in the dipole moment and are therefore IR active.

In the low temperature phase, the cell multiplicity is kept, thus there are still 48 modes. Due to the loss of the screw axis and of the inversion center, the symmetry as been lowered. The only symmetry operations present in this Cs character table is the identity (E) and the mirror (m). Thus only two irreducible representations are allowed: the totally symmetric A' and the one which is antisymmetric with respect to the glide plane: A$''$.

C_s	E	m		
A'	1	1	X,Z	X^2,Y^2,Z^2,XZ
A"	1	-1	Y	XY,YZ

Table 3.2: character table of Cs point group

$$\Gamma^{LT} = 24A' + 24A'' \tag{3.7}$$

$$\Gamma_a^{LT} = 2A' + 1A'' \quad and \quad \Gamma_o^{LT} = 22A' + 23A'' \tag{3.8}$$

Due to the loss of the inversion symmetry, the rule of mutual exclusion is not valid anymore and a mode can be both IR and Raman active.

3.3.3.1 Identification of the soft mode

To study the critical behavior of a soft mode, its identification is primordial and simplify its study. Through symmetry considerations, one can reduce massively the candidates.

As it is mentioned above, one of the phenomena occurring at the phase transition is a dimerization of neighboring donor and acceptor entities inside the same chain. Focusing on one chain, no matter the direction chosen for the dimerization, the result will be equivalent. But as soon as the two chains of the unit cell are taken into account in this collective motion, two possibilities are allowed. For example, if we take the TTF from one chain, they can relatively move, at first, towards the CA located in the +a direction with respect to their positions. The next chain in the unit cell can move in phase with respect to the previous chain, meaning that all the chains move simultaneously towards equivalent neighbors. But this chain can also, at first, move towards the neighbors located in -a direction (out of phase). In any of these two cases, the dimerization occurring in the chains is not only along the a axis. Due to steric hindrance, the dimerization displacement imply a small component along b and c axis. Since a dimerization is associated with a symmetry breaking, such a modes is ungerad. According to the character table, we can classify the dimerization mode in two categories, either Au or Bu.

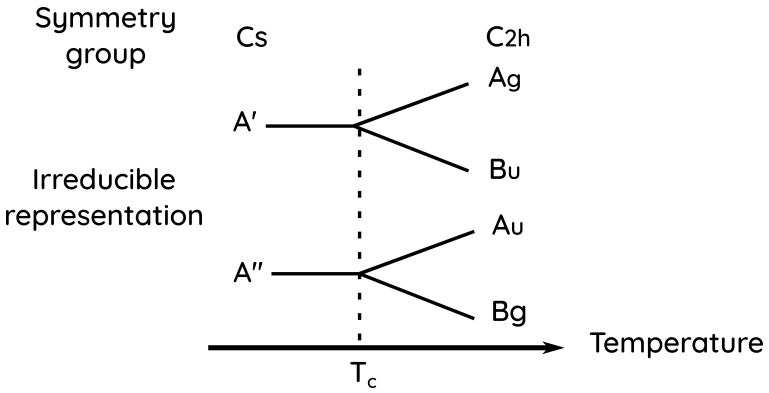

Figure 3.13: Mode symmetry evolution as a function of the temperature.

A Bu dimerization mode will therefore, not respect the inversion symmetry, nor the 2_1 fold axis but will be unchanged by the glide plane operation. If the TTF of one chain move towards the +a and -b direction, the one in the next chain will move in the +a +b direction, in order to be unchanged under the action of the glide plane. This movement (represented in red in the Fig.3.14) is considered as "in phase dimerization" because all the chains move simultaneously towards equivalent neighbors along the a axis. Due to this symmetry considerations, the dipolar

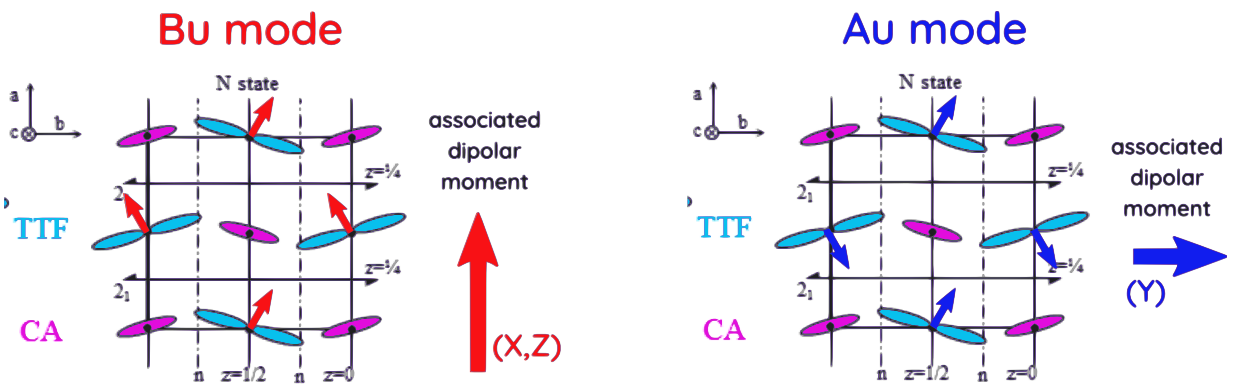

Figure 3.14: Schematic representation of Bu (red) and Au (blue) dimerization modes in TTF-CA

moment component directed towards $\vec{b}$ axis in one chain is compensating the $\vec{b}$ component of the next chain. The resulting net dipolar moment will be directed along $\vec{a}$ and $\vec{c}$ axis as shown in the character table for Bu mode with XZ components. A resonant excitation of such dimerization mode can be achieved using a low energy radiation polarized along (a,c) directions.

A Au dimerization mode will not respect the glide plane nor the inversion symmetry, but remain unchanged under the action of 2 fold axis. From one chain to the other, the movement will be directed towards opposite neighbors and will be "out of phase". Thus each $\vec{a}$ and $\vec{c}$ components of the dipolar moment will be compensated by the next chain. The associated net dipolar moment is directed along the $\vec{b}$ axis.

C_{2h}	E	C_2	I	m		
Ag	1	1	1	1	Ry	X^2,Y^2,Z^2,XZ
Bg	1	-1	1	-1	Rx,Rz	XY,YZ
Au	1	1	-1	-1	Y	
Bu	1	-1	-1	1	X,Z	

Since the glide plane is kept at the transition, at T_{NI}, all the high temperature modes that were unchanged through the action of this symmetry operator (+1) will be gathered in the totally symmetric irreducible representation of the low temperature character table: A'. All the others (-1) will be gathered in the A" irreducible representation (See Fig.3.13). In a displacive phase transition, a soft mode belonging to a certain irreducible representation of the high temperature phase is freezing its displacement to reach the low temperature positions. This high temperature mode involved in such phase transition must, therefore fulfill all the symmetry operations of the low temperature phase. Except the identity, the only symmetry operator remaining in the low temperature phase is the glide plane n. The soft mode is thus a Bu dimerization mode or "in phase dimerization" mode represented in red in Fig 3.14.

Due to a weak interchain interaction, those two modes will have a similar frequency and can be identified only by polarization dependent study.

3.3.3.2 Experimental evidence of the softening of the Bu mode

Several studies evidenced the softening of Peierls modes in TTF-CA [Moreac et al., 1996; Masino et al., 2003; Girlando et al., 2008]. While the only direct measurement of a clear softening was measured by Moreac et al. the use of a mosaicity of crystal prevent from the assignement of the mode symmetry.

On the contrary, several polarization dependent experiments [Masino et al., 2003; Girlando et al., 2008] indirectly revealed the softening of Bu modes.

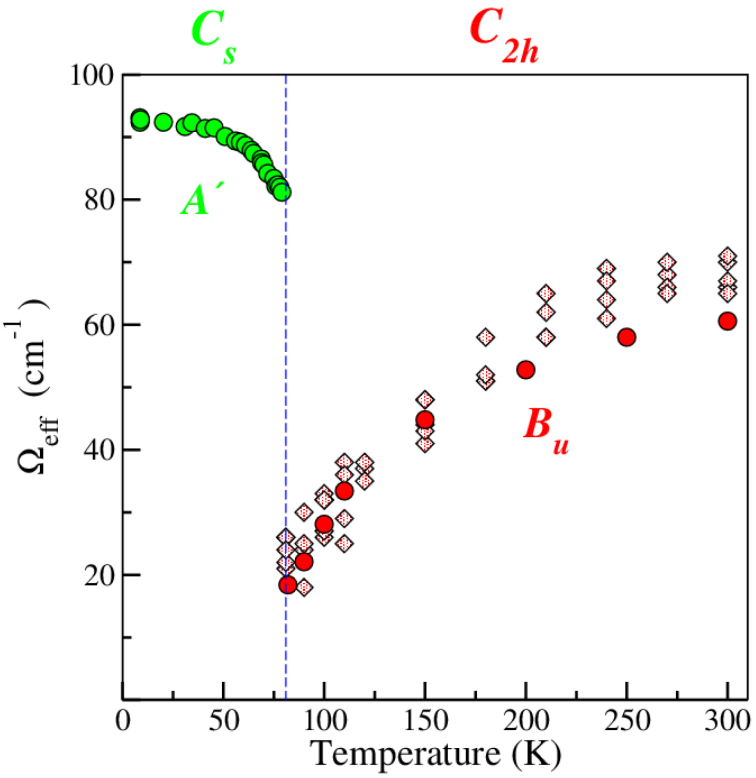

Figure 3.15: Temperature dependence of the frequency of Peierls modes of A' (green) and Bu (red dots and white squares) symmetry in TTF-CA. Red dots: effective soft mode frequency (Bu) calculated from conductivity measurements between 0 and 100 cm^{-1} [Girlando et al., 2008]. White squares: softening of sidebands related to the soft mode frequency (Bu). Measured by IR and Raman around 1000 cm^{-1} [Masino et al., 2003]. Figure from [Masino et al., 2017].

The first study [Masino et al., 2003] focuses on the temperature evolution of combination bands located in the mid-IR range (around 1000 cm^{-1}) measured by both IR spectroscopy and Raman. These bands were assigned to the coupling between some totally symmetric Raman modes (A_g) and soft modes of Bu symmetry. The softening of those two sidebands are reported in Fig.3.15 (white squares) and are related to the Peierls mode softening.

The second study [Girlando et al., 2008] evidenced the presence of several Peierls-coupled mode of Bu symmetry through a low frequency conductivity spectrum measurements (between 0 and 100 cm^{-1}). The multiple temperature evolution of their frequency allowed to compute one effective mode softening presented in Fig.3.15 (red dots).

The very good agreement between these studies is revealing, in TTF-CA, the presence of a Peierls mode of Bu symmetry whose frequency soften from 70 cm^{-1} at high temperature to 20 cm^{-1} upon cooling down to T_{NI}.

3.4 About photo-induced phase transition in TTF-CA

In 1999, Koshihara et al. discussed how, in TTF-CA, a localized charge transfer induced by light pulses could result in a macroscopic phase switching within less than 1 ns to induce a photo-induced phase transition (PIPT). In this compound, the quasi-degeneracy of the Neutral and Ionic states makes it particularly suitable for photo-induced phase transition. For this experiment, they used an optical (1.55 eV) pump white light probe. They demonstrated the bidirectionality of this process by inducing both an Ionic to Neutral phase transition below the phase transition temperature T_{NI} but also the Neutral to Ionic phase transition above this temperature. The

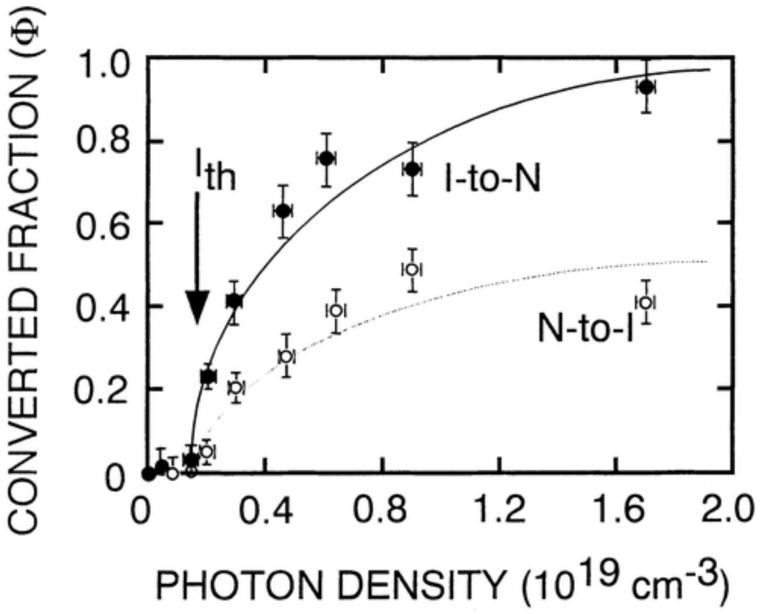

Figure 3.16: Evolution of the converted fractions as a function excitation density for both N-I (white circles) and I-N transitions (black circles). Figure from [Koshihara et al., 1999]

cooperativity of this phenomenon was evidenced by an excitation threshold. Below this threshold, the phase conversion is proportional to the excitation density. Above this threshold, the phase conversion grows non-linearly with respect to the excitation density (See Fig.3.16).

While the Ionic to Neutral phase transition could have been caused by a heating process following the laser absorption, the Neutral to Ionic phase transition and its loss of symmetry elements are arguments in favor of a non-thermal mechanism. The proposed mechanism for the PIPT in TTF-CA is that above the transition temperature, in the Neutral stacks, a localized optical excitation whose photon energy is above the CT gap creates an exciton. A molecule is ionized. This Charge transfer exciton propagates to neighboring molecules and forms CT stacks via electron-electron coupling. The relaxation of this exciton causes the dimerization of the stacks by electron-phonon coupling [Koshihara et al., 1999].

In 2003, Collet et al. showed the emergence of a long-range ordering after an optical excitation through a time-resolved X-ray diffraction measurements. During this experiment, they observed the appearance of (030) and (0-30) Bragg peaks (See Fig.3.17) following the pump excitation. As explained above, these peaks are witnessing the loss of the screw axis, symbol of 3D long range ferroelectric order and a macroscopic Neutral to Ionic phase transition.

The precise dynamic of both phase transitions was studied by Okamoto et al. [Okamoto et al., 2004] using a femtosecond pump probe experiment. They followed the change of the probe reflectivity following a resonant CT excitation (0.65 eV). Various probe energies located around the "IMT" band (intermolecular transition band) i.e between 2 and 2.5 eV were used. Asides from the different dynamics measured for both transitions, they observed oscillations of period roughly equal to 0.6 ps (56 cm^{-1}) above and below the phase transition. The frequency of these oscillations was extracted at 4 K, 77 K and 90 K and was similar in the three cases. The maximum amplitude of these oscillations was measured at 2.25eV (See Left Fig.3.18). Since the charge of the TTF molecule is influencing the position of this IMT band, they assigned the oscillations to the charge modulation of TTF induced by the dimeric movement of the DA pairs i.e to the Spin-Peierls instability.

Another study was investigating the amplification and the control of these dimeric oscillations, through coherent control. In their study, Iwai et al. were tracking the change of reflectivity of the 2.25 eV probe beam following an optical excitation. First, using a single pulse, they succeeded

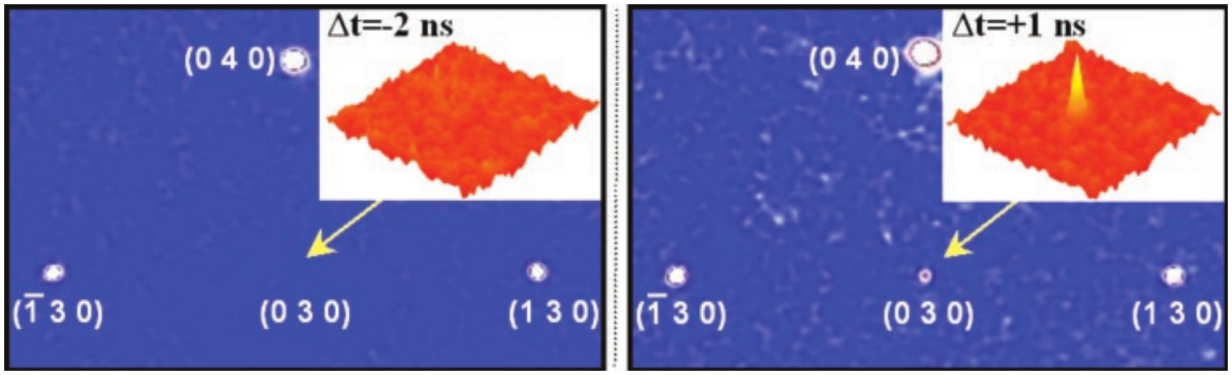

Figure 3.17: Optical pump X-ray Probe experiment performed on TTF-CA. Reconstructed intensity in the reciprocal (a*,b*) planes. Left: before the Optical excitation. Right: 1 ns after the Optical excitation). Figure from [Collet et al., 2003].

to observe the same vibrations at 54 cm^{-1} (See Right Fig. 3.18). Then, using a second optical pump pulse they were able to enhance the amplitude of the vibration when the pulse were sent successively with a time delay equivalent to an oscillation period. On the contrary, an out-of-phase configuration led to the disappearance of the oscillation.

Interestingly in this study, they noticed that the frequency of this oscillation (54 cm^{-1}) remains constant upon cooling and is therefore not matching with the softening of the Bu mode reported by Masino et al. Thus, this oscillation could correspond to another mode linked to dimeric displacements.

3.5 State of art: THz pump Optical probe experiment on TTF-CA

As already mentioned, the TTF-CA owns a large electronic ferroelectric contribution which is directed in opposite direction from the conventional "ionic ferroelectricity" [Kobayashi et al., 2012]. By a resonant CT excitation, the multiplication of the photo-induced Neutral stacks in the Ionic phase can take tens of ps. But, due to this electronic ferroelectricity and the importance of electronic charge transfer from donor to acceptor in this compound, it is possible to directly control polarization state on a sub-picosecond timescale using very intense THz single cycle electric fields. In 2013, Miyamoto et al. related an ultrafast control of the ferroelectric polarization by THz excitation [Miyamoto et al., 2013]. Later, they even succeeded in inducing a transient macroscopic polarization in the Neutral phase of TTF-CA by THz excitation [Morimoto, Miyamoto, Yamakawa, Terashige, Ono, Kida and Okamoto, 2017].

3.5.1 Ultrafast control of ferroelectric polarization induced by intense THz electric fields in TTF-CA

This section will be dealing with the work done by Miyamoto et al. [Miyamoto et al., 2013]. In this study, they performed different THz pump probe experiments. They used either an Optical (2.2 eV) probe to follow the change of ionicity of TTF molecules or a SH probe (2.6 eV) to follow the change of polarization.

First they used a THz pump/optical (2.2 eV) probe in Reflectivity configuration. This 2.2 eV is centered on the IMT ("intramolecular transition" band) of TTF and the position of this band is sensitive to the charge of the TTF molecule. Thus, any charge transfer transiently induced by the THz beam will be accompanied by a change of reflectivity. The pump (THz) is polarized parallel to the stacks ($\vec{a}$) and the probe is polarized perpendicular to $\vec{a}$. They compared the photo-induced

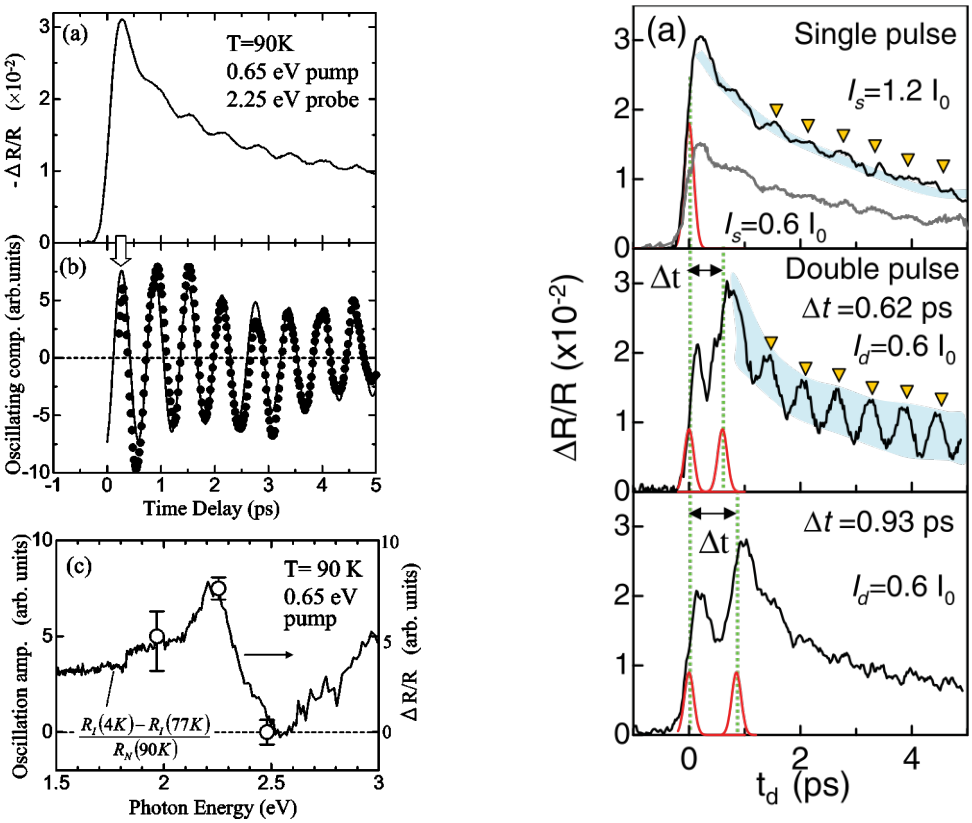

Figure 3.18: Left: Figures from [Okamoto et al., 2004](a) time traces of the transient change of Reflectivity of the 2.25 eV probe following a resonant CT excitation (0.65 eV). T=90 K. (b) extraction of the oscillatory component of (a). (c) Amplitude of the oscillations as a function of the probe energy (circles) compared to the differential spectrum $(R_{4K} - R_{77K})/R_{90K}$ (solid lines). Right: Figures from [Iwai et al., 2006]. (a) time traces of the transient change of Reflectivity of the 2.25 eV probe following a 1.55 eV excitation. (b) time traces of the double pulse experiment where the second pulse was delayed by an oscillation period with respect to the first pump pulse ($\Delta t = 0.62ps$). (c) time traces of the double pulse experiment where the second pulse was delayed by 1.5 oscillation period with respect to the first pump pulse ($\Delta t = 0.93ps$)

change of reflectivity obtained at 78 and 82 K (T_{NI}=81 K) following a 38 kV/cm THz electric field excitation (See Fig. 3.19). Above T_{NI}, in the Neutral phase, no photo-induced signal was seen. Below T_{NI}, they obtained an important ($\Delta R/R=3.10^{-3}$) photo-induced signal. On the short timescales (t<1 ps), the signal follows linearly the THz time traces. This proportionality is confirmed via a measure as a function of the Electric field amplitude (not shown here). This linear electro optic effect was assigned to THz-induced electronic charge transfer whose timescale is much faster than the picosecond. As a consequence it follows the THz time traces.

In this photo-induced signal, after the removal of the contribution originating from the THz electric field, the Fourrier transform revealed a 54 cm^{-1} phonon mode. This mode was already mentioned in some Optical pump Optical probe experiments and assigned to a dimeric displacement [Okamoto et al., 2004; Iwai et al., 2006] (See section 3.4).

Using a pair of wire-grid polarizers they showed that the sign of the photo-induced signal was reversed when the THz single cycle was pointing in the opposite direction. In other terms, it is possible to enhance or reduce the charge transfer by selectively orientate the THz electric field.

Finally, they performed a THz pump SHG probe measurement (Second harmonic of a 1.3 eV beam: 2.6 eV). The non-centrosymmetric behavior of the Ionic phase implies that SH can already

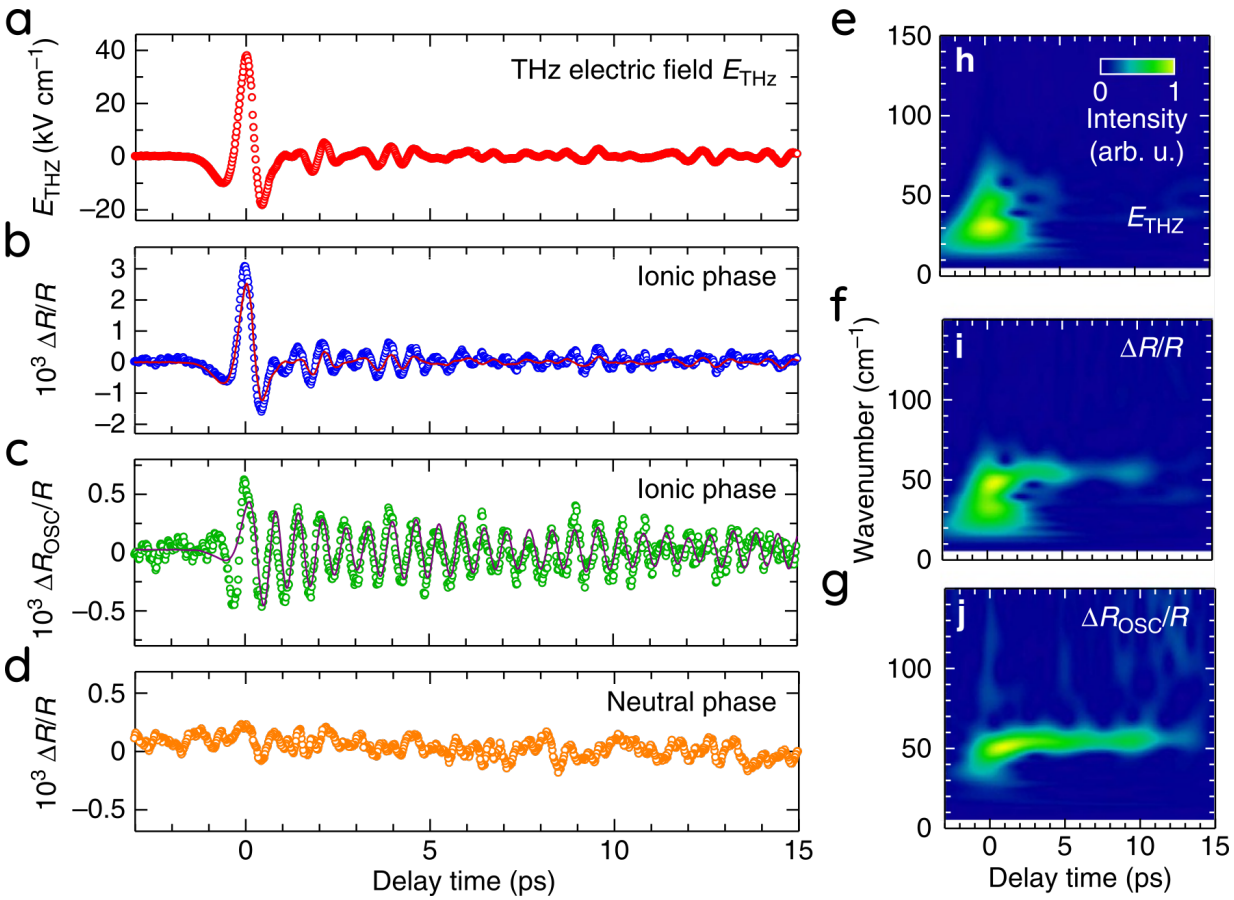

Figure 3.19: (a) time traces of the THz electric field $E_{THz}(t)$. (b) transient modulation of the reflectivity $\Delta R/R(t)$ measured at 78 K. (c) Focus on the oscillatory component of (b) by removing the normalized $E_{THz}(t)$. (d) transient modulation of the reflectivity $\Delta R/R(t)$ at 82 K. No photo-induced signal is observed above T_{NI}. (e)(f) and (g) are the time dependent Fourier Power spectra of (a)(b) and (c) respectively. Figure from [Miyamoto et al., 2013]

be obtained without any THz excitation. Thus they measured the modulation of SHG induced by the THz electric field. This modulation was again following the THz time traces and seems to confirm that the modulation of the charge transfer witnessed by the change of Optical reflectivity is inducing a modulation of the ferroelectric polarization (electronic ferroelectricity).

In conclusion, they showed a sub-ps control of the ferroelectric polarization, in the Ionic phase of TTF-CA using THz electric fields. The ultrafast timescale at which this modulation occurs allows to conclude that the origin of the change of polarization is purely electronic and does not involve any domain-wall motion.

3.5.2 Transient macroscopic polarization induced by THz in the Neutral phase of TTF-CA

In their study Morimoto et al. [Morimoto, Miyamoto, Yamakawa, Terashige, Ono, Kida and Okamoto, 2017] wanted to induce an intermolecular charge transfer via the application of a THz field, in the Neutral phase of TTF-CA. This modification of the charge distribution would lead to the appearance of transient macroscopic polarization.

The methodoly used for of this experiment is similar to the one presented in section 3.5.1. They used a 400 kV/cm THz pump beam and a 1.3 eV probe collected in Reflectivity configuration (See Fig.3.20). Both beams are polarized along the stacks ($\vec{a}$). The probe is centered on the CT band and is therefore sensitive to the charge modulation.

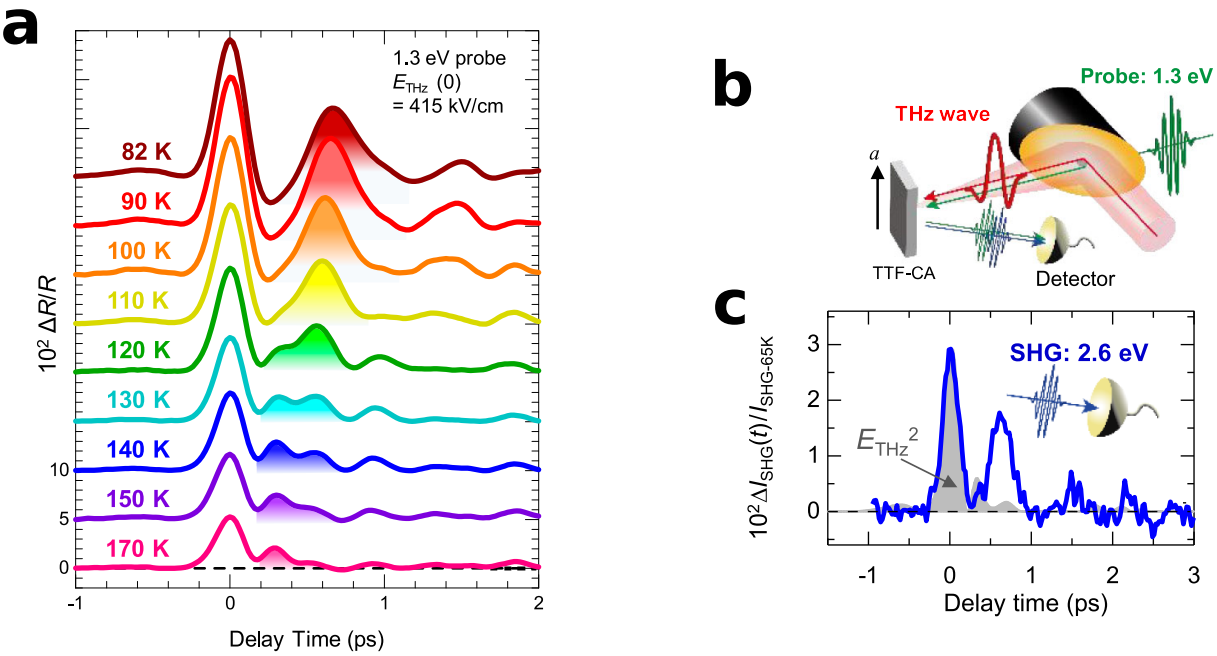

Figure 3.20: (a) Temperature dependence of the THz-induced signal time traces in the Neutral phase of TTF-CA. (b) Experimental setup: THz pump NIR (1.3 eV) probe. Both Pump (red) and Probe (green) beams are polarized along the $\vec{a}$ axis. (c) times traces of the THz-induced SHG measured at 90 and normalized by the SH measured at 65 K, Figure (b) and (c) from [Morimoto, Miyamoto, Yamakawa, Terashige, Ono, Kida and Okamoto, 2017]

They observed a signal made of successive oscillations of the reflectivity for T< 170 K. From 170 K to 100 K, this signal seems to be always positive. For lower temperature, a negative component appears in between the two main oscillations (i.e at 0.2 ps). The amplitude of these peaks grows while cooling to reach 15% of relative change of Reflectivity at T=82 K. The temporal spacing between the two first maxima of the oscillating reflectivity is also increasing with the decrease of the temperature.

They couldn't interpret this increase of the oscillation period by the softening of the Bu mode reported by Masino et al..

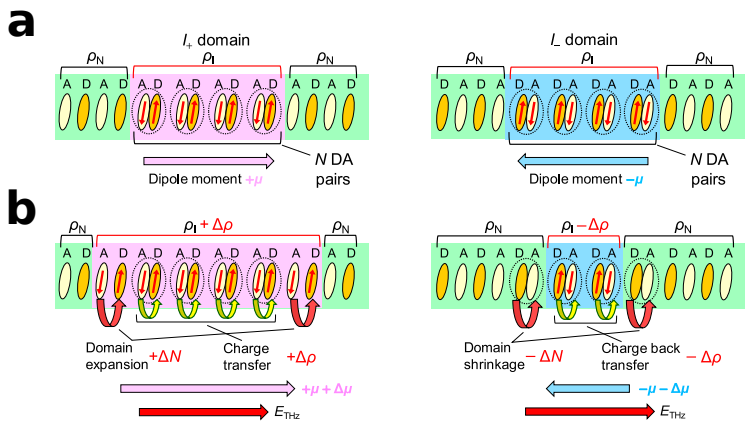

Figure 3.21: **a**: Net polarization in the I+ (left) and I- (right) domains of the neutral phase of TTF-CA. **b**: Influence of the application of a THz electric field on their net polarization. THz field induces NIDW and a modulation of the CT. Adapted from [Morimoto, Miyamoto and Okamoto, 2017]

Their interpretation was that this "long lived" signal was caused by a domain wall motion

induced by the THz electric field as shown in Figure 3.21. In the Neutral phase of TTF-CA, close to the phase transition, 1D ionic domains start to be formed in the Neutral phase [Buron-Le Cointe et al., 2006]. Again, at t=0 ps, the signal oscillates, signature of a THz-induced intermolecular charge transfer. But their interpretation was that, in opposition to the phenomena obtained in the Ionic case, in the Neutral phase, the THz electric field do not only increase (or decreases) the charge transfer $\Delta\rho(t)$ within the ionic domains. It also increases (or decreases) their size by modulating a number $\Delta N(t)$ of DA pairs. The physical separation between the Neutral and Ionic domains (so called "NIDW" for Neutral Ionic Domain Wall) are, as a consequence, oscillating in space. It explains why the photo-induced signal last for delays longer than the pump pulse duration. This charge transfer and motion of domain wall was interpreted as being responsible for a transient symmetry breaking and the creation of a macroscopic polarization, in the Neutral phase. This symmetry breaking is confirmed by the appearance of Second Harmonic. This SHG measurement was found to be scaling with the change of Optical reflectivity (See (a) and (c) Fig.3.20). They made a comparison between the THz-induced SHG and the one obtained without any pump excitation, in the Ionic phase (at 65 K), to quantify the modification induced by the THz beam. They estimated that, at 90 K, the THz excitation transiently increased the charge by 27% and the size of the ionic domain by 43%.

As a summary they succeeded to generate a transient macroscopic polarization in the Neutral phase of TTF-CA via the application of a THz intense electric field. They interpreted this transient polarization as originating from an intermolecular charge transfer inside the ionic domain $\Delta\rho(t)$ and an NIDW motion $\Delta N(t)$, both caused by this THz excitation.

Part II: Towards THz control of ferroelectricity in TTF-CA

In the following sections, I will present some terahertz pump optical probe experiments that I performed at the Institute of Physics of Rennes, on TTF-CA. First, I will provide a summary of the experimental conditions. Then, I will show the evolution of the response to THz excitation with temperature and electric field amplitude. Finally, I will provide an interpretation of the results alongside with some future prospects.

3.6 Materials and methods

The TTF-CA crystals that I used were synthesized by Yann Le Gal at the ISCR (Institut des Sciences Chimiques de Rennes) by co-sublimation of TTF and CA, which resulted in crystals of 300 µm typical size. For each crystal used for experiment, we checked the crystalline orientation by X-ray diffraction for mounting the sample with stacking axis a aligned with the polarization of the THz electric field. For TTF-CA at room temperature the lattice parameters are equal to a=7.41 Å, b=7.62 Å, c=14.57 Å and $\beta = 99.27°$.

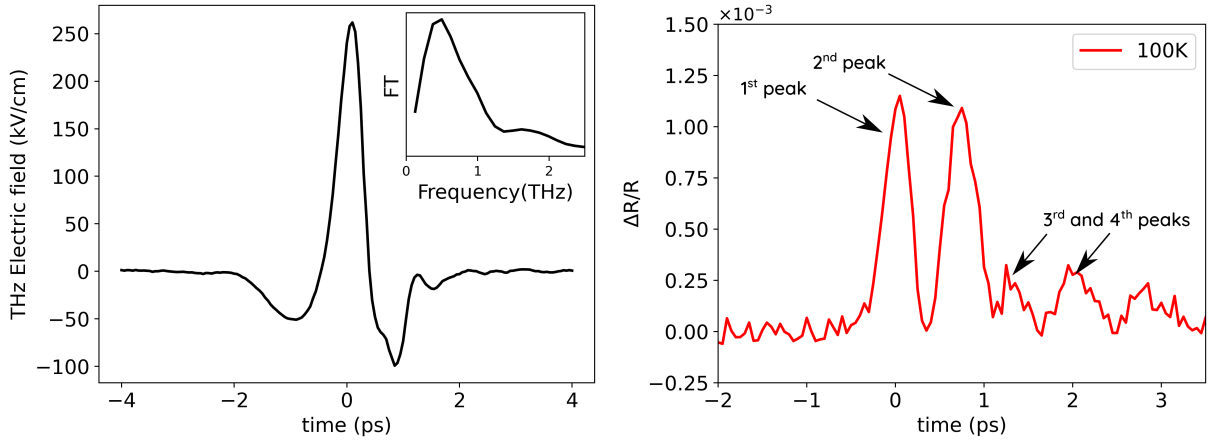

Figure 3.22: Left: time traces and Fourier Transform amplitude of the THz electric field used for the THz pump Optical probe experiment. Right: Typical time dependence of optical reflectivity change probed at 540 nm after terahertz pump (T=100 K)

To perform such experiments, we used an intense THz pulse generated by optical rectification in $LiNbO_3$ and focused at the sample position by a parabolic mirror (focal length of 50.8 mm). This technique enabled us to obtain a peak electric field of about 250 kV/cm at the sample position (measured by EOS with a 300 µm thick Gallium Phosphide). The terahertz beam, can be, on demand, attenuated using a pair of THz polarizers. In the Figure 3.22 is presented the time dependence of the THz electric field and the frequency range of the terahertz envelope, spanning from 0 to 2 THz and centered around 0.5 THz. A beam waist of 800 µm by 1100 µm in full width half maximum (FWHM) was measured at the focal point by a pyroelectric camera (Pyrocam III). We used an experimental setup similar to the one presented in the previous chapter, as shown in Fig. 3.23.

I used the output beam of an optical parametric amplifier (Light Conversion - TOPAS) as probe for monitoring time-resolved reflectivity change induced by the THz excitation. The wavelength of the probe was set to 540 nm (2.3 eV). This wavelength probes an intramolecular transition band (IMT) sensitive to the charge ρ of the TTF, as the energy position of this band varies from 2.5 eV (495 nm) in the N phase (90 K) and 2.25 eV (532 nm) in the I phase (77 K) [Miyamoto et al., 2013; Dressel and Peterseim, 2017](See Fig. 3.24). This band is also sensitive to molecular vibration modes, which modulate the transfer integral [[Uemura and Okamoto, 2010; Iwai et al., 2006]. An important transient variation of the reflectivity measured at 540 nm perpendicularly to the $\vec{a}$ axis is therefore expected in case of a THz mediated charge transfer,

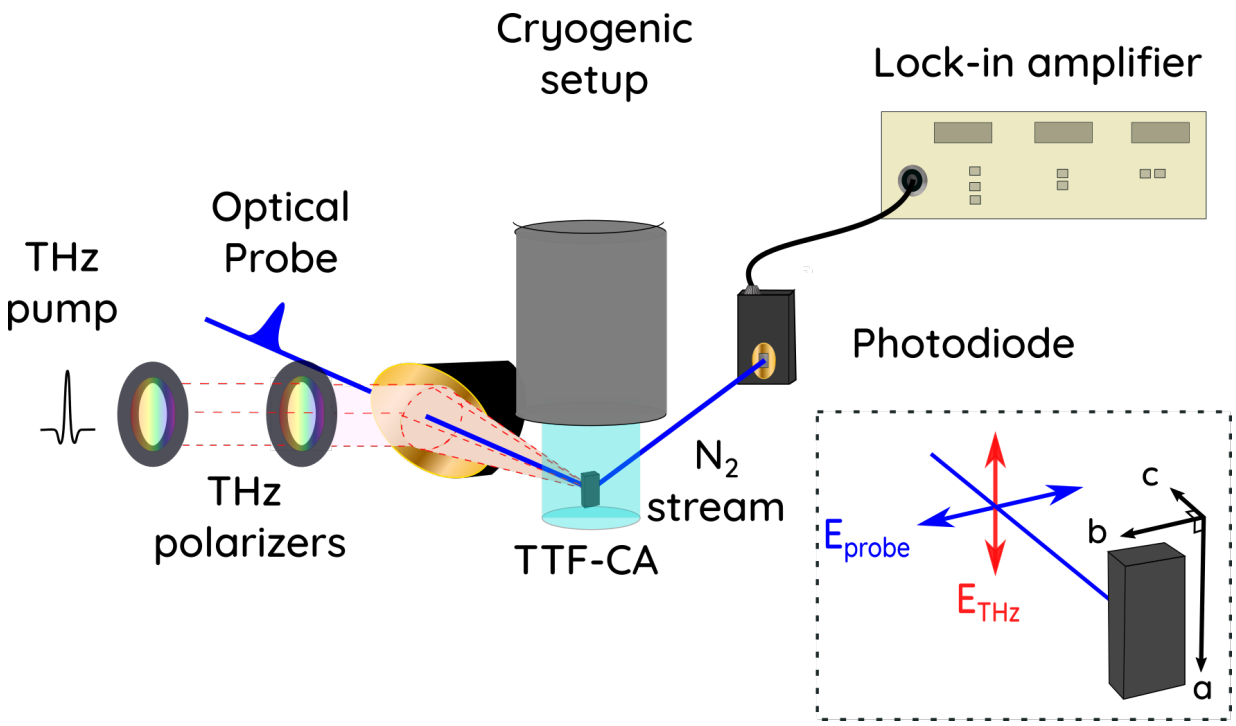

Figure 3.23: Schematic representation of the TeraHertz pump Optical Probe setup used for the experiments on the TTF-CA crystals

molecular vibrations or phase transition.

We oriented the crystal in such a way that the propagation direction of both pump and probe beams was mainly along the $\vec{c}$ axis of the crystal. The polarization of the terahertz beam was set parallel to the stacking axis ($\vec{a}$ axis) of the crystal, while the one of the probe was set along the $\vec{b}$ axis in order to match the conditions used for the static reflectivity measurements.

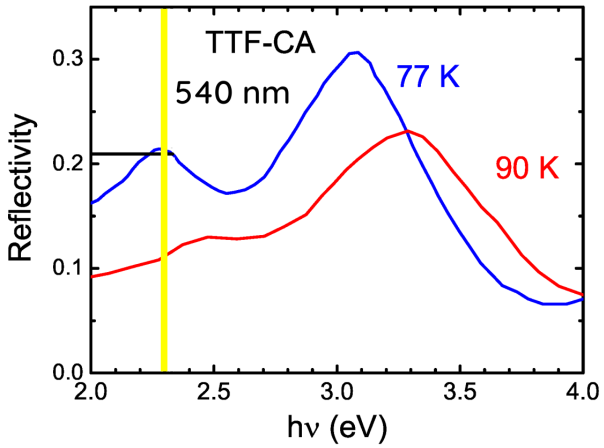

Figure 3.24: Comparison of reflectivity spectra measured perpendicular to $\vec{a}$ axis in both Neutral Paralectric phase (red) and Ionic Ferroelectric phase (blue). The selected probe energy (2.3 eV) appears in Yellow. Figure adapted from [Dressel and Peterseim, 2017]

A crossed polarization configuration for pump and probe beams also allows to filter the residual contributions from 800 nm radiation, used to generate the THz pump beam, on the detector, leading to a reduction of the noise floor. The probe beam reflected by the sample was focused on a photodiode connected to a Lock in amplifier (Stanford Research SR830). Finally, a cryostream cooler (Oxford Cryostream) was used as cryogenic system, enabling the cooling of single crystals

from room temperature down to 85 K (N_2 stream) with a precise and reliable monitoring of the temperature of the order of 0.1 K.

3.7 Temperature-dependent response of TTF-CA to THz excitation

This section is focusing on the temperature evolution of the THz-induced reflectivity change signal probed at 540 nm with a beam polarized perpendicular to the stacking axis $\vec{a}$. The THz excitation was polarized along the stacking axis $\vec{a}$.

The THz-induced signal is made of successive peaks or oscillations of the reflectivity. Their amplitude grows with decreasing temperature. Thus, before talking about the temperature evolution of the THz-induced signal, the typical low temperature signal is shown in Figure 3.22 (right) in order to clarify the naming of those features.

The thermal dependence of the temporal photoresponse is presented in Fig.3.25 in the 220-90 K range. My results are quite similar to the ones reported by Morimoto et al. At 220 K, the signal is made of a single reflectivity peak centered around 0 ps (first peak) with duration similar to the THz pulse duration. On decreasing the temperature, its amplitude is growing. A second peak appears below 140 K while more oscillations are perceptible on approaching the transition temperature (T≤100K). The low temperature signal is, thus, made of equally spaced peaks. In this oscillating signal, the peak spacing is about 0.75 ps at T=90K (See Fig. 3.26).

The temperature evolution of the amplitude of each peak can be found in Fig.3.26 and reveals some unexpected behaviors. At high temperatures, only the first peak is perceptible. At 140 K a second peak starts to grow. Its amplitude increases much faster than for the first peak. Therefore, at temperature close to the transition temperature, the amplitudes of both peaks are similar. Indeed, while the first peak seems to increase linearly with the lowering of the temperature, the second one sees its amplitude growing much faster on approaching the transition temperature. This difference in temperature evolution might be the signature of different phenomena contributing to this overall photo-induced signal, which will be discussed hereafter.

The time spacing between the peaks can also be monitored. This oscillation period is increasing on cooling (See vertical lines in Fig.3.25) from 0.55 ps for 130 K to 0.75 ps at T=90 K (See Fig. 3.26).

We can notice that both the amplitude and frequency behavior analysis are in agreement with the one presented by Okamoto's group in [Morimoto, Miyamoto, Yamakawa, Terashige, Ono, Kida and Okamoto, 2017](See section 3.5.2), where a clear increase of the peak spacing while cooling is perceptible. Concerning the amplitude, even though, in their case, the first peak remains the main one, the faster increase of the second peak amplitude with the temperature is also present in their work. Finally, we confirm the presence of an intriguing feature that was barely perceptible in their study. Indeed, a small negative signal appears at t≈0.3 ps, i.e in between the two first peaks, at T=90 K (See in section 3.5.2) differs from the purely positive signals obtained at any higher temperature.

This oscillating signal was interpreted by Morimoto et al. as the result of both an intermolecular charge transfer $\Delta\rho$ within ionic domains and breathing of the NIDW in the paraelectric Neutral phase induced by THz excitation. Close to the transition temperature, some 1D ionic domains I_+ and I_- of opposite dipole moment ($\pm\mu$) are present in the neutral phase. The THz excitation causes a fractional charge transfer leading to an increase of the charge density $+\Delta\rho$ within these I_+ domains and an increase of the number of DA pairs involved in this ionic domain $+\Delta N$. The I_- ionic domains will experience the opposite behavior. They considered that $\Delta R \propto \Delta\rho\Delta N$. Since each of those two contributions is proportional to the THz electric field amplitude, the dependence of the reflectivity must be quadratic with respect to the THz electric field amplitude.

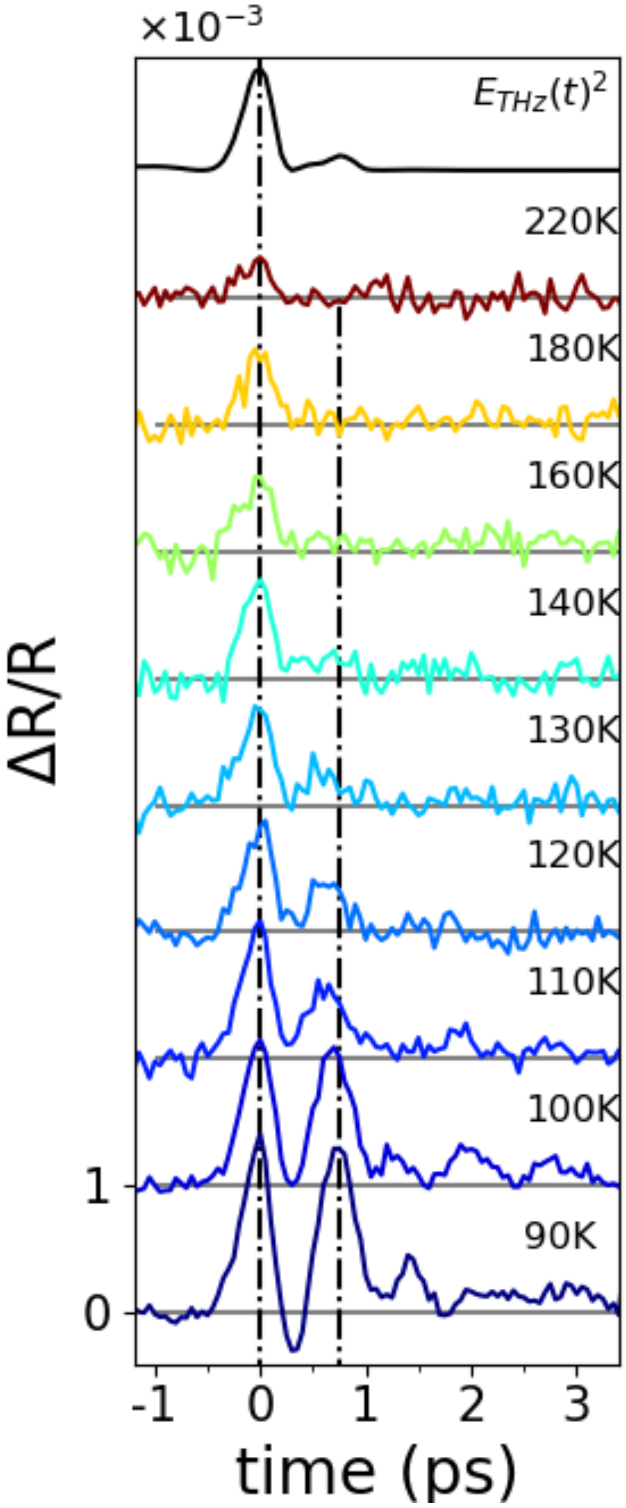

Figure 3.25: Evolution of transient reflectivity change at 540 nm induced by a THz excitation in TTF-CA as a function of temperature

Due to a significant increase of the amplitude of the signal at temperature lower than 110 K, we performed a careful analysis of the THz-induced signal on approaching the T_{NI} temperature (See Left Fig.3.27).

For T=95 K and T=90 K, a positive signal corresponding to an exponential decay superposes to the oscillation mentioned previously and is increasing on lowering the temperature. This feature

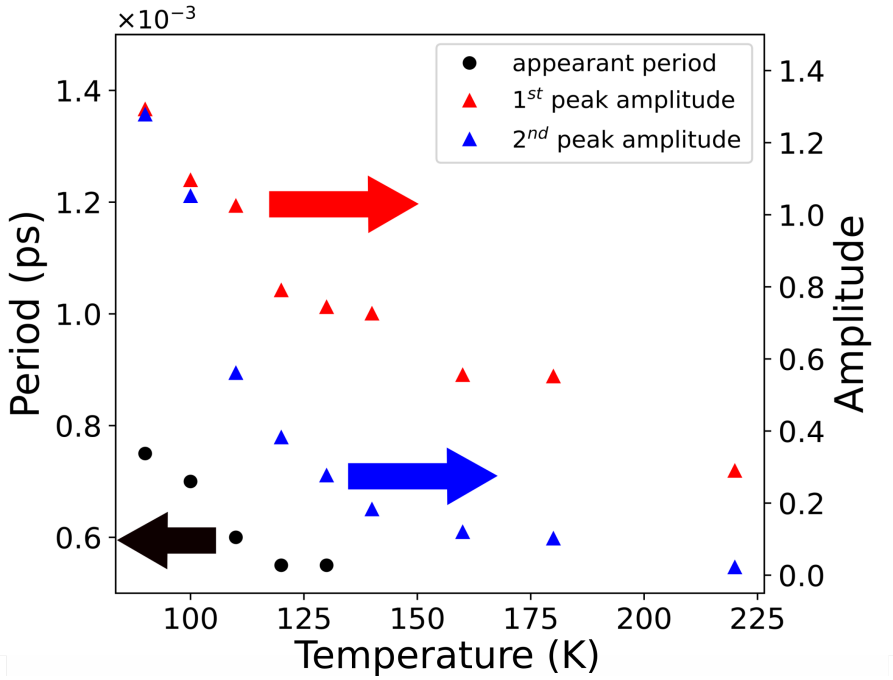

Figure 3.26: Left axis: Evolution of the observed period between two closest peaks as a function of temperature. Above 140 K oscillations are hard to distinguish, the period is thus not measured anymore. Right: Evolution of the amplitude for each peaks, as a function of temperature.

persist for t>1 ps, i.e. when the THz excitation pulse is over. Again, close the T_{NI} the signal also exhibits a small negative component located in between the two first peaks (t≈0.3 ps).

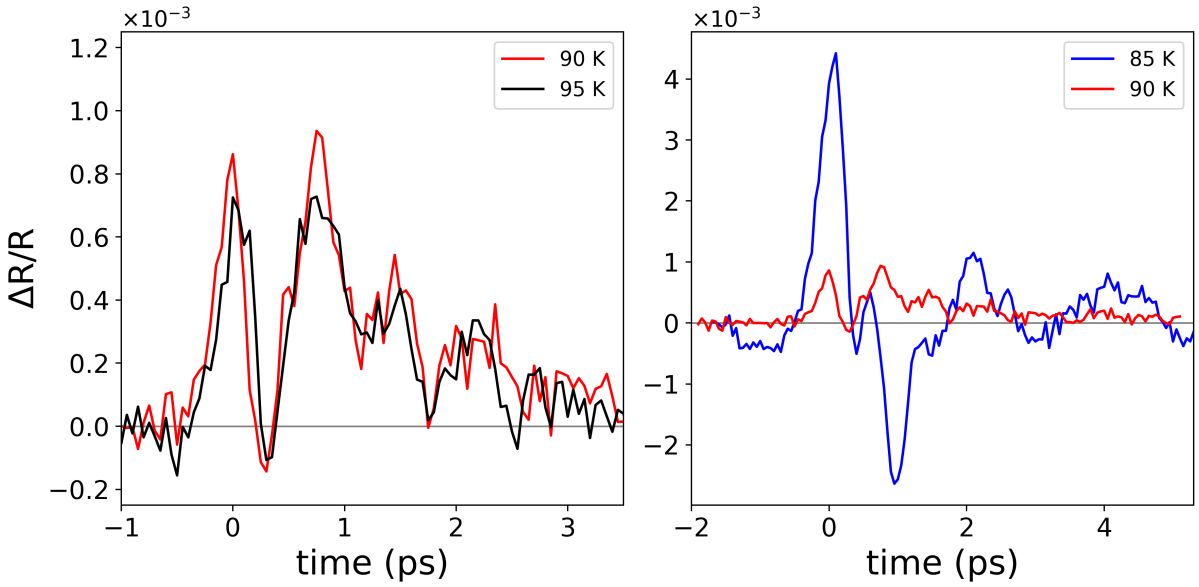

Figure 3.27: Transient reflectivity following THz excitation, measured on approaching the phase transition. Left panel: measurements at T=95 K and T=90 K. Right Panel: T=90 K and T=85 K

Finally, at T=85 K, i.e. 2 K above the thermal hysteresis, the signal is highly enhanced with an amplitude five times larger than at higher temperature (See Right Fig.3.27). The signal has a very important negative peak around 0.7 ps and an average positive signal after 1.5 ps.

Oscillations with period larger than the one measured at higher temperatures are perceptible. The signal obtained is very similar to the one obtained by Miyamoto et al. [Miyamoto et al., 2013] by exciting with a THz intense pulse the low temperature ionic ferroelectric phase at 77 K ($T< T_{NI}$)(See section 3.5.1), except that THz excitation of the Ionic Ferroelectric phase induces optical reflectivity oscillation around an average zero value.

3.8 THz Field-dependent response of TTF-CA

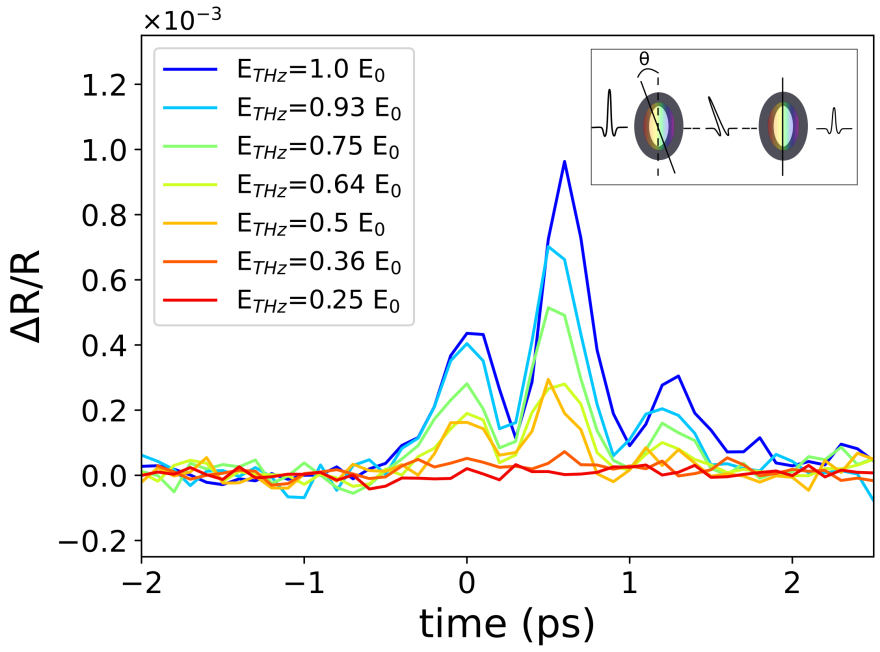

Figure 3.28: Transient reflectivity as a function of the electric field amplitude E_{THz}. T=100 K

This section is about the study of the THz-induced signal at T=100 K for various THz electric field amplitudes.

The electric field amplitude was modified thanks to a pair of THz polarizers. A first polarizer was set in the collimated THz beam, before the parabolic mirror. Its transmission axis was kept vertical (i.e. // to the $\vec{a}$ axis). A second polarization was then installed upstream, on a rotating mount. By changing the polarization direction of the rotating mount with respect to the vertical direction (θ angle on inset of Fig. 3.28), the projection of the terahertz electric field amplitude on the transmission axis of the other polarizer attenuates the THz electric field amplitude.

This study is shown in Fig.3.28. First, we can notice that, due to different experimental conditions (spatial overlap and different crystal), the signal slightly differs from the one shown in previous sections. This signal is made of three equally spaced peaks instead of two mains peaks in the typical signals presented earlier. The second peak has the greatest amplitude while the two others have a similar intensity. The maximum value of each peak was extracted for various polarizer configurations. The progressive rotation of the polarizer causes a reduction of the signal. Since, $E_{THz}(\theta)$=$E_0\cos^2(\theta)$, we can consider that the three peaks follow the same trend and vary quadratically with the THz electric field amplitude (Fig. 3.29 lower panel) rather than linearly (Fig.3.29 upper panel). Thus, the THz-induced signal is proportional to the energy deposited by the THz pulse.

This quadratic dependance is also in complete agreement with the results found by Morimoto et al. [Morimoto, Miyamoto, Yamakawa, Terashige, Ono, Kida and Okamoto, 2017].

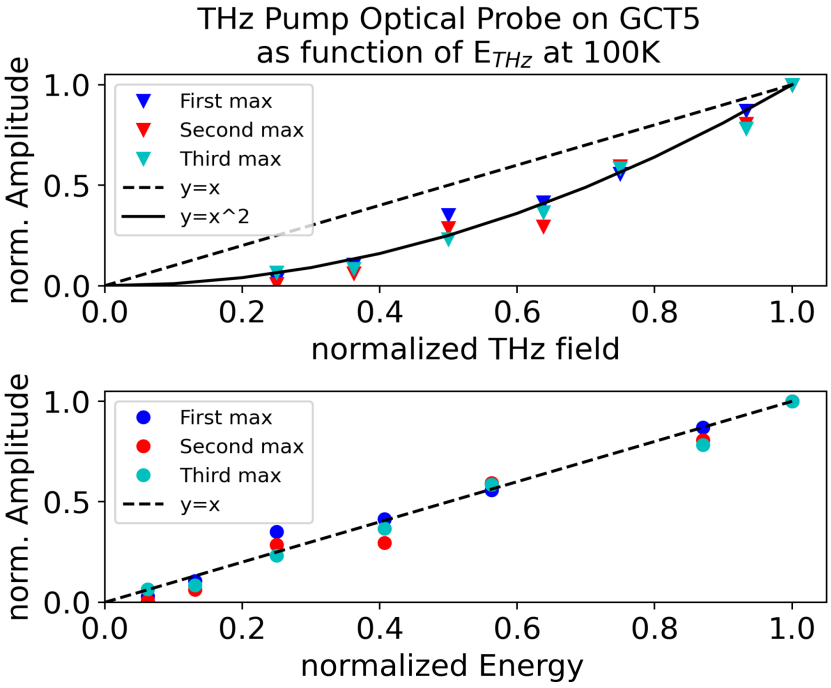

Figure 3.29: Amplitude of the photoinduced signal as a function of the TeraHertz field (upper panel) and TeraHertz deposited energy (lower panel). The first peak is represented in blue, the second peak in red and the third in cyan.

3.9 Resonant THz excitation of the Bu mode

My results presented above are complementary to the ones obtained by Morimoto et. al [Morimoto, Miyamoto, Yamakawa, Terashige, Ono, Kida and Okamoto, 2017], who suggested that the photoinduced response and oscillations were related to a THz induced intermolecular charge transfer, within the same ionic domain and a modification of the number of DA pairs involved in this ionic domain (Domain Wall motion).

In this section, I will show that the experimental results can be interpreted as resulting from a resonant excitation of the ferroelectric mode by the THz excitation.

Indeed, the THz-induced reflectivity change signal includes different components. On the one hand, as discussed by Morimoto et al, there is a quadratic electro optic effect (Kerr-like effect), due to the response of ultrafast degrees of freedom (electronic response and eventually fast structural degrees of freedom) to the THz pulse. The temporal evolution of this signal is proportional to $E^2_{THz}(t)$. Such effect might be of particular importance in the case of TTF-CA, due to its very strong electronic ferroelectricity. However, we do think that this instantaneous response ($\propto E^2_{THz}$) is not the only contribution to the feature obtained at t=0 ps as a coherent oscillation triggered by the THz field and lasting for several picosecond is also contributing to the signal at t=0 ps. I will show hereafter that the oscillation in the reflectivity signal, interpreted by Morimoto et al. as the motion of Neutral Ionic Domain Wall, is due to the resonant excitation of a ferroelectric Bu mode.

Hereafter we discuss in more detail our model used to fit the experimental data and considering two main contributions: one is an instantaneous response and the other is a much slower response related to the excitation of the Bu mode. Since the 2.3 eV beam probe the IMT band, which is a band sensitive to the TTF charge, both contributions are inducing a charge transfer perceptible by the change of reflectivity.

The first contribution is an instantaneous response with respect to the THz excitation. This response can be linked, as suggested in [Morimoto, Miyamoto, Yamakawa, Terashige, Ono, Kida

and Okamoto, 2017; Miyamoto et al., 2013], to electronic effects such as the intermolecular charge transfer induced by the THz excitation. The response of very fast phonons can also be inserted in this contribution. Due to symmetry considerations, in this centrosymmetric phase, only second order terms are allowed, thus the temporal evolution of the reflectivity change $\Delta R(t)/R$ must be proportional to the time dependence of the squared electric field: $\Delta R(t)/R \propto E^2_{THz}(t)$ as shown by the blue curve in Fig.3.30.

The second contribution takes into account the response of the system to the THz excitation of the Bu mode. This oscillation of the system along the Bu mode coordinates will modulate the transfer integrals and, as a consequence, will modify its ionicity (charge density), as discussed hereafter and therefore the amplitude of the IMT band probed. This contribution is made of a convolution between the THz time traces $E_{THz}(t)$ and a damped oscillator (See red in Fig.3.30). Again due to some symmetry considerations, explained in the section below, the second contribution will correspond to the square of this convolution.

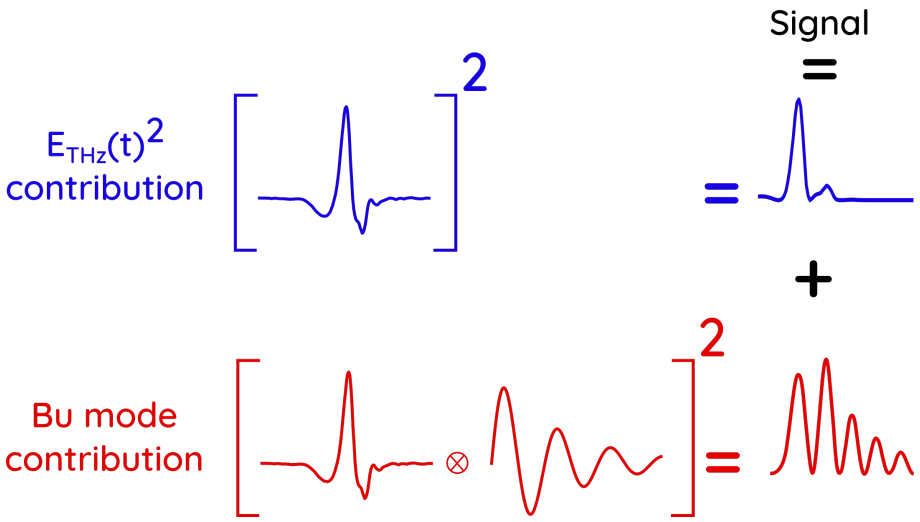

Figure 3.30: Schematic representation of the two contributions used in our model. In blue: the instantaneous response, in red: the response to Bu mode excitation by the THz field

3.9.1 Charge transfer modulation by ferroelectric mode

In this section is explained the consequence of a resonant excitation of a symmetry breaking mode (e.g Bu), on the TTF charge in the centrosymmetric phase of TTF-CA.

In TTF-CA, the charge transfer between donors and acceptors is linked to the overlap of π electron orbitals. This overlap of orbitals is related to the transfer integral t. At the phase transition, the degree of CT changes from ρ=0.3 in the neutral phase to ρ=0.7 in the ionic phase. Similarly, any modification of this transfer integral caused by an external excitation will modify the IMT band and therefore the reflectivity at 540 nm. Indeed, the modulation of the IMT was used to probe the photoinduced dynamics associated with the excitation of the neutral phase [Iwai et al., 2006; Uemura and Okamoto, 2010] .

As discussed in the introduction of this chapter, in the case of high temperature phase in TTF-CA, a Bu mode located around 1 THz (33 cm^{-1}), at low temperature, and softening from 70 to 20 cm^{-1} on approaching the phase transition has been measured [Masino et al., 2003; Girlando et al., 2008]. Therefore, we should consider that the THz pulse, having an envelope spanning from 0 to 2 THz, and polarized along the $\vec{a}$ axis can resonantly excite this Bu mode involved in the ferroelectric neutral-ionic transition, as symmetry-allowed.

To understand the effect of a resonant excitation of the Bu mode, lets consider a 1D chain

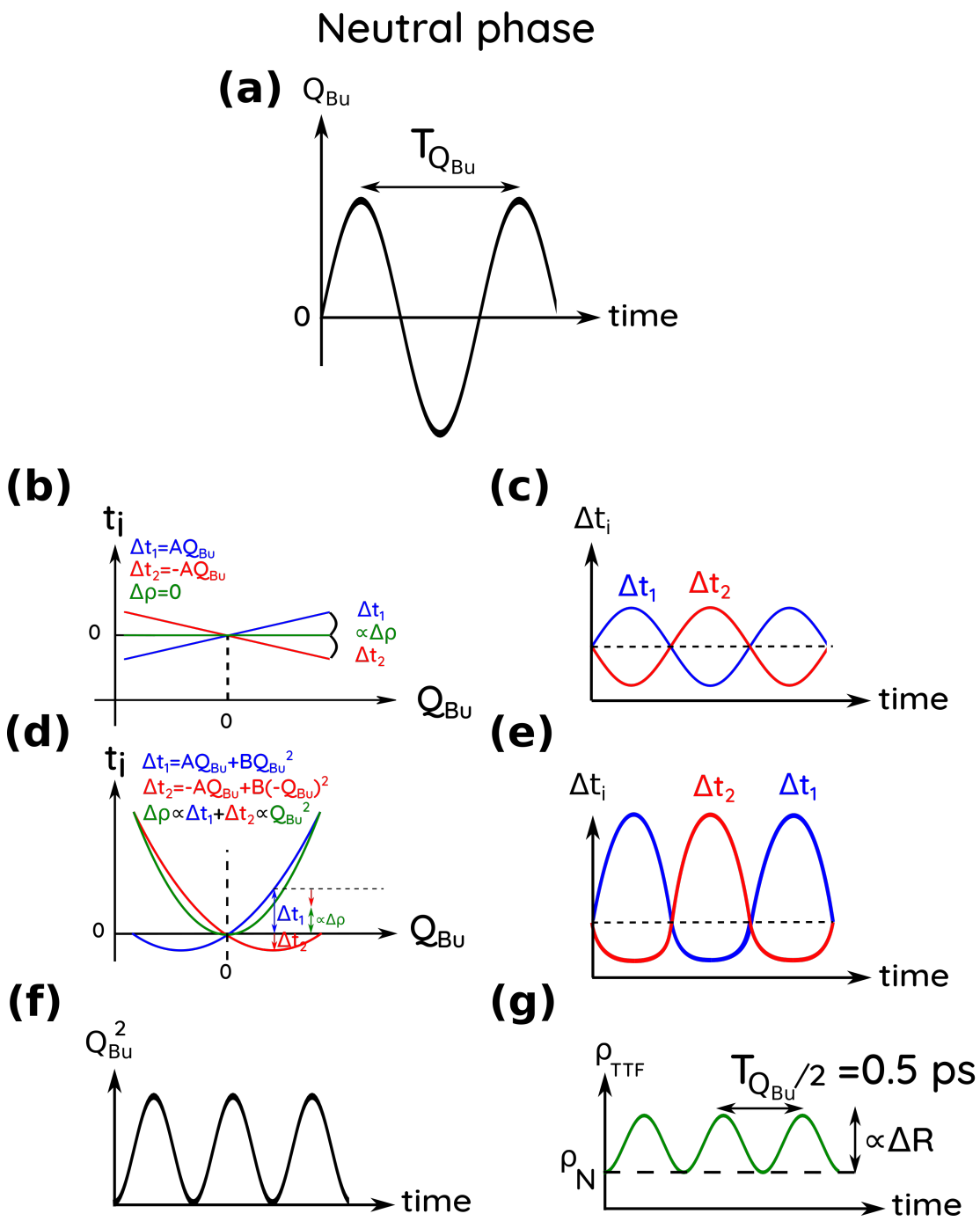

Figure 3.31: (a) Schematic representation of the Q_{Bu} (neutral paraelectric phase) mode coordinate oscillating, in time, with a period $T_{Q_{Bu}}$ following the resonant excitation of this Bu mode. (b) and (d) modulation of both transfer integrals following a movement along the Q_{Bu} coordinate ((b) first order, (d) second order Taylor expansion). (c) and (e) time dependent modulation of the transfer integral Δt_i ((c) first order (e) second order) (f) time dependent squared coordinate of Bu mode. (g) time dependent modulation of the TTF charge following the resonant excitation of Bu mode

made of alternating TTF (donors) and CA (acceptors). As schematically shown in Figure 3.32, every TTF molecule has a partial transfer integral t_1 (blue in Fig.3.32) and t_2 (red) with both surrounding CA alternating along the stack. In the equilibrium structure, where TTF lies on inversion symmetry, $t_1 = t_2 = t$.

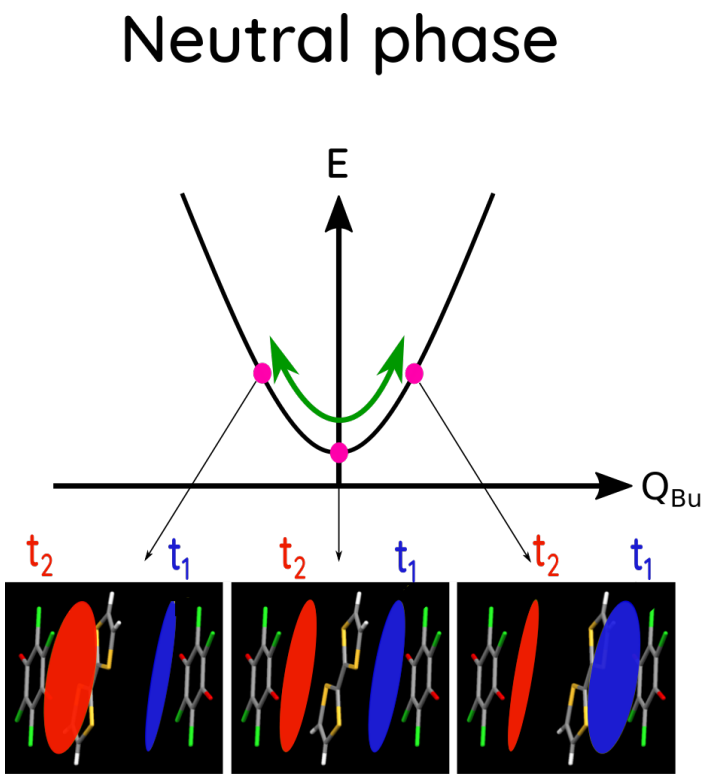

Figure 3.32: Schematic representation of the potential well of the system in the neutral paraelectric phase and the oscillation of TTF molecule along, Bu dimerization mode coordinates

In the Neutral phase, the THz pulse can resonantly excite Bu modes, when the electric field is along the $\vec{a}$ axis and when the frequency of the THz pulse corresponds to the frequency of the Bu mode, as given by Fermi's golden rule. The transition probability $\Gamma_{i\to f}$ based on time-dependent perturbation theory is:

$$\Gamma_{i\to f} \propto \left| < f|\vec{E}_{THz}.\vec{d}|i > \right|^2 \tag{3.9}$$

where $\vec{d}$ is the dipolar moment vector and $\vec{E}_{THz}$ the THz polarization.

This resonant excitation is efficient when $\vec{E}_{THz}//\vec{d}$ and E_f-E_i=hω. In the case of the Bu ferroelectric mode, $\vec{E}_{THz}$ should be set mainly parallel to $\vec{a}$ as $\vec{d}$ is mainly parallel to $\vec{a}$ (See Table 3.1) and the frequency ω should be in the 0.5 - 2 THz (Fig.3.15). Following this excitation, the system will oscillate along the Q_{Bu} coordinate. This Q_{Bu} coordinate measures the relative distance from the initial high symmetry position with molecules lying on inversion symmetry (Q_{Bu}=0), in the Neutral phase, as shown in Fig.3.32.

At equilibrium, the charge of the TTF is:

$$\rho_N \propto (t_1 + t_2)/2 \propto t \tag{3.10}$$

as $t_1 = t_2 = t$.

As shown in Fig.3.31a, the Q_{Bu} mode oscillates with a period T_{QBu}. The activation of the Q_{Bu} mode modulates the TTF-CA distances and consequently the transfer integrals t_1 and t_2. Any motion from the TTF towards a CA molecule will lead to an increase of this transfer integral $+\Delta t_i$. On the contrary, moving away from this CA molecule will lead to a decrease $-\Delta t_i$.

The modulation of the transfer integrals by the vibration mode can be described by a Taylor expansion around the equilibrium position $Q_{Bu} = 0$:

$$
\begin{aligned}
t_1(Q_{Bu}) &= t_1 + \Delta t_1(Q_{Bu}) = t + AQ_{Bu} + BQ_{Bu}^2 \\
&\text{and by symmetry considerations} \\
t_2(Q_{Bu}) &= t_2 + \Delta t_2(Q_{Bu}) = t - AQ_{Bu} + B(-Q_{Bu})^2
\end{aligned}
\tag{3.11}
$$

Fig.3.31b shows that the modulation of t_1 and t_2 by Q_{Bu} compensate each other at first order, which leaves the TTF charge constant ρ_N=cte (Fig.3.31c). Fig.3.31d includes the Q_{Bu}^2 terms. Fig.3.31e shows that $\Delta t_1(Q_{Bu})$ and $\Delta t_2(Q_{Bu})$ do not compensate each other anymore and consequently the TTF charge is modulated by Q_{Bu}: $\rho_N(Q_{Bu}) \propto 2BQ_{Bu}^2$.

Therefore, the resonant excitation by the THz pulse of the Q_{Bu} mode, which oscillates with a period T_{QBu}. modulates the TTF charge with a period $T_{QBu}./2$. In other words, the resonant excitation of the Q_{Bu} mode, oscillating with a frequency ω, translates into an oscillation of the TTF charge, and therefore of the reflectivity signal probed at 540 nm, with a frequency 2ω.

Using this consideration, the observed period (i.e the delay difference between two maxima) of the oscillation of the reflectivity showed in Fig.3.26 would correspond to Bu mode frequency falling in the THz envelope (e.g 0.5 ps at 130 K corresponds to 33 cm^{-1} i.e 1 THz) and seems to corresponds to the Q_{Bu} mode frequency reported experimentally (See Fig.3.35), confirming our interpretation of resonant THz excitation of the Q_{Bu} mode.

This symmetry analysis of our time-dependent signal is also valid to explain the time-dependent optical reflectivity signal induced by THz excitation published by Morimoto et al.

Finally, we should consider that the resonant excitation of the Q_{Bu} mode is not instantaneous with an exponentially decaying sinus form. Indeed, the Q_{Bu} mode is driven by the $E_{THz}(t)$ and its temporal envelop. The time evolution of Q_{Bu} is therefore the convolution of $E_{THz}(t)$ with the damped sinus oscillation. The reflectivity signal scales with the squared convolution as shown by the red curve in Fig.3.30.

3.9.2 Modelization of the photo-induced signal

Hereafter, we performed a fit of the THz-induced reflectivity change signal for T<140 K, as a weighted sum of the two contributions (instantaneous response and the response to the resonant excitation of the Bu mode) shown in Fig.3.30. Some fits are shown in Fig.3.33. For temperatures higher than 130 K, no oscillations are observed. It is sufficient to consider only the instantaneous contribution to fit the data. At 130 K, a rise of the first peak amplitude and the appearance of a second oscillation reveal the emergence of the contribution of the Bu mode. Both contributions are now necessary to fit the data. By decreasing further the temperature, the importance of this mode response is growing. Oscillations are seen up to 3 ps. This contribution is now preponderant compared to the instantaneous response.

Below 100 K, our study and the one presented by Morimoto et al. showed that a negative contribution emerges in between the two main peaks (t=0.3ps) (See Fig. 3.34).

This contribution remains unclear and can originate from electronic effects such as electronic ferroelectricity (charge-transfer), creation of ionic domains within the neutral phase or from a symmetry-breaking allowed Pockels effect. The contribution may also explain the decrease of amplitude seen by Morimoto et. al at T=100 K (See Fig.2 (a) and (b) [Morimoto, Miyamoto, Yamakawa, Terashige, Ono, Kida and Okamoto, 2017]). This contribution has to be studied carefully to be incorporated to the model, even though we are more interested in what occurs after THz excitation and not during.

3.9.3 Softening of the resonantly excited Q_{Bu} mode

From the fit, we were able to extract the mode frequency for temperatures between 90 and 130 K, as shown by the red dots in Fig.3.35, where we observe a mode softening from 32 to 22 cm^{-1}.

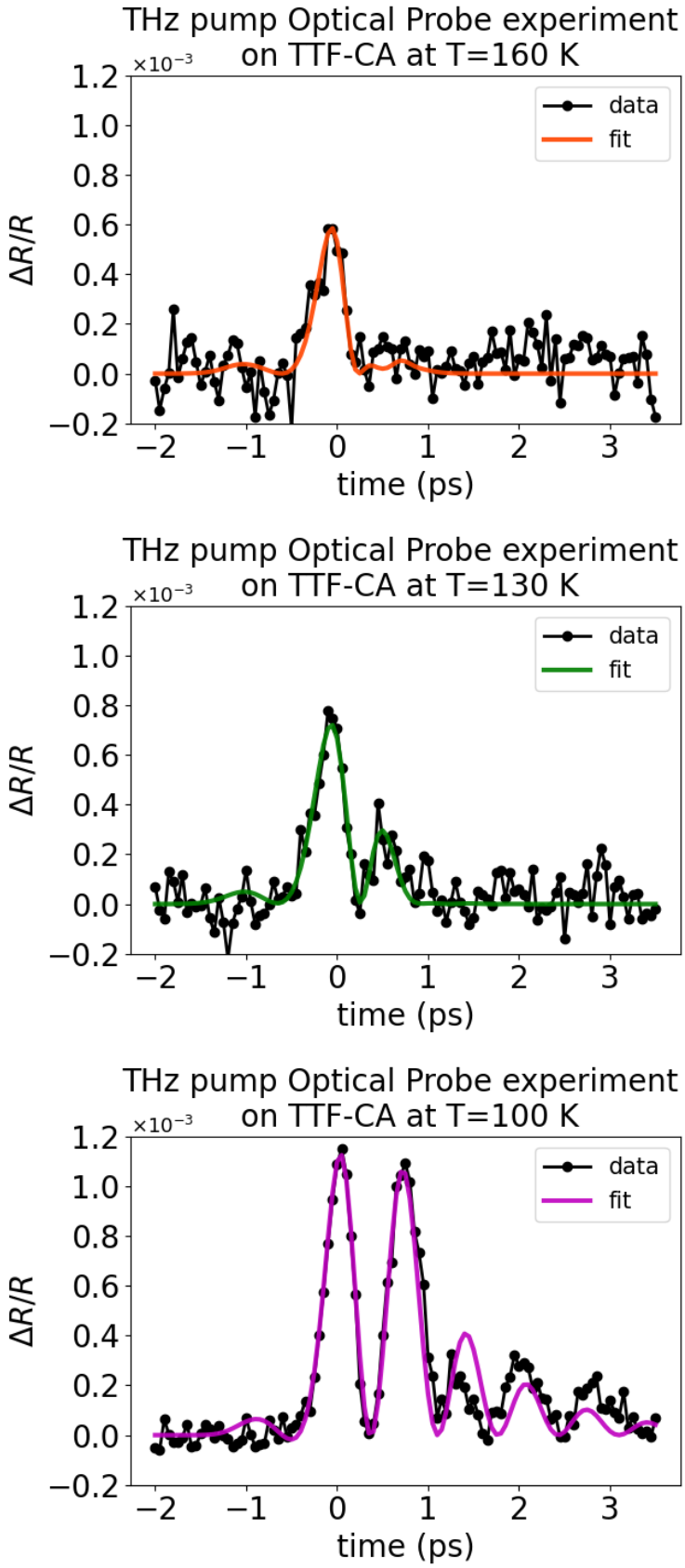

Figure 3.33: Comparison of the photo-induced signal (black) and the fits (colored) for various temperature: 160 K (left), 130 K (center), 100 K (right).

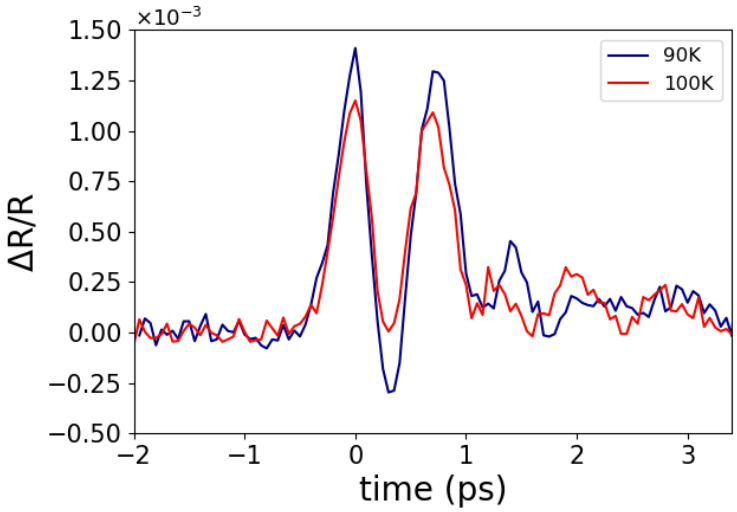

Figure 3.34: Focus on the appearance of a negative contribution around t=0 ps for T<100 K

For temperature above 130 K, the weak amplitude of the oscillations did not allowed extracting the oscillating component.

This temperature dependence follows very well the evolution of the frequency of the Bu mode reported by conventional spectroscopy by Masino et al. (sidebands measurement) [Masino et al., 2003] (See Fig. 3.35).

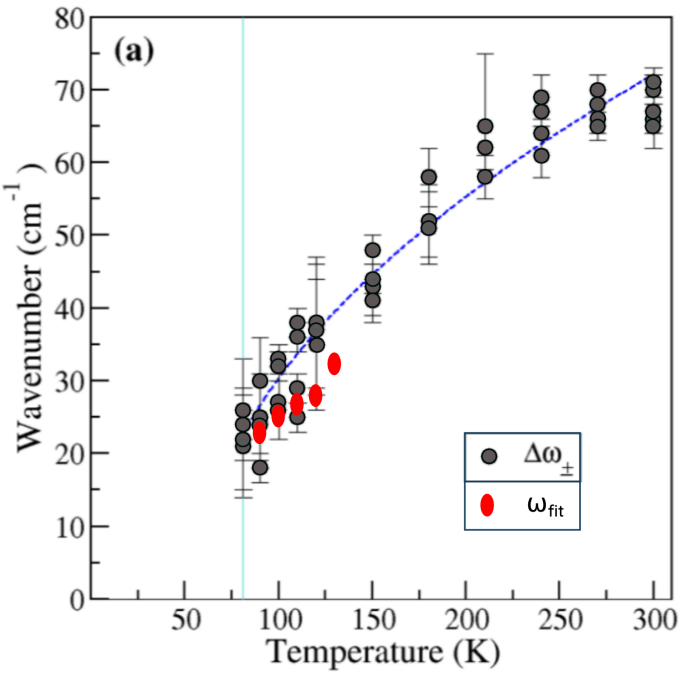

Figure 3.35: Comparison of the soft mode frequency extracted from our fit of the THz-induced reflectivity change (red) and the Bu mode frequency obtained by Masino et. al [Masino et al., 2003] by measuring the Temperature dependence of sideband frequencies in the mid-IR range (around 1000 cm^{-1}, in grey)

3.9.4 Amplitude of the mode response

In addition to the frequency change of the oscillation, another interesting point to discuss is the thermal dependence of the amplitude of the oscillating component. It can be monitored through the evolution of the amplitude of the second peak, which decreases with increasing temperature and almost vanishes above 140 K as shown in Figure 3.26.

The energy deposited by the THz pulse on the phonon mode scales as E^2_{THz}. However, the energy deposited by our THz source depends on the THz frequency, as shown in Figure 3.36. It is interesting to plot the amplitude of the oscillating signal, also scaling as E^2_{THz}, through the thermal dependence of the frequency ω(T) of the Bu mode. The green dots in Fig.3.36 represent the amplitude of the oscillating reflectivity change measured at a temperature T, which corresponds to a frequency ω(T) of the Bu mode. The comparison of these two curves shows that the resonant excitation of the mode is observed mainly below 140 K, where the spectral power is stronger.

This provides a qualitative explanation of the resonant excitation process of the Q_{Bu} mode by our THz source:
- Above 140 K, the frequency of the Q_{Bu} mode is above 40 cm^{-1} (1.3 THz), where the spectral power is very weak. The frequency of the Q_{Bu} mode is out of the spectral window of the THz excitation source.
- Below 140 K, the frequency of the mode enters a spectral window where the spectral power is high, which allows efficient and resonant excitation of the Q_{Bu} mode. This resonant excitation gets more and more efficient on cooling due to the mode softening.

This explains why oscillations are difficult to distinguish above 140 K. It confirms that the reflectivity oscillations are induced by the resonant excitation of the Q_{Bu} mode by the THz pulse.

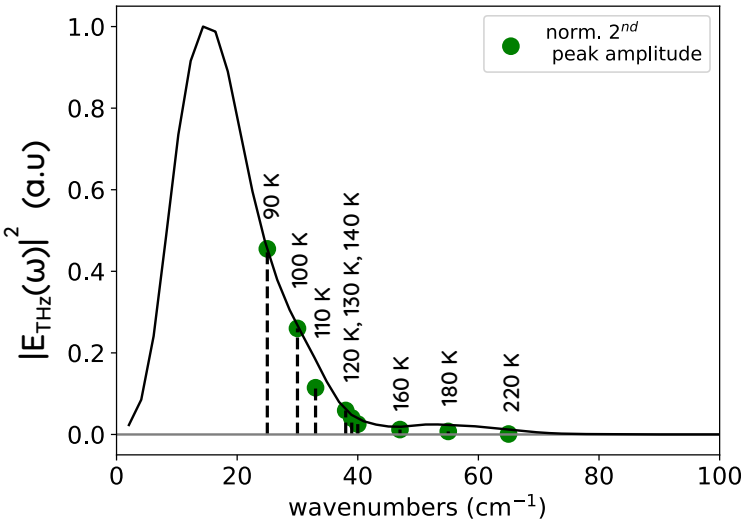

Figure 3.36: Black line: Fourier Power spectrum of THz field. Green dot: amplitude of the second peak. The green dots are normalized to match approximately $|E_{THz}(\omega = 25cm^{-1})|^2$

3.9.4.1 Summary

In this section we have shown that the coherent oscillation of optical reflectivity induced by a THz pulse, can be interpreted as resulting from the resonant excitation of the Q_{Bu} mode in the N phase. Indeed, the excitation pulse has a polarization $E_{THz}//\vec{a}$, which can therefore resonantly excite a Bu mode whose dipolar moment is partly along the stacking axis. However, the resonant excitation of this mode (frequency ν_{Bu}) modulates, by symmetry, the optical reflectivity with a frequency $2\nu_{Bu}$. The analysis of our data shows that the frequency ν_{Bu} of the mode and its

thermal dependence, extracted from our THz-pump optical probe experiment are in very good agreement with the ones experimentally reported by conventional spectroscopic techniques at thermal equilibrium. In addition, this mode is efficiently excited in a temperature range where its frequency enters the spectral window of the THz excitation with significant energy.

The nice correspondence between our data, the model and the data from the literature allows to propose a new interpretation of the coherent oscillation of optical reflectivity as resulting from the resonant excitation of the Q_{Bu} mode by the THz pulse.

3.10 Enhanced response on approaching T_{NI}

In this section we discuss the enhancement of the response when the temperature approaches the transition temperature (T_{NI}=81-83 K). We will focus on signals obtained at 95 K, 90 K and 85 K.

At 95 K and 90 K, in addition to the instantaneous response, that we will call "Kerr" like trend (KE(time)) and the response linked to the resonant excitation of the soft mode (Osc(time)) reported previously, an exponentially decaying signal is perceptible (See in FIg.3.37). We focus on the oscillating region (time$\geq$ 0.3 ps) which is extending well after the application of the THz field. This region is the most interesting for the physics of THz-induced ferroelectricity.

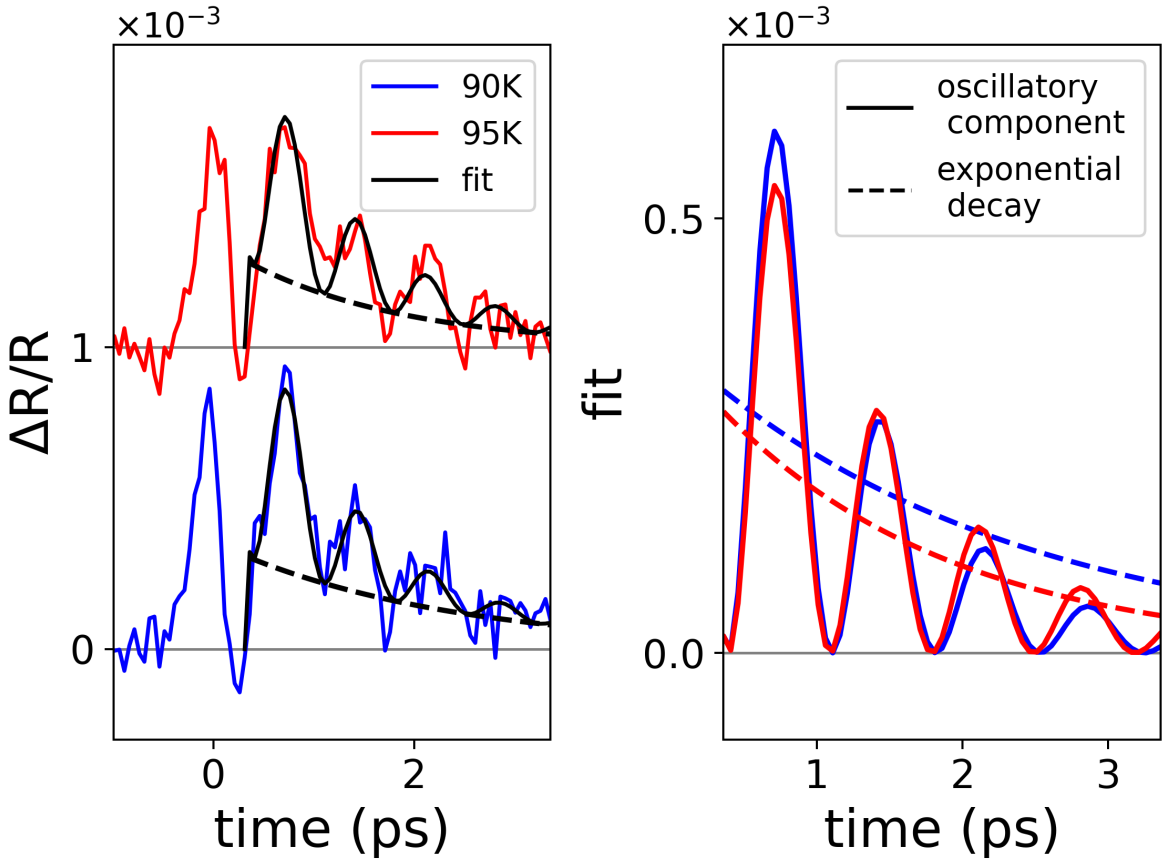

Figure 3.37: Left: Photoinduced signals obtained at T=90 K and T=95K and their fits for t>1 ps. Right: Respective contributions of both oscillatory and exponential components of the fit.

Since we are probing the TTF band, sensitive to the degree of CT, we may interpret this exponential decay as a transient change of CT driven by the THz pulse. In addition, the fit of

the data, shown in Fig.3.37, indicates that the amplitude of the exponential signal is larger at 90 K compared to 95 K and the relaxation constant increases from 1.6 ps at 95 K to 2.3 ps at 90 K.

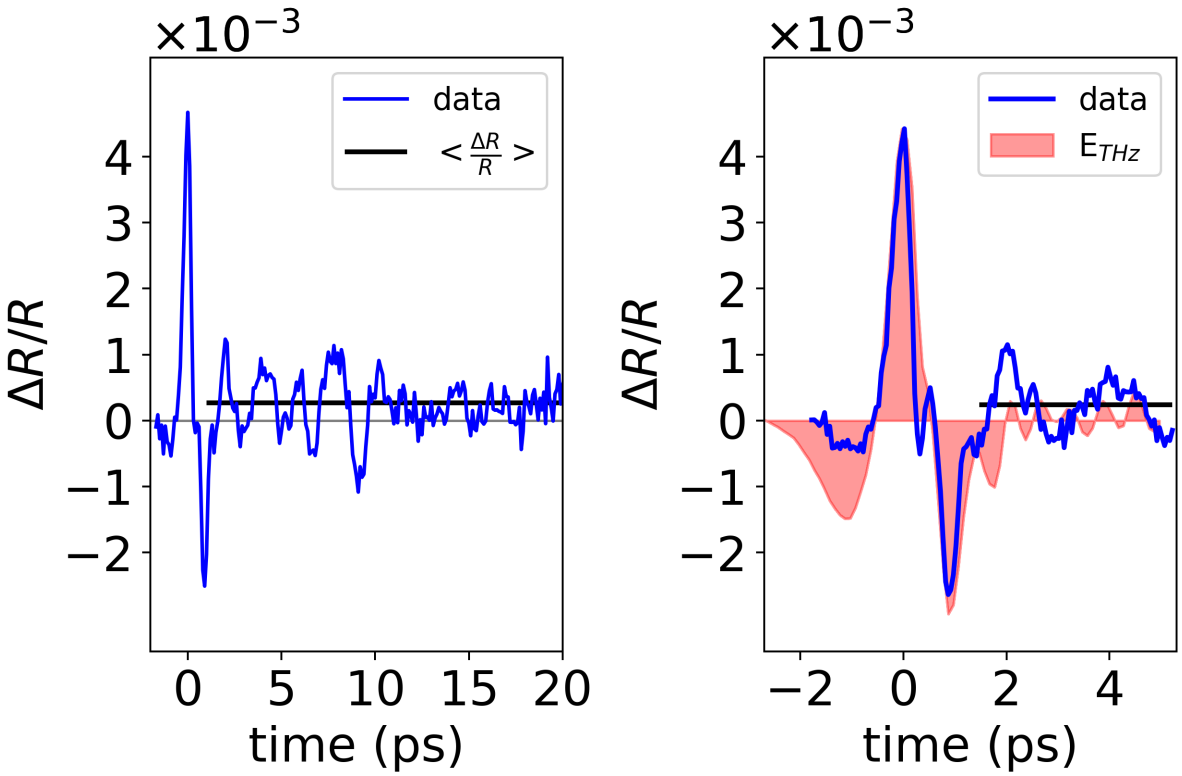

Figure 3.38: Left: THz-induced signal obtained at T=85 K and measured up to 20 ps. The black line represents the mean change of reflectivity after the THz excitation. Right: Comparison between the THz-induced signal obtained at 85 K (blue) and the time traces of the THz pulse excitation (redish area)

Figure 3.38 shows that at 85 K, the amplitude of the signal is much larger (5 times) and its shape is very different. The time dependent signal is similar to the one observed by Miyamoto et al [Miyamoto et al., 2013] by exciting with a THz pulse the low temperature Ionic ferroelectric phase (See Section 3.5.1). However, our experiment is performed at 85 K in the N phase (the thermal hysteresis is in the 81-83 K range). Our THz-induced signal at 85 K in the N phase exhibits similarities with the THz-induced signal from the ferroelectric phase reported by Miyamoto et al., with an important increase followed by a decrease of the reflectivity is observed between -1 and 1.5 ps, which seems to be linked to the profile of THz times traces (represented by the redish area in Fig. 3.38). This may be an indication that the signal follows linearly the THz electric field (Pockels effect).

Both the exponential decay and the change of signal at 85 K were not reported by Morimoto et al. in their THz excitation of the neutral phase.

In addition, several discrepancies exist between those studies. First, in our case, the experiment was performed in low humidity conditions (4%). Consequently, our signal is less affected by the signal originating from water. Secondly, in our case, the Pockels like effect is followed by oscillations of approximately 2.2 ps (0.45 THz or 15 cm^{-1}) period damped after 10 ps, while a 54 cm^{-1} frequency mode, lasting for a tens of picosecond, was observed below T_{NI} in their study. Also, in their article, the THz-induced signal measured in the I ferroelectric phase at positive delay, oscillates around zero. On the contrary, in our data, we see a clear average increase of reflectivity after THz excitation. Since the probe wavelength is sensitive to the charge located around TTF molecules, this behavior, lasting for more than 20 ps can be tentatively interpreted

as a transient THz induced charge transfer towards the I ferroelectric phase..

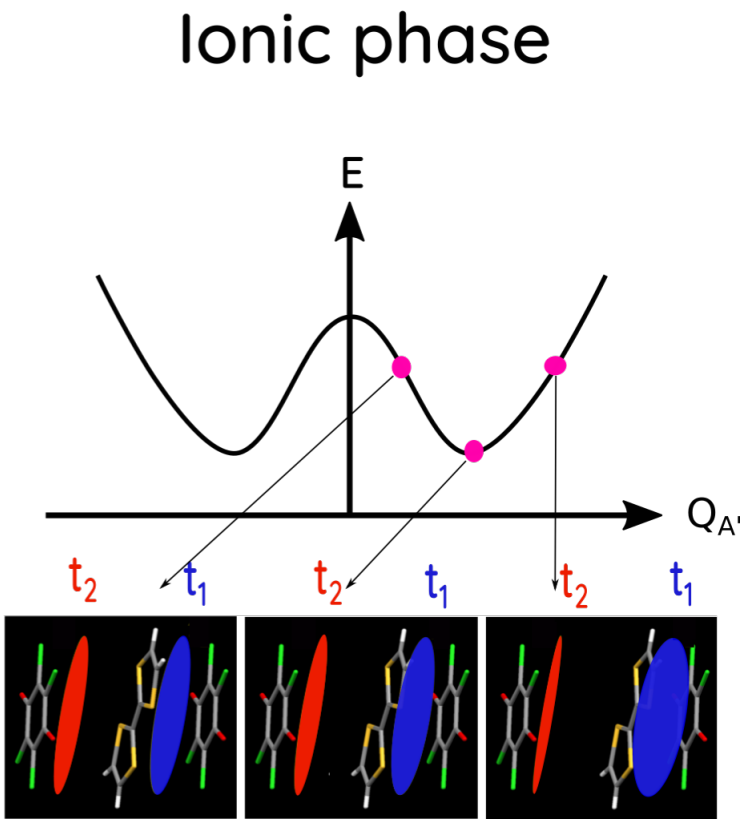

Figure 3.39: Schematic representation of the potential well of the system in the Ionic ferroelectric phase and the oscillation of TTF molecule along A' dimerization mode coordinates

We should also underline that if the Ionic ferroelectric phase is reached, the molecule oscillates around a new equilibrium position, which corresponds to the dimerized structure (Figure 3.39). The ferroelectric mode therefore belongs to the identity representation A' of the Pn space group in the ferroelectric phase. Consequently, the reflectivity is modulated the same frequency as the one of the $Q_{A'}$ mode (Figure 3.40), because t_1 will not increase as t_2 decreases due to symmetry consideration. Therefore, the oscillation at 15 cm^{-1} may be due to the dimerization mode $Q_{A'}$ in the ionic ferroelectric phase.

While this lack of inversion symmetry, represented by the Pockels effect is expected in the ferroelectric phase, this behavior is quite surprising for temperature located above the phase transition. This peculiar feature, added to the non zero mean reflectivity measured at positive delays may therefore be due to THz-driven N-I ferroelectric phase transition, with a change from N paraelectric to I ferroelectric states, associated with reflectivity increase and ferroelectric order responsible for the Pockels effect. Unfortunately, the present data sets do no enable us to firmly conclude on the THz-induced N-I ferroelectric phase transition, as a direct measurement of the symmetry-breaking after the Pockels effect is lacking. In order to confirm this hypothesis and quantify the change of ionicity and the symmetry of the THz-induced state, complementary measurements must be performed soon.

We plan to perform THz pump Second Harmonic Generation probe to witness any long-lived THz induced symmetry breaking, to monitor possible THz-induced ferroelectric order, lasting well after the THz pulse.

A THz-induced ferroelectric order is made easier with large E_{THz} field and on approaching the phase transition. This may be the reason why the THz-induced signal is very different at 85

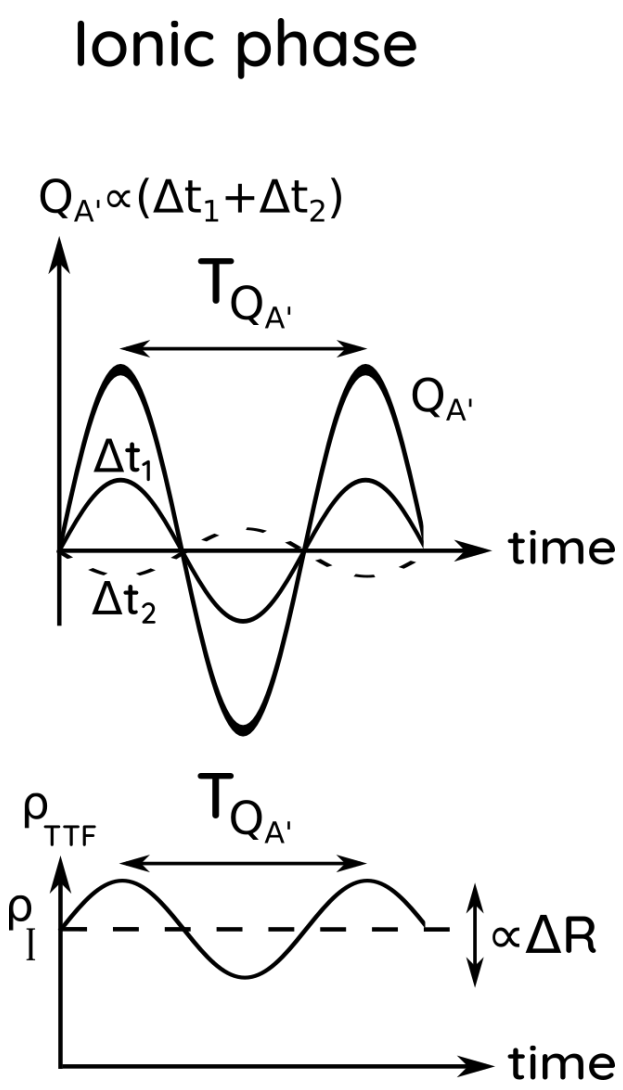

Figure 3.40: Schematic representation of the $Q_{A'}$ (ionic ferroelectric phase) mode oscillating with a period $T_{Q_{A'}}$. Consequently the reflectivity is modulated by $Q_{A'}$ with a period $T_{Q_{A'}}$

K ($T_{N-I} + 2 - 4$ K) than at 90 K. An additional investigation in the 81-90 K range will allow tracking how the response changes on approaching the phase transition. We should underline that the E_{THz} field used here (250 kV/cm) is two orders of magnitude larger than the coercitive field (few kV) swithing the ferroelectric domains at 80 K [Kobayashi et al., 2012].

Another important point will be to explore how the system responds with the amplitude of the THz field excitation to track any threshold response from the signal characteristic of the neutral phase to the one characteristic of the I ferroelectric phase.

3.11 Conclusion

In this chapter, after introducing basic key points about ferroelectricity and TTF-CA, I showed the time resolved response of this compound under THz excitation. I proved that the data can be interpreted as resulting from a resonant excitation of the Q_{Bu} ferroelectric mode by the THz pulse. This interpretation, supported by a model, is different from the one reported in the literature, which did not allow to explain all the features observed. The transient change of reflectivity induced by an intense THz pulse can be interpreted as a combination of an instantaneous response originating probably from an intermolecular CT and the response of the resonant excitation of the Bu soft mode of TTF-CA involved in the neutral-ionic phase transition whose frequency is

contained within the THz envelope ($\approx$ 1 THz). Due to symmetry considerations, this oscillation modulates the reflectivity at twice the frequency of this Bu mode. A similar approach was given by Li et al [Li et al., 2019] to interpret a paraelectric to ferroelectric phase transition induced by THz excitation in $SrTiO_3$. Using this hypothesis, I found a good agreement between the frequency extracted for the THz-driven oscillation and static spectroscopic measurements reported in the literature [Masino et al., 2003]. Approaching T_{NI} (T $\leq$ 95 K) an exponential decay is visible. We interpret this additional signal as a transient change of CT driven by the THz pulse. At 85 K, the overall shape of the photo-induced signal changes drastically, compared to those obtained at higher temperatures and is similar to the one obtained by Miyamoto et al. below T_{NI} in the Ionic phase. The fact that the signal follows linearly the THz field around t=0 ps and the non zero mean value obtained for positive delays are arguments supporting the THz induced paraelectric to ferroelectric phase transition hypothesis. However, further experiments must be performed to confirm our interpretation. What is discussed in this chapter is therefore paving the way for THz-control of molecular ferroelectric for resonant excitation of ferroelectric modes, which may induce transient dynamical response and may also allow for moving the system towards a ferroelectric phase.

Conclusion

During my thesis, I developed two experimental set-ups of particular interest in solid state physics: the THz time domain spectroscopy (THz-TDS) and the THz Pump / Optical-probe set-ups. Both set-ups are using the 250 kV/cm (measured by EOS) intense THz source available at the IPR. Its bandwidth spans from 0 to 2.5 THz. The intensity of this source can be reduced by a set of THz polarizers. A control of the humidity content allows the removal of water vapor absorption lines. Finally, we installed a cryogenic device (N_2 stream) on this THz source to perform measurements from 85 K to RT.

In the THz Pump / Optical probe set-up, the sample position is located at the focal point of the THz beam. The output of an OPA, which I carefully aligned and calibrated, was used as probe. It monitors the change of optical properties (Reflectivity/Transmission) induced by the THz excitation on some specifics bands located in the visible range (e.g CT bands). For the THz-TDS set-up, two parabolic mirrors must be installed after the sample position to collect the THz. Using EOS, it is possible to compare the THz time traces with and without the sample in order to extract the complex transmission. The THz-TDS set-up can be considered as a useful tool for sample characterization because features such quasi DC conductivity and low frequency absorption modes can be measured. Due to the intensity of the THz field, non-linear spectroscopy can also be performed.

During this thesis, I mainly focused on THz Pump - Optical Probe set-ups but both instruments are now intensively used to study different scientific topics within our department.

Concerning the study of V_2O_3, we focused on acoustic effects such as the generation and detection of strain waves in the PM phase of this compound. We compared the transient optical transmission obtained for Optical and THz excitation. The photo-induced signals were interpreted as the superposition of a depth-dependent static strain, and dynamical strain waves traveling back and forth in the sample layer. We showed that the strain waves were generated via a thermoelastic process and that different penetration depths of excitation pulses induce different strain wave profiles. Using a model, we reconstructed at any time and depth the strain wave. This study revealed the uniform profile of the THz induced strain wave within our experimental conditions. A tailoring of the strain profile can be performed by a modification of the penetration depth. This peculiarity can be interesting to perform strain-induced phase transition in V_2O_3.

Concerning the study of TTF-CA, we performed a resonant excitation of the soft phonon mode involved in the paraelectric to ferroelectric phase transition. Using symmetry considerations, we showed that, following such excitation, the reflectivity oscillates at twice the frequency of the mode. The temperature dependence of the extracted frequency matches with the softening of the Bu mode reported in the literature [Masino et al., 2017]. This comparison agrees with our interpretation, different from the one proposed by Miyamoto et al. [Miyamoto et al., 2013] discussing a THz induced motion of domain walls. Finally, on approaching T_{NI}, the enhancement of the signal, the change of profile of the instantaneous response and the long-lived photo-induced signal are arguments in favor of a THz-induced paraelectric to ferroelectric phase transition. However, this major result should be confirmed by a measurement at different excitation power and by the

detection of THz-induced Second Harmonic Generation to witness any loss of centrosymmetry.

The development of an intense single cycle THz source coupled to an optical probe during my PhD made it possible to apply THz-pump / optical-probe techniques to study out-of-equilibrium dynamics related to very different types of physics. My investigations are based on the selective excitation of a highly responsive degree of freedom, allowing to induce acoustic or optical phonon mode excitation via the use of THz radiations.

In the view of performing photo-induced phase transition we showed that THz can be the appropriate choice. For example, for the V_2O_3, it is justified by the homogeneity of the generated strain, for the TTF-CA, by the frequency of the soft mode entering within our THz bandwidth.

This work can be extended to lots of other molecular ferroelectrics, since lots of their polar modes are located in the THz range, or to other volume changing materials. In the field of multiferroics, the control of electric polarization could enable a modification of magnetic or ferroelastic properties. Such possibilities to modulate physical properties of materials by a THz pulse excitation can present several advantages : ultrafast, contactless and non destructive. Thus, it will be of great interest for THz based photonic devices such as memories, where the control of ferroelectric polarization states and resistivity is primordial.

In this manuscript, we evidenced that the out-of-equilibrium dynamics induced by THz excitation is complex, but the results obtained open promising perspectives for driving materials with THz pulses.

Bibliography

Abreu, E. [2014], 'Electronic and structural dynamics of vanadates and nickelates: effect of temperature, strain and photoexcitation'.
URL: *https://open.bu.edu/handle/2144/15110*

Abreu, E., Corder, S. N. G., Yun, S. J., Wang, S., Ramírez, J. G., West, K., Zhang, J., Kittiwatanakul, S., Schuller, I. K., Lu, J. et al. [2017], 'Ultrafast electron-lattice coupling dynamics in vo 2 and v 2 o 3 thin films', *Physical Review B* **96**(9), 094309.

Abreu, E., Wang, S., Ramírez, J. G., Liu, M., Zhang, J., Geng, K., Schuller, I. K. and Averitt, R. D. [2015], 'Dynamic conductivity scaling in photoexcited v 2 o 3 thin films', *Physical Review B* **92**(8), 085130.

Anisimov, S. I., Kapeliovich, B. L. and Perel'Man, T. L. [1974], 'Electron emission from metal surfaces exposed to ultrashort laser pulses', *Soviet Journal of Experimental and Theoretical Physics* **39**, 375–377.

Ashcroft, N. W. and Mermin, N. D. [2022], *Solid state physics*, Cengage Learning.

Auston, D. H. and Cheung, K. [1985], 'Coherent time-domain far-infrared spectroscopy', *JOSA B* **2**(4), 606–612.

Azzolina, G., Bertoni, R., Ecolivet, C., Tokoro, H., Ohkoshi, S.-I. and Collet, E. [2020], 'Landau theory for non-symmetry-breaking electronic instability coupled to symmetry-breaking order parameter applied to prussian blue analog', *Physical Review B* **102**(13), 134104.

Berozashvili, Y., Machavariani, S., Natsvlishvili, A. and Chirakadze, A. [1989], 'Dispersion of the linear electro-optic coefficients and the non-linear susceptibility in gap', *Journal of Physics D: Applied Physics* **22**(5), 682.

Boyd, R. W. [2020], *Nonlinear optics*, Academic press.

Buron-Le Cointe, M., Collet, E., Toudic, B., Czarnecki, P. and Cailleau, H. [2017], 'Back to the structural and dynamical properties of neutral-ionic phase transitions', *Crystals* **7**(10), 285.

Buron-Le Cointe, M., Lemée-Cailleau, M., Cailleau, H., Ravy, S., Bérar, J., Rouzière, S., Elkaïm, E. and Collet, E. [2006], 'One-dimensional fluctuating nanodomains in the charge-transfer molecular system ttf-ca and their first-order crystallization', *Physical review letters* **96**(20), 205503.

Buron-Le Cointe, M., Lemée-Cailleau, M., Cailleau, H., Toudic, B., Moréac, A., Moussa, F., Ayache, C. and Karl, N. [2003], 'Thermal hysteresis phenomena and mesoscopic phase coexistence around the neutral-ionic phase transition in ttf-ca and tmb-tcnq', *Physical Review B* **68**(6), 064103.

Charlemagne, D. and Handi, A. [1969], 'Sur la biréfringence et le pouvoir rotatoire du quartz dans l'infrarouge lointain à la température de l'azote liquide et à température ordinaire', *Optica Acta: International Journal of Optics* **16**(1), 53–60.

Chen, X., Karpinski, P., Shvedov, V., Boes, A., Mitchell, A., Krolikowski, W. and Sheng, Y. [2016], 'Quasi-phase matching via femtosecond laser-induced domain inversion in lithium niobate waveguides', *Optics Letters* **41**(11), 2410–2413.

Collet, E. and Azzolina, G. [2021], 'Coupling and decoupling of spin crossover and ferroelastic distortion: Unsymmetric hysteresis loop, phase diagram, and sequence of phases', *Physical Review Materials* **5**(4), 044401.

Collet, E., Lemée-Cailleau, M.-H., Buron-Le Cointe, M., Cailleau, H., Wulff, M., Luty, T., Koshihara, S.-Y., Meyer, M., Toupet, L., Rabiller, P. et al. [2003], 'Laser-induced ferroelectric structural order in an organic charge-transfer crystal', *Science* **300**(5619), 612–615.

Coutaz, J.-L. [2012], *Optoélectronique térahertz*, EDP Sciences.

Cross, L. and Newnham, R. [1987], 'History of ferroelectrics', *Ceramics and civilization* **3**, 289–305.

Dressel, M. and Peterseim, T. [2017], 'Infrared investigations of the neutral-ionic phase transition in ttf-ca and its dynamics', *Crystals* **7**(1), 17.

Duvillaret, L., Garet, F. and Coutaz, J.-L. [1996], 'A reliable method for extraction of material parameters in terahertz time-domain spectroscopy', *IEEE Journal of selected topics in quantum electronics* **2**(3), 739–746.

Edward, D. P. and Palik, I. [1985], 'Handbook of optical constants of solids'.

Fastampa, R., Pilozzi, L. and Missori, M. [2017], 'Cancellation of fabry-perot interference effects in terahertz time-domain spectroscopy of optically thin samples', *Physical Review A* **95**(6), 063831.

Fischer, B., Walther, M. and Jepsen, P. U. [2002], 'Far-infrared vibrational modes of dna components studied by terahertz time-domain spectroscopy', *Physics in Medicine & Biology* **47**(21), 3807.

Fouque, J.-P., Garnier, J., Papanicolaou, G. and Solna, K. [2007], *Wave propagation and time reversal in randomly layered media*, Vol. 56, Springer Science & Business Media.

Gallot, G., Zhang, J., McGowan, R., Jeon, T.-I. and Grischkowsky, D. [1999], 'Measurements of the thz absorption and dispersion of znte and their relevance to the electro-optic detection of thz radiation', *Applied Physics Letters* **74**(23), 3450–3452.

Giorgianni, F., Sakai, J. and Lupi, S. [2019], 'Overcoming the thermal regime for the electric-field driven Mott transition in vanadium sesquioxide', *Nat Commun* **10**(1), 1159.
URL: *http://www.nature.com/articles/s41467-019-09137-6*

Girlando, A., Masino, M., Painelli, A., Drichko, N., Dressel, M., Brillante, A., Della Valle, R. and Venuti, E. [2008], 'Direct evidence of overdamped peierls-coupled modes in the temperature-induced phase transition in tetrathiafulvalene-chloranil', *Physical Review B* **78**(4), 045103.

Glover III, R. and Tinkham, M. [1957], 'Conductivity of superconducting films for photon energies between 0.3 and 4 0 k t c', *Physical Review* **108**(2), 243.

Gournay, L. [2022], Development of an intense pulsed THz source to trigger structural and electronic response of materials, PhD thesis, Université Rennes 1.

Gray, A. X., Hoffmann, M. C., Jeong, J., Aetukuri, N., Zhu, D., Hwang, H., Brandt, N., Wen, H., Sternbach, A., Bonetti, S. et al. [2018], 'Ultrafast terahertz field control of electronic and structural interactions in vanadium dioxide', *Physical Review B* **98**(4), 045104.

Grischkowsky, D., Keiding, S., Van Exter, M. and Fattinger, C. [1990], 'Far-infrared time-domain spectroscopy with terahertz beams of dielectrics and semiconductors', *JOSA B* **7**(10), 2006–2015.

Guo, J., Chen, W., Chen, H., Zhao, Y., Dong, F., Liu, W. and Zhang, Y. [2021], 'Recent progress in optical control of ferroelectric polarization', *Advanced Optical Materials* **9**(23), 2002146.

Hansmann, P., Toschi, A., Sangiovanni, G., Saha-Dasgupta, T., Lupi, S., Marsi, M. and Held, K. [2013], 'Mott-Hubbard transition in V $_2$ O $_3$ revisited: Mott-Hubbard transition in V $_2$ O $_3$ revisited', *Phys. Status Solidi B* **250**(7), 1251–1264.
URL: *https://onlinelibrary.wiley.com/doi/10.1002/pssb.201248476*

Harris, C. R., Millman, K. J., van der Walt, S. J., Gommers, R., Virtanen, P., Cournapeau, D., Wieser, E., Taylor, J., Berg, S., Smith, N. J., Kern, R., Picus, M., Hoyer, S., van Kerkwijk, M. H., Brett, M., Haldane, A., del Río, J. F., Wiebe, M., Peterson, P., Gérard-Marchant, P., Sheppard, K., Reddy, T., Weckesser, W., Abbasi, H., Gohlke, C. and Oliphant, T. E. [2020], 'Array programming with NumPy', *Nature* **585**(7825), 357–362.
URL: *https://doi.org/10.1038/s41586-020-2649-2*

Hebling, J., Almasi, G., Kozma, I. Z. and Kuhl, J. [2002], 'Velocity matching by pulse front tilting for large-area thz-pulse generation', *Optics Express* **10**(21), 1161–1166.

Hineno, M. and Yoshinaga, H. [1974], 'Far-infrared spectra of mono-, di-and tri-saccharides in 50-16 cm- 1 at liquid helium temperature', *Spectrochimica Acta Part A: Molecular Spectroscopy* **30**(2), 411–416.

Hirori, H., Doi, A., Blanchard, F. and Tanaka, K. [2011], 'Single-cycle terahertz pulses with amplitudes exceeding 1 mv/cm generated by optical rectification in linbo 3', *Applied Physics Letters* **98**(9), 091106.

Hoffmann, M. C. and Fülöp, J. A. [2011], 'Intense ultrashort terahertz pulses: generation and applications', *Journal of Physics D: Applied Physics* **44**(8), 083001.

Huitric, G., Rodriguez-Fano, M., Gournay, L., Godin, N., Herve, M., Privault, G., Tranchant, J., Khaldi, Z., Cammarata, M., Collet, E. and Odin, C. [2022], 'Impact of the terahertz and optical pump penetration depths on generated strain waves temporal profiles in a v_2o_3 thin film.', *Faraday Discussions* .

Hunter, J. D. [2007], 'Matplotlib: A 2d graphics environment', *Computing in Science & Engineering* **9**(3), 90–95.

Iwai, S., Ishige, Y., Tanaka, S., Okimoto, Y., Tokura, Y. and Okamoto, H. [2006], 'Coherent control of charge and lattice dynamics in a photoinduced neutral-to-ionic transition of a charge-transfer compound', *Physical review letters* **96**(5), 057403.

Jacobsen, C. S. and Torrance, J. [1983], 'Behavior of charge-transfer absorption upon passing through the neutral-ionic phase transition', *The Journal of Chemical Physics* **78**(1), 112–115.

Jepsen, P. U., Cooke, D. G. and Koch, M. [2011], 'Terahertz spectroscopy and imaging–modern techniques and applications', *Laser & Photonics Reviews* **5**(1), 124–166.

Jewariya, M., Nagai, M. and Tanaka, K. [2010], 'Ladder climbing on the anharmonic intermolecular potential in an amino acid microcrystal via an intense monocycle terahertz pulse', *Physical review letters* **105**(20), 203003.

Kalcheim, Y., Adda, C., Salev, P., Lee, M.-H., Ghazikhanian, N., Vargas, N. M., del Valle, J. and Schuller, I. K. [2020], 'Structural manipulation of phase transitions by self-induced strain in geometrically confined thin films', *Advanced Functional Materials* **30**(49), 2005939.

Kampfrath, T., Tanaka, K. and Nelson, K. A. [2013], 'Resonant and nonresonant control over matter and light by intense terahertz transients', *Nature Photonics* **7**(9), 680–690.

Katsidis, C. C. and Siapkas, D. I. [2002], 'General transfer-matrix method for optical multilayer systems with coherent, partially coherent, and incoherent interference', *Applied optics* **41**(19), 3978–3987.

Kaushik, M., Ng, B. W.-H., Fischer, B. M. and Abbott, D. [2012], 'Terahertz scattering by two phased media with optically soft scatterers', *Journal of Applied Physics* **112**(11), 113112.

Keer, H., Dickerson, D., Kuwamoto, H., Barros, H. and Honig, J. [1976], 'Heat capacity of pure and doped V2O3 single crystals', *Journal of Solid State Chemistry* **19**(1), 95–102.
URL: *https://linkinghub.elsevier.com/retrieve/pii/0022459676901559*

Kitaeva, G. K. [2008], 'Terahertz generation by means of optical lasers', *Laser Physics Letters* **5**(8), 559–576.

Kobayashi, K., Horiuchi, S., Kumai, R., Kagawa, F., Murakami, Y. and Tokura, Y. [2012], 'Electronic ferroelectricity in a molecular crystal with large polarization directing antiparallel to ionic displacement', *Physical review letters* **108**(23), 237601.

Koshihara, S., Ishikawa, T., Okimoto, Y., Onda, K., Fukaya, R., Hada, M., Hayashi, Y., Ishihara, S. and Luty, T. [2022], 'Challenges for developing photo-induced phase transition (pipt) systems: From classical (incoherent) to quantum (coherent) control of pipt dynamics', *Physics Reports* **942**, 1–61.

Koshihara, S.-y., Takahashi, Y., Sakai, H., Tokura, Y. and Luty, T. [1999], 'Photoinduced cooperative charge transfer in low-dimensional organic crystals'.

Kuroda, N. and Fan, H. [1977], 'Raman scattering and phase transitions of v 2 o 3', *Physical Review B* **16**(11), 5003.

Lantz, G., Mansart, B., Grieger, D., Boschetto, D., Nilforoushan, N., Papalazarou, E., Moisan, N., Perfetti, L., Jacques, V. L., Le Bolloc'h, D. et al. [2017], 'Ultrafast evolution and transient phases of a prototype out-of-equilibrium mott–hubbard material', *Nature communications* **8**(1), 1–7.

Le Cointe, M., Lemée-Cailleau, M., Cailleau, H., Toudic, B., Toupet, L., Heger, G., Moussa, F., Schweiss, P., Kraft, K. and Karl, N. [1995], 'Symmetry breaking and structural changes at the neutral-to-ionic transition in tetrathiafulvalene-p-chloranil', *Physical Review B* **51**(6), 3374.

Lee, Y.-S. [2009], *Principles of terahertz science and technology*, Vol. 170, Springer Science & Business Media.

Levchuk, A., Wilk, B., Vaudel, G., Labbé, F., Arnaud, B., Balin, K., Szade, J., Ruello, P. and Juvé, V. [2020], 'Coherent acoustic phonons generated by ultrashort terahertz pulses in nanofilms of metals and topological insulators', *Physical Review B* **101**(18), 180102.

Li, X., Qiu, T., Zhang, J., Baldini, E., Lu, J., Rappe, A. M. and Nelson, K. A. [2019], 'Terahertz field–induced ferroelectricity in quantum paraelectric srtio3', *Science* **364**(6445), 1079–1082.

Liu, M., Hwang, H. Y., Tao, H., Strikwerda, A. C., Fan, K., Keiser, G. R., Sternbach, A. J., West, K. G., Kittiwatanakul, S., Lu, J. et al. [2012], 'Terahertz-field-induced insulator-to-metal transition in vanadium dioxide metamaterial', *Nature* **487**(7407), 345–348.

Liu, M. K., Pardo, B., Zhang, J., Qazilbash, M. M., Yun, S. J., Fei, Z., Shin, J.-H., Kim, H.-T., Basov, D. N. and Averitt, R. D. [2011], 'Photoinduced Phase Transitions by Time-Resolved Far-Infrared Spectroscopy in V 2 O 3', *Phys. Rev. Lett.* **107**(6), 066403.
URL: *https://link.aps.org/doi/10.1103/PhysRevLett.107.066403*

Luo, Y., Su, F., Zhang, C., Zhong, L., Pan, S., Xu, S., Wang, H., Dai, J. and Li, G. [2017], 'Terahertz transport dynamics in the metal-insulator transition of v2o3 thin film', *Optics Communications* **387**, 385–389.
URL: *https://www.sciencedirect.com/science/article/pii/S0030401816309580*

Mansart, B., Boschetto, D., Sauvage, S., Rousse, A. and Marsi, M. [2010], 'Mott transition in cr-doped v2o3 studied by ultrafast reflectivity: electron correlation effects on the transient response', *EPL (Europhysics Letters)* **92**(3), 37007.

Mariette, C., Lorenc, M., Cailleau, H., Collet, E., Guérin, L., Volte, A., Trzop, E., Bertoni, R., Dong, X., Lépine, B. et al. [2021], 'Strain wave pathway to semiconductor-to-metal transition revealed by time-resolved x-ray powder diffraction', *Nature communications* **12**(1), 1–11.

Masino, M., Castagnetti, N. and Girlando, A. [2017], 'Phenomenology of the neutral-ionic valence instability in mixed stack charge-transfer crystals', *Crystals* **7**(4), 108.

Masino, M., Girlando, A. and Soos, Z. G. [2003], 'Evidence for a soft mode in the temperature induced neutral-ionic transition of ttf-ca', *Chemical physics letters* **369**(3-4), 428–433.

Masson, J.-B. and Gallot, G. [2006], 'Terahertz achromatic quarter-wave plate', *Optics letters* **31**(2), 265–267.

Matsuda, O., Larciprete, M. C., Li Voti, R. and Wright, O. B. [2015], 'Fundamentals of picosecond laser ultrasonics', *Ultrasonics* **56**, 3–20.
URL: *https://linkinghub.elsevier.com/retrieve/pii/S0041624X14001541*

Matsuda, O. and Wright, O. [2002], 'Reflection and transmission of light in multilayers perturbed by picosecond strain pulse propagation', *JOSA B* **19**(12), 3028–3041.

McWhan, D., Menth, A., Remeika, J., Brinkman, W. and Rice, T. [1973], 'Metal-insulator transitions in pure and doped v 2 o 3', *Physical Review B* **7**(5), 1920.

Misochko, O., Tani, M., Sakai, K., Kisoda, K., Nakashima, S., Andreev, V. and Chudnovsky, F. [1998], 'Optical study of the mott transition in v 2 o 3: comparison of time-and frequency-domain results', *Physical Review B* **58**(19), 12789.

Mitsas, C. and Siapkas, D. [1995], 'Generalized matrix method for analysis of coherent and incoherent reflectance and transmittance of multilayer structures with rough surfaces, interfaces, and finite substrates', *Applied Optics* **34**(10), 1678–1683.

Miyamoto, T., Yada, H., Yamakawa, H. and Okamoto, H. [2013], 'Ultrafast modulation of polarization amplitude by terahertz fields in electronic-type organic ferroelectrics', *Nature Communications* **4**(1), 1–9.

Miyamoto, T., Yamakawa, H., Morimoto, T. and Okamoto, H. [2018], 'Control of electronic states by a nearly monocyclic terahertz electric-field pulse in organic correlated electron materials', *Journal of Physics B: Atomic, Molecular and Optical Physics* **51**(16), 162001.

Moreac, A., Girard, A., Delugeard, Y. and Marqueton, Y. [1996], 'The neutral-to-ionic phase transition of ttf-ca: A raman and infrared study versus temperature at atmospheric pressure', *Journal of Physics: Condensed Matter* **8**(20), 3553.

Morimoto, T., Miyamoto, T. and Okamoto, H. [2017], 'Ultrafast electron and molecular dynamics in photoinduced and electric-field-induced neutral–ionic transitions', *Crystals* **7**(5), 132.

Morimoto, T., Miyamoto, T., Yamakawa, H., Terashige, T., Ono, T., Kida, N. and Okamoto, H. [2017], 'Terahertz-field-induced large macroscopic polarization and domain-wall dynamics in an organic molecular dielectric', *Physical Review Letters* **118**(10), 107602.

Mott, N. F. and Peierls, R. [1937], 'Discussion of the paper by de Boer and Verwey', *Proc. Phys. Soc.* **49**(4S), 72–73.
URL: *https://iopscience.iop.org/article/10.1088/0959-5309/49/4S/308*

Müller, K., Berlinger, W. and Waldner, F. [1968], 'Characteristic structural phase transition in perovskite-type compounds', *Physical Review Letters* **21**(12), 814.

Nahata, A., Weling, A. S. and Heinz, T. F. [1996], 'A wideband coherent terahertz spectroscopy system using optical rectification and electro-optic sampling', *Applied physics letters* **69**(16), 2321–2323.

Nasu, K. [2004], *Photoinduced phase transitions*, World Scientific.

Neu, J. and Schmuttenmaer, C. A. [2018], 'Tutorial: An introduction to terahertz time domain spectroscopy (thz-tds)', *Journal of Applied Physics* **124**(23), 231101.

Nicoletti, D. and Cavalleri, A. [2016], 'Nonlinear light–matter interaction at terahertz frequencies', *Advances in Optics and Photonics* **8**(3), 401–464.

Okamoto, H., Ishige, Y., Tanaka, S., Kishida, H., Iwai, S. and Tokura, Y. [2004], 'Photoinduced phase transition in tetrathiafulvalene-p-chloranil observed in femtosecond reflection spectroscopy', *Physical Review B* **70**(16), 165202.

Okimoto, Y., Peng, X., Tamura, M., Morita, T., Onda, K., Ishikawa, T., Koshihara, S., Todoroki, N., Kyomen, T. and Itoh, M. [2009], 'Ultrasonic propagation of a metallic domain in pr 0.5 ca 0.5 coo 3 undergoing a photoinduced insulator-metal transition', *Physical review letters* **103**(2), 027402.

Planken, P. C., Nienhuys, H.-K., Bakker, H. J. and Wenckebach, T. [2001], 'Measurement and calculation of the orientation dependence of terahertz pulse detection in znte', *JOSA B* **18**(3), 313–317.

Qazilbash, M. M., Schafgans, A. A., Burch, K. S., Yun, S. J., Chae, B. G., Kim, B. J., Kim, H. T. and Basov, D. N. [2008], 'Electrodynamics of the vanadium oxides V O 2 and V 2 O 3', *Phys. Rev. B* **77**(11), 115121.
URL: *https://link.aps.org/doi/10.1103/PhysRevB.77.115121*

Reimann, K. [2007], 'Table-top sources of ultrashort thz pulses', *Reports on Progress in Physics* **70**(10), 1597.

Roggenbuck, A., Schmitz, H., Deninger, A., Mayorga, I. C., Hemberger, J., Güsten, R. and Grüninger, M. [2010], 'Coherent broadband continuous-wave terahertz spectroscopy on solid-state samples', *New Journal of Physics* **12**(4), 043017.

Ruello, P. and Gusev, V. E. [2015], 'Physical mechanisms of coherent acoustic phonons generation by ultrafast laser action', *Ultrasonics* **56**, 21–35.
URL: *https://linkinghub.elsevier.com/retrieve/pii/S0041624X1400153X*

Salén, P., Basini, M., Bonetti, S., Hebling, J., Krasilnikov, M., Nikitin, A. Y., Shamuilov, G., Tibai, Z., Zhaunerchyk, V. and Goryashko, V. [2019], 'Matter manipulation with extreme terahertz light: Progress in the enabling thz technology', *Physics reports* **836**, 1–74.

Schick, D., Herzog, M., Bojahr, A., Leitenberger, W., Hertwig, A., Shayduk, R. and Bargheer, M. [2014], 'Ultrafast lattice response of photoexcited thin films studied by X-ray diffraction', *Structural Dynamics* **1**(6), 064501.
URL: *http://aca.scitation.org/doi/10.1063/1.4901228*

Scott, J. [2007], 'Applications of modern ferroelectrics', *science* **315**(5814), 954–959.

Thomsen, C., Grahn, H. T., Maris, H. J. and Tauc, J. [1986], 'Surface generation and detection of phonons by picosecond light pulses', *Phys. Rev. B* **34**(6), 4129–4138.
URL: *https://link.aps.org/doi/10.1103/PhysRevB.34.4129*

Torrance, J., Vazquez, J., Mayerle, J. and Lee, V. [1981], 'Discovery of a neutral-to-ionic phase transition in organic materials', *Physical Review Letters* **46**(4), 253.

Tropf, W. J., Thomas, M. E. and Harris, T. J. [1995], 'Properties of crystals and glasses', *Handbook of optics* **2**, 33–.

Uemura, H. and Okamoto, H. [2010], 'Direct detection of the ultrafast response of charges and molecules in the photoinduced neutral-to-ionic transition of the organic tetrathiafulvalene-p-chloranil solid', *Physical review letters* **105**(25), 258302.

Valasek, J. [1920], 'Minutes of the washington meeting, april 23 and 24, 1920', *Phys. Rev.* **15**, 505–564.
URL: *https://link.aps.org/doi/10.1103/PhysRev.15.505*

Valasek, J. [1921], 'Piezo-electric and allied phenomena in rochelle salt', *Physical review* **17**(4), 475.

Vecchio, I. L., Baldassarre, L., D'Apuzzo, F., Limaj, O., Nicoletti, D., Perucchi, A., Fan, L., Metcalf, P., Marsi, M. and Lupi, S. [2015], 'Optical properties of v 2 o 3 in its whole phase diagram', *Physical Review B* **91**(15), 155133.

Vicario, C., Jazbinsek, M., Ovchinnikov, A. V., Chefonov, O. V., Ashitkov, S. I., Agranat, M. B. and Hauri, C. P. [2015], 'High efficiency thz generation in dstms, dast and oh1 pumped by cr:forsterite laser', *Opt. Express* **23**(4), 4573–4580.
URL: *http://www.osapublishing.org/oe/abstract.cfm?URI=oe-23-4-4573*

Vicario, C., Monoszlai, B., Lombosi, C., Mareczko, A., Courjaud, A., Fülöp, J. and Hauri, C. [2013], 'Pump pulse width and temperature effects in lithium niobate for efficient thz generation', *Optics Letters* **38**(24), 5373–5376.

Virtanen, P., Gommers, R., Oliphant, T. E., Haberland, M., Reddy, T., Cournapeau, D., Burovski, E., Peterson, P., Weckesser, W., Bright, J., van der Walt, S. J., Brett, M., Wilson, J., Millman, K. J., Mayorov, N., Nelson, A. R. J., Jones, E., Kern, R., Larson, E., Carey, C. J., Polat, İ., Feng, Y., Moore, E. W., VanderPlas, J., Laxalde, D., Perktold, J., Cimrman, R., Henriksen, I., Quintero, E. A., Harris, C. R., Archibald, A. M., Ribeiro, A. H., Pedregosa, F., van Mulbregt, P. and SciPy 1.0 Contributors [2020], 'SciPy 1.0: Fundamental Algorithms for Scientific Computing in Python', *Nature Methods* **17**, 261–272.

Wang, Y., Zhao, Z., Qin, J., Liu, H., Liu, A. and Xu, M. [2020], 'Rapid in situ analysis of l-histidine and α-lactose in dietary supplements by fingerprint peaks using terahertz frequency-domain spectroscopy', *Talanta* **208**, 120469.

Winey, J., Gupta, Y. and Hare, D. [2001], 'R-axis sound speed and elastic properties of sapphire single crystals', *Journal of Applied Physics* **90**(6), 3109–3111.

Wu, Q. and Zhang, X.-C. [1996], 'Ultrafast electro-optic field sensors', *Applied physics letters* **68**(12), 1604–1606.

Yang, M.-M. and Alexe, M. [2018], 'Light-induced reversible control of ferroelectric polarization in bifeo3', *Advanced Materials* **30**(14), 1704908.

Yeh, K.-L., Hoffmann, M., Hebling, J. and Nelson, K. A. [2007], 'Generation of 10 μ j ultrashort terahertz pulses by optical rectification', *Applied Physics Letters* **90**(17), 171121.

Yelon, W. and Keem, J. [1979], 'The elastic constants of v2o3 in the insulating phase', *Solid State Communications* **29**(11), 775–777.

Zelsmann, H., Excoffon, P. and Marechal, Y. [1984], 'Far-infrared spectra of imidazole monocrystals', *Chemical physics letters* **110**(3), 285–290.

Zewail, A. H. [2000], 'Femtochemistry: Atomic-scale dynamics of the chemical bond', *The Journal of Physical Chemistry A* **104**(24), 5660–5694.

Zhang, W. and Xiong, R.-G. [2012], 'Ferroelectric metal–organic frameworks', *Chemical reviews* **112**(2), 1163–1195.

UNIVERSITÉ DE RENNES 1

Titre : Dynamiques hors équilibre ultra-rapides dans les matériaux pilotées par des excitations Terahertz et/ou Optique

Mots clés : TeraHertz, pompe-sonde, photo-induit, phénomènes ultra-rapides

Résumé : Il est possible de modifier les propriétés des matériaux à l'aide d'impulsions lumineuses ultra-brèves. Aussi, la génération d'impulsions THz monocycles à champs électriques forts permet un contrôle de l'état excité différent de celui proposé par excitation visible.

Cette thèse traite des dynamiques hors-équilibre induites par des impulsions THz intenses et ouvre de nouvelles perspectives dans le but de contrôler les propriétés des matériaux via l'excitation THz.

Dans le V_2O_3, l'important saut de volume associé à la transition de Mott suggère qu'une transition de phase induite par onde de déformation est réalisable. Ainsi, dans cette thèse, nous avons étudié la génération et la propagation d'ondes de déformations dans la phase PM du V_2O_3. En comparant les résultats obtenus suite à une excitation THz ou optique, nous avons conclu que les disparités dans les réponses photo-induites sont attribuables aux différences de profils de ces ondes. Ceux-ci sont eux-mêmes déterminés par la longueur de pénétration de l'impulsion excitatrice

Aussi, nous avons étudié la réponse du TTF-CA à une excitation THz. A l'aide de considérations de symétrie et d'un modèle adapté, nous avons montré que le signal obtenu dans la phase paraélectrique, peut être interprété comme la réponse à une excitation résonante d'un mode mou ferroélectrique impliqué dans la transition de phase paraélectrique à ferroélectrique de ce composé.

Title : Ultrafast out of equilibrium dynamics of materials driven by terahertz and/or optical excitations

Keywords : TeraHertz, pump-probe, photo-induced, ultrafast phenomena

Abstract : Nowadays, it is possible to tune material properties and induce new stable macroscopic order using ultrashort light pulses. Recent developments in THz generation techniques allow to obtain THz single cycles with strong electric fields. This type of excitation provides a different control of the target excited state from the one provided by optical excitations.

This thesis is mainly focusing on the study of out-of-equilibrium dynamics induced by intense THz pulses and opens new perspectives to achieve a control of material properties via a THz excitation.

In V_2O_3, the important change of volume associated with the Mott transition suggests that a strain-induced phase transition can be achieved. Thus, in this thesis, we studied the generation and propagation of themoelastically generated strain waves in the PM phase of V_2O_3 thin films. By comparing the material response to THz or Optical excitation we showed that the disparities in the photo-induced responses are attributed to the difference in strain wave profile. This profile is itself determined by the pump penetration depth.

We also studied the response of TTF-CA to a THz excitation. Using symmetry considerations and an appropriate model we showed that the signal obtained in the paraelectric phase, can be interpreted as the resonant excitation of the ferroelectric soft mode involved in the paraelectric to ferroelectric phase transition in TTF-CA.